Technische Universität München

Department of Chemistry and Catalysis Research Center

Chair of Technical Electrochemistry

Methods to elucidate fundamental electrolyte reactions in Li-ion-Batteries

Sophie Solchenbach

Vollständiger Abdruck der von der Fakultät für Chemie der Technischen Universität München zur Erlangung des akademischen Grades eines

Doktors der Naturwissenschaften (Dr. rer. nat.)

genehmigten Dissertation.

Vorsitzender:	Prof. Dr.-Ing. Kai-Olaf Hinrichsen
Prüfer der Dissertation:	1. Prof. Dr. Hubert A. Gasteiger
	2. Prof. Dr. Tom Nilges
	3. Prof. Dr. Brett L. Lucht

Die Dissertation wurde am 25.09.2018 bei der Technischen Universität München eingereicht und durch die Fakultät für Chemie am 25.10.2018 angenommen.

Abstract

Electrolyte side reactions are a main reason for the limited lifetime of high-voltage Li-ion batteries. In this thesis, the Li-ion electrolyte decomposition reactions were investigated by combining on-line electrochemical mass spectrometry (OEMS), Fourier-transform infrared (FTIR) spectroscopy, nuclear magnetic resonance (NMR) spectroscopy and electrochemical impedance spectroscopy. As part of this thesis, a micro-reference electrode setup for impedance measurements of individual electrodes in a full cell was developed. Using both full cells with conventional electrolyte mixtures and single-solvent model electrolytes in a 2-compartment battery cell, we elucidated the reductive decomposition of electrolyte components and their solid electrolyte interphase (SEI) products, the influence of additive concentrations, electrolyte oxidation and related follow-up reactions, as well as the effect of transition metal dissolution on the SEI stability.

Kurzfassung

Elektrolyt-Nebenreaktionen sind ein Hauptgrund für die begrenzte Lebensdauer von Hochspannungs-Lithium-Ionen-Batterien. In dieser Arbeit wurden Zersetzungsreaktionen von Lithium-Ionen-Elektrolyten mittels einer Kombination von on-line elektrochemischer Massenspektrometrie (OEMS), Fourier-Transform-Infrarotspektroskopie (FTIR), Kernspinresonanzspektroskopie (NMR) und elektrochemischer Impedanzspektroskopie untersucht. Als Teil dieser Arbeit wurde eine Mikro-Referenzelektrode für die Impedanzmessung von einzelnen Elektroden in Batterie-Vollzellen entwickelt. Unter Verwendung von Vollzellen mit herkömmlichen Elektrolytmischungen sowie Modellelektrolyten aus einzelnen Lösungsmitteln in 2-Kompartment-Zellen wurden die reduktive Zersetzung von Elektrolyt-Bestandteilen und deren Produkte in der Festelektrolyt-Grenzschicht (SEI, engl. solid electrolyte interphase), die Auswirkungen von Additiv-Konzentrationen, Elektrolytoxidation und zugehörige Folgereaktionen, und der Effekt von Übergangsmetall-Ionen auf die Stabilität der SEI aufgeklärt.

Contents

List of Acronyms

Abbreviation	**Description**
ATR-FTIR	Attenuated total reflection Fourier-transform infrared spectroscopy
BET	Brunauer-Emmett-Teller
DiFEC	Difluoroethylene carbonate
DMSO	Dimethyl sulfoxide
EC	Ethylene carbonate
EDX	Energy-dispersive X-ray spectroscopy
FEC	Fluoroethylene carbonate
GWRE	Gold wire micro-reference electrode
LCO	Lithium cobalt oxide
LEDC	Lithium ethylene dicarbonate
LFP	Lithium iron phosphate
LNMO	Lithium nickel manganese spinel
NCA	Lithium nickel cobalt aluminum oxide
NMC	Lithium nickel manganese cobalt oxide
NMR	Nuclear magnetic resonance
OEMS	On-line electrochemical mass spectrometry
OCV	Open circuit voltage
PC	Propylene carbonate
SEI	Solid electrolyte interphase
TEM	Transmission electron microscopy
VEC	Vinyl ethylene carbonate
VC	Vinylene carbonate
XPS	X-ray photoelectron spectroscopy

1 Introduction

With its introduction in 1991 by Sony, Li-ion battery technology emerged to be a keystone for portable electronic devices, such as laptops, cameras and smartphones. Recently, Li-ion batteries have been implemented to power electric vehicles, reducing their CO_2 emissions as long as the electricity used for charging the battery is partially produced from a renewable source. For example, the current European Union electricity mix corresponds to CO_2 emissions of ~100 g/km for a fully electric vehicle, compared to gasoline- or diesel-powered cars with an average CO_2 emission of 120-180 g/km.[1]

Still, Li-ion batteries for automotive applications struggle with three main issues that need to be overcome to make electric vehicles succeed in the mass market: 1) Higher volumetric energy densities to achieve longer driving ranges, 2) faster charging rates, and 3) lower cost.[2,3] Over the last 27 years, the energy density increased from 200 Wh/L (80 Wh/kg)[4] in the original Sony cell to almost 650 Wh/L (250 Wh/kg) on the cell level.[5,6] Yet, to achieve target energy densities of more than 800 Wh/L and 300 Wh/kg, new low-cost active materials with significantly higher specific energies are needed.[2] Although a number of materials that fulfill these requirements are already tested in lab-scale or prototype cells, their use in commercial applications is so far prevented by their limited lifespan.

While conventional liquid electrolyte solutions for Li-ion batteries have little effect on cell energy density, side reactions between electrolyte and active materials play a crucial role in the lifetime of Li-ion cells. Optimized electrolyte formulations can significantly improve capacity retention, gas evolution and resistance growth of cells with new materials[7,8] or enable higher potential ranges for established cell chemistries.[9–11] However, many electrolyte/electrode interactions are not yet fully

understood. Furthermore, “cross-talk”-phenomena, where species produced at one electrode are transported through the electrolyte and react with the other electrode, can have tremendous influence on the overall cell performance.[12,13] Hence, the scope of this thesis is to develop and apply methods which help to gain new insights into the fundamental decomposition reactions of lithium-ion battery electrolytes.

1.1 The working principles of Li-ion batteries

Today's Li-ion batteries contain a lithium transition metal oxide or -phosphate positive electrode, a graphite negative electrode and a Li-ion conducting electrolyte (see Figure 1.1). To provide a sufficiently large electrochemically active surface area, the electrodes consist of micrometer-sized active material particles that are fixed with a polymer binder onto a current collector metal foil. The electrodes are electronically separated by a porous, electrolyte-filled polymer membrane, the so-called separator. During charge, lithium ions de-intercalate from the cathode material (i.e., $LiMO_2$, see equation (1)), move through the electrolyte and insert into the graphite host structure (see equation (2)). The electrons are transferred through an external electrical circuit.

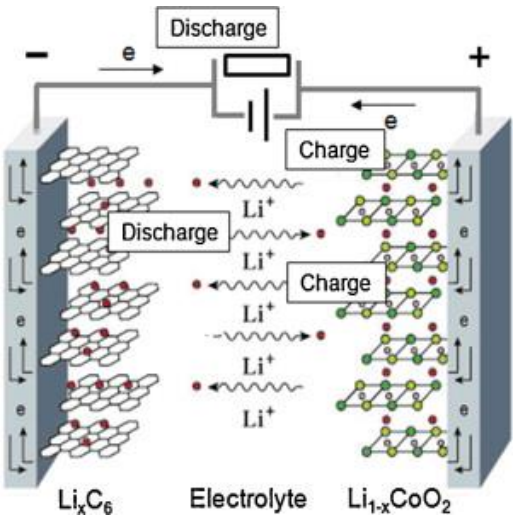

Figure 1.1: Schematic drawing of a Li-ion battery taken from ref. 14. Reprinted under a Creative Commons BY-NC-ND 4.0 license.

$$LiMO_2 \rightarrow Li_{1-x}MO_2 + x\,Li^+ + x\,e^- \quad (1)$$

$$C_6 + x\,Li^+ + x\,e^- \rightarrow Li_xC_6 \quad (2)$$

The process is inversed during discharge, releasing the stored electrical energy via the external circuit. Based on convention, the negative electrode is referred to as "anode" and the positive electrode is termed "cathode", independent of the reaction

direction on the respective electrode (i.e., oxidation or reduction). The capacity achieved during charge or discharge is directly linked to the amount of lithium that is transferred, whereas the corresponding cell voltage is determined by the potential difference between the two electrode reactions. Upon lithium (de)intercalation, the host materials are reduced (oxidized), but their morphology remains intact, making the electrode reactions highly reversible. Hence, the coulombic efficiency of a full cell, i.e., the ratio of discharge to charge capacity, is typically close to 100%. In the following, the main cell components of state-of-the-art commercial Li-ion batteries are briefly described.

The cathode material provides the active lithium that can be shuttled between the electrodes, and thus governs the capacity of the full cell. To further maximize cell energy density, a high operating potential of the cathode is desired. All currently commercially used cathode materials rely on 3d transition metals (Mn, Fe, Co, Ni) as active redox centers. Based on their structure, cathode materials can be classified into three categories: 1) phospho-olivines, 2) spinel oxides, and 3) layered oxides (see Figure 1.2). The most common olivine cathode material is $LiFePO_4$ (LFP) with a theoretical specific capacity of 170 mAh/g, but relatively low voltage of 3.4 V vs. Li^+/Li. Still, its longevity, thermal stability and low cost make it suitable for stationary applications.[15] Spinel-type materials with the formula $LiMn_2O_4$ deliver a theoretical specific capacity of 148 mAh/g around 4.0 V vs. Li^+/Li. In theory, the spinel structure can accommodate lithium up to a stoichiometry of $Li_2Mn_2O_4$, which yields a specific capacity of 285 mAh/g upon its complete delithiation. However, the intercalation of lithium into $Li_xMn_2O_4$ at $x > 1$ is associated with a strong Jahn-Teller distortion of the host lattice, which leads to severe material degradation during extended cycling.[16] In practical applications, lithium contents > 1 are therefore omitted. Even at $x \leq 1$, the $Li_xMn_2O_4$ host lattice suffers from the dissolution of manganese especially at high temperatures, which compromises the cathode capacity and induces further side reactions at the anode (see chapter 1.3). Layered oxides ($LiMO_2$, M = Mn, Ni, Co) are thermally less stable than spinels and olivines, evolving O_2 during a thermal runaway that can act as a fire accelerant.[17] Nevertheless, they are currently the most prevalent cathode materials in Li-ion cells.[4] While pure $LiNiO_2$ and $LiMnO_2$ were abandoned due to structural

instabilities,[18,19] $LiCoO_2$ (LCO) was successfully employed in the first commercial Li-ion cells by Sony in 1991. Today, $LiNi_xMn_yCo_zO_2$ (NMC, x+y+z = 1) materials are widespread for automotive applications,[4] as they show an improved thermal stability over the original LCO[20] and contain less cobalt, which is costly and mined under often hazardous conditions. The theoretical specific capacity of layered oxides is 275 mAh/g, but high degrees of delithiation lead to material decomposition: At lithium contents ≤ 0.2, lattice oxygen is released accompanied by the formation of an oxygen-depleted spinel- or rocksalt-like surface layer, which significantly increases the charge transfer resistance of the material and triggers electrolyte decomposition.[21] Therefore, the practical capacity of NMCs and LCO is limited to 150-180 mAh/g by adjusting the upper cutoff potential. New materials with high Ni contents (60-85%) deliver a larger share of their capacity at lower potentials, effectively increasing the specific capacity for a given cut-off potential. For example, the Ni-rich derivative $LiNi_{0.8}Co_{0.15}Al_{0.05}O_2$ (NCA) used in Tesla's model S reaches a practical capacity of 190 mAh/g below 4.2 V vs. Li^+/Li.[2,20] However, Ni-rich layered oxides are also more prone to thermal decomposition[22,23] and reactions with ambient humidity,[24] which is why current research focuses on stabilizing the surface of Ni-rich layered oxide.

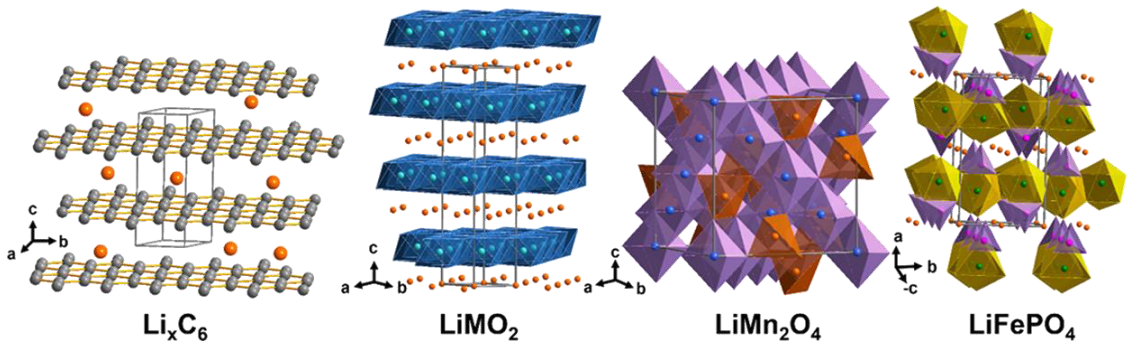

Figure 1.2: Structures of Li_xC_6, layered $LiMO_2$, spinel $LiMn_2O_4$ and olivine $LiFePO_4$. Reprinted from ref. 5 under the open-access ACS AuthorChoice agreement.

The anode of present Li-ion batteries consists of natural or synthetic graphite, replacing the so-called "hard carbon" originally used in Sony's first commercial Li-ion battery. With ~360 mAh/g (theoretical: 372 mAh/g), the specific capacity of graphite is more than two-fold higher compared to cathode materials, yet the volumetric capacity, crucial for mobile applications, is ~800 mAh/cm^3 for both

graphite and cathode active materials, due to the higher density of transition metal oxides.[6] The intercalation of lithium into Li_xC_6 occurs during two main plateaus at 70 mV ($1 > x > 0.5$) and 125 mV vs. Li^+/Li ($0.5 > x > 0.2$).[25] As the operating potential of graphite is lower than the reductive stability of common electrolytes, a so-called solid electrolyte interface (SEI, see chapter 1.3 for details) forms on its surface. Due to the proximity of the graphite lithium intercalation potential to the Li^+/Li potential, graphite is at risk for lithium plating during lithiation (i.e., charging of the battery), leading to the loss of active lithium and the formation of lithium dendrites, which can grow through the separator and cause cell short-circuits. To prevent lithium plating caused by unintended variations of the cathode areal capacities and by misalignments of the electrode stack, the anode is geometrically and capacitively oversized. However, lithium plating can still occur if concentration gradients across the anode or high overpotentials for lithium intercalation lead to local anode potentials below 0 V vs. Li^+/Li. Consequently, the charging rate in today's lithium ion batteries is limited by the performance of the anode. An approach to increase the attainable charging rate is to use particles with a different morphology or orientation, which facilitate ion transport through the electrode pores. Alternatively, hard carbons are re-examined as fast-charging anode materials: While their specific capacity and coulombic efficiency is lower compared to graphite,[26] the higher average potential makes them less prone to lithium plating.

As the high voltage of Li-ion cells exceed the potential stability of aqueous electrolytes (~1.23 V), Li-ion electrolytes consist of a lithium salt dissolved in an aprotic solvent. Standard solvents are mixtures of ethylene carbonate and linear carbonates, such as diethyl-, dimethyl- or ethylmethyl carbonate (see Figure 1.3), where EC ensures a dissolution of the salt due to its high dielectric constant and the formation of a stable SEI,[27] while the linear carbonates decrease the electrolyte viscosity and freezing point.[28]

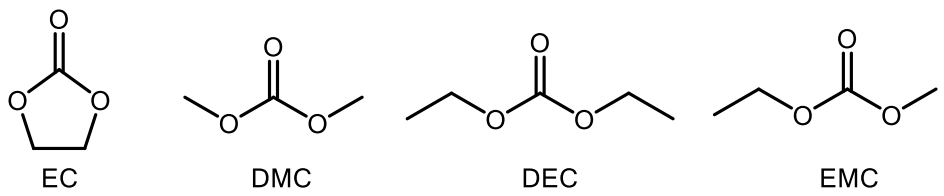

Figure 1.3: Solvents for Li-ion battery electrolytes: Ethylene carbonate (EC), dimethyl carbonate (DMC), diethyl carbonate (DEC) and ethylmethyl carbonate (EMC)

Many electrolyte formulations also contain additives which improve the SEI layer properties (see chapter 1.3), protect the cell during overcharge or scavenge water. As salt, $LiPF_6$ is used because of its high solubility and conductivity, its compatibility with graphite anodes and its ability to passivate the aluminum cathode current collector against anodic dissolution.[28,29] The use of $LiPF_6$ however limits battery operation to < 60 °C, as $LiPF_6$ disproportionates into insoluble LiF and PF_5 at higher temperatures.[30] The final electrolyte solution has a electrochemical stability window of ~4 V (~0.8-4.8 V vs. Li^+/Li),[29] whereby lower potentials on the anode lead to reductive SEI formation (see chapter 1.3), while the electrolyte is oxidized at the cathode above 4.8 V. In some instances, the radical cations produced during electrolyte oxidation can subsequently react with PF_6^-, forming highly corrosive HF.[31] Additionally, trace water hydrolyzes $LiPF_6$ to HF;[32,33] to minimize this reaction, electrolytes are kept under inert atmosphere, electrodes and cell components are dried vigorously, and cells are assembled in a dry-room. The electrolyte solution can also undergo reactions with the cathode material or impurities therein, e.g., O_2 released from the crystal lattice or residual LiOH.[21,34,35] In commercial cells, the ratio of electrolyte to active material is kept low to achieve a high energy density on the cell level; excessive electrolyte consumption leads to dry-out, gas formation, and severe cell failure. In this sense, the electrolyte decomposition reactions are critical for the lifetime of a Li-ion cell.

1.2 Next generation cell chemistries

The development of new active materials is aimed at increasing both the gravimetric and the volumetric energy density of Li-ion cells. Some currently investigated new cathode material candidates are close relatives of existing intercalation materials, performing at higher potentials or allowing the extraction of more lithium. In contrast, the capacity of anode materials that operate at low potentials can only be improved significantly by shifting to alloy- or conversion-type materials. In the course of this PhD project, two next-generation electrode active materials and their reaction with electrolyte components were investigated.

$LiNi_{0.5}Mn_{1.5}O_4$ (LNMO), along with other members of the "5 V spinels" class ($LiM_{0.5}Mn_{1.5}O_4$ with M = Fe, Cr, Co, Ni or Cu),[36] is a derivative of $LiMn_2O_4$. Similar to its parent material, LNMO has a higher thermal and chemical stability compared to NMCs, and is free of cobalt. Initially developed to stabilize the spinel lattice during overlithiation ($x > 1$ in $Li_xNi_{0.5}Mn_{1.5}O_4$),[16] Zhong et al.[37] found that the Ni substitution shifted the potential plateaus at $0 < x < 1$ from 4.0 V to 4.7-4.75 V vs. Li^+/Li, effectively increasing the material's energy density by ~20%. Opposite to other new cathode materials with higher practical specific capacity (e.g. Ni-rich NMCs), a higher operating voltage does not require more active material at the anode side to accommodate the additional lithium, which is why LNMO/graphite cells are predicted to achieve volumetric energy densities around 800 Wh/L, surpassing conventional NMC- and NCA-based cells.[6] In contrast to $LiMn_2O_4$, where the manganese oxidation state increases from an average of +3.5 to +4 during delithiation, nickel changes from +2 at $x = 1$ to +4 at $x = 0$ in a perfectly ordered LNMO, while manganese remains at +4 and thus is less susceptible to dissolution.[38] Still, LNMO/graphite full cells show poor capacity retention at elevated temperatures. At these conditions, the high operating potential provokes severe electrolyte oxidation, generating HF which attacks the spinel lattice. The dissolved nickel and manganese ions deposit on the graphite anode, where they impair the SEI and consume active lithium.[12,39] Furthermore, many SEI-improving additives have a lower oxidative stability than the base electrolyte solution. If used in excess, the oxidation products of these additives deteriorate the full cell performance.[40,41]

Accordingly, the development of an optimized electrolyte system which suppresses the formation of HF and protects the anode efficiently is a key requirement for the future commercialization of LNMO/graphite cells.

Silicon, a promising next-generation anode material, is abundant, low-cost and easy to process.[15] The alloying of silicon to $Li_{15}Si_4$ delivers a theoretical specific capacity of 3578 mAh/g (2194 mAh/cm^3),[42] which corresponds to a 10-fold higher gravimetric and a 3-fold higher volumetric capacity compared to graphite. With an average potential around 0.3-0.4 V vs. Li^+/Li, silicon anodes are also less prone than graphite to experience lithium plating during fast charging. However, silicon undergoes a volume expansion of +280% during lithiation, which induces mechanical stress and particle fracturing in the material. While silicon particles, wires or rods with diameters < 300 nm withstand a particle fracturing upon cycling, the high surface area of these nanoparticles leads to further SEI formation and thus a higher full cell capacity loss in the first cycle.[43] The expansion/contraction of silicon also causes an ongoing consumption of electrolyte and active lithium, as the SEI is reformed during each cycle on the freshly exposed surface. Numerous studies have shown that fluoroethylene carbonate (FEC)-based electrolytes improve the cyclability of silicon significantly due to a modified SEI chemistry (see chapter 1.3),[44–47] yet this effect endures only until all FEC is depleted,[48,49] which poses a challenge for commercial cells where the electrolyte amounts should be kept low.[50] A more stable cycling performance is also achieved by limiting the depth of discharge, i.e., the amount of extracted lithium per cycle, which comes however at the expense of usable capacity.[45,51–53] Similarly, silicon alloy or silicon-carbon composites mitigate the volume expansion and improve electronic conductivity between particles while reducing the specific capacity.[54]

1.3 The solid-electrolyte interphase

The operating potential of most anodes in Li-ion batteries, such as graphite, lithium metal, silicon, and most lithium alloys, is lower than the reductive stability of essentially all practical electrolyte. On these anode materials, electrolyte molecules are reduced to form a passivating layer, the so-called solid electrolyte interphase (SEI), which blocks electron transfer between electrode and electrolyte and thus prevents further electrolyte decomposition. While it was known before that lithium metal spontaneously forms passivating surface films upon contact with an organic electrolyte,[55] Peled first introduced the concept of this interlayer as a solid lithium ion conductor (thus the term "solid electrolyte interphase").[56] Later, this notion was extended to carbon- and alloy-based anodes, where the SEI is created once the electrode potential is brought below the electrolyte stability window during the first lithiation.

The capacity of a Li-ion full cell is limited by the active lithium provided from the cathode material. For many graphite-based cell chemistries, the loss of active lithium is the major reason for their capacity fade upon extended charge/discharge cycling.[57,58] As each electrolyte reduction reaction consumes active lithium, the lifetime of a Li-ion cell is determined by how well the SEI prevents this electron transfer. Additionally, the graphite SEI needs to strip the solvation shell from Li-ions in solution, as otherwise cointercalated solvent molecules exfoliate the graphite layers. While many other solvents like ethers and nitriles lead to graphite exfoliation, organic carbonates have shown to form stable and protective layers on graphite.[59,60] An exception to this rule is propylene carbonate (PC), which cointercalates into graphite before forming a stable SEI layer.[61] Fong et al.[62] found that by replacing PC with ethylene carbonate (EC), the reversibility of lithium intercalation into graphite was greatly improved, enabling the successful implementation of graphite anodes in Li-ion batteries. State-of-the-art Li-ion battery electrolytes for graphite anodes, based on EC, linear carbonates and $LiPF_6$, are optimized towards an effective SEI formation: EC is reduced at higher potentials (0.8 V vs. Li^+/Li) than the less passivating linear carbonates,[27] creating a stable SEI together with insulating lithium fluoride (LiF) from $LiPF_6$ decomposition.[63]

To further improve the coulombic efficiency of graphite anodes, SEI additives are dosed to the base electrolyte in low concentrations (< 10 wt%).[64] These additives are reduced at higher potentials than EC and are often derivatives of organic carbonates (see Figure 1.4), such as the prevalent vinylene carbonate (VC),[65] but sulfur-, boron- and phosphor-based organic compounds are reported as well.[66,67] These "enablers" are also applied to improve the SEI stability at high temperatures[68,69] or to allow for long-term cycling of graphite anodes in EC-free electrolytes.[10] However, excess amounts of SEI additives can increase the anode impedance and/or the irreversible capacity during the first cycle,[70,71] meaning that the additive concentration needs to be carefully balanced. Hereby, the higher ratio of electrolyte to active material in lab-scale cells has to be taken into account when results from different cell types are compared.[8]

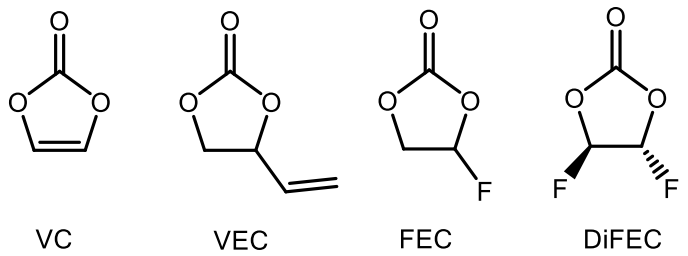

Figure 1.4: Selected SEI-forming additives: Vinylene carbonate (VC), vinyl ethylene carbonate, fluoroethylene carbonate (FEC) and *trans*-difluoroethylene carbonate (DiFEC)

To achieve a stable SEI on silicon, which expands and contracts by almost 300% upon (de-)lithiation, is more challenging: Each cycle exposes fresh, unpassivated silicon surface, leading to a continuous reduction of electrolyte. The associated active lithium loss results in a full cell lifespan of less than a few hundred cycles.[51] With electrolyte additives such as fluoroethylene carbonate (FEC, see Figure 1.4) and CO_2, the cyclability of silicon was greatly enhanced.[44,48,49,72] Both additives have previously shown to improve the reversibility of lithium metal anodes, which also undergo constant SEI reformation during lithium plating/stripping.[73–76] Despite these advances, the significantly lower coulombic efficiency in comparison to graphite needs to be overcome in order to use silicon as primary anode material in Li-ion batteries.

In search for tailor-made additives, the SEI composition was systematically studied by numerous analytical techniques, e.g., energy-dispersive X-ray spectroscopy (EDX),[27,45,77] X-ray photoelectron spectroscopy (XPS),[78–81] nuclear magnetic resonance (NMR) spectroscopy[27,63,82–86] and Fourier-transform infrared (FTIR) spectroscopy.[87–89] Pioneers in this field, the Aurbach group found that the sample preparation for ex-situ measurements can introduce impurities such as water, which react with SEI species; thus pointing out how important it is to handle battery materials also post-mortem in a glovebox.[90,91] Hence, *operando*- or *in-situ*- methods are of great value when investigating SEI formation. Additionally, the identification of gaseous species that evolve during SEI formation by on-line electrochemical mass spectrometry (OEMS) or gas chromatography (GC) has helped to understand the reduction reactions of electrolyte components.[92–98] A number of calculation-based approaches complemented the elucidation of the SEI formation pathways.[86-93]

The main reduction products of EC are lithium ethylene dicarbonate (LEDC) and C_2H_4,[27,74,91,93] whereas a minor decomposition pathway by a direct 2-electron reduction yields CO and lithium glycolate.[97,102] By transmission electron microscopy (TEM), the thickness of an EC-derived SEI after formation was estimated to 10-20 nm.[27] Linear carbonates such as dimethyl carbonate, diethyl carbonate and ethylmethyl carbonate are reduced to the respective lithium alkyl carbonates, carbon monoxide and soluble lithium alkoxides, which prompt the transesterification of intact solvent molecules.[27,98,107] Vinylene carbonate forms CO_2 and an organic carbonate polymer when reduced;[85,95,108] the latter continues to grow through a radical chain polymerization, which is why excess concentrations of VC increase the anode resistance.[70,109] Similarly, FEC is reduced to CO_2, LiF, and polymeric species.[46,85,110–112] In contrast to VC, the polymerization of FEC is thought to proceed through an electrochemical reaction and thus is self-limiting, which allows the use of FEC as a co-solvent without impeding the anode resistance.[86,113]

For CO_2-saturated electrolytes, Aurbach and co-workers found an enrichment of lithium carbonate on both carbon and lithium electrode surfaces,[74,114] which led them to propose the reduction of CO_2 to Li_2CO_3 and CO. However, recent studies show that CO_2 is consumed at the anode without the release of an additional

gas,[13,72,115] which questions this mechanism. The effect of CO_2 on SEI composition, solvent decomposition reactions and cycling performance of full cells will be the topic of chapter 3.2.

2 Experimental Methods

2.1 Impedance spectroscopy with a reference electrode

In electrochemical impedance spectroscopy, a small sinusoidal voltage perturbation V_t at the frequency $\omega = 2\pi f$ is applied to the cell, while the current response I(t) is measured. Alternatively, an alternating current excitation I(t) is applied and the resulting voltage V(t) is recorded. For complex electrochemical systems such as battery cells, which contain also capacitive and inductive elements, the current response can be shifted in phase by φ:[116]

$$V(t) = V_A \sin(\omega t) \tag{3}$$

$$I(t) = I_A \sin(\omega t + \varphi) \tag{4}$$

Analogous to Ohm's law (R = V/I), the impedance Z is defined as:[116]

$$Z = \frac{V(t)}{I(t)} = \frac{V_A \sin(\omega t)}{I_A \sin(\omega t + \varphi)} = |Z| \frac{\sin(\omega t)}{\sin(\omega t + \varphi)} \tag{5}$$

with V_A and I_A as the voltage and the current amplitude. Using Euler's equation $e^{ix} = \cos(x) + i \sin(x)$, the impedance Z can be written as a complex number, whereas Re(Z) and Im(Z) stand for the real and the imaginary part of Z:[116]

$$Z = |Z| e^{i\varphi} = Re(Z) + i\, Im(Z) \tag{6}$$

Both the phase shift φ and the magnitude |Z| depend on the applied frequency ω. In a Bode diagram, φ and |Z| versus the logarithm of the frequency are shown, whereas the more common Nyquist representation used for electrochemical systems

displays the negative imaginary part -Im(Z) over the real part Re(Z) for each measured frequency.

In Li-ion cells, individual processes (mass transport, charge transfer reactions) have different time constants. The impedance spectra contain information about each process occurring in the measured frequency range. However, the time constants of the corresponding anode and cathode processes are often similar, which means that they superpose. To deconvolute the different processes, a separation of the contributions of anode and cathode to the impedance spectrum is crucial. Cells with a lithium metal counter electrode ("half cells") are even less suitable for this purpose, because the large impedance of lithium metal buries the impedance of the electrode of interest.[117] Another approach is the use of symmetric cells, which contain two nominally identical electrodes; the impedance of one electrode corresponds to the spectrum of the symmetric cell divided by two.[118,119] While this is approach leads to reliable impedance spectra of individual electrodes, it requires the disassembly of the original cell. A solution to separate anode and cathode impedance "in-situ" is to introduce a reference electrode in the cell. In this way, the voltage excitation is applied between one electrode (e.g., the positive electrode) and the reference electrode, while current is measured between positive and negative electrode. If the negative electrode is equipped with an additional potential sensor, also the impedance of the counter electrode can be assessed. The sum of positive and negative electrode impedance corresponds to the full cell impedance.

Under certain conditions, the use of a reference electrodes can lead to artefacts when separating anode and cathode impedance. Generally, these artefacts occur when a) the reference drifts in potential during the impedance measurement, which leads to errors at low frequencies;[120] b) the reference electrode is placed in a position where one of the electrodes is closer to the reference, as then the potential field of the closer electrode biases the reference electrode;[121–125] c) the surface area of the positive and the negative electrode differ significantly,[122,126] or d) the impedance of the reference electrode is very high, resulting in high-frequency artefacts.[127,128] While case a) will also lead to distortions in the full cell spectra when measured in potential-controlled mode, the artefacts in cases b)-d) cancel out when adding positive and negative impedance, which can make them difficult to spot. To

ensure a constant potential in the Li-ion containing electrolyte, reference electrodes are typically made of lithium metal,[125,126] lithium intercalation materials[127,129,130] or lithium alloys.[131–134] Conventional T-cells[135] and coaxial designs of three-electrode cells[123,125,126] place the reference electrode at the edge of the electrode stack, where already small horizontal misalignments between the electrodes lead to a biased potential field around the reference electrode.[121–125,136] This issue can be overcome if the reference electrode is placed centrally between the electrodes, far away from their edges.[121,129,136] However, to not disturb the ionic current between both electrodes, the reference electrode has to be thin relative to the distance between positive and negative electrode.[121,137] Micro-reference electrodes[131,133,138] consist of a thin, insulated wire sandwiched between the electrodes and two separators; their active surface is only exposed at the wire tip by removing the insulation there. The wire tip is then lithiated by applying a small current between one of the electrodes and the wire, which leads – depending on the wire material – to either lithium metal plating onto the wire surface, or to an alloying of the wire material with lithium. Yet, previously reported in-situ generated micro-reference electrodes have only limited potential stability, as the plated or alloyed lithium is dissolved by self-discharge reactions and potential gradients across the reference electrode over time.

In this PhD project, a micro-reference setup for Swagelok T-cells was developed using a polyimide-insulated gold wire with a diameter of 50 µm (Goodfellow Cambridge Ltd., United Kingdom). Gold was chosen as reference material because it has high electronic conductivity, is chemically inert, shows a flat potential profile[139] and the formed alloy is relatively stable against delithiation.[140,141] Prior to experiments with a gold wire, the electrochemical alloying of gold with lithium was investigated on gold disc electrodes. The potential curve of a gold disc vs. a lithium metal counter electrode during lithiation and the corresponding open-circuit voltage (OCV) points are shown in Figure 2.1. As can be seen, the lithiation of gold proceeds in two stages with OCV potentials at ~0.31 V (Li_xAu with $0 < x < 1.7$) and ~0.15 V vs. Li^+/Li ($1.7 < x < 3.0$), respectively. The first potential plateau is already reached at very low degrees of lithiation ($x \approx 0.2$), which means that a low lithiation capacity will be sufficient to provide the gold wire reference electrode (GWRE) with a stable potential.

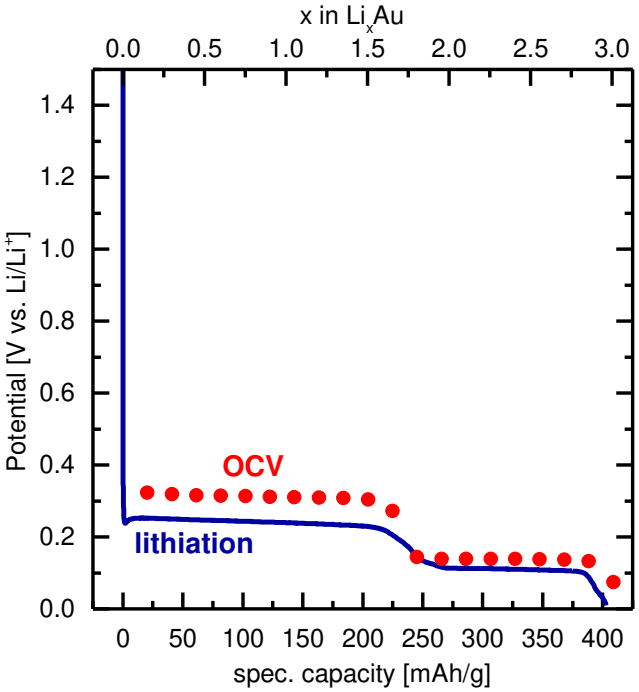

Figure 2.1: Potential during lithiation (blue line) and intermittent OCV measurements (red circles) of a gold disc (25 µm thickness, 11 mm diameter) vs. Li metal in a Swagelok T-cell with 2 glassfiber separators and 60 µL electrolyte (LP57 EC:EMC 3:7, 1M $LiPF_6$). The lithiation was performed at C/20 (≡ 1 mAh/cm^2) based on a nominal capacity of 408 mAh/g_{Au}. Each OCV points of the Li-Au alloy was measured after 1 h of lithiation (C/20) and 1 h rest.

To mount the gold wire in the Swagelok T-cell, the reference stamp was shortened and provided with a hole (1 mm diameter, 2.5 mm depth) at the flat top side. At approximately 2 mm from the top edge, a screw thread was cut into the side of the reference stamp. The insulation of the last 0.3 cm of a ~1.5 cm long gold wire was removed with a scalpel. This end of the wire was then inserted in the hole and fixed with one or two screws. To reduce the surface area on which self-delithiation reactions can occur, the insulation was not removed at the free end of the wire, leaving only the cut cross-section of the gold wire as electrochemically active area (see Figure 2.2a). The free end of the wire was then threaded through a hole in the polymer lining of the T-cell during cell assembly, while the reference stamp was fixed to the T-cell body with a Swagelok nut. Experimentally, it was found that a lithiation current of 150 nA for one hour was sufficient to bring the gold wire reference electrode (GWRE) to a reproducible potential of 0.311 vs. Li^+/Li. Figure 2.2 shows an SEM image of the gold wire tip before (a) and after lithiation (b). After

lithiation, the flat cross-section seen in (a) is visibly roughened, yet the polyimide insulation remains intact around the wire tip.

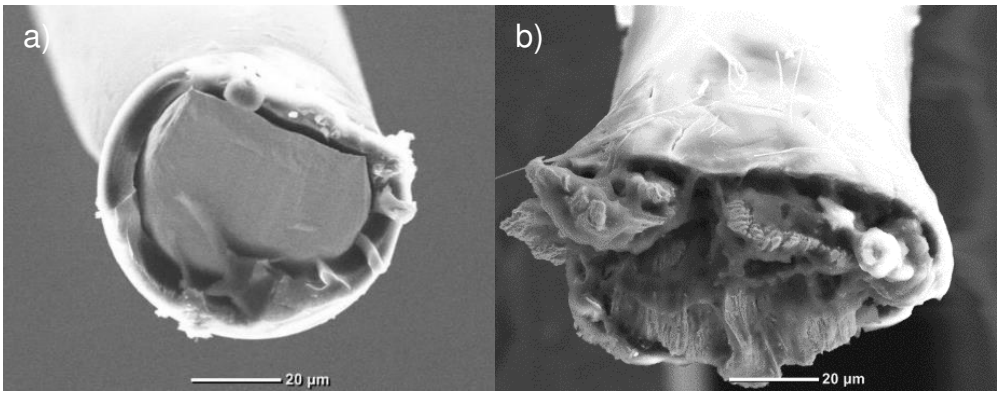

Figure 2.2: Scanning electron micrographs of the GWRE tip before (a) and after lithiation with 150 nA for 1 h in a LFP/graphite cell with 60 µL LP57 and 2 glassfiber separators (b).

In both Li/Li and LFP/graphite cells, the GWRE potential remained stable at 0.311 V vs. Li^+/Li for more than 3 weeks, as long as the cell temperature did not exceed the temperature which was used during the GWRE lithiation. However, it was found that the GWRE potential started to drift significantly in LNMO/graphite full cells within the first 10 cycles at 40 °C. Apparently, the Li-Au alloy reacts with electrolyte oxidation products like HF formed at the high-voltage LNMO cathode (~4.7-4.8 V vs. Li^+/Li), leading to a gradual delithiation of the GWRE. Therefore, the GWRE was re-lithiated (150 nA, 1 h) in-situ before each impedance measurement in the study presented in chapter 3.1.3. As the lithiation capacity of 0.15 µAh is less than 0.01% of the capacity of a typical cathode (~1.8 mAh in the study in chapter 3.1.3), even multiple relithiation steps are not expected to measurably lower the cell capacity. Later studies on LNMO/graphite cells showed that the long-term potential drift of the delithiated GWRE is < 0.1 mV/s, which is why for these measurements the GWRE could be used as a pseudo-reference electrode without re-lithiation.[142,143]

While the lithiated GWRE fulfills all requirements for an artefact-free impedance measurement based on cases a)-c), the small diameter and the limitation of the electrochemical surface area to the cut cross-section of the wire tip lead to a high electrode impedance. As previously mentioned, this can result in artefacts at high frequencies. To assess this effect, Raijmakers et al.[128] proposed a simple experimental procedure. In this approach, potential-controlled impedance of one

full cell electrode vs. the reference electrode is first measured in a regular setup (see Figure 2.3a). Hereby, both the potentiostat connectors for potential and current for the working electrode (WE(U) and WE(I) in Figure 2.3) are connected to the cathode terminal (red) of the full cell, whereas the potential connector for the reference electrode RE(U) is connected to the reference electrode terminal of the cell (yellow), and the current connector for the counter electrode CE(I) is connected to the anode of the full cell (blue). During the impedance measurement, the potential is controlled between the potential connectors WE(U) and RE(U), i.e., cathode and reference electrode (solid black line), while the current response is measured between the current connectors WE(I) and CE(I), i.e., cathode and anode (dashed gray line). Then, the impedance of the same electrode is recorded in a reversed setup, where the two ends of the potential and the current connectors are exchanged (see Figure 2.3b).

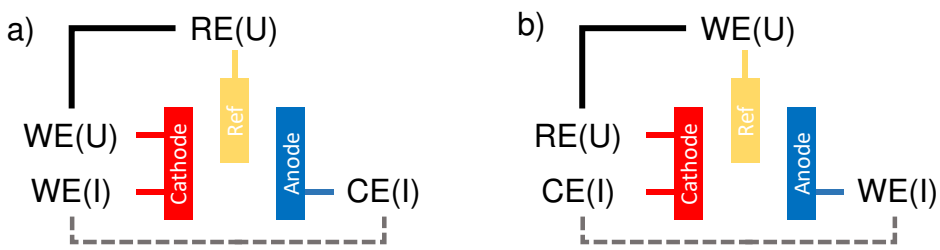

Figure 2.3: Scheme of the regular (a) and the reversed setup (b) for the detection of high-frequency artefacts in impedance measurements according to Raijmakers et al.[128] In the regular setup (a), the potentiostat connectors for current WE(I) and potential WE(U) are connected to the cathode (red), while the potential connector for the reference electrode RE(U) and the current connector for the counter electrode CE(I) are connected to the reference electrode (yellow) and the anode (blue). In the reversed setup (b), the potential connector for the reference electrode RE(U) and the current connector for the counter electrode CE(I) are both connected to the cathode(red), whereas the potential and current connectors for the working electrode WE(U) and WE(I) are connected to the reference electrode (yellow) and the anode (blue), respectively. In both setups, impedance spectroscopy is measured by applying a voltage excitation between the potential connectors (solid black lines) and measuring the resulting current response between the current connectors (dashed gray lines).

An artefact-free impedance measurement would give identical spectra in both setups. Hence, differences between the impedance spectra from the regular and reversed setup indicate at which frequencies artefacts occur. The impedance spectra of a pristine graphite electrode recorded by using the regular and the reversed setup is presented in Figure 2.4a, whereas Figure 2.4b shows the relative difference between the impedance magnitudes ($|Z|_{reversed}/|Z|_{regular} - 1$) of the two

measurements. At frequencies < 31 kHz, the relative difference becomes < 2% (see grey area in Figure 2.4b), which is why only the frequency range of 31 kHz-100 mHz was evaluated for the study presented in chapter 3.1.2.

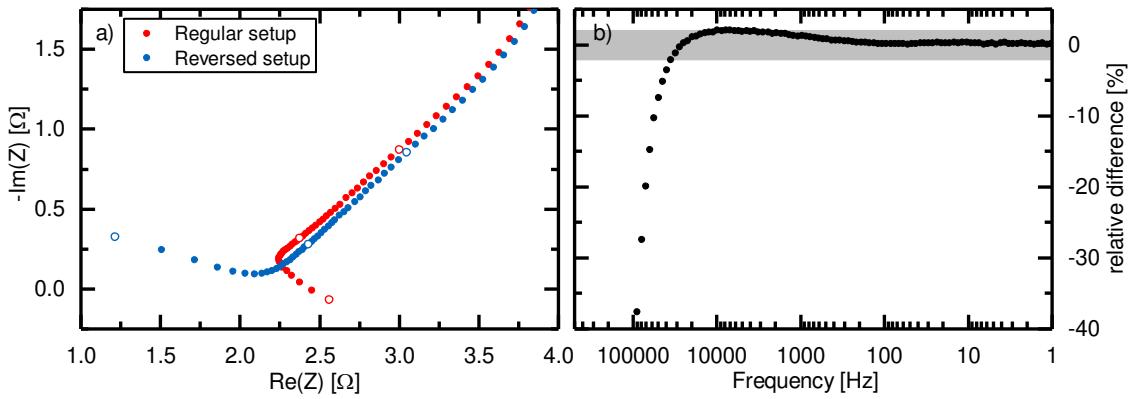

Figure 2.4: a) Impedance spectra of a pristine graphite electrode vs. lithiated GWRE in a graphite/LFP cell (60 µL LP57, 2 glassfiber separators, 25 °C) measured with the regular (red symbols) and the reversed setup (blue symbols) as shown in Figure 2.3; open symbols represent spectra at 100 kHz, 10 kHz and 1 kHz. b) Relative difference of the impedance magnitudes from the reversed and the regular setup calculated as $|Z|_{reversed}/|Z|_{regular} - 1$.

To evaluate impedance measurements, the data are fitted with an electrical equivalent circuit model. The porous structure of a Li-ion battery electrode can be depicted by a transmission line model of two parallel resistor rails,[144–147] which represent the ionic resistance of the liquid electrolyte in the electrode pores and the electronic resistance of the active material (see Figure 2.5a). If the electronic conductivity within the electrode is much higher (x100) than the effective ionic transport in the pores, its contribution to the overall electrode impedance can be neglected.[148] Perpendicular elements connecting the two rails describe the transfer of electrons and/or ions across the solid-liquid interface. These processes are characterized by a resistance R (the kinetic barrier for the charge transfer reaction) in parallel with a capacitance C (the double-layer capacitance of the electrode surface). In a Nyquist plot, the R/C element gives a semicircle with a maximum at the characteristic frequency f_{max} (see Figure 2.5b):[116]

$$f_{max} = 1/2\pi RC \tag{7}$$

The capacitance C is often replaced by a constant phase element Q, which accounts for an inhomogeneous electrode surface.[116] If several interfacial processes take

place (e.g., an ion in the electrolyte transfers first into a solid surface film and then into the intercalation material), multiple R/C or R/Q elements are used in series.[149] The electron transfer between current collector and electrode coating is also described by an R/C or R/Q-element, which is however located outside the porous electrode structure (i.e., in series with the transmission line model).

In the literature, the ionic resistance of the electrode pores is often ignored, and the assignment of an R/C or R/Q element to a specific physical process is prone to misconceptions. The specific double-layer capacitance of an electrode surface, i.e., the capacitance C normalized by the respective BET (Brunauer-Emmett-Teller) surface area, is typically 1-5 $\mu F/cm^2_{BET}$ in a Li-ion cell, independent of the electrode material.[143,150] Thus, the electrochemically active BET surface area can be estimated from the absolute capacitance C. Considering the roughness factor, i.e., the ratio of BET surface area to geometric area, helps to distinguish interfacial processes on the active material (roughness factor ~50-500 cm^2_{BET}/cm^2_{geom}) from the contact resistance between electrode coating and current collector (roughness factor ~1 cm^2/cm^2_{geom}).[151] Hence, the contact resistance appears at significantly higher frequencies in the Nyquist plot (region II in in Figure 2.5b). In so-called "blocking conditions" (red line in Figure 2.5b), lithium intercalation is hindered by the use of a non-intercalating electrolyte or the application of a potential where lithium insertion/removal is thermodynamically unfavorable.[144,146] According to equation (7), the significantly increased (> 10^4) charge transfer resistance shifts the corresponding semicircle to lower frequencies and thus enables a separation of the ionic pore resistance and the charge transfer resistance (region III in Figure 2.5b, red line) which is not possible in non-blocking conditions (blue line in Figure 2.5b).

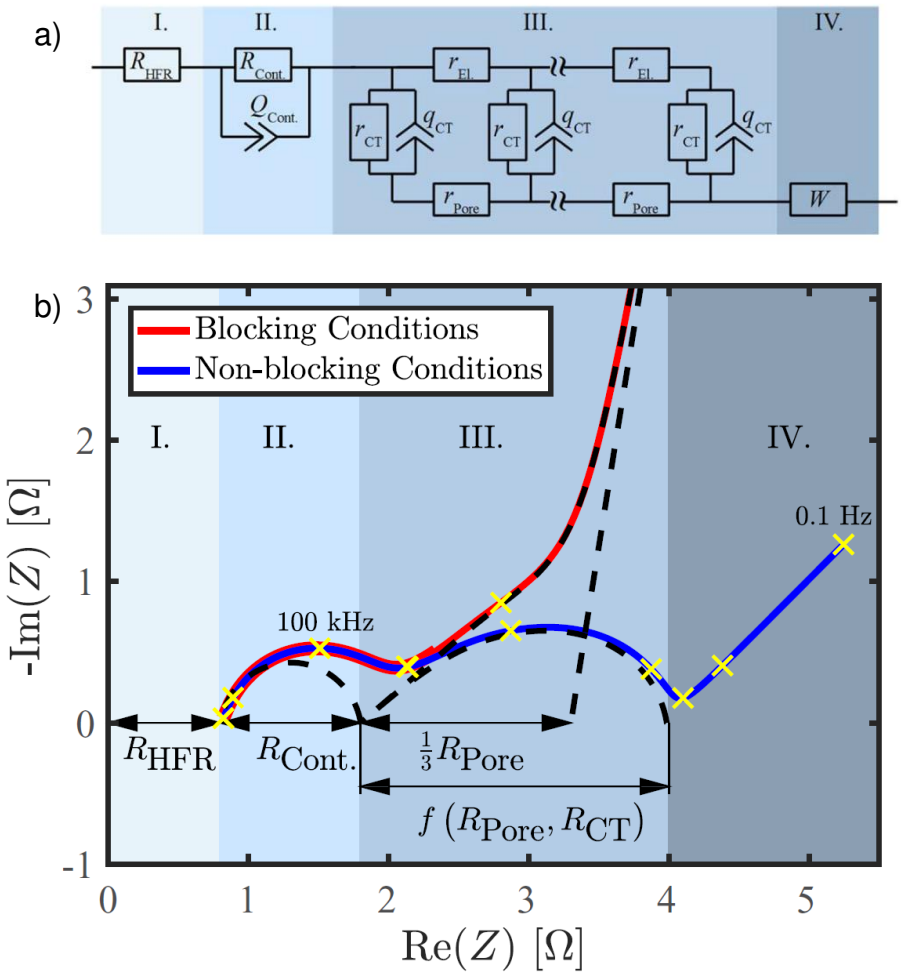

Figure 2.5: a) Electrical equivalent circuit used for porous electrodes consisting of a separator and setup resistance (I), a contact resistance (II), the transmission line model including ionic pore resistance and charge transfer (III), and a Warburg diffusion element (IV). b) Simulated impedance spectra of a porous electrode in blocking conditions (red line) or non-blocking conditions (blue line) using the equivalent circuit shown in a). For model parameters please see Table I in ref. 142. Reprinted from ref. 142 under a Creative Commons BY-NC-ND 4.0 license.

Another method to assign the physical origin of a resistor in an electrical equivalent circuit is the determination of its activation energy. The activation energy E_A can be calculated from the linear slope of an Arrhenius graph, which plots the logarithmic resistance over inverse temperature:

$$E_A = R_G \frac{d \ln R}{d \ln(1/T)} \tag{8}$$

Here, R stand for the resistance at temperature T, while R_G corresponds to the universal gas constant (8.314 J/mol K). While electronic resistances show negligible temperature dependency ($E_A \approx 1$ kJ/mol), the activation energy of resistances

related to the ionic conductivity of the electrolyte is typically around 10-20 kJ/mol.[143,145,146] Interfacial and charge transfer resistances show the highest activation energies in the range of 60-80 kJ/mol.[145,146] A non-Arrhenius behavior signifies a convolution of two different processes (i.e., charge transfer and ionic resistance).[145,152] Thus, if an equivalent circuit model is physically meaningful, the temperature dependence of the extracted resistances should follow an Arrhenius-type behavior.[146]

2.2 On-line electrochemical mass spectrometry

As described in chapters 1.1 and 1.3, gas evolution is a by-product of many chemical, electrochemical and thermal electrolyte decomposition reactions in Li-ion batteries. In some cases, the evolved gaseous species allow a direct identification of the corresponding decomposition mechanism; for example, C_2H_4 is a characteristic product of the reduction of ethylene carbonate.[93,108] In contrast, CO_2 can be released from numerous processes, such as electrolyte oxidation,[153–155] the reduction of additives,[111,156] or the chemical reaction of EC with nucleophilic species.[34,157]

In the course of this PhD project, the gas evolution during different electrolyte decomposition phenomena was monitored and quantified by on-line electrochemical mass spectrometry (OEMS). The OEMS system at the Chair for Technical Electrochemistry at TUM was first described in a publication by Tsiouvaras et al.[158] In this system, a custom-made electrochemical cell with a headspace volume of 9-10 mL is attached to the mass spectrometer via a crimped capillary leak with a leak rate of 2 x 10^{-5} atm-cc/s (~1 µL/min, Vacuum technologies, United States), reducing the pressure from atmospheric (~ 1 bar) to 10^{-5} mbar in one step. The mass spectrometer (QMA 410, Pfeiffer Vacuum, Germany) is equipped with a tungsten filament in a closed cross-beam ionization chamber, a quadrupole mass analyzer (atomic mass units range 1-128) and a secondary electron multiplier detector (detection limit ~10^{-14} mbar). Due to the continuous sampling through the capillary leak, the pressure in the cell decreases over time, which limits the measurement time of a single experiment to < 40 h (~25% pressure drop). As the cell is a closed system, also the consumption of voluntarily added gases or gaseous products can be monitored. While this reflects the situation in a commercial Li-ion cell, the possibly simultaneous evolution and consumption of the same species, e.g. CO_2, can be a challenge for the quantification of both processes. Additionally, electrolytes with high vapor pressure such as LP57 (EC:EMC 3:7, 1 M $LiPF_6$) can exhibit mass signals which superpose with mass signals of evolved species/consumed species of interest. Figure 2.6 shows the background signals of different electrolyte systems on the mass signals characteristic for H_2 (m/z = 2), C_2H_4 (m/z = 25-27), CO (m/z = 28) and CO_2 (m/z = 44). If the composition of the electrolyte changes during the course of the experiment, as in the case for

EMC-based electrolytes by transesterification reactions, a differentiation between signals from gaseous species and solvent background signals becomes difficult. Therefore, single-solvent electrolytes with low vapor pressure (e.g., EC/$LiPF_6$, green bars in Figure 2.6) or with no changes in the background signals due to transesterification reactions (e.g., DMC/$LiPF_6$, yellow bars in Figure 2.6) were employed as model electrolytes instead of LP57 in many studies comprised in this PhD project.

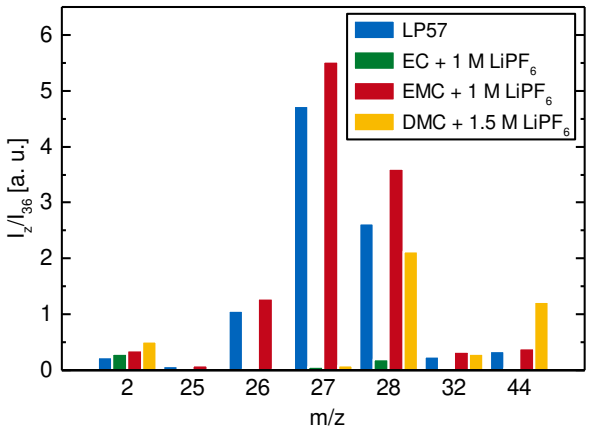

Figure 2.6: Background signals of LP57 (EC:EMC 3:7 w/w, 1M $LiPF_6$), EC/$LiPF_6$, EMC/$LiPF_6$ and DMC/$LiPF_6$ electrolytes on relevant mass traces for m/z = 2 (H_2), m/z = 25-27 (C_2H_4), m/z = 28 (CO) and m/z = 44 (CO_2).

Throughout this project, both 1-compartment cell setups (chapters 3.2.1 and 3.3.1) and 2-compartment cell setups (chapters 3.2.2, 3.2.3 and 3.3.2) were used. The 1-compartment OEMS cell corresponds to the Li-O_2 cell design described by Meini et al.,[159] but with an additional ¼" VCR connection at the top plate to mount the crimped capillary leak.[158] A 1-compartment cell assembly contains of a 17 mm counter electrode, two polymer separators (H2013, Celgard, United States or FS 24316, Freudenberg, Germany) with a diameter of 28 mm, a 15 mm working electrode and 120-150 µL electrolyte. In order to be permeable for gases while allowing electrical contact from the mesh current collector on top, the working electrode is coated on a porous substrate, such as a separator membrane or a perforated aluminum foil (Microgrid Al 25, Dexmet, United States). In the 1-compartment cell, gas evolution from both the working electrode on top of the electrode stack and from the counter electrode at the bottom of the electrode stack is sampled continuously by OEMS, as the diffusion time of gases through the

separator is approximately less than 2 min.[155] Additionally, the 1-compartment cell allows crosstalk of soluble and gaseous species that are produced at one electrode and consumed at the other, such as CO_2 (see chapter 3.2.1) and HF (see chapter 3.3.1).

The 2-compartment cell (Figure 2.7a, see references [160] and [161] for details) features an aluminum edge-sealed lithium ion conductive glass ceramics ("Ohara glass", Ohara Corp., Japan, see Figure 2.7b and c as well as "I" in Figure 2.7a), which divides the cell into a lower compartment and an upper compartment. The lower compartment ("M") contains a 17 mm lithium counter electrode ("L"), a 22 mm glassfiber separator ("K", VWR, Germany) and 250 µL electrolyte, while the upper compartment holds a 17 mm separator, a 15 mm working electrode ("E") on a porous substrate and 80-150 µL electrolyte. As the lower compartment is hermetically sealed from the upper compartment by a PTFE O-ring ("H", APSO parts, Germany), only the gas evolution/consumption at the working electrode is monitored, as was demonstrated by Metzger et al.[155] Furthermore, any cross-talk between working and counter electrode is prohibited. In this way, the electrolyte decomposition reactions of an isolated electrode can be investigated. However, due to the lower ionic conductivity of the Ohara glass and the additional interfacial resistances between Ohara glass and liquid electrolyte,[162] the cell impedance of the 2-compartment cell is significantly increased, resulting in low frequency resistances of 300-1500 Ohm cm^2_{geom}. Consequently, the 2-compartment cell setup is not suitable for experiments with high current densities (> 0.1 mA/cm^2_{geom}), as this results in high overpotentials and means that the working electrode potential vs. Li^+/Li cannot longer be approximated by the cell voltage.

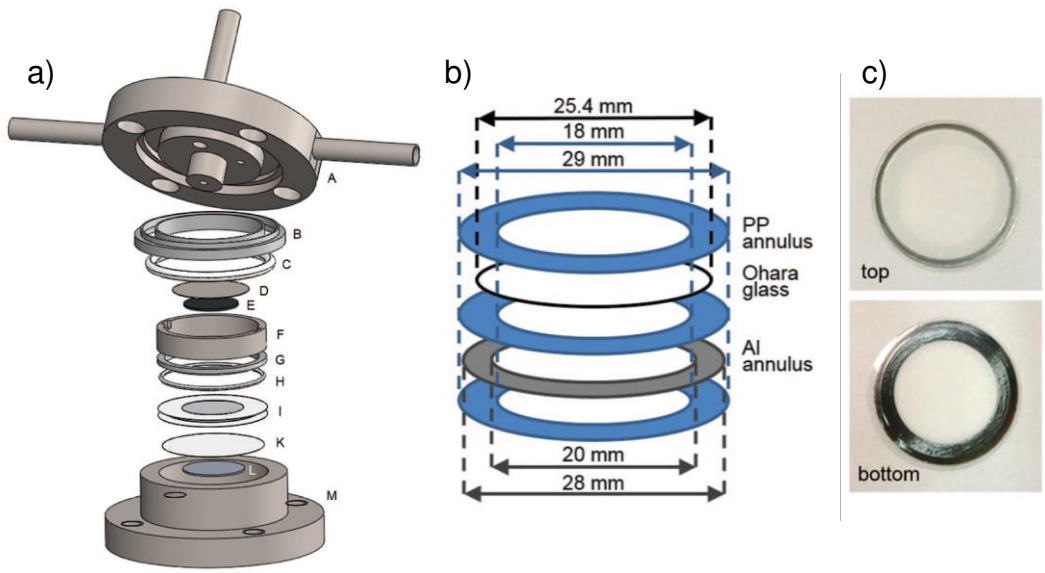

Figure 2.7: (a) Isometric view of the 2-compartment cell setup reprinted from ref. [160]. (b, c) Schematic drawing and photograph of the aluminum edge-sealed Ohara glass reprinted from ref. [155]. Reprinted under the Creative Commons BY-NC-ND 4.0 license.

In chapter 3.3.1, the thermal decomposition of dry $LiPF_6$, which occurs at 150-200 °C,[30] was investigated by OEMS. As we found that polymer O-rings used in the conventional OEMS cell did not withstand these temperatures, a modified cell setup containing only metallic pieces was developed in the context of Masamitsu Egawa's Master Thesis.[163] This setup consists of a Swagelok T-piece with two metal end caps (see Figure 2.8). The crimped capillary leak is mounted to the third opening of the T-piece. The cell was equipped with a temperature sensor and wrapped with heating cord which were both connected to a temperature control unit (Horst, Germany). Afterwards, the cell was covered with thermally insulating felt to ensure a homogeneous and constant temperature across the cell.

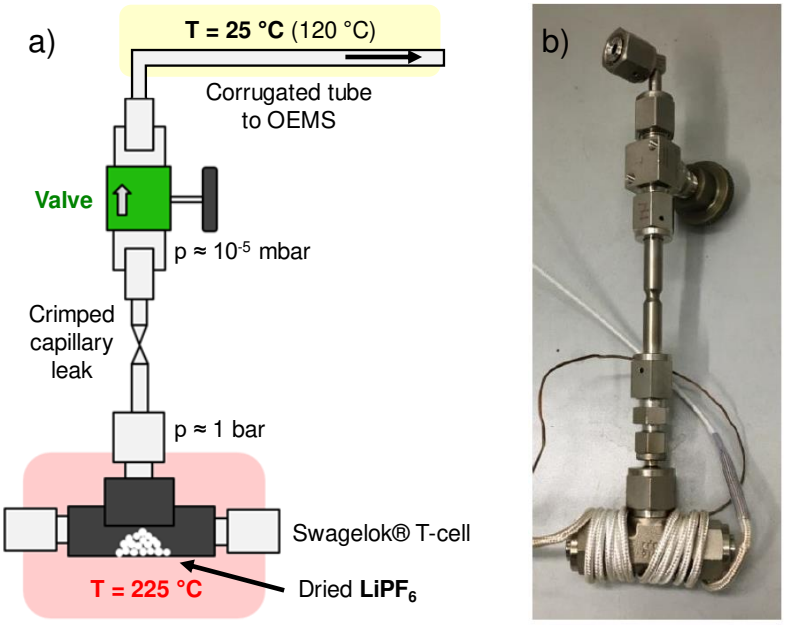

Figure 2.8: Schematic drawing (a) and photograph (b, taken from ref. [163]) of the modified OEMS cell setup used for $LiPF_6$ thermal decomposition experiments comprising of a Swagelok T-piece connected to the crimped capillary leak.

Irrespective of the cell setup, the OEMS data treatment was performed as described in ref. 161: First, the ion current I_z of a given m/z channel was divided by the ion current of the ^{36}Ar isotope (I_{36}) to account for pressure fluctuations. The normalized signal was then smoothed by a Savitzky-Golay routine with 120-300 data points or a percentile filter with 50-200 data points; the percentile filter was used when the Savitzky-Golay routine was insufficient to represent very steep or sudden changes in gas evolution. The electrolyte background on the respective m/z channel during the initial 4 hours of open circuit voltage (OCV) was fitted with a second order exponential decay function or a combined exponential/linear function. This function was then extrapolated over the measurement time and subtracted from the normalized I_z/I_{36} signal to correct for the electrolyte background. Calibration was performed after each measurement by first flushing the cell for ~30 min with argon to remove any accumulated gases and to determine the electrolyte background, followed by purging the cell for ~30 min with calibration gas (Westphalen, Germany) containing either H_2, CO, O_2, C_2H_4 and CO_2 (each 2000 ppm) or H_2, CO, O_2, CO and CO_2 (each 2000 ppm). Again, the ion current of the respective m/z channel was normalized to the ^{36}Ar isotope ion current, the electrolyte background during the initial argon purging was fitted with a second order

exponential decay function, and this function was subtracted from the normalized I_z/I_{36} signal; however, no smoothing routine was applied. Afterwards, the calibration factor corresponding to 2000 ppm of the respective gas was determined by averaging the treated m/z signal during the last ~15 min of the purge with calibration gas. Typical values for calibration factors are given in the publication presented in chapter 3.2.2. The normalized, background-corrected signals recorded during the OEMS measurement were then calculated into relative concentrations (ppm) or absolute amounts referenced to active material surface area or mass (μmol/m^2 or μmol/g) by taking into account active material loading and specific surface area, cell volume, pressure and temperature during the respective experiment.

2.3 Nuclear magnetic resonance (NMR) spectroscopy

NMR spectroscopy is a widely used method to determine the structure of organic molecules, to detect impurities and to quantify reaction products. In the context of Li-ion battery electrolytes, ^{1}H- and ^{13}C-NMR spectroscopy has been applied to identify electrolyte reduction products[27,63,82–86] and to quantify trace water,[164] whereas decomposition reactions of $LiPF_6$[165–171] and consumption rates of additives[49,172] were investigated by ^{19}F- and ^{31}P-NMR spectroscopy. In the study presented in chapter 3.2.1, the consumption of FEC during cycling in LNMO/Silicon-graphite (SiG) cells was monitored by ^{19}F-NMR spectroscopy. The measurement procedure was described by Jung et al.[49] and has by now been extended to other studies on silicon-based cells in our group.[50,173] Within this project, LNMO/SiG coin cells were opened inside an Ar-filled glovebox after a specific number of cycles. To extract the electrolyte, the retrieved separators were soaked with ~0.5 mL DMSO-d_6, which was then filled into air-tight NMR glass tubes. The NMR measurements were performed on a Bruker Ascend 400 (400 MHz) with 256 scans and no proton decoupling to enhance the quantification accuracy. As the concentration of PF_6^- in the electrolyte is assumed to remain approximately constant during cycling, PF_6^- was used as an internal standard, and the FEC peak integral was normalized to the integral of the PF_6^- peaks. By comparison with the FEC/PF_6^- integral ratio of the fresh electrolyte, the consumption of FEC could thus be determined. The SEI composition with and without CO_2 (see chapter 3.2.3) was also investigated by NMR spectroscopy. Here, harvested graphite electrodes were first washed with DMC to remove residual electrolyte, dried under dynamic vacuum and then soaked in D_2O. The resulting solute was then analyzed by ^{1}H- ^{13}C- and ^{19}F-NMR spectroscopy.

2.4 Attenuated total reflection Fourier-transform infrared spectroscopy (ATR-FTIR)

Fourier-transformed infrared spectroscopy has been extensively used to study the SEI, as many organic SEI components have distinct IR absorption bands. For example, it is possible to differentiate polycarbonates, alkyl carbonates and lithium carbonate by FTIR.[82,83,85] However, other prevalent SEI species, such as LiF, are hardly detectable by infrared spectroscopy,[174] which means that a combination of methods (i.e., FTIR and NMR spectroscopy) is necessary to comprehensively elucidate the SEI composition. In chapter 3.2.3, ATR-FTIR was used to investigate SEI products on graphite anodes after formation in electrolytes containing different concentrations of VC or FEC as well as $^{12}CO_2$ and/or $^{13}CO_2$. The effect of Mn^{2+} and Ni^{2+} ions on the SEI chemistry of graphite electrodes was also investigated by ATR-FTIR (see chapter 3.3.2). In both studies, the harvested graphite electrodes were carefully rinsed with 1.5 mL anhydrous DMC (H_2O < 10 ppm as determined by Karl-Fischer titration) to remove any excess electrolyte and then dried under dynamic vacuum at room temperature. The ATR-FTIR measurements were performed inside an Ar-filled glovebox with a Spectrum Two spectrometer (Perkin Elmer) on a MIRacle germanium ATR (Pike Technologies) between 4000-600 cm^{-1} with a resolution of 4 cm^{-1}.

3 Results

This chapter presents the published work as well as unpublished manuscripts of this PhD thesis. The journal articles/manuscripts are grouped into three main sections. Chapter 3.1 shows the application of impedance spectroscopy as a diagnostic tool for Li-ion batteries. In chapter 3.1.1, the concept of the gold-wire micro reference (GWRE) is presented. The following two studies show the use of impedance with a GWRE: the use of blocking conditions to monitor the SEI resistance of a graphite anode during formation is demonstrated in chapter 3.1.2, whereas chapter 3.1.3 investigates the effect of vinylene carbonate concentration on anode and cathode impedance in LNMO/graphite cells.

As many commercially relevant additives release CO_2, including all of the additives used in chapter 3.1, the second chapter deals with the effect of CO_2 on electrolyte decomposition reactions. Chapter 3.2.1 elucidates the use of lithium oxalate in LNMO/graphite and LNMO/SiC cells, which releases CO_2 during decomposition. Chapter 3.2.2 describes the effect of CO_2 on the trans-esterification reactions of linear carbonates, while chapter 3.2.3 takes a closer look at the SEI products on graphite electrodes formed with $^{12}CO_2$ and $^{13}CO_2$.

The last section (chapter 3.3) elucidates follow-up reactions of electrochemical electrolyte oxidation on inert electrodes (i.e., without oxygen release). Chapter 3.3.1 presents the origin and quantification of POF_3, a decomposition product of $LiPF_6$ that is commonly observed at high potentials. The resulting HF formation leads to the dissolution of transition metal ions from the cathode material; thus, the effect of manganese and nickel induced side reactions on the anode SEI is investigated in chapter 3.3.2.

3.1 Deconvolution of impedance contributions to Li-ion full cells

To conclusively interpret electrochemical impedance spectra of Li-ion cells, a separation of anode and cathode contributions to the full cell impedance spectrum is crucial. Therefore, chapter 3.1.1 describes the development and validation of a gold-wire micro reference electrode (GWRE) for impedance measurements of individual electrodes. However, even after the separation of anode and cathode, processes with similar time constants are difficult to separate in the impedance spectrum. Blocking conditions, in which the charge transfer resistance is shifted towards significantly lower frequencies (ideally, to infinitely low frequencies), has previously been used by our group to separate individual resistance contributions, such as the ionic resistance of Li-ion electrodes.[142–144] In chapter 3.1.2, we apply this concept to graphite anodes in LFP/graphite cells before, during and after formation to follow the evolution of the SEI resistance *in-situ*. Lastly, we show how impedance spectroscopy with a reference electrode can be used to determine the optimal electrode/additive ratio in LNMO/graphite cells with VC, where an additive excess leads to parasitic oxidation reactions at the cathode.

3.1.1 A gold micro-reference electrode for potential and impedance measurements

The article "A gold micro-reference electrode for potential and impedance measurements" was submitted in June 2016 to the peer-reviewed *Journal of the Electrochemical Society* and published online in July 2016. The main findings of this paper were presented by Sophie Solchenbach at the PRiME Meeting in Honolulu, Hawaii, in October 2016 (Abstract Number 211). The article is published "open access" under the Creative Commons Attribution 4.0 License (CC BY). A permanent link to this article can be found under http://jes.ecsdl.org/content/163/10/A2265.

The objective of this work was the development of a reference electrode suitable for impedance measurements in lab-scale test cells. As described in chapter 2.1, previous studies, e. g., by Ender et al.,[122] had described the geometric requirements for reference electrodes in order to yield artefact-free impedance measurements. Considering these results, the reference stamp of a Swagelok®-type T-cell was modified to accommodate a 50 µm thick, insulated gold wire, which was introduced between two 200 µm thick glassfiber separators and in-situ lithiated from one of the T-cell electrodes. Opposite to existing micro-reference designs, only the cut front face of the wire was exposed to the electrolyte, which minimized self-delithiating side reactions. The lithiated gold wire exhibited remarkable potential stability (> 500 h in symmetric lithium/lithium cells at both 25 °C and 40 °C), as long as the measurement temperature did not exceed the lithiation temperature. By comparison with impedance spectra of the corresponding symmetric cells, it was verified that the impedance measurements of cathode and anode in an LFP/graphite cell after formation using the gold-wire micro reference electrode (GWRE), were indeed artefact-free. To further validate the newly developed reference electrode, we conducted a study similar to the one previously published by Burns et al.[70] on LCO/graphite pouch cells with different concentrations of vinylene carbonate (VC) as electrolyte additive, where impedance measurements were performed in symmetric cells. However, to account for the significantly higher electrolyte to active materials ratio in the Swagelok T-cells, we adapted the VC concentrations to yield the same VC/graphite active material mass ratios. As we

found the same linear trend of rising graphite impedance with increasing VC concentration in our LFP/graphite cells with GWRE, we could confirm that the additive/active material ratio, rather than the additive concentration, is the key parameter when comparing results from lab-scale and commercial-scale Li-ion cells.

Author contributions

S. S. and D. P. developed the concept of using an insulated gold wire and alloying it with lithium. D. P. and J. L. designed the reference stamp that accommodates the gold wire. S. S., D. P. and E. Y. K. prepared electrodes and performed the electrochemical tests. S. S., D. P. and J. L. evaluated the data. S. S. and H. A. G. wrote the manuscript. All authors discussed on the data and commented on the manuscript.

A Gold Micro-Reference Electrode for Impedance and Potential Measurements in Lithium Ion Batteries

Sophie Solchenbach,[a,*,z] Daniel Pritzl,[a,*] Edmund Jia Yi Kong,[a,b] Johannes Landesfeind,[a,*] and Hubert A. Gasteiger[a,]**

[a]*Chair of Technical Electrochemistry, Department of Chemistry and Catalysis Research Center, Technische Universität München, D-85748 Garching, Germany*
[b]*Singapore Institute of Technology, Singapore*

Impedance measurements of lithium-ion batteries are a powerful tool to investigate the electrolyte/electrode interface. To separate the contributions of anode and cathode to the full-cell impedance, a reference electrode is required. However, if the reference electrode is placed inappropriately, the impedance response can easily be biased and lead to erroneous conclusions. In this study, we present a novel micro-reference electrode for Swagelok-type T-cells which is suitable for long-term impedance and reference potential measurements. The reference electrode consists of a thin insulated gold wire, which is placed centrally between cathode and anode and is in-situ electrochemically alloyed with lithium. The resulting lithium-gold alloy reference electrode shows remarkable stability (>500 h) even during cycling or at elevated temperatures (40°C). The accuracy of impedance measurements with this novel reference electrode is carefully validated. Further, we investigate the effect of different vinylene carbonate (VC) contents in the electrolyte on the charge transfer resistance of LFP/graphite full cells and demonstrate that the ratio of VC to active material, rather than the VC concentration, determines the impedance of the anode SEI.

Manuscript submitted June 7, 2016; revised manuscript received July 26, 2016. Published August 19, 2016. This article is a version of Paper 211 from the Honolulu, Hawaii, Meeting of the Society, October 2–7, 2016.

The lifetime of lithium-ion batteries strongly depends on the properties of the interfaces between each electrode and the electrolyte. Electrochemical impedance spectroscopy (EIS) is a simple and non-destructive method to investigate the kinetics of active materials, the resistance of electrode/electrolyte interfaces, and the effect of electrolyte additives.[1,2] As impedance measurements of full-cells always reflect the sum of both electrodes, it is difficult to deconvolute the individual contributions by the cathode and the anode. To gain insight into the impedance of individual electrodes, measurements on symmetric cells have been proposed, where two cathodes or two anodes from nominally identical cells are reassembled to symmetric cells.[3,4] While this method leads to reliable results, it requires the disassembly and destruction of the original cells. Hence, for the impedance investigation of cells at different state-of-charge (SOC) values or at different points in their cycle life, a large number of nominally identical cells operated or aged at identical conditions is required.

An alternative approach is the use of a reference electrode, where the AC potential perturbation is measured between working and reference electrode, while the current is applied between working and counter electrode. A number of cell designs for impedance measurements with a reference electrode have been suggested, with the reference electrode either placed between anode and cathode,[5–9] or placed in-plane with anode or cathode through a central hole (also referred to as co-axial arrangement).[10–12] The more commonly used design, however, is a Swagelok T-cell design with the reference electrode (typically consisting of a lithium metal disc) being placed perpendicularly to the anode and cathode, outside the active area.[13] Yet, experiments and numerical simulations by Ender et al.[14] showed that the impedance measurements with the latter reference electrode placement can display significant distortions caused by small in-plane offsets between anode and cathode (referred to as geometrical asymmetry) and/or by large differences in the impedance response of anode and cathode (referred to as electrical asymmetry), consistent with earlier work by Dees et al.[15] This is also the case for coaxially located reference electrodes, for which the measured anode or cathode impedance is shown to be highly sensitive toward misplacements of the electrodes.[10,12,16] The impedance artefacts in both of these designs stem from the location of the reference electrode being *at the edge* of the working and the counter electrodes, where the current density is not homogeneous. If one electrode is now shifted slightly toward the reference electrode, the potential field around the reference electrode is dominated by this electrode, which leads to a biased impedance response. In contrast, if the reference electrode is placed *centrally between* the electrodes far away from their edges, small relative shifts of the electrodes do not affect the impedance response.[15] This geometry is typically realized by using a thin wire with an electronic insulator around its perimeter, being exposed only at its end, which is placed well inside the active area.[6–8] Yet, this location of the reference electrode can block parts of the working electrodes and thus alter the potential field between them. In order to minimize this effect, the reference electrode needs to be small compared to the size of the electrodes and the distance between them. Dees et al.[15] showed that a 25 μm thick reference electrode, between two electrodes separated by 100 μm, delivered sufficiently accurate potential and impedance measurements.

Unfortunately, the design of a micro-reference electrode, i.e., an insulated wire with small diameter (25–50 μm) imposes difficult requirements on the choice of material. Lithium metal, which is typically used as reference electrode in lithium ion cells, is difficult to accurately produce and handle in micron-sized dimensions. On the other hand, the potential of the reference electrode should be well-defined and stable in a lithium-ion electrolyte, as the reference electrode should (ideally) also be able to record the absolute potential of both electrodes during cycling. Additionally, potential drifts during impedance measurements can lead to a biased impedance response.[17] Zhou et al.[7] successfully plated lithium in-situ onto a thin, insulated copper wire as reference electrode. As the wire insulation was only removed at the very tip of the wire, the reference electrode active area was small and located far away from the electrode edges. However, they also showed that the potential stability of the reference electrode depends strongly on the plating parameters, as thin films of high surface area lithium can be completely dissolved or disconnected due to continuous SEI growth.

A similar approach has been followed by Abraham et al.[6] using an insulated tin-coated copper wire. Yet, instead of plating metallic lithium on a non-alloying copper wire like Zhou et al.,[7] lithium was in-situ electrochemically alloyed with the tin coating at the wire tip, where the insulation had been removed. While the long-term potential stability of this reference electrode is also limited, it can

*Electrochemical Society Student Member.
**Electrochemical Society Fellow.
[z]E-mail: sophie.solchenbach@tum.de

nevertheless be used for impedance measurements of individual electrodes during long-term cycling studies by short re-lithiation prior to the measurement.[8,18] The use of lithium alloys as reference electrode brings – in theory – a number of advantages: i) lithium forms alloys with a large number of metals, which are readily available as thin wires and at high purity;[19,20] and ii) the volume expansion and thus the specific surface area of lithium alloys is smaller compared to in-situ plated lithium, which means that the alloy should be less prone to self-delithiation surface reactions. Yet, only few lithium alloys have been employed as reference electrodes apart from Li-Sn:[6,8,18] a lithiated aluminum wire has been used as reference electrode by Verbrugge et al.;[9] and Gómez-Cámer and Novák[21] recently demonstrated the use of a lithium-bismuth alloy as reference electrode in their specifically designed impedance cell with a coaxial reference electrode.

So far, the viability of lithium-gold alloys as reference electrodes has not yet been examined. Studies on the electrochemical lithiation of gold are limited, as its poor capacity retention, high cost and low specific capacity compared to other alloys disqualify gold as a potential anode material. The Li_3Au phase is the most lithium-rich composition which can be obtained electrochemically, corresponding to a specific capacity of 408 mAh/g_{Au}.[19,22–26] The lithiation of gold proceeds in two main potential plateaus, with the first stage having an OCV potential of ~0.3 V vs. Li/Li^+, and the second ~0.2 V vs. Li/Li^+.[25] Surprisingly, the intermediate phases detected between α-Au and Li_3Au during electrochemical alloying could not be assigned to any of the known thermodynamic Li-Au phases.[27–30] Bach et al.[30] recently identified the metastable Li_3Au_2, Li_5Au_3, Li_3Au_5 and $LiAu_2$ phases by in-situ high energy X-ray diffraction during the electrochemical lithiation and delithiation of gold thin film electrodes.

Despite its drawbacks as an anode, several properties of the lithium-gold alloy make it an interesting reference electrode material: i) the potentials of both stages are very flat, and already low degrees of lithiation will result in an OCV of around 0.31 V vs. Li/Li^+; ii) it is difficult to completely delithiate a lithium-gold alloy by electrochemical or chemical means;[24,26] iii) gold is chemically resistant against HF and does not form any substantial surface oxide films;[31] and, iv) the high electrical conductivity of gold means that the potential drop along the length of the reference electrode wire is negligible.

In this study, we developed a novel micro-reference electrode based on a 50 μm thick, insulated gold wire, which we integrated into a conventional T-cell design. This gold wire reference electrode (GWRE) is placed centrally between both electrodes and two 200 μm thick glass fiber separators. Analogous to the approach used by Abraham et al.[6] for a tin-based reference electrode, we achieve a stable potential of the gold wire by in-cell electrochemical alloying with lithium. We show that the potential of the lithiated GWRE is stable for several weeks, even under elevated temperatures (40°C). With this lithiated GWRE, we are able to record the potential of both electrodes in LFP/graphite full-cells for more than 200 cycles. Further, we evaluate the capabilities of the lithiated GWRE to accurately measure the impedance of individual electrodes in full-cells, which we verify by symmetric cell measurements. As a proof of concept, we conduct a similar study as Burns et al.[32] on the impedance growth of anode and cathode in the presence of different concentrations of vinylene carbonate (VC) in LFP/graphite full-cells, using however our lithiated GWRE instead of a symmetric cell approach. We can reproduce the findings by Burns et al.[32] and further demonstrate that the total amount of VC per active material, rather than its concentration, is the key parameter for the electrolyte/anode interface resistance. This result is important when electrolyte additives are tested in laboratory cells, as these cells typically have a higher electrolyte to active material ratio than commercial lithium-ion cells.

Experimental

Electrode preparation.—Lithium iron phosphate ($LiFePO_4$, LFP) electrodes were prepared by mixing LFP (BASF SE, Germany), carbon black (Super C65, Timcal), and polyvinylene diflouride (PVDF, Kynar) in a mass ratio of 93:3:4 with NMP (N-methyl pyrrolidone, anhydrous, Sigma-Aldrich, Germany) in a planetary mixer (Thinky Corp.) for 15 min. The resulting ink was coated on carbon-coated aluminum foil (MTI) with a doctor blade mounted on an automatic coater and dried at 50°C in a convection oven for at least 3 h. The final LFP coating had a loading of 11.7 mg_{LFP}/cm^2 (≡ 2.0 mAh/cm^2 based on 170 mAh/g_{LFP}). Electrodes with a diameter of 11 mm were punched out and pressed to 35% porosity (2 × 60 s at 260 MPa) with a KBr press (Mauthe, PE-011). Graphite electrodes were prepared by mixing graphite (T311, SGL Carbon GmbH) and PVDF in a mass ratio of 95:5 with NMP, following the same procedure. The graphite ink was doctor-blade coated on copper foil (MTI) and dried in a convection oven at 50°C for at least 3 h. The final loading of the graphite coating was 5.9 $mg_{graphite}/cm^2$ (≡ 2.2 mAh/cm^2 based on 372 $mAh/g_{graphite}$) at a porosity of 40%. Both types of electrodes were dried under dynamic vacuum at 120°C overnight and transferred to an Argon-filled glove box (MBraun, Germany) without exposure to air.

Cell design and assembly.—The reference electrode current collector of a 3-electrode Swagelok T-cell (see Figure 1a) was modified to be able to host the GWRE. To this purpose, a small hole (1 mm diameter, 2.5 mm depth) was drilled into the flat front side of the reference current collector. To fix the GWRE wire, a thread was cut into the side of the reference current collector at approximately 2 mm distance from the front edge. For the actual reference electrode, a gold wire with a core diameter of 50 μm, coated with a 7 μm thick polyimide insulation (Goodfellow Cambridge Ltd., United Kingdom), was cut into pieces of ~1.5 cm. The last 3 mm of one end of the wire was slightly scratched with a scalpel to allow good electrical contact of the wire to the reference electrode current collector. The scratched end of the wire was then inserted into the hole of the reference current collector and fixed with a small set screw. During cell assembly, the GWRE was inserted through a hole in the polymer lining of the T-cell (green lines in Fig. 1) and cushioned between two glassfiber separators (see Figure 1b); note that the insulation at the wire perimeter was not removed and that the only segment of the wire accessible to the electrolyte is the cut cross-section at the tip of the wire (see Figure 1c). The SEM image of the wire tip in Figure 1c shows that the polyimide insulation is almost completely intact around the edge of the cut cross-section, and that the exposed gold surface is relatively smooth. As the sealing and all other cell components are left unchanged compared to the conventional T-cell design, we could omit any benchmarking and air permeation tests that are normally required when developing a new electrochemical cell for the lithium ion chemistry. T-cells with GWRE were assembled with graphite as anode, LFP as cathode, and 2 glassfiber sheets (Whatman) as separator soaked with 60 μL electrolyte.

As standard electrolyte, 1 M lithium hexafluorophosphate ($LiPF_6$) in a mixture of ethylene carbonate (EC) and ethyl methyl carbonate (EMC) at a weight ratio of 3:7 was used (LP57, BASF SE, Germany). The water content of this electrolyte was determined via Karl-Fischer-Titration to be <10 ppm. Vinylene carbonate (VC, BASF SE, Germany) was added in weight ratios of 0.17% and 0.52% to the standard electrolyte. These concentrations were chosen as they yielded g_{VC}/Ah_{Cell} ratios equal to 2% and 6% VC additive (same solvent/salt) in 225 mAh full-cells used in a study on the anode and cathode impedance growth in the presence and absence of VC by Burns et al.[32] For stability measurements of the gold wire electrode, symmetrical lithium/lithium cells with a GWRE were built using 11 mm lithium discs (450 μm thickness, Rockwood, USA) as both cathode and anode.

Cell cycling and impedance measurements.—The gold wire reference was lithiated by applying a current of 150 nA between the working electrode (LFP or lithium) and the gold wire reference electrode using a potentiostat (VMP300, BioLogic, France). Please note that the selected current range of 10 μA has an accuracy of 0.1%, which leads to an error of ~10 nA. LFP/graphite cells were cycled

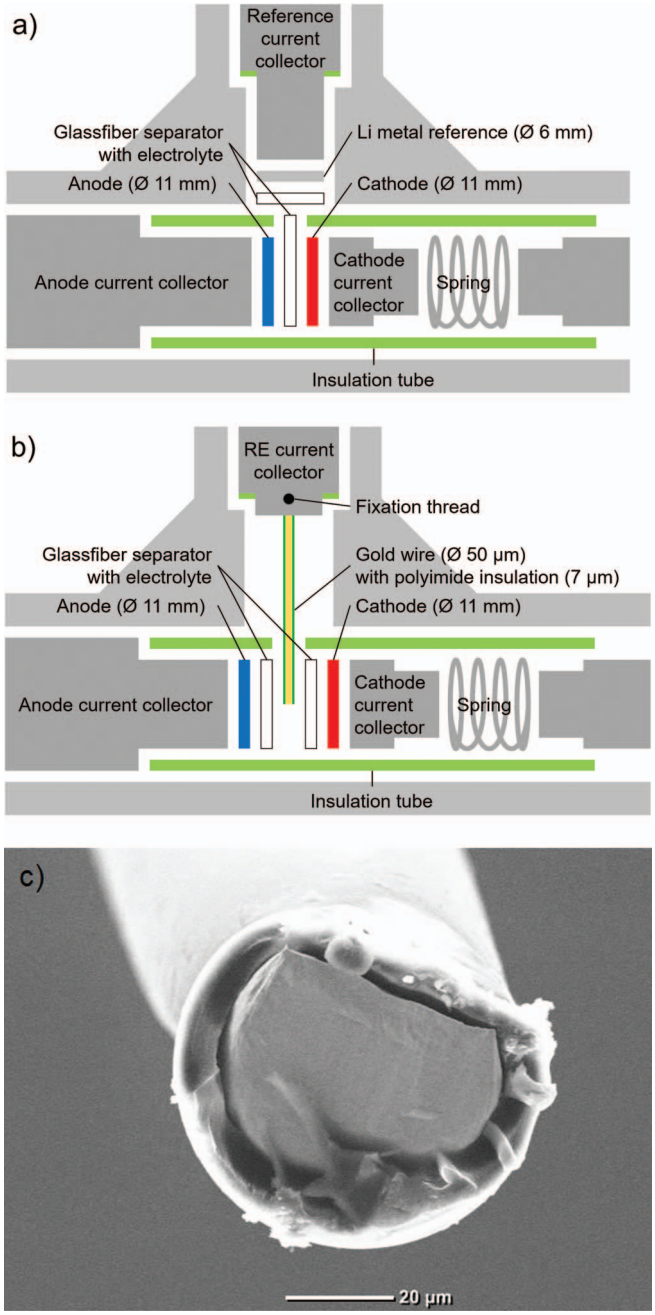

Figure 1. a) Conventional Swagelok T-cell design, b) modified T-cell design with gold wire reference electrode (GWRE), c) SEM image of the cut cross-section of gold wire tip prior to lithiation.

between cell voltages of 2 and 4 V using a BioLogic potentiostat and a CCCV charge/CC discharge procedure with a C/20 current cutoff to end the CV phase. During cycling, the cells were placed inside a climatic chamber with a constant temperature of 25°C or 40°C. Electrochemical impedance spectroscopy (EIS) measurements were conducted either potential controlled with a perturbation of 5 mV at OCV (referred to as PEIS, with the AC voltage perturbation applied between working and reference electrode) or current controlled with a perturbation of 0.5 mA (referred to as GEIS), both in a frequency range of 100 kHz–0.1 Hz. The impedance measurements were conducted at 50% SOC and 25°C or 10°C. Prior to the measurement, the cells were allowed to rest at OCV and thermally equilibrate for 15 min.

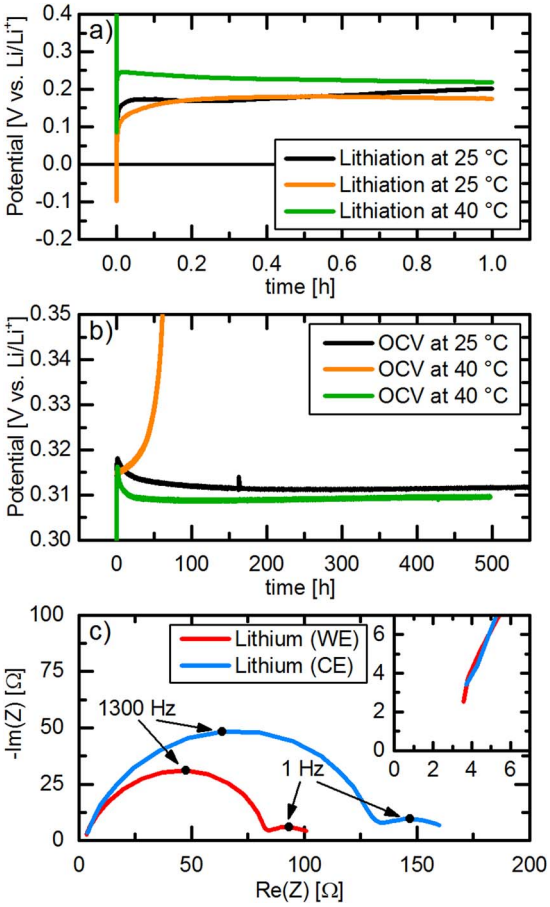

Figure 2. a) Potential of two GWREs during lithiation at 25°C (black and orange lines) and of one GWRE during lithiation at 40°C (green line) with 150 nA for 1 h. b) Potential of GWREs lithiated at 25°C during subsequent OCV at 25°C (black line) or at 40°C (orange line) as well as of the GWRE lithiated at 40°C during subsequent OCV at 40°C (green line). c) Nyquist plot of the lithium electrodes in a lithium/lithium cell at OCV at 25°C after lithiation of the GWRE at 25°C (PEIS, 100 kHz to 0.1 Hz, 5 mV AC perturbation). All potentials are given vs. Li/Li^+ and experiments were conducted in LP57 electrolyte.

Results and Discussion

Suitability of the GWRE to quantify individual electrode impedance in full-cells.—As a first step, the potential stability of a lithiated GWRE was investigated in symmetric lithium-lithium T-cells with our modified design (see Fig. 1b). The GWRE was lithiated by applying a current of 150 nA for 1 h between one of the lithium electrodes and the GWRE. The black curve in Figure 2a shows the potential of the GWRE vs. Li/Li^+ during galvanostatic lithiation at 25°C. The potential drops briefly below 0 V vs. Li/Li^+ and then stays constant at ~0.2 V vs. Li/Li^+ during the entire lithiation procedure, which is similar to the first potential plateau observed during the electrochemical lithiation of gold thin films.[25] The overpotential at the first moments of lithiation have been attributed to the reduction of surface oxides[19] or the nucleation of the lithium-gold alloy phase.[25] During the subsequent OCV at 25°C (see black curve in Figure 2b), the potential of the GWRE shoots up to 0.318 V and then quickly relaxes to ~0.311 V vs. Li/Li^+, which corresponds to the OCV potential of a Li_xAu alloy with $0 < x < \sim 1.2$.[25] The lithiated GWRE potential remains stable for more than 500 h, varying by less than 2 mV after the initial 20 h of the OCV period. This means that the lithiated GWRE might not be suitable for highly accurate potential measurements during initial cycles, but is sufficient for tracking electrode potentials during prolonged cycling. Further, no morphological

changes of the wire could be observed visually after disassembly of the cells.

As many battery cycling tests are performed at higher temperatures to accelerate aging and to reflect more realistic operating conditions, it is desirable that the GWRE also functions at higher temperatures. However, if the GWRE is lithiated at 25°C and the cell temperature is then increased to 40°C for OCV measurements, the gold wire potential starts to drift to more positive values after less than 10 hours (see orange curve in Figures 2a and 2b). This is in accordance with Abraham et al.,[6] who reported that the potential of a lithiated tin wire is substantially less stable at elevated temperatures, where the rate of SEI growth and the concomitant self-delithiation is generally enhanced. Once the cell is heated to 40°C, this effect must lead to a rather rapid depletion of lithium at the wire's tip, resulting in the observed potential drift. Interestingly, a re-lithiation of the wire with the same procedure at 25°C restored a stable GWRE potential of 0.311 V vs. Li/Li^+, as long as the cell was kept at 25°C. We also observed that the GWRE potential stability over long time was limited in combination with high voltage cathodes (>4.7 V vs. Li/Li^+), and also here the GWRE could be relithiated.[33]

After further investigations, we found that if the gold wire lithiation is conducted at 40°C (see green curve in Figures 2a and 2b), the GWRE shows the same stability during OCV at 40°C as was observed at 25°C, only shifted downwards by 1–2 mV. It is reported that an SEI formed at higher temperatures contains more inorganic species,[34] which we hypothesize might form a more effective surface film on the lithium-gold alloy. While high temperature SEI formation was shown to lead to inferior capacity retention on graphite anodes during cycling,[34] the more inorganic SEI could be advantageous in the absence of cycling-induced volume changes, i.e., for reference electrodes. However, the exact mechanism behind this enhanced stability by lithiation at higher temperatures is not clear at this point. We further believe that the stable potential of the GWRE for over hundreds of hours at up to 40°C is partly due to the fact that, contrary to previous micro-electrode designs,[6,7] the reference electrode area exposed to the electrolyte is limited to the cross-sectional area of the tip (see Figure 1c), minimizing side reactions with the electrolyte. The stable potential over 500 h indicates that the lithium diffusion along the wire (i.e., away from the tip) must be sufficiently slow to prevent a significant depletion of lithium at the tip.

To evaluate if the GWRE in the modified T-cell design is suitable for impedance measurements of individual electrodes, we also measured the impedance of a symmetrical lithium/lithium cell with a GWRE (see Figure 2c). Arbitrarily, one of the lithium electrodes was designated as working electrode (WE), while the other was designated as counter electrode (CE). Prior to the impedance measurement in the lithium/lithium cell, the GWRE was lithiated at 25°C as described above from the lithium electrode designated as WE. The high frequency resistance (see inset) is identical for both lithium electrodes, which indicates that the GWRE is located centrally between the electrodes. Hence, a first precondition for an artefact-free measurement is fulfilled.[14] Both lithium electrodes show a large semicircle in the high-frequency region (100 kHz–20 Hz, with the apex at ≈1.3 kHz), followed by a smaller semicircle at frequencies between 20 and 0.1 Hz (with the apex at ≈1 Hz), as reported previously for lithium metal electrodes.[35,36] While the high-frequency semicircle has been ascribed to the SEI resistance, the semicircle in the low-frequency region is thought to represent the charge transfer resistance.[36] Interestingly, both semicircles of the electrode used for the lithiation of the GWRE (designated as WE, see red line in Figure 2c) are about 35% smaller compared to the other electrode (≡ CE, s. blue line). We believe that this originates from the stripping of lithium from the WE electrode during lithiation of the GWRE, as this would cause a roughening of the lithium surface, leading to higher surface area and thus smaller impedance.

As a next step, the use of the GWRE in a LFP/graphite full-cell is tested and evaluated. Here, we also want to assess whether lithiation of the reference electrode is necessary for impedance measurements, i.e., whether the non-lithiated Au wire can be used as pseudo-GWRE.

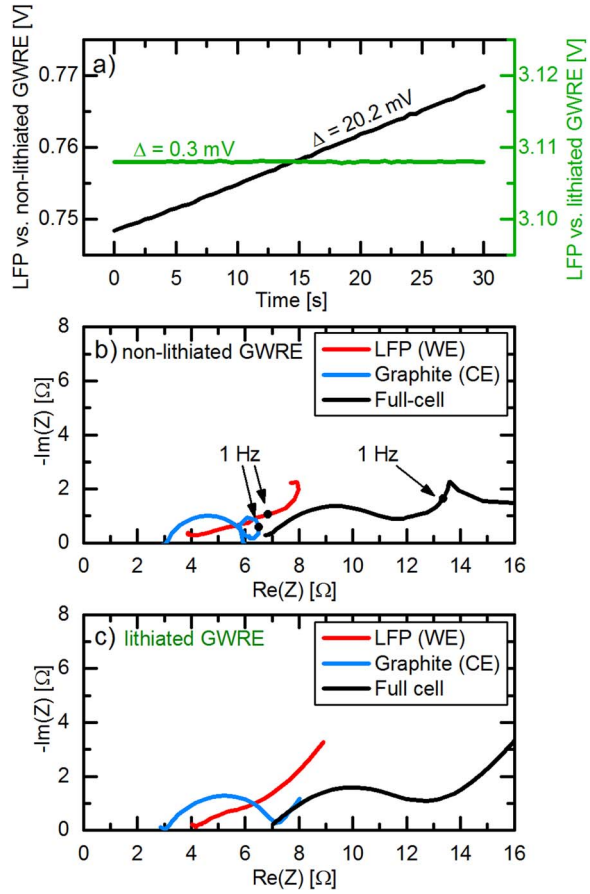

Figure 3. Comparison of voltage drift and impedance quality for a lithiated GWRE and a non-litiated pseudo-GWRE in LFP/graphite full-cells. a) Measured potential between the LFP working electrode (WE) and either the non-lithiated pseudo-GWRE (black line) or the lithiated GWRE (green line). b) Nyquist plot of an LFP/graphite full-cell obtained with a non-lithiated pseudo-GWRE before lithiation. c) Nyquist plot of an LFP/graphite full-cell obtained with a lithiated GWRE. Conditions: 25°C, LP57 electrolyte, PEIS with 5 mV amplitude at OCV (100 kHz–0.1 Hz).

To this purpose, we built identical LFP/graphite cells with GWRE: in one case, we lithiated the GWRE with 150 nA for 1 h at 25°C from the LFP electrode (note that the 150 nAh needed for lithiation of the GWRE are negligible compared to the LFP cathode capacity of 1.95 mAh); in the other case, we did not lithiate the GWRE. Subsequently, both cells underwent one formation cycle (at a rate of C/10) at 25°C and then were charged to 50% SOC. Figure 3a shows the potential of the LFP cathodes vs. the non-lithiated pseudo-GWRE and vs. the lithiated GWRE during 30 seconds of OCV prior to the impedance measurement. As the potential of the LFP electrode does not change significantly during the measurement, all potential changes can be ascribed to changes in the GWRE potential. While the LFP potential vs. the non-lithiated GWRE drifts about 20 mV during 30 seconds (black curve in Figure 3a), the LFP potential vs. lithiated GWRE remains stable within 0.3 mV (green curve in Figure 3a). In the subsequent potential-controlled impedance measurement (PEIS; 5 mV amplitude, 100 kHz–0.1 Hz) at OCV, the cell with the non-lithiated GWRE (see Figure 3b) shows significant distortions at frequencies near/below 1 Hz: i) the graphite impedance (blue line) displays an inductive loop; ii) the LFP impedance (red line) bends toward lower Re(Z) values; and, iii) even the full-cell impedance (black line) shows an irregular sharp peak. These distortions appear at frequencies near or below 1 Hz, where the average potential drift of 0.67 mV/s of the non-lithiated pseudo-GWRE (see black line in Figure 3a) is no longer significantly lower than the change of the AC voltage amplitude of

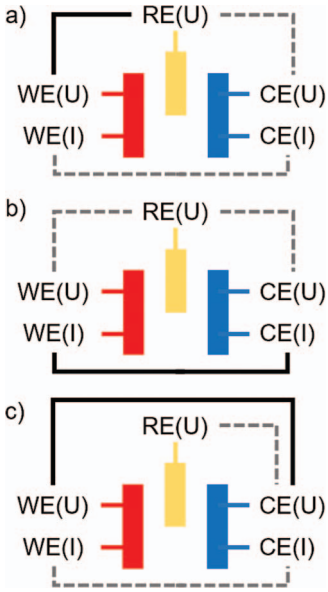

Figure 4. Systematic scheme of impedance measurements modes. a) Potential-controlled impedance spectroscopy (PEIS): The potential perturbation is controlled between WE and RE (black solid line), while current and potential between WE - CE are measured (gray dotted lines). A drift of the RE will lead to bias current between WE and CE. b) Current-controlled impedance spectroscopy (GEIS): The current perturbation is applied between WE and CE (black solid line), while potentials between WE - RE and CE - RE are measured. c) Modified potential-controlled impedance spectroscopy (PEIS): The potential perturbation is controlled between WE and CE (black solid line), while current between WE - CE and potential between RE - CE are measured (gray dotted lines).

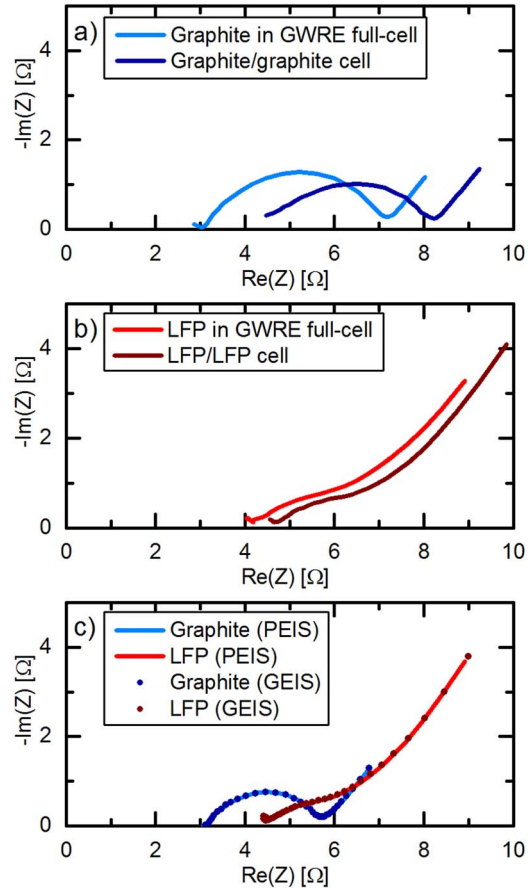

Figure 5. Impedance measurements on LFP and graphite electrodes after one C/10 formation cycle at 25°C and subsequent charge to 50% SOC. a) Nyquist plot of the graphite electrode of an LFP/graphite full-cell with lithiated GWRE (blue line) and of a symmetrical graphite/graphite cell divided by 2 (dark blue). b) Nyquist plot of the LFP electrode of an LFP/graphite full-cell with lithiated GWRE (red line) and of a symmetrical LFP/LFP cell divided by 2 (dark red). c) Comparison of the impedance response (100 kHz–0.1 Hz) of graphite and LFP electrodes under potential-controlled (PEIS at 5 mV amplitude, straight lines) and current-controlled (GEIS at 0.5 mA amplitude, dotted lines) conditions. All impedance measurements were conducted at 25°C.

5 mV. In contrast, the impedance spectra of the cell with the lithiated GWRE (Figure 3c) do not show these distortions, as the reference potential drift is almost two orders of magnitude lower in this case (0.01 mV/s). Our measurements are in agreement with simulations by Victoria et al.,[17] who showed that linear potential drifts on the order of 0.1 mV/s during impedance measurements can lead to these types of artefacts below 1 to 0.1 Hz, depending on the excitation amplitude. The potentiostatic impedance measurement mode used here (see Figure 4a), where the potential between WE and RE is controlled, leads to a particularly detrimental effect: As the base potential between RE and WE is fixed, the WE potential has to drift in the same way as the RE, which leads to a bias current between WE and CE. This continuously increasing current renders the full system non-linear and time-variant, leading to the full cell impedance artefacts observed at low frequencies. While normally the full cell impedance should be unaffected by artefacts related to the reference electrode,[14] this comparison shows that it is crucial to use a reference electrode with a stable and defined potential for WE - RE potential controlled impedance measurements at low frequencies. To avoid the effects of a drifting pseudo-reference electrodes on the full cell impedance, one could either use a current-controlled measurement mode (GEIS, see Figure 4b), or control the potential between WE and CE during the impedance measurement (Figure 4c). Yet, artefacts of a non-stable RE will still be visible in the half cell impedance in these measurement setups.

Next, we take a closer look at the impedance spectra of the LFP and graphite electrodes recorded with a lithiated GWRE (Figure 3c). In contrast to the previous setup with two lithium electrodes, the HFR of both electrodes is not identical here. Gaberscek et al.[37] showed that the contact resistance between an aluminum current collector and an LFP electrode composite can be on the order of several Ωcm^2. Our own measurements confirm that the through-plane resistance of the used LFP electrodes is about 1 Ωcm^2 higher compared to the graphite electrodes (data not shown). Thus, the $\approx$1 Ω difference in HFR originates from the higher contact resistance between the LFP coating and the current collector (1 Ωcm^2 corresponds to $\approx$1 Ω for our electrode area of 0.95 cm^2). The charge transfer semicircle of the LFP electrode is small and almost invisible, which suggests the lack of a resistive cathode film.[38,39] At the same time, the graphite anode shows a clearly distinguishable semicircle. As this semicircle is not visible in graphite electrodes prior to cycling, we attribute it to a combined SEI/charge transfer resistance on the graphite surface.

To further validate the impedance data measured in a full-cell with a lithiated GWRE, we compare its impedance response with that of symmetric cells, which are commonly used for accurate impedance measurements.[4] Figures 5a and 5b show the comparison of the impedance spectra of a graphite and a LFP electrode measured in a full-cell with lithiated GWRE and in reassembled symmetric LFP/LFP and graphite/graphite cells, all after one C/10 formation cycle at 25°C and subsequent charge to 50% SOC. Note that the impedances of the symmetric cells have been divided by 2 in order to account for the two nominally identical electrodes in the symmetric cells. Apart from a slight shift in HFR, the impedance response of the symmetric cells and the full-cell with the lithiated GWRE are essentially identical for both graphite (Figure 5a) and LFP (Figure 5b) electrodes. The HFR shift is probably introduced by a weaker compression of the glassfiber seperators in the symmetric cells, caused by the slightly different assembly

procedure for cells with and without GWRE. The additional high frequency contact resistance feature visible in the impedance spectra of symmetric cells by Dahn's group,[4] which results from the contact resistance between the cell housing and the electrode coating on the back side, does not appear in our symmetric cell impedance spectra (see Figures 5a and 5b), as we use single-side coated electrodes for both symmetric cells and full cells.

As a final consistency check, we performed a potential-controlled impedance measurement (PEIS) followed by a current-controlled impedance measurement (GEIS) on the same LFP/graphite full-cell with a lithiated GWRE (see Figure 5c). Mathematically speaking, both measurements should give identical results in a Nyquist plot; hence any differences between them would indicate a biased impedance response.[21] However, Figure 5c shows that the two methods deliver completely identical impedance spectra. These results confirm that the presented cell setup with the lithiated GWRE is free of measurement artefacts and is suitable for the impedance investigation of individual electrodes in full-cells. In summary, our modified T-cell design with a lithiated GWRE is able to provide accurate impedance measurements of individual electrodes in full-cells in a wide frequency range (100 kHz–0.1 Hz). A stable potential of the GWRE is especially crucial for measurements at low frequencies. If lithiated at elevated temperature, the potential of the GWRE is stable for several weeks at up to 40°C, which we partially attribute to the small area exposed to the electrolyte.

Anode & cathode impedances during cycling in full-cells with GWRE.—In the following, we want to demonstrate the suitability of the lithiated GWRE to investigate the evolution of anode and cathode impedances during extended charge/discharge cycle tests in full-cells. To this purpose, LFP/graphite full-cells with lithiated GWRE were cycled at 25°C for 200 cycles at a rate of 1C after two initial formation cycles at C/10. Impedance measurements were performed at 50% SOC after 5, 10, and each subsequent 10th cycle at 25°C. Figures 6a and 6b show the potential of the cathode and anode vs. the lithiated GWRE potential (left y-axis) during cycles 10, 50, 100 and 200 (for the sake of clarity, cycles in between were omitted), which can easily be converted into the Li/Li$^+$ scale by adding 0.311 V (right y-axis). The LFP charge and discharge plateaus are centered around 3.11 V vs. the lithiated GWRE (see Figure 6a and also Figure 3a), corresponding to a calculated value of 3.42 V vs. Li/Li$^+$, which matches well with the true LFP equilibrium potential.[40] The LFP potential center vs. lithiated GWRE remains constant during cycling, meaning that the lithiated GWRE maintains its stable potential of 0.311 V vs. Li/Li$^+$. Throughout cycling, the overpotentials of both electrodes do not change, yet the maximum potential of the graphite anode at the discharge end point moves upwards (see dark blue to light blue lines in Figure 6b). At the same time, the minimum potential of the cathode also moves upwards (see dark red to light red lines in Figure 6a), which indicates that the SOC of both electrodes slip against each other. Figure 6c shows the impedance spectra of both cathode and anode after 10, 50, 100 and 200 cycles. Note that both the cathode and anode impedance decrease slightly from cycle 5 (data not shown) to cycle 10, which could be related to the dissolution of gasses evolved during formation and/or improved wetting over the first cycles. Between cycle 10 and 200, the high frequency resistance of both electrodes increases slightly by about 0.1–0.2 Ω. This could be due to an increased electrical resistance between the electrode coatings and the current collectors, implying a very slow delamination of the composite electrodes, or a higher ionic resistance within the bulk electrolyte. While the cathode impedance shows no further changes during cycling, the anode semicircle increases slightly from ~1.9 Ω after cycle 10 to ~2.2 Ω after cycle 200, which indicates a very slow SEI growth. Overall, the potential changes of both electrodes during cycling and the small but measureable impedance growth of the anode can be related to the loss of active lithium due to a slow but steady SEI growth, which has been identified as the dominant aging mechanism in LFP/graphite cells.[41–45]

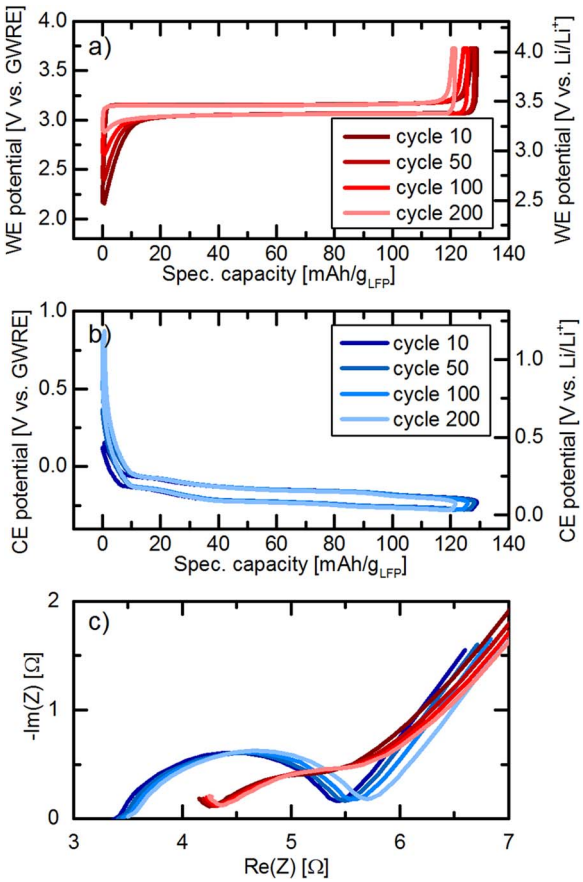

Figure 6. Charge/discharge of an LFP/graphite full-cell with a lithiated GWRE at a rate of 1C after two initial formation cycles at C/10 (LP57 electrolyte, 25°C). a) Cathode potential vs. the lithiated GWRE of cycles 10, 50, 100 and 200. b) Anode potential vs. the lithiated GWRE of cycles 10, 50, 100 and 200. The conversion to the Li/Li$^+$ scale (right axis in a and b) was done by adding 0.311 V to the GWRE potential. c) Nyquist plot of the PEIS (5 mV amplitude, 25°C) at 50% SOC of both the graphite anode (shown in the range from 100 kHz to 0.1 Hz) and the LFP cathode (shown in the range from 100 kHz to 0.3 Hz) after cycle number 10, 50, 100 and 200.

Application of the GWRE to anode & cathode impedance growth during full-cell formation.—Vinylene carbonate (VC) is one of the most commonly used electrolyte additives, as it leads to improved SEI stability at elevated temperatures and thus enhanced cycle life of lithium ion cells.[46,47] However, high concentrations of VC have shown to increase the impedance of both anode and cathode,[32] which in turn leads to higher overpotentials and heat generation during cycling. Freiberg et al.[48] recently indicated that the absolute amount of an additive per active material, instead of its concentration, is the crucial parameter when comparing larger cells (e.g. commercial cells) and small lab-scale cells (e.g. coin cells). Therefore, we want to compare the effect of different amounts of VC in LP57 electrolyte on both anode and cathode impedance in LFP/graphite full-cells obtained with a lithiated GWRE to the study by Burns et al.,[32] who used 225 mAh LCO/graphite pouch cells with the same electrolyte and examined the effect of VC on the impedance of the individual electrodes via symmetric cell measurements. In Burns' study, it was shown that the charge transfer resistance of a graphite anode decreases slightly from 0% to 0.5% VC in the electrolyte and increases roughly linearly with VC concentration between 1% and 6% VC (see Figure 9b in Ref. 32). At the same time, the impedance of the LCO cathode from Burns' study (see Figure 9a in Ref. 32) decreases about 50% from 0% to 2% VC and then gradually increases again up to VC concentrations of 6% to a value which is still below the 0% VC case. Unfortunately, the exact amount of active material in the cells used by Burns et al. was not

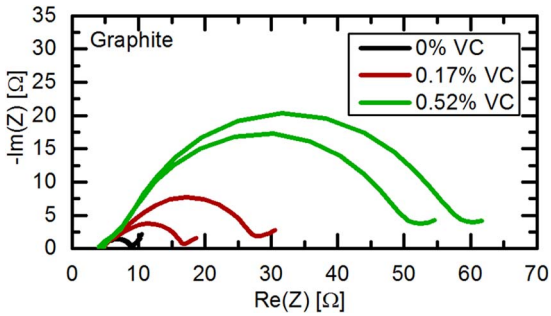

Figure 7. Nyquist plot of the graphite anode impedance after one formation cycle and recharge to 50% SOC at 40°C of LFP/graphite full-cells with a lithiated GWRE in LP57 electrolyte containing 0%, 0.17%, and 0.52% VC in the electrolyte. PEIS was measured at 10°C between 100 kHz–0.1 Hz with an amplitude of 5 mV.

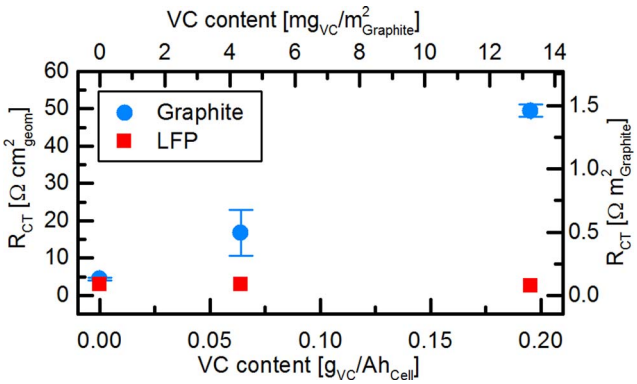

Figure 8. R_{ct} of the graphite anode and the LFP cathode after formation in LFP/graphite full-cells with different VC amounts added to LP57 electrolyte. Impedance data were obtained with a lithiated GWRE (PEIS at 5 mV amplitude and 10°C between 100 kHz and 0.1 Hz) and fitted by an equivalent circuit consisting of a resistor for the electrolyte, an RQ-element for the electrolyte/electrode interface resistance, and a Warburg element for solid-state diffusion. Note that the upper x-axis and the right y-axis display the VC content and charge transfer resistance normalized to the graphite BET surface area.

given. However, the specific capacities of LCO and LFP are similar, and our anode to cathode capacity ratio of 1.1 is close to a commercial balancing. Hence, we think it is reasonable to assume that the masses of both anode and cathode active materials are proportional to the respective cell capacity. As the ratio of electrolyte to cell capacity (and thus active material) in our lab-scale T-cell design is 11.6 times higher compared to Burns et al.[32] (38 $g_{electrolyte}/Ah_{Cell}$ vs. 3.3 $g_{electrolyte}/Ah_{Cell}$), we adjusted the amount of VC in the electrolyte accordingly. Thus, our chosen concentrations of 0.17% and 0.52% VC represent the same g_{VC}/Ah_{Cell} ratio, namely 0.06 g_{VC}/Ah_{Cell} and 0.2 g_{VC}/Ah_{Cell}, as cells with 2% and 6% VC in the study by Burns et al.[32] After lithiation of the GWRE and one formation cycle at 40°C, the LFP/graphite cells were charged to 50% SOC and the impedance measurements were then conducted at 10°C, i.e., under the same conditions as reported by Burns et al.[32]

Figure 7 shows the Nyquist plot of graphite electrodes after formation with different concentrations of VC. For each concentration, two cells are shown to assess the cell to cell variation. Quite clearly, the cells with 0.17% and 0.52% VC show an increased charge transfer resistance of the graphite anodes. These results already indicate that electrolytes cannot be compared without considering the amount of active material, as the anode charge transfer resistance decreases up to a VC concentration of 0.5% in the study by Burns et al.,[32] while Figure 7 shows that the anode charge transfer resistance increases substantially within the same VC concentration range.

To quantify the charge transfer resistances, the impedance spectra of cathode and anode of each cell were fitted using a simple electrochemical equivalent circuit composed of: i) a resistor for the electrolyte, ii) a resistor and a constant phase element in parallel to describe the electrolyte/electrode interface resistance, and, iii) a Warburg-type diffusion element in series representing solid state diffusion. This circuit is a simplified version of a model used by Illig et al.[35] for LFP electrodes; we omitted the electrode contact resistance and the low frequency capacitor, as both are not visible within our measurement range. Figure 8 shows the average fitted charge transfer resistances (left y-axis), normalized to the geometrical electrode area, of both electrodes at different g_{VC}/Ah_{Cell} ratios (lower x-axis). The anode charge transfer resistance is ~5 Ωcm^2 for cells without VC and increases to ~16 Ωcm^2 and ~47 Ωcm^2 for cells with 0.06 g_{VC}/Ah_{Cell} (≡0.17% VC) and 0.2 g_{VC}/Ah_{Cell} (≡0.52% VC), respectively. In comparison, Burns et al.[32] showed an anode charge transfer resistance of ~30 Ωcm^2, ~60 Ωcm^2 and ~150 Ωcm^2 for cells with identical g_{VC}/Ah_{Cell} ratios (0%, 2% and 6% VC in their study). The linear increase in charge transfer resistance from 0.033 to 0.2 g_{VC}/Ah_{Cell} that has been observed by Burns et al.[32] (corresponding to 1%-6% VC in their study) is also found in our results within the same g_{VC}/Ah_{Cell} range, although our absolute VC concentrations are completely different (0–0.52% VC). This further proves that the amount of additive per active material (here corresponding to the g_{VC}/Ah_{Cell} ratio) determines the effect of an additive on the surface of an electrode, and not its concentration. The differences in absolute resistance values between Burns' study[32] and ours could be explained by differences in active material loading and BET surface area of the used electrodes: As the impedance of an electrode is inversely proportional to the electrochemical active area, a higher roughness factor (i.e., electrode surface area per geometric area) will result in an overall lower impedance, even if the surface chemistry is identical. While our electrodes are loaded with 5.9 mg/cm^2 graphite having a BET surface area of ~5 m^2/g, we can estimate the anodes investigated by Burns et al.[32] to have a loading of ~10 mg/cm^2 graphite[49] with a BET surface area of ~0.7 m^2/g.[50,51] In total, this would give a ~5-fold higher roughness factor in our study, which would fit with the measured ~4 times lower absolute charge transfer resistance values. However, it is to note that the assumed values for loading and BET were taken from other publications by the Dahn group and not directly from Burns et al.,[32] and hence this is only an estimate. A different BET surface area would also affect the amount of additive per unit surface, and thus result in a different charge transfer resistance. To make our data more comparable to future studies, we therefore included the amount of VC per graphite BET surface area (mg$_{VC}$/m$^2_{Graphite}$, upper x-axis) and the charge transfer resistance normalized to the graphite BET surface area (Ω m$^2_{Graphite}$, right y-axis) in Figure 8. An additional difference between our cells and the study by Burns et al.[32] is the different cycling protocol: Our impedance data was recorded after one formation cycle, whereas the cells by Burns et al.[32] were disassembled for impedance measurements of symmetric cells after 23 cycles. However, further cycling and impedance measurements of our LFP/graphite cells showed that the impedances of both electrodes does not change significantly with cycle number once the formation cycle is completed.

The charge transfer resistance of the LFP cathode in our study does not show any dependency on the VC content (see Figure 8). In contrast, Burns et al.[32] found that the impedance of an LCO cathode decreases about half by the addition of low concentrations of VC (0.5–2%) and increases again slightly at higher VC concentrations (4–6%). This discrepancy can be understood considering the studies by El Ouatani et al.,[52,53] which showed that LCO cathodes form a surface film of poly(VC) in VC-containing electrolytes, while this film is lacking on LFP cathodes. Thus, the cathode charge transfer resistance remains constant and independent from the VC content in LFP/graphite cells. As VC reacts on the LCO surface,[52,53] one can imagine that slightly less VC is available for SEI formation in LCO/graphite than in LFP/graphite cells. This could in turn also partially explain the deviations of the absolute values for the anode charge

transfer resistance at points of equal g_{VC}/Ah_{Cell} in our study compared to Burns et al.[32] Hence, we can conclude that not only the ratio of additive to active material, but also the cell chemistry of cathode and anode and their reactivity toward the additive is an important aspect to consider when comparing additives across different cell types.

Conclusions

In this study, we introduce a novel micro-reference electrode in a Swagelok T-cell design, which is suitable for impedance and potential measurements of both working and counter electrode individually. The reference electrode consists of a thin, insulated gold wire and is placed centrally between both electrodes and two 200 μm thick glass fiber separators. By electrochemical alloying with lithium, we achieve a defined potential of 0.311 V vs. Li/Li^+ of the gold wire reference electrode (GWRE), which is stable for several weeks during cycling and even under elevated temperatures (40°C). In contrast to previous micro-reference designs, only the cut cross-section of the wire's tip is the electrochemically active area, which supposedly minimizes side reactions with the electrolyte and contributes to the long-term stable potential of the GWRE. The cell setup with GWRE was validated by impedance measurements of the corresponding symmetrical cells. Further, we demonstrated the suitability of the lithiated GWRE for impedance and potential measurements in LFP/graphite full-cells for up to 200 cycles. Based on these measurements, we could identify lithium inventory loss due to SEI growth as the dominant aging mechanism in LFP/graphite cells at room temperature, in agreement with literature.

As a proof of concept, we investigated LFP/graphite full-cells with a lithiated GWRE and different VC contents in the electrolyte. Using symmetrical cells, Burns et al.[32] showed that the charge transfer of a graphite anode depends almost linearly on the concentration of vinylene carbonate (VC) in the electrolyte. We can reproduce the findings by Burns et al.[32] using a lithiated GWRE, and further demonstrate that the ratio of mass VC to active material, rather than the VC concentration, is the key parameter for the electrolyte/anode interface resistance. This result needs to be considered when electrolyte additives are tested in laboratory cells, as these cells typically have a higher electrolyte to active material ratio than commercial lithium-ion cells.

Acknowledgment

This work is financially supported by the BASF SE Battery Research Network. J. L. gratefully acknowledges the funding by the Bavarian Ministry of Economic Affairs and Media, Energy, and Technology for its financial support under the auspices of the EEBatt project.

References

1. M. Klett, J. A. Gibson, S. E. Trask, B. J. Polzin, A. N. Jansen, D. W. Dees, and D. P. Abraham, *J. Electrochem. Soc.*, **163**, A875 (2016).
2. N. Ogihara, S. Kawauchi, C. Okuda, Y. Itou, Y. Takeuchi, and Y. Ukyo, *J. Electrochem. Soc.*, **159**, A1034 (2012).
3. C. H. Chen, J. Liu, and K. Amine, *J. Power Sources*, **96**, 321 (2001).
4. R. Petibon, C. P. Aiken, N. N. Sinha, J. C. Burns, H. Ye, C. M. VanElzen, G. Jain, S. Trussler, and J. R. Dahn, *J. Electrochem. Soc.*, **160**, A117 (2013).
5. T. S. Ong and H. Yang, *J. Electrochem. Soc.*, **149**, A1 (2002).
6. D. P. Abraham, S. D. Poppen, A. N. Jansen, J. Liu, and D. W. Dees, *Electrochim. Acta*, **49**, 4763 (2004).
7. J. Zhou and P. H. L. Notten, *J. Electrochem. Soc.*, **151**, A2173 (2004).
8. A. N. Jansen, D. W. Dees, D. P. Abraham, K. Amine, and G. L. Henriksen, *J. Power Sources*, **174**, 373 (2007).
9. M. W. Verbrugge, D. R. Baker, and B. J. Koch, *J. Power Sources*, **110**, 295 (2002).
10. S. Klink, E. Madej, E. Ventosa, A. Lindner, W. Schuhmann, and F. La Mantia, *Electrochem. commun.*, **22**, 120 (2012).
11. C. Bünzli, H. Kaiser, and P. Novák, *J. Electrochem. Soc.*, **162**, A218 (2015).
12. C. Delacourt, P. Ridgway, V. Srinivasan, and V. S. Battaglia, *J. Electrochem. Soc.*, **161**, A1253 (2014).
13. V. R. Koch, C. Nanjundiah, G. B. Appetecchi, and B. Scrosati, *J. Electrochem. Soc.*, **142**, L116 (1995).
14. M. Ender, A. Weber, and E. Ivers-Tiffée, *J. Electrochem. Soc.*, **159**, A128 (2012).
15. D. W. Dees, A. N. Jansen, and D. P. Abraham, *J. Power Sources*, **174**, 1001 (2007).
16. S. Klink, D. Höche, F. La Mantia, and W. Schuhmann, *J. Power Sources*, **240**, 273 (2013).
17. S. N. Victoria and S. Ramanathan, *Electrochim. Acta*, **56**, 2606 (2011).
18. D. P. Abraham, M. M. Furczon, S.-H. Kang, D. W. Dees, and A. N. Jansen, *J. Power Sources*, **180**, 612 (2008).
19. A. N. Dey, *J. Electrochem. Soc.*, **118**, 1547 (1971).
20. J. Wang, I. D. Raistrick, and R. A. Huggins, *J. Electrochem. Soc.*, **133**, 457 (1986).
21. J. L. Gómez-Cámer and P. Novák, *Electrochem. commun.*, **34**, 208 (2013).
22. T. L. Kulova, A. M. Skundin, V. M. Kozhevin, D. A. Yavsin, and S. A. Gurevich, *Russ. J. Electrochem.*, **46**, 877 (2010).
23. Y. J. Lee, Y. Lee, D. Oh, T. Chen, G. Ceder, and A. M. Belcher, *Nano Lett.*, **10**, 2433 (2010).
24. K. Nishio, K. Yuda, and H. Masuda, *ECS Electrochem. Lett.*, **2**, C1 (2012).
25. P. Bach, M. Stratmann, I. Valencia-Jaime, A. H. Romero, and F. U. Renner, *Electrochim. Acta*, **164**, 81 (2015).
26. G. Taillades, N. Benjelloun, J. Sarradin, and M. Ribes, *Solid State Ionics*, **152-153**, 119 (2002).
27. G. Kienast and J. Verma, *Zeitschrift für Anorg. und Allg. Chemie*, **310**, 143 (1961).
28. A. D. Pelton, *Bull. Alloy Phase Diagrams*, **7**, 228 (1986).
29. S. Misra, N. Liu, J. Nelson, S. S. Hong, Y. Cui, and M. F. Toney, *ACS Nano*, **6**, 5465 (2012).
30. P. Bach, I. Valencia-Jaime, U. Rütt, O. Gutowski, A. H. Romero, and F. U. Renner, *Chem. Mater.*, **28**, 2941 (2016).
31. B. D. Craig and D. S. Anderson, *Handbook of Corrosion Data*, p. 439, (1994).
32. J. C. Burns, R. Petibon, K. J. Nelson, N. N. Sinha, A. Kassam, B. M. Way, and J. R. Dahn, *J. Electrochem. Soc.*, **160**, A1668 (2013).
33. D. Pritzl, S. Solchenbach, and H. A. Gasteiger, Manuscript in preparation.
34. S. B. Lee and S. Il Pyun, *Carbon N. Y.*, **40**, 2333 (2002).
35. J. Illig, M. Ender, T. Chrobak, J. P. Schmidt, D. Klotz, and E. Ivers-Tiffée, *J. Electrochem. Soc.*, **159**, A952 (2012).
36. R. Mogi, M. Inaba, S.-K. Jeong, Y. Iriyama, A. Abouimrane, and Z. Ogumi, *J. Electrochem. Soc.*, **149**, A1578 (2002).
37. M. Gaberscek, J. Moskon, B. Erjavec, R. Dominko, and J. Jamnik, *Electrochem. Solid-State Lett.*, **11**, A170 (2008).
38. N. Dupré, J.-F. Martin, J. Degryse, V. Fernandez, P. Soudan, and D. Guyomard, *J. Power Sources*, **195**, 7415 (2010).
39. M. Cuisinier, N. Dupré, J.-F. Martin, R. Kanno, and D. Guyomard, *J. Power Sources*, **224**, 50 (2013).
40. A. Yamada, H. Koizumi, S.-I. Nishimura, N. Sonoyama, R. Kanno, M. Yonemura, T. Nakamura, and Y. Kobayashi, *Nat. Mater.*, **5**, 357 (2006).
41. L. Castro, R. Dedryvère, J.-B. Ledeuil, J. Bréger, C. Tessier, and D. Gonbeau, *J. Electrochem. Soc.*, **159**, A357 (2012).
42. M. Dubarry, C. Truchot, and B. Y. Liaw, *J. Power Sources*, **258**, 408 (2014).
43. M. Kassem, J. Bernard, R. Revel, S. Pélissier, F. Duclaud, and C. Delacourt, *J. Power Sources*, **208**, 296 (2012).
44. T. G. Zavalis, M. Klett, M. H. Kjell, M. Behm, R. W. Lindström, and G. Lindbergh, *Electrochim. Acta*, **110**, 335 (2013).
45. H. Zheng, L. Chai, X. Song, and V. S. Battaglia, *Electrochim. Acta*, **62**, 256 (2012).
46. D. Aurbach, K. Gamolsky, B. Markovsky, Y. Gofer, M. A. Schmidt, and U. Heider, *Electrochim. Acta*, **47**, 1423 (2002).
47. B. Zhang, M. Metzger, S. Solchenbach, M. Payne, S. Meini, H. A. Gasteiger, A. Garsuch, and B. L. Lucht, *J. Phys. Chem. C*, **119**, 11337 (2015).
48. A. Freiberg, M. Metzger, D. Haering, S. Bretzke, S. Puravankara, T. Nilges, C. Stinner, C. Marino, and H. A. Gasteiger, *J. Electrochem. Soc.*, **161**, A2255 (2014).
49. R. Petibon, E. C. Henry, J. C. Burns, N. N. Sinha, and J. R. Dahn, *J. Electrochem. Soc.*, **161**, A66 (2013).
50. A. J. Smith, J. C. Burns, X. Zhao, D. Xiong, and J. R. Dahn, *J. Electrochem. Soc.*, **158**, A447 (2011).
51. X. Xia, P. Ping, and J. R. Dahn, *J. Electrochem. Soc.*, **159**, A1834 (2012).
52. L. El Ouatani, R. Dedryvère, C. Siret, P. Biensan, and D. Gonbeau, *J. Electrochem. Soc.*, **156**, A468 (2009).
53. L. El Ouatani, R. Dedryvère, C. Siret, P. Biensan, S. Reynaud, P. Iratçabal, and D. Gonbeau, *J. Electrochem. Soc.*, **156**, A103 (2009).

3.1.2 Monitoring SEI formation on graphite anodes by impedance spectroscopy

The manuscript with the title "Monitoring SEI formation by impedance spectroscopy" is currently in preparation and will be submitted in Spring 2019. The main findings of this study were presented by Sophie Solchenbach at the AiMES Meeting in Cancun, Mexico, in October 2018 (Abstract Number 442).

With the development of the gold-wire micro reference electrode (GWRE) setup (see chapter 3.1.1), a separation of anode and cathode impedance contributions to the full cell impedance has become feasible. However, on graphite anodes the charge transfer and the SEI resistance are often convoluted, as both processes correspond to a similar electrochemical double-layer capacitance and thus appear in the same frequency range. Ogihara et al.[146] demonstrated that "blocking conditions", where lithium intercalation is thermodynamically hindered, can be used to quantify resistances which are otherwise superposed by the charge-transfer resistance (see chapter 2.1). This concept has recently been applied by our group to deconvolute the individual impedance contributions to the cathode and anode resistance of an LNMO/graphite full cell;[142,143] still, a separation of SEI and anode charge transfer resistance was not attempted there. The present study investigates the use of impedance spectroscopy in blocking conditions on graphite anodes in LFP/graphite cells to isolate the SEI resistance during formation in electrolytes with either no additive, 1 wt% VC, 1 wt% FEC or 1 wt% DiFEC. As equivalent circuit model, a one-rail transmission line model with two R/Q-elements representing the charge transfer and the SEI impedance is used, as this model showed the best results for graphite anodes in a study by Illig et al.[145] The comparison of impedance spectra in blocking and non-blocking conditions after formation shows that SEI and charge transfer resistance can be easily separated in blocking conditions, while they are indistinguishable in non-blocking conditions. To further validate this approach, the activation energy of the SEI resistance in blocking conditions was determined and compared to literature data. Lastly, a potential-stepping procedure, which alternates between reductive and blocking conditions, was developed and applied during SEI formation of graphite electrodes

in LFP/graphite cells. Using this procedure, the SEI resistance during formation was monitored, which makes this approach valuable for the investigation of SEI additives or to evaluate different formation protocols.

Author contributions

S. S. and X. H. prepared the electrodes and performed the electrochemical measurements. J. L. created the "EIS breaker" software used for data evaluation. S. S., D. P. and J. L. developed the models used for data fitting. S. S. and H. A. G. wrote the manuscript. All authors discussed the data and commented on the manuscript.

Monitoring SEI Formation on Graphite by Impedance Spectroscopy

Sophie Solchenbach,[#] Xinyi Huang, Daniel Pritzl, Johannes Landesfeind, and Hubert A. Gasteiger

Chair of Technical Electrochemistry, Department of Chemistry and Catalysis Research Center, Technische Universität München, Munich, Germany

[#]Corresponding author: sophie.solchenbach@tum.de

Abstract

In this work, we target to separate the SEI resistance of graphite electrodes from charge transfer resistance by impedance spectroscopy in blocking conditions, i.e., where the charge transfer resistance is significantly enlarged (~10^4 Ωcm^2_{geom}) and thus shifted to lower frequencies. For this, we measure impedance spectra of graphite/LFP cells with a gold-wire reference electrode (GWRE) in blocking (graphite potential 2 V vs. Li^+/Li, 0% SOC) and non-blocking conditions (graphite potential 0.12 V vs. Li^+/Li, 40% SOC) after formation. As electrolytes, we use LP57 (EC:EMC 3:7 + 1 M $LiPF_6$) with either no additive, 1 wt% VC, 1 wt% FEC, or 1 wt% DiFEC. By fitting the impedance data to a transmission line-based model, we show that SEI and charge transfer resistance are indistinguishable in non-blocking conditions, whereas the SEI resistance R_{SEI} is easily extracted from blocking condition impedance spectra. We validate our approach by determining the activation energies for the obtained ionic and SEI resistance. Finally, we introduce a potential-controlled cycling procedure which allows to asses of R_{SEI} during formation. Here, we show that SEI evolution follows the electrolyte reduction potentials, which makes this method a useful tool to study film formation on Li-ion battery anodes.

Introduction

Impedance spectroscopy is a powerful in-situ analytical technique to characterize electrochemical interfaces, which has made it a popular method to investigate film-forming additives in Li-ion batteries. To interpret impedance data is however not trivial, as electronic resistances, electrolyte resistance within the separator or the electrodes, surface film resistances, diffusion processes and the charge transfer resistances of both electrodes all contribute simultaneously to the impedance spectra of a Li-ion full cell.[1–3] Even less appropriate for impedance measurements are cells with a lithium metal counter electrode ("half cells"), as the impedance of the lithium metal is generally larger due to its much smaller surface area compared to a porous electrode and changes drastically while the lithium surface roughens during plating/stripping, superposing the impedance of the electrode of interest.[4–7] Symmetric cells consisting of two identical electrodes give reliable impedance data of only cathode or anode, but require the deconstruction of the original cell.[8,9] To separate the contribution of cathode and anode to the full cell impedance "in-situ", a micro-reference electrode can be placed centrally between the two electrodes,[10–12] as implemented in our previous studies.[6,13–17]

The evaluation of impedance spectra requires fitting the data to an electrical equivalent circuit model. In these models, interfacial processes are commonly represented by a series of parallel resistances and capacitances (*R/C*) or constant phase elements (*R/Q*),[18] describing multiple (depressed) semicircles in a Nyquist plot. Typically, each *R/C* or *R/Q* element is assigned to a physical process (contact resistance, charge transfer, film resistance) by its characteristic frequency f_{max}, which marks the semicircle maximum:

$$f_{\max} = 1/(2\pi RC) \quad (1)$$

Interestingly, the specific double-layer capacitance in battery electrolytes was found to be 1-5 µF per cm² active surface, regardless of the electrode material.[15,19] Thus, the contact resistance between electrode coating and current collector can easily be assigned in the impedance spectrum, as the small interfacial area and thus low capacitance makes it appear at very high frequencies (> 10 kHz), with little interference from other electrochemical processes.[14,17,20] In contrast, the solid electrolyte interphase (SEI) resistance (i.e., the removal of its solvation shell and the incorporation of a Li^+-ion into the SEI) and the charge transfer (i.e., the intercalation of a Li^+-ion from the SEI into the graphite layers) are both governed by the total surface area of the graphite active material. Consequently, the corresponding semicircles are often superimposed, and even if two *R/C*-type processes can be extracted from the impedance response, they cannot be assigned to SEI or charge transfer based on their characteristic frequency. Still, most of literature arbitrarily ascribes the SEI resistance on graphite to higher frequencies, while the charge transfer reaction is ascribed to lower frequencies.[7,8,18,21–24]

Equation 1 also shows that if the charge transfer is huge because lithium (de)intercalation is not possible, the maximum of the corresponding semicircle is shifted towards very low frequencies. These "blocking conditions" are reached by using a non-intercalating electrolyte[2] or by equilibrating the electrode at a potential where lithium (de)intercalation is thermodynamically inhibited.[1,14,15,25] In this way, a separation between charge transfer and SEI resistance in frequency space becomes possible, at least if the film resistance is largely independent of state of charge (SOC), as was shown previously[3,22,26] and thus is assumed in this work. For electrodes with commercially relevant loadings (> 2 mAh/cm²), the ionic resistance of the electrode pore structure also contributes significantly to the total electrode impedance.[1,3,14,25] Transmission-line based models take both ionic and interfacial resistances into account. Illig et al.[3] found that a transmission line model (TLM) with two interfacial R/Q-elements in series, representing SEI and charge transfer resistance, provided the best description of the graphite electrode impedance at various states of charge (SOC) and temperatures.

In this paper, we investigate the SEI resistance in LFP/graphite cells with electrolytes containing either no additives, 1 wt% vinylene carbonate (VC), 1 wt% fluoroethylene carbonate (FEC) or 1 wt% difluoroethylene carbonate (DiFEC). We isolate the SEI resistance by measuring impedance spectra with a gold wire micro-reference electrode (GWRE)[6] in blocking conditions, i.e., at graphite potentials of ~2 V vs. Li^+/Li, where lithium intercalation cannot take place. Using a transmission line model with two *R/Q* elements at the interface between active material and electrolyte as described by Illig et al.,[3] we compare the results with impedance data from the same cells in non-blocking conditions. To further validate our approach, we determine the activation energies for ionic and SEI resistances obtained from blocking condition impedance spectra. Lastly, we subject graphite/LFP cells to a potential stepping method which alternates between blocking and non-blocking potentials; by evaluating the impedance in blocking conditions after each step, we can follow the SEI resistance growth as a function of potential during formation.

Experimental

Electrode and electrolyte preparation – Graphite electrodes were prepared by mixing 95% graphite (T311, BET surface area 3 m²/g, SGL Carbon, Germany) and 5% polyvinylene difluoride (PVDF, Kynar HSV 900, Arkema, France) with N-methyl pyrrolidone (NMP, anhydrous, Sigma-Aldrich, United States) in a planetary mixer (2000 rpm, 10 min). The ink (50 wt% solid content) was coated onto copper foil (MTI, United States) using a 100 µm four edge blade and dried at 50 °C for 6 h in a convection oven, resulting in an average loading of 4.4 ± 0.3 mg/cm² (≡1.6 ± 0.1 mAh/cm², 70 µm thickness, 64% porosity). We purposely chose a low loading and high porosity to reduce the ionic resistance (which scales with the electrode thickness) and to emphasize the interfacial resistance contributions (which increase with decreasing electrochemically active surface area) on the overall electrode impedance, as demonstrated by Ogihara et al.[25] Lithium iron phosphate ($LiFePO_4$, LFP) electrode sheets were purchased from Custom cells (Itzehoe, Germany, 3.5 mAh/cm²). Both coatings were punched into 11 mm electrodes. Along with the separators (glass fiber, 11 mm diameter, VWR, Germany), they were dried under dynamic vacuum at 120 °C for 12 h and then transferred into an argon-filled glovebox (MBraun, Germany) without exposure to air. Electrolyte solutions were prepared by adding 1 wt% vinylene carbonate (VC, BASF SE, Germany), 1 wt% fluoroethylene carbonate (FEC, BASF SE, Germany) or 1 wt% 1,2-difluoroethylene carbonate (DiFEC, HSC Corporation, China) to a solution of 30 wt% ethylene carbonate (EC) and 70 wt% ethyl methyl carbonate (EMC) with 1M $LiPF_6$ (LP57, BASF SE, Germany).

Cell assembly and electrochemical testing – Swagelok® T-cells were assembled inside an Ar-filled glovebox (MBraun, Germany) with graphite anodes and LFP cathodes, 60 µL electrolyte, 2 glassfiber separators (VWR, Germany) and a gold-wire reference electrode (GWRE).[6] Prior to cell cycling, the GWRE was lithiated by applying a charging current of 150 nA for 2 h at 45 °C (activation energy experiments) or 25 °C (all other experiments) between the LFP electrode and the GWRE. For conventional galvanostatic formation, cells were cycled for 2 cycles at C/10 (based on a graphite capacity of 360 mAh/g) and 25 °C. As the lithiated GWRE has a stable potential (> 500 h) of 0.31 V vs. Li^+/Li in LFP/graphite cells,[6] the graphite potential was controlled between 1.7 V and -0.3 V vs. the GWRE (2.01-0.01 V vs. Li^+/Li). For the readers' convenience, graphite potentials vs. GWRE were calculated back to Li^+/Li scale throughout this work.

Alternatively, formation was done by a potential-stepping procedure: The graphite potential of the respective step was approached in a voltage scan at 0.5 mV/s and then held for 30 min; thereafter, the graphite potential was scanned back to 2.01 V vs. Li^+/Li at 0.5 mV/s, where the potential was held for another 30 min. With each step, the lower potential was first decreased by 0.2 V between 1.81-0.01 V vs. Li^+/Li and then raised by 0.2 V between 0.01-1.81 V vs. Li^+/Li. A detailed explanation of this procedure is given in Figure 6. Cyclic voltammetry was performed on graphite electrodes in Swagelok® T-cells with an LFP counter and a lithium metal reference electrode (Rockwood Lithium, 450 µm, USA) and a scan rate of 0.03 mV/s between OCV (~3 V vs. Li^+/Li) to 0.01 V and back to 2.0 V vs. Li^+/Li. All experiments (cycling and impedance) were performed in temperature-controlled chambers (Binder, Germany and ThermoTEC, Germany).

Electrochemical impedance spectroscopy – Impedance spectroscopy was performed between 100 kHz and 100 mHz with a potential perturbation of 10 mV using the GWRE as a reference electrode. To improve data quality, we recorded 20 points/decade in logarithmic spacing and averaged 5 cycles per frequency. Prior to formation, impedance spectra of the pristine graphite electrodes were recorded at open circuit voltage at 25 °C. To achieve blocking conditions after galvanostatic formation, the cells were held at 2.01 V vs. Li^+/Li (1.7 V vs. GWRE) for 30 min, followed by an impedance measurement directly afterwards. The graphite anodes were then charged to 40% SOC at C/10. After a rest period of 30 min, the graphite impedance in non-blocking conditions was recorded. For activation energy experiments, impedance spectra of the pristine graphite electrodes were recorded at open circuit voltage at 5, 15, 25 35 and 45 °C. To allow for thermal equilibration, the cells were held for 30 min at each temperature prior to the impedance measurement. After galvanostatic formation, the cells were held at 2.01 V vs. Li^+/Li and impedance was measured at 5, 15, 25 35 and 45 °C, again with 30 min at each temperature to allow for thermal equilibration. During potential stepping formation, an impedance measurement was performed at 2.01 V vs. Li^+/Li after each step.

Data evaluation and fitting – Micro-reference electrodes can be subject to high-frequency artefacts.[27] We tested this effect by a reversed setup as described by Raijmakers et al.[27] As the impedance magnitude of the regular and the reversed setup differ by more than 2% at frequencies above 31 kHz, only data in the frequency range between 31 kHz-100 mHz was considered for fitting of electrical equivalent circuits. Fitting was performed with a MATLAB-based application ("EIS Breaker", © J. Landesfeind) based on the *fminsearch* MATLAB function using a Nelder-Mead simplex algorithm and modulus weighing. Errors are given as standard deviation between multiple nominally identical cells / measurements.

Results and Discussion

Graphite impedance in non-blocking and in blocking conditions – As a first step, we investigate how different additives affect the graphite impedance after formation. Figure 1 shows the impedance spectra of graphite anodes from LFP/graphite full cells with a gold-wire reference electrode (GWRE) after two formation cycles (C/10, 25 °C) in LP57 (blue squares), LP57 + 1 wt% FEC (yellow triangles), LP57 + 1 wt% VC (red diamonds) and LP57 + 1 wt% DiFEC (green triangles). After the formation cycles, the graphite electrodes were lithiated to 40% SOC (based on first discharge capacity, ~0.12 V vs. Li^+/Li), and impedance spectroscopy was measured in non-blocking conditions. All impedance spectra show a ~45° line at high frequencies, followed by a depressed semicircle and a diffusion branch at low frequencies. As seen in Figure 1, the semicircle size depends strongly on the used additive. For LP57 and the electrolyte with 1 wt% FEC, the overall graphite impedance is rather low, whereas formation in LP57 + 1 wt% VC results in a higher anode impedance. The highest impedance is found for the DiFEC electrolyte. These findings agree with previous reports which showed that VC and DiFEC increase the anode impedance after formation,[6,9,13,28–32] whereas FEC has little effect.[33,34]

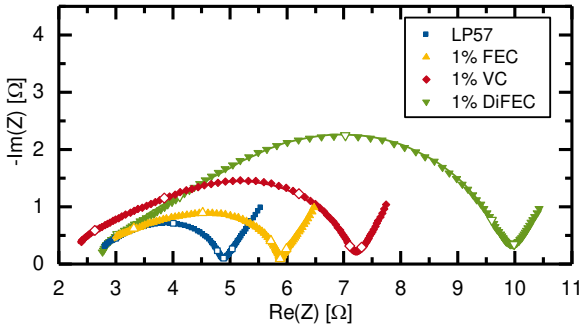

Figure 1: a) Impedance of graphite electrodes in non-blocking conditions (40% SOC, 0.12 V vs. Li^+/Li), measured vs. GWRE in a graphite/LFP cell at 25 °C after formation (2x C/10, 25 °C) in LP57 (1M $LiPF_6$ EC:EMC 3:7, blue squares), LP57 + 1 wt% FEC (yellow triangles), LP57 + 1 wt% VC (red diamonds) or 1 wt% DiFEC (green triangles). Each frequency decade (10 kHz, 1 kHz, 100 Hz, 10 Hz, 1 Hz) is marked by an open symbol.

Next, we want to examine the impedance spectra of the same cells after formation under blocking conditions, and how they differ from a pristine electrode. Figure 2a shows the impedance response of a pristine graphite electrode at OCV (~3 V vs. Li^+/Li, gray spheres) as well as the impedance spectra of graphite electrodes at 0% SOC (2.01 V vs. Li^+/Li) after two formation cycles in LP57 (blue squares), LP57 + 1 wt% FEC (yellow triangles), LP57 + 1 wt% VC (red diamonds) and LP57 + 1 wt% DiFEC (green triangles). All spectra approach a straight line at low frequencies, thus reaching quasi-blocking conditions. The inset in Figure 2b displays a zoom-in at the high and medium frequency region of Figure 2a. The pristine electrode (gray spheres) shows a 45° transmission line, corresponding to the ionic resistance in the electrode pores at high frequencies (> 100 Hz), and a close-to-vertical capacitive branch at frequencies below 100 Hz. In the impedance spectra of the graphite electrodes after formation, the region between the original 45° transmission line and the capacitive branch is extended, indicating that an additional resistance has formed here. Overall, the apparent size of this additional feature in the blocking condition impedance spectra follows the trend of the anode impedance of the different additives in non-blocking conditions, with FEC and LP57 showing the lowest and DiFEC showing the highest impedance growth.

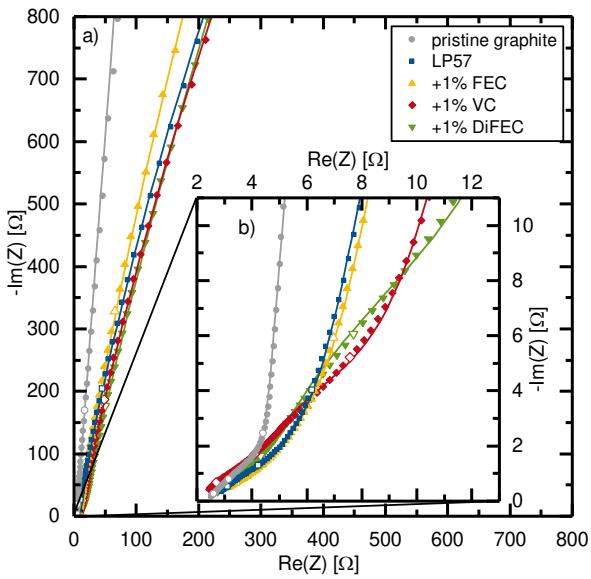

Figure 2: a) Impedance of a pristine graphite electrode (gray spheres) and graphite electrodes in blocking conditions (0% SOC, 2.01 V vs. Li^+/Li) measured vs. GWRE in a graphite/LFP cell at 25 °C after formation (2x C/10, 25 °C) in LP57 (1M $LiPF_6$ EC:EMC 3:7, blue squares), LP57 + 1 wt% FEC (yellow triangles), LP57 + 1 wt% VC (red diamonds) or 1 wt% DiFEC (green triangles). Each frequency decade (10 kHz, 1 kHz, 100 Hz, 10 Hz, 1 Hz) is marked by an open symbol. b) Zoom-in of the high frequency region of a).

To extract the SEI resistance from the impedance spectra in blocking conditions, we applied a one-rail transmission line model (TLM, see Figure 3) with different surface impedance elements to describe the active material/electrolyte interface. As a first step, we fitted the impedance spectrum of each pristine graphite electrode (see gray spheres in Figure 2 as an example) to a simplified TLM with only a constant phase element (q_{CT}) as interfacial element (see Model 1 in Figure 3), in order to extract the ionic resistance of the electrode.[1,2,15] The averaged results from all pristine electrodes used in this study are shown in Table 1. Considering 64% electrode porosity (uncompressed anodes) and a thickness of 70 µm, the ionic resistance of 5.8 Ωcm^2_{geom} corresponds to an electrode tortuosity τ of ~5, which is typical for laboratory-made, highly porous graphite electrodes.[2]

Table 1: Average parameters obtained from fitting the impedance spectra of pristine graphite electrodes (70 µm thickness, 64% porosity) to Model 1 (see Figure 3). Errors are based on standard deviations from multiple cells/measurements.

Parameter	Value
R_{Sep} [Ω cm^2_{geom}]	2.2 ± 0.3
R_{Ion} [Ω cm^2_{geom}]	5.8 ± 1.0
Q_{CT} [µF $s^{(\alpha-1)}/cm^2_{geom}$]	0.99 ± 0.02
α [-]	0.95 ± 0.01
τ [-]	4.9 ± 0.2

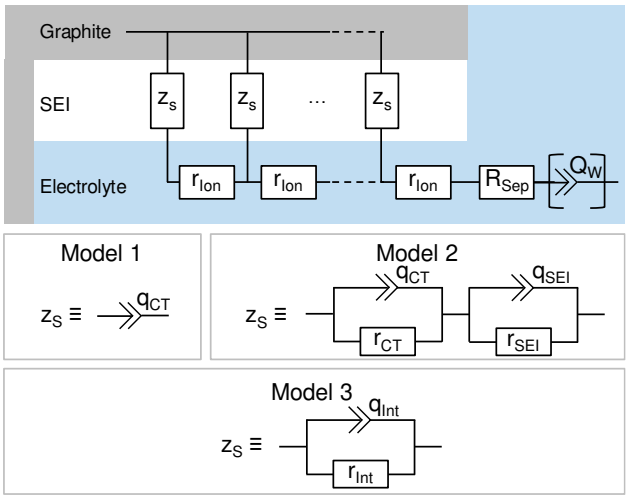

Figure 3: Equivalent circuit of the one-rail transmission line model used in this study. The electronic resistance rail was neglected due to the high electronic conductivity of graphite. For pristine graphite, a constant phase element was used as only interfacial element z_S (Model 1). After formation, graphite electrodes in blocking conditions were fitted with two *R/Q* elements as interfacial element z_S, representing charge transfer and SEI (Model 2). For non-blocking conditions, only one *R/Q* element was used as z_S, representing the convolution of SEI and charge transfer resistance (Model 3); in this case, an additional constant phase element Q_W was added to account for the diffusion branch at low frequencies.

Next, we fitted the impedance spectra in blocking conditions (Figure 2) after formation of graphite electrodes in different electrolytes to a one-rail TLM (see Figure 3). The ionic resistance was now fixed to R_{Ion} of the pristine electrode. Naturally, one would assume that the electrode porosity decreases during formation, which would result in an increased ionic resistance. However, the SEI is typically thinner than 20 nm,[35,36] and even if we consider a 20 nm thick, continuous SEI film on the graphite surface area (3 m^2_{BET}/g), this would lower the porosity and thus increase the ionic resistance of the graphite electrode by less than 10%. Thus, the increase in ionic resistance due to SEI products was neglected in this study. As interfacial element, we used two *R/Q* elements for the SEI and the charge transfer (huge resistance of the low frequency capacitive branch in Figure 2), respectively (Model 2 in Figure 3). To reduce the number of free parameters, we set the exponent α of both constant phase elements q_{SEI} and q_{CT} to be equal. The fitted spectra and the fit residuals are shown as lines in Figure 1 and symbols in Figure 4a, respectively. The largest deviations between data and model appear at very low (< 0.5 Hz) and very high (>10 kHz) frequencies, staying below 2% on average (see residuals in Figure 4a). Apparently, the additional impedance feature which appeared after formation is well represented by the SEI *R/Q*-element.

At first, we also attempted to fit the impedance spectra in non-blocking conditions from Figure 1 to Model 2; however, the use of two *R/Q* elements resulted in overfitting, i.e., we found several combinations for R_{SEI}, R_{CT}, Q_{SEI} and Q_{CT} which resulted in a similarly good fit. Therefore, only one interfacial *R/Q*-element was used for evaluating the non-blocking impedance spectra, representing SEI and charge transfer combined (see Model 3 in Figure 3). Additionally, the equivalent circuit was extended by a constant phase element Q_W, which represents the Li^+-ion diffusion in the bulk electrolyte; we used a constant phase element instead of the typically applied semi-infinite Warburg element,[14] as the diffusive branch at the low frequency end in Figure 1 was slightly steeper than 45°. Note that this diffusion element is not needed in the model used for blocking

conditions, because the lacking (de-)intercalation of Li^+-ions at low frequencies does not create concentration gradients in the electrolyte. The residuals of the impedance spectra in non-blocking conditions fitted to Model 3 are shown Figure 4b.

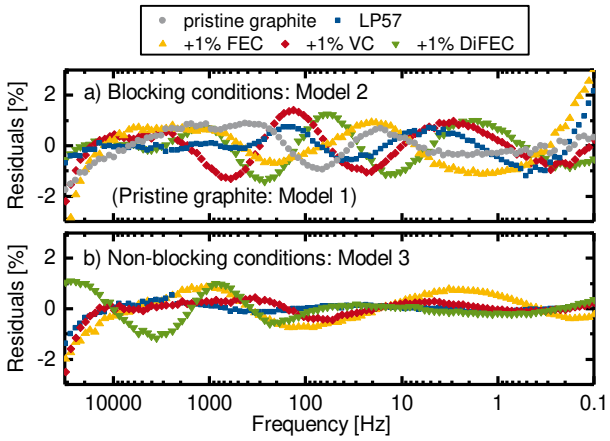

Figure 4: a) Residuals of the fit of Model 1 to the impedance response of a pristine graphite electrode and residuals of the fit of Model 2 to the impedance spectra of graphite electrodes in blocking conditions (see Figure 2) with R_{Ion} fixed after formation in LP57 (blue squares), LP57 + 1% FEC (yellow triangles), LP57 + 1% VC (red diamonds) and LP57 + 1% DiFEC (green triangles) in LFP/graphite cells with a GWRE. b) Residuals of the fit of Model 3 to the impedance spectra of graphite electrodes in non-blocking conditions (see Figure 1), with R_{Ion} fixed from pristine graphite electrodes.

Figure 5 compares R_{SEI} from fitting the blocking condition spectra and R_{Int} (SEI and charge transfer resistance combined) from the non-blocking conditions spectra fit. For each electrolyte, both resistances are very similar. This congruence between R_{Int} and R_{SEI} indicates that the charge transfer resistance in non-blocking conditions is probably very small ($\lesssim 0.5\ \Omega cm^2_{geom}$ based on error bars in Figure 5), similar as previously shown for the true charge transfer of an LNMO cathode, where it was 0.2-0.5 Ωcm^2_{geom}.[14] However, to directly extract the non-blocking charge transfer resistance is less straightforward for graphite, as i) an independence of the SEI resistance from SOC or potential is not necessarily given,[37] and ii) the edge and basal planes contribute differently in blocking and non-blocking conditions: in blocking conditions, the SEI resistance over both edge and basal planes is measured, while only the SEI at the edge planes, where lithium intercalation occurs, is measured during non-blocking conditions. Nevertheless, Figure 5 shows that the overall intercalation resistance of a graphite electrode will be governed by the SEI resistance, which should be considered in mitigation strategies for lithium plating.

The fitted parameters from Model 2 and Model 3 are given in Table 2. Both Q_{CT} and Q_{SEI} from the blocking conditions fit stay within each other's error range, demonstrating that an assignment of SEI and charge transfer based solely on the capacitance of the respective *R/Q* element is not feasible: in non-blocking conditions, the *R/Q*-elements representing SEI and charge transfer would be so close in frequency that a separation becomes impossible, which explains why Model 2 led to overfitting when applied to non-blocking conditions. Accordingly, the interfacial capacitance Q_{Int} of the single *R/Q* element that we finally used for fitting the non-blocking conditions lies just between Q_{CT} and Q_{SEI}.

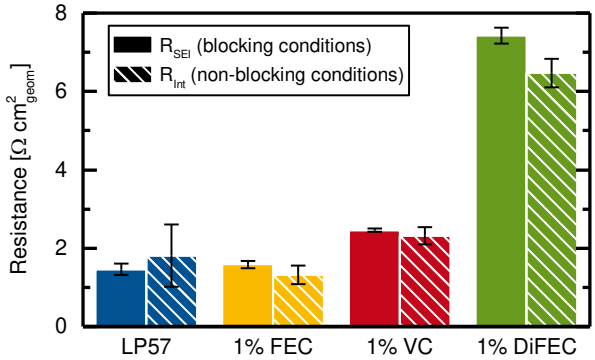

Figure 5: R_{SEI} (solid bars) and R_{Int} (dashed bars) obtained from fitting impedance spectra of graphite electrodes after formation in LP57 (blue bars), LP57 + 1wt% FEC (yellow bars), LP57 + 1 wt% VC (red bars) and LP57 + 1 wt% DiFEC (green bars) in blocking conditions (0% SOC, 2.01 V vs. Li^+/Li, see Figure 2) to Model 2 and in non-blocking conditions (40% SOC, 0.12 V vs. Li^+/Li, see Figure 1) to Model 3. In both cases, the ionic resistance R_{Ion} was fixed to the value obtained from the fit of Model 1 to the impedance spectrum of the pristine graphite electrode in each cell. Errors are based on standard deviations from multiple cells/measurements.

Table 2: Averaged parameters obtained from fitting impedance spectra of graphite electrodes after formation in LP57, LP57 + 1wt% FEC, LP57 + 1 wt% VC and LP57 + 1 wt% DiFEC in blocking conditions (0% SOC, 2 V vs. Li^+/Li, see Figure 2) to Model 2 (see Figure 3) as well as in non-blocking conditions (40% SOC, 0.12 V vs. Li^+/Li, see Figure 1) to Model 3. In both cases, the ionic resistance R_{Ion} was fixed to the value obtained from the fit of Model 1 to the impedance spectrum of the pristine graphite electrode in each cell. Errors are based on standard deviations from multiple cells/measurements.

Parameter	LP57	+ 1 wt% FEC	+ 1 wt% VC	+ 1 wt% DiFEC
Blocking conditions: Model 2 fitted to the data shown in Figure 2				
R_{Sep} [Ω cm²$_{geom}$]	2.3 ± 0.1	2.2 ± 0.3	2.2 ± 0.5	2.2 ± 0.1
R_{SEI} [Ω cm²$_{geom}$]	1.5 ± 0.2	1.6 ± 0.1	2.5 ± 0.1	7.4 ± 0.2
Q_{SEI} [μF/cm²$_{geom}$]	1.3 ± 0.2	1.1 ± 0.04	0.7 ± 0.1[4]	0.6 ± 0.04
R_{CT} [kΩ cm²$_{geom}$]	19 ± 7	16 ± 7	9 ± 2	47 ± 16
Q_{CT} [μF/cm²$_{geom}$]	0.8 ± 0.2	0.75 ± 0.04	0.97 ± 0.05	0.94 ± 0.03
$\alpha_{SEI,CT}$ [-]	0.88 ± 0.01	0.90 ± 0.01	0.86 ± 0.01	0.86 ± 0.01
Non-blocking conditions: Model 3 fitted to the data shown in Figure 1				
R_{Sep} [Ω cm²$_{geom}$]	2.1 ± 0.2	2.1 ± 0.2	2.2 ± 0.5	2.2 ± 0.1
R_{Int} [Ω cm²$_{geom}$]	1.8 ± 0.8	1.3 ± 0.2	2.3 ± 0.2	6.5 ± 0.4
Q_{Int} [μF/cm²$_{geom}$]	0.83 ± 0.06	0.81 ± 0.3	0.9 ± 0.1	0.82 ± 0.14
α_{Int} [-]	0.84 ± 0.01	0.85 ± 0.08	0.79 ± 0.02	0.82 ± 0.05
Q_W [F/cm²$_{geom}$]	1.1 ± 0.1	1.1 ± 0.1	0.9 ± 0.2	1.3 ± 0.1
α_W [-]	0.60 ± 0.02	0.64 ± 0.05	0.67 ± 0.02	0.68 ± 0.05

Activation energy of the SEI resistance – While electronic and ionic resistances only show a low temperature dependency, the effect of temperature on interfacial resistances is typically much larger.[1,3] Determining the activation energy is thus a powerful tool to classify the origin of a measured resistance.[15] Therefore, we investigated the temperature behaviour of the SEI resistance after formation in LP57, LP57 + 1 wt% FEC, LP57 + 1 wt% VC, or LP57 + 1 wt% DiFEC. At first, the impedance spectra of the pristine graphite electrodes

were recorded at 5, 15, 25, 35 and 45 °C. After formation (2 x C/10 at 25 °C), impedance was measured in blocking conditions (2 V vs. Li^+/Li) at the same temperatures. As before, the ionic resistance (R_{Ion}) of each cell and temperature was fitted from the pristine graphite spectra using Model 1 (see Figure 3); R_{Ion} at the respective temperature was then kept fixed during fitting the data to Model 2 after formation. Figure 6 shows R_{Ion} (gray spheres) and R_{Sep} (black open spheres) from the pristine LP57 cells along with R_{SEI} after formation in LP57 (blue squares), LP57 + 1 wt% FEC (yellow triangles), LP57 + 1 wt% VC (red diamonds) or LP57 + 1 wt% DiFEC (green triangles) in an Arrhenius-type diagram (here represented as the 10-based logarithm of the resistance vs. inverse temperature). All resistances show a linear Arrhenius behavior. The apparent activation energy E_A was calculated using equation (2), where R_G is the universal gas constant (8.314 J/mol K) and m is the linear regression slope of each data set in Figure 6.

$$E_A = m\, R_G \ln(10) \tag{2}$$

Table 3 summarizes the apparent activation energies of the different resistances. The activation energies for R_{Sep} and R_{Ion} lie around 23-27 kJ/mol; as both resistances depend on the ionic conductivity of the electrolyte, a similar activation energy is expected. For R_{SEI}, the activation energy is much larger (85-115 kJ/mol), increasing in the order of 1 wt% FEC < LP57 < 1 wt% VC ≈ 1 wt% DiFEC. Previous studies found activation energies in the range of 14-16 kJ/mol for the ionic and 60-75 kJ/mol for the interfacial resistances.[1,3,19] Borodin et al.[38] calculated an activation energy of 64-84 kJ/mol for the ionic conductivity of lithium ethylene dicarbonate, which is the main component of an EC-based SEI.[36] Although our activation energies for both the ionic and the SEI resistances differ by a factor of ~1.5 from literature values, we still see a ~5 times higher activation energy for R_{SEI} compared to R_{Ion} and R_{Sep}, just as reported by Ogihara et al.[1] and Illig et al.[3] These results confirm that the additional resistance evolving during formation (as seen in Figure 2) is not caused by a higher ionic resistance of the electrode, but a newly formed interfacial barrier. The lower activation energy of the SEI resistance with FEC compared to LP57 and other additives might in part explain its success as a low-temperature additive.[39]

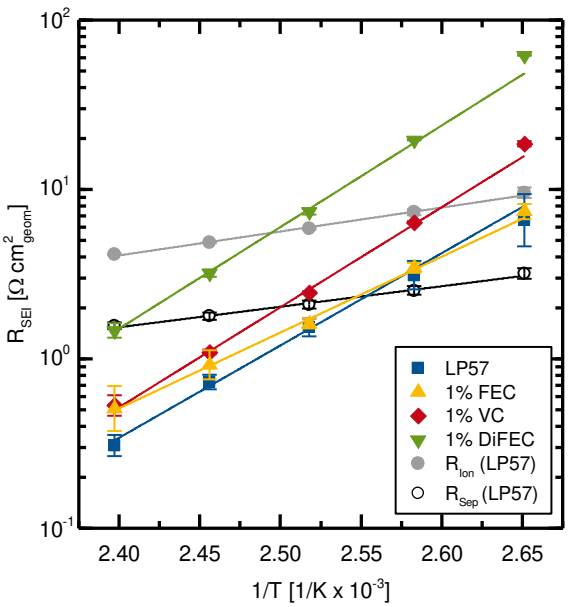

Figure 6: Arrhenius representation of R_{SEI} from fitting impedance spectra of graphite electrodes in blocking conditions at 5, 15, 25, 35 and 45 °C after formation (2 cycles at C/10 and 25 °C) in LP57 (blue squares), LP57 + 1wt% FEC (yellow triangles), LP57 + 1 wt% VC (red diamonds) and LP57 + 1 wt% DiFEC (green triangles) to the one-rail TLM (see Figure 3) to Model 2. For comparison, R_{Ion} (grey spheres) and R_{Sep} (black open spheres) from fitting the impedance spectra of pristine graphite electrodes in LP57 to Model 1 are also given. Errors are based on standard deviations from multiple cells/measurements.

Table 3: Activation energies for R_{Sep} and R_{Ion} of pristine graphite electrodes in LP57 and R_{SEI} after formation of graphite electrodes in LP57, LP57 + 1wt% FEC, LP57 + 1 wt% VC or LP57 + 1 wt% DiFEC, as determined from the linear regression slopes in Figure 6. Errors are based on standard deviations from multiple cells/measurements.

Electrolyte	Activation energy [kJ/mol]
R_{SEI} in LP57	104 ± 5.2
+ 1% FEC	85 ± 2.9
+ 1% VC	113 ± 4.0
+ 1% DiFEC	115 ± 3.0
R_{Sep} (LP57)	23 ± 1.2
R_{Ion} (LP57)	27 ± 1.1

Monitoring SEI formation – Depending on the electrolyte and additives used, the SEI forms on graphite between 1.5-0.5 V vs. Li^+/Li.[36,40] Unfortunately, the charge transfer resistance changes drastically within this potential range,[15] which makes it difficult to directly observe SEI formation by impedance spectroscopy. However, as the potential-dependence of the SEI resistance is assumed to be low,[3,22,26] we can use impedance measurements in blocking conditions to make SEI formation visible. Therefore, we developed a potential stepping formation procedure, which is shown in Figure 7. In this procedure, the pristine graphite is scanned from 2.01 V vs. Li^+/Li to a lower voltage (i.e., 1.81 V), which is held for 30 min. Thereafter, we move the graphite to blocking conditions by reversing the potential scan back to 2.01 V vs. Li^+/Li, where we take an impedance measurement after another constant voltage phase of 30 min. By moving to blocking conditions,

the electrolyte reduction reactions are interrupted and the SEI is "frozen" in the state of the previous lower potential. If we now decrease the lower vertex potential in each step from 1.81 to 0.01 V, we can follow the SEI evolution by evaluating the successive impedance spectra taken at 2.01 V vs. Li^+/Li.

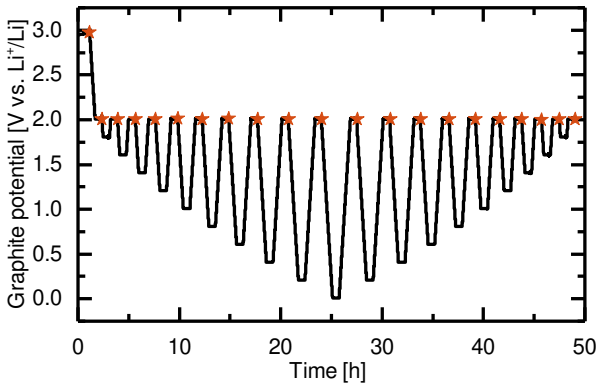

Figure 7: Graphite potential during potential stepping formation at 25 °C. The graphite potential was controlled vs. GWRE (0.31 V vs. Li^+/Li) and calculated back into Li^+/Li scale. Each step consisted of a voltage scan at 0.5 mV/s to the lower potential and a constant voltage phase of 30 min. Thereafter the potential was scanned back at 0.5 mV/s to 2.01 V vs. Li^+/Li (1.7 V vs. GWRE). After the potential was held at 2.01 V vs. Li^+/Li for 30 min, an impedance measurement was performed (orange stars). With each step, the lower potential was first decreased by 0.2 V between 1.81-0.01 V vs. Li^+/Li and then raised by 0.2 V between 0.01-1.81 V vs. Li^+/Li.

To determine the reduction potentials of the used electrolyte solutions, we also performed slow voltage scans (0.03 mV/s) to 0.01 V vs. Li^+/Li on pristine graphite electrodes in graphite/LFP cells with a lithium metal reference (Figure 8a). The reduction potentials (see dotted lines in Figure 8a) increase in the order LP57 (blue line) < LP57 + 1 wt% VC (red line) < LP57 + 1 wt% FEC (yellow line) < LP57 + 1 wt% DiFEC (green line), in agreement with previous reports.[32,40,41] Figure 8b-d shows R_{SEI} from fitting the blocking conditions spectra of the stepping formation procedure (see Figure 7) to Model 2 (see Figure 3). In LP57 (Figure 8b), R_{SEI} increases to ~1.5 Ωcm^2_{geom} between 0.8-0.4 V vs. Li^+/Li and remains constant thereafter, which fits to both the LP57 reduction peak at ~0.7 V vs. Li^+/Li in Figure 8a and the R_{SEI} after galvanostatic formation (1.5 Ωcm^2_{geom}, see Figure 5). The VC-containing electrolyte (Figure 8c) shows a slow rise of R_{SEI} between 1.4-0.8 V to 0.8 Ωcm^2_{geom} and a stronger growth between 0.8-0.4 V to ~2 Ωcm^2_{geom}. The reductive current (red line in Figure 8a) reflects this course, as between 1.7 and 0.9 V vs. Li^+/Li, the reduction current increases linearly, until it peaks at 0.8 V vs. Li^+/Li. During the positive-going steps (from right to left in Figure 8c), R_{SEI} grows slightly from 2 to 2.2 Ωcm^2_{geom}, suggesting that the evolution of the SEI, i.e., the polymerization of VC, continues. With FEC (Figure 8d), R_{SEI} increases rapidly to 1.4 Ωcm^2_{geom} between 1.4-1.0 V vs. Li^+/Li and remains constant thereafter; accordingly, the reduction current for LP57 + 1 wt% FEC recedes after a peak at 1.2 V (see yellow line in Figure 8a). The SEI resistance in the DiFEC electrolyte (Figure 8e) appears already at 1.6 V and rises to 1 Ωcm^2_{geom} until 1 V, concurrent with a large reduction peak between 1.9-1.2 V (green line in Figure 8a). Apparently, this initial SEI is not sufficiently passivating, as we see a significant reduction current between 1.0-0.6 V along with a continuous rise of R_{SEI} to 2.8 Ωcm^2_{geom} between 1.0-0.2 V vs. Li^+/Li. The SEI impedance grows further to 3.5 Ωcm^2_{geom} during the positive-going steps, which is however still lower than the R_{SEI} of 7.4 Ωcm^2_{geom} after galvanostatic formation (see Figure 5).

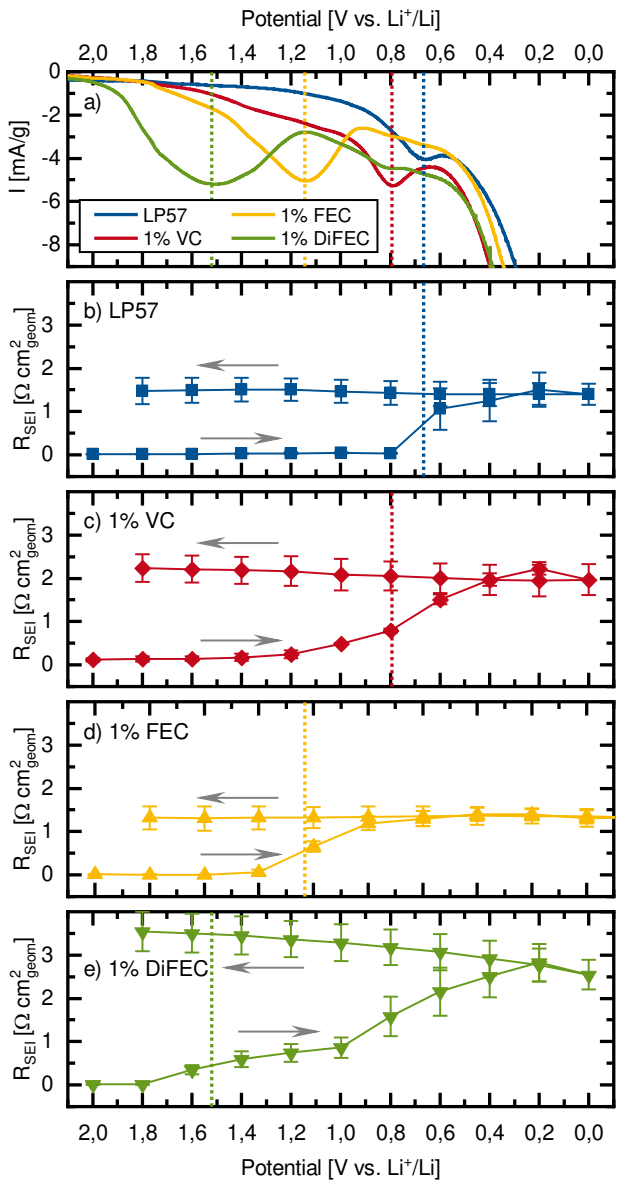

Figure 8: a) Current density vs. potential during the reductive CV (0.03 mV/s) of a graphite electrode in a graphite/LFP T-cell with lithium metal reference and LP57 (blue line), LP57 + 1 wt% VC (red line), LP57 + 1 wt% FEC (yellow line) or LP57 + 1 wt% DiFEC (green line) electrolyte. b-e) R_{SEI} after each potential step (see procedure in Figure 7) in graphite/LFP cells with GWRE, obtained from fitting impedance spectra in blocking conditions to Model 2 (see Figure 3). Dotted lines mark the maximum of the respective reduction peak in a). The grey arrows indicate the R_{SEI} evolution over time. Errors are based on standard deviations from multiple cells/measurements.

To investigate whether SEI formation is completed after the stepping procedure formation shown in Figure 7, we subjected the cells to a second potential stepping cycle and recorded the graphite impedance in blocking conditions thereafter. The fitted values of R_{SEI} after the first and the second stepping cycle are shown in Figure 9. Interestingly, the SEI resistance for both electrolytes with either 1 wt% VC or 1 wt% FEC stays constant, whereas R_{SEI} grows to 1.8 Ωcm^2_{geom} for LP57 and 3.8 Ωcm^2_{geom} for the electrolyte with DiFEC.

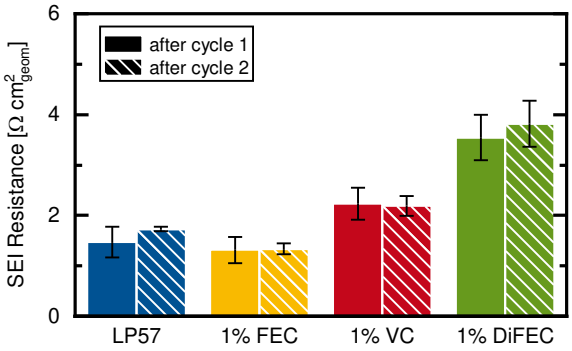

Figure 9: SEI resistance (R_{SEI}) after the first cycle (solid bars) and the second cycle (dashed bars) of potential-stepping formation (see Figure 7), obtained from fitting impedance spectra of graphite electrodes cycled in LP57 (blue bars), LP57 + 1 wt% FEC (yellow bars), LP57 + 1 wt% VC (red bars) and LP57 + 1 wt% DiFEC (green bars) in blocking conditions (0% SOC, 2.01 V vs. Li^+/Li) to Model 2. Errors are based on standard deviations from multiple cells/measurements.

Summarizing the findings from Figure 8 and Figure 9, the evolution of SEI resistances combined with the electrolyte reduction potentials give valuable insights about the SEI formation dynamics in the different electrolytes. As expected, the SEI formation in LP57 occurs simultaneously with the reduction of EC, yet the slight increase in resistance during the second cycle points towards a further growth or aging process. The FEC-containing electrolyte forms an SEI at higher potentials compared to LP57; this SEI has a low resistance, which remains constant over time. This self-limiting behaviour of FEC is likely a reason why FEC can be used in high concentrations as an electrolyte co-solvent,[42] which is not the case for other additives. While the SEI formed by VC is also stable over time, it has a higher resistance and is assumed to grow by a radical polymerization reaction;[40,43,44] accordingly, the amount of VC has to be carefully adjusted to not create a highly resistive SEI.[6,13,29] The SEI formed in the electrolyte with DiFEC starts to evolve at the most positive potential of all tested additives, but grows continuously, resulting in a highly resistive SEI after only few cycles. Additionally, the SEI resistance grows even throughout the second cycle, which indicates that the passivating properties of DiFEC on graphite are inferior to VC or FEC.

Conclusions

In this work, we analyse the SEI resistance of graphite electrodes from impedance spectra in blocking conditions, i.e., at potentials where the charge transfer resistance is significantly enlarged (~10^4 Ωcm^2_{geom}) and thus shifted to very low frequencies. We demonstrated that in non-blocking conditions, SEI and charge transfer resistance are indistinguishable, whereas the SEI resistance can be isolated from impedance spectra in blocking conditions by fitting to a transmission line model with a predetermined ionic resistance. With this method, we investigated the SEI resistance of graphite electrodes in an additive-free electrolyte (LP57) as well as in electrolytes containing 1 wt% VC, 1 wt% FEC or 1 wt% DiFEC. By determining the activation energies of the ionic and the SEI resistances, we could exclude the effect of a changed electrode porosity and thus confirm

our approach. Finally, we used a formation procedure based on potential steps, which allowed us to measure R_{SEI} at different stages during formation. Here, we showed that the SEI resistance appears at the respective electrolyte reduction potentials. Additionally, we found that SEI formation with LP57, VC- or FEC-containing electrolytes is largely completed after the electrolyte reduction peak in the first cycle, whereas the SEI in the electrolyte with DiFEC continues to grow both after electrolyte reduction during the first cycle as well as throughout further cycling. Hence, this novel method is a potentially powerful tool to study film formation kinetics on Li-ion battery electrodes.

Acknowledgment

Financial support by the BASF SE through its Research Network on Electrochemistry and Batteries is gratefully acknowledged. J. L. gratefully acknowledges the funding by the BMBF (Federal ministry of Education and research, Germany) for its financial support under the auspices of the ExZellTUM II project, grant number 03XP0081.

References

1. N. Ogihara, S. Kawauchi, C. Okuda, Y. Itou, Y. Takeuchi, and Y. Ukyo, *J. Electrochem. Soc.*, **159**, A1034–A1039 (2012).
2. J. Landesfeind, J. Hattendorff, A. Ehrl, W. A. Wall, and H. A. Gasteiger, *J. Electrochem. Soc.*, **163**, A1373–A1387 (2016).
3. J. Illig, M. Ender, A. Weber, and E. Ivers-Tiffée, *J. Power Sources*, **282**, 335–347 (2015).
4. J. Y. Song, H. H. Lee, Y. Y. Wang, and C. C. Wan, *J. Power Sources*, **111**, 255–267 (2002).
5. R. Hernandez-Maya, O. Rosas, J. Saunders, and H. Castaneda, *J. Electrochem. Soc.*, **162**, A687–A696 (2015).
6. S. Solchenbach, D. Pritzl, E. J. Y. Kong, J. Landesfeind, and H. A. Gasteiger, *J. Electrochem. Soc.*, **163**, 2265–2272 (2016).
7. M. Steinhauer, S. Risse, N. Wagner, and K. A. Friedrich, *Electrochim. Acta*, **228**, 652–658 (2017).
8. C. H. Chen, J. Liu, and K. Amine, *J. Power Sources*, **96**, 321–328 (2001).
9. R. Petibon, C. P. Aiken, N. N. Sinha, J. C. Burns, H. Ye, C. M. VanElzen, G. Jain, S. Trussler, and J. R. Dahn, *J. Electrochem. Soc.*, **160**, A117–A124 (2013).
10. J. Zhou and P. H. L. Notten, *J. Electrochem. Soc.*, **151**, A2173 (2004).
11. D. P. Abraham, S. D. Poppen, A. N. Jansen, J. Liu, and D. W. Dees, *Electrochim. Acta*, **49**, 4763–4775 (2004).
12. M. Ender, J. Illig, and E. Ivers-Tiffée, *J. Electrochem. Soc.*, **164**, 71–79 (2017).
13. D. Pritzl, S. Solchenbach, M. Wetjen, and H. A. Gasteiger, *J. Electrochem. Soc.*, **164**, A2625–A2635 (2017).
14. J. Landesfeind, D. Pritzl, and H. A. Gasteiger, *J. Electrochem. Soc.*, **164**, A1773–A1783 (2017).

15. D. Pritzl, J. Landesfeind, S. Solchenbach, and H. A. Gasteiger, *J. Electrochem. Soc.*, **165**, A2145-2153 (2018).

16. M. Wetjen, S. Solchenbach, H. A. Gasteiger, D. Pritzl, J. Hou, and V. Tileli, *J. Electrochem. Soc.*, **165**, 1503–1514 (2018).

17. D. Pritzl, A. E. Bumberger, M. Wetjen, J. Landesfeind, S. Solchenbach, and H. A. Gasteiger, *J. Electrochem. Soc.*, **166**, A582–A590 (2019).

18. M. D. Levi and D. Aurbach, *J. Phys. Chem. B*, **5647**, 4630–4640 (1997).

19. H. Schranzhofer, J. Bugajski, H. J. Santner, C. Korepp, J. O. Besenhard, M. Winter, and W. Sitte, **153**, 391–395 (2006).

20. M. Gaberscek, J. Moskon, B. Erjavec, R. Dominko, and J. Jamnik, *Electrochem. Solid-State Lett.*, **11**, A170 (2008).

21. D. Aurbach, M. D. Levi, E. Levi, H. Teller, B. Markovsky, and G. Salitra, *J. Electrochem. Soc.*, **145**, 3024–3034 (1998).

22. M. Umeda, K. Dokko, Y. Fujita, M. Mohamedi, I. Uchida, and J. R. Selman, **47**, 885–890 (2001).

23. B. K. Antonopoulos, F. Maglia, F. Schmidt-stein, and J. P. Schmidt, 1–13 (2018).

24. O. S. Mendoza-hernandez, H. Ishikawa, Y. Nishikawa, Y. Maruyama, Y. Sone, and M. Umeda, *Electrochim. Acta*, **131**, 168–173 (2014).

25. N. Ogihara, Y. Itou, T. Sasaki, and Y. Takeuchi, *J. Phys. Chem. C*, **119**, 4612–4619 (2015).

26. T. S. Ong and H. Yang, *J. Electrochem. Soc.*, **149**, A1 (2002).

27. L. H. J. Raijmakers, M. J. G. Lammers, and P. H. L. Notten, *Electrochim. Acta*, **259**, 517–533 (2018).

28. R. Petibon, E. C. Henry, J. C. Burns, N. N. Sinha, and J. R. Dahn, *J. Electrochem. Soc.*, **161**, A66–A74 (2013).

29. J. C. Burns, R. Petibon, K. J. Nelson, N. N. Sinha, A. Kassam, B. M. Way, and J. R. Dahn, *J. Electrochem. Soc.*, **160**, A1668–A1674 (2013).

30. L. Ma, S. L. Glazier, R. Petibon, J. Xia, J. M. Peters, Q. Liu, J. P. Allen, R. N. C. Doig, and J. R. Dahn, *J. Electrochem. Soc.*, **164**, 5008–5018 (2017).

31. J. Xia, R. Petibon, A. Xiao, W. M. Lamanna, and J. R. Dahn, *J. Electrochem. Soc.*, **163**, A1637 (2016).

32. M. Wetjen, D. Pritzl, G. Hong, S. Solchenbach, and H. A. Gasteiger, *ECS Meet. Abstr.*, **01**, 213 (2017).

33. I. A. Profatilova, S.-S. Kim, and N.-S. Choi, *Electrochim. Acta*, **54**, 4445–4450 (2009).

34. M. Klett, J. A. Gibson, S. E. Trask, B. J. Polzin, A. N. Jansen, D. W. Dees, and D. P. Abraham, *J. Electrochem. Soc.*, **163**, A875–A887 (2016).

35. F. Jeschull, J. Maibach, K. Edström, and D. Brandell, *J. Electrochem. Soc.*, **164**, 1765–1772 (2017).

36. M. Nie, D. Chalasani, D. P. Abraham, Y. Chen, A. Bose, and B. L. Lucht, *J. Phys. Chem. C*, **117**, 1257–1267 (2013).

37. I. A. J. Gordon, S. Grugeon, H. Takenouti, B. Tribollet, M. Armand, C. Davoisne, A. Débart, and S. Laruelle, *Electrochim. Acta*, **223**, 63–73 (2017).

38. O. Borodin, G. V Zhuang, P. N. Ross, and K. Xu, *J. Phys. Chem. C*, **117**, 7433–7444 (2013).

39. B. Liu, B. Li, and S. Guan, *Electrochem. Solid-State Lett.*, **15**, A77 (2012).

40. B. Zhang, M. Metzger, S. Solchenbach, M. Payne, S. Meini, H. A. Gasteiger, A. Garsuch, and B. L. Lucht, *J. Phys. Chem. C*, 150512180451000 (2015).

41. B. Strehle, S. Solchenbach, M. Metzger, K. U. Schwenke, and H. A. Gasteiger, *J. Electrochem. Soc.*, **164**, A2513–A2526 (2017).

42. T. Teufl, B. Strehle, M. Philipp, H. A. Gasteiger, and M. A. Mendez, *J. Electrochem. Soc.*, **165**, 2718–2731 (2018).

43. M. Nie, J. Demeaux, B. T. Young, D. R. Heskett, Y. Chen, A. Bose, J. C. Woicik, and B. L. Lucht, *J. Electrochem. Soc.*, **162**, A7008–A7014 (2015).

44. L. El Ouatani, R. Dedryvère, C. Siret, P. Biensan, and D. Gonbeau, *J. Electrochem. Soc.*, **156**, A468 (2009).

3.1.3 Analysis of vinylene carbonate (VC) as additive in graphite/LNMO cells

The paper entitled "Analysis of Vinylene Carbonate (VC) as additive in Graphite/$LiNi_{0.5}Mn_{1.5}O_4$ Cells" was submitted in June 2017 to the *Journal of the Electrochemical Society* and published online in August 2017. The results of this study were presented by Daniel Pritzl at the PRiME Meeting in Honolulu, Hawaii in October 2016 (Abstract Number 567). The article was published "open access" under the Creative Commons Attribution Non-Commercial No Derivatives 4.0 License (CC BY-NC-ND). A permanent link to this article can be found under: http://jes.ecsdl.org/content/164/12/A2625.

In previous reports, the use of vinylene carbonate (VC) in LNMO-based cells resulted in a rapid capacity drop and poor cycle life due to the oxidation of VC at the LNMO cathode.[40,41,175] However, the loss of active lithium is a predominant fading mechanism in LNMO/graphite cells; hence, SEI-forming additives like VC could be an effective way to improve the SEI stability and thus the capacity retention in these cells. Considering the results from chapter 3.1.1, where we found that the additive to active material ratio governs the anode impedance, and thus additives are often "overdosed" in studies using lab-scale cells with high electrolyte to active material ratios, we re-visited the effect of VC in LNMO/graphite cells.

The study presented here applies impedance spectroscopy of LNMO/graphite cells with a GWRE to investigate the effect of different VC concentrations on the anode and cathode impedance. Thereby, the VC concentrations (0.09-0.52 wt%) were chosen to correspond to amounts that would be realistic in commercial-scale cells (1-6 wt%) based on the different electrolyte to active material mass ratios. Using OEMS, the oxidation of vinylene carbonate was found to occur at potentials > 4.3 V vs. Li^+/Li, i.e., well below the operating potential of the LNMO cathode (~4.7 V vs. Li^+/Li). The oxidation of VC correlated with an impedance increase on the cathode and a decline in the capacity retention in LNMO/graphite cells. As the anode impedance at the same VC/graphite ratio was significantly lower in the LNMO/graphite cells of the present study compared to the LFP/graphite cells from

the study in chapter 3.1.1, it became apparent that the VC oxidation competes with the reduction of VC. However, at the lowest tested concentration (0.09 wt%, corresponding to ~1% in commercial-scale cells), all VC could be consumed at the graphite anode before the LNMO potential exceeded 4.3 V vs. Li^+/Li. Accordingly, this concentration showed no increase of the cathode impedance and an improved cycling performance.

Author contributions

D. P. performed the electrochemical testing and impedance measurements. S. S. conducted and evaluated the OEMS measurements. D. P. and M. W. calculated the monolayer coverage for different VC concentrations. D. P., S. S. and H. A. G. developed the VC oxidation mechanism. D. P. and H. A. G. wrote the manuscript. All authors discussed the data and commented on the manuscript.

Analysis of Vinylene Carbonate (VC) as Additive in Graphite/$LiNi_{0.5}Mn_{1.5}O_4$ Cells

Daniel Pritzl,[*,z] Sophie Solchenbach,[*] Morten Wetjen, and Hubert A. Gasteiger[**]

Chair for Technical Electrochemistry, Department of Chemistry and Catalysis Research Center, Technical University of Munich, Munich, Germany

Vinylene Carbonate (VC) is an effective electrolyte additive to produce a stable solid electrolyte interphase (SEI) on graphite anodes, increasing the capacity retention of lithium-ion cells. However, in combination with $LiNi_{0.5}Mn_{1.5}O_4$ (LNMO) cathodes, VC drastically decreases cell performance. In this study we use on-line electrochemical mass spectrometry (OEMS) and electrochemical impedance spectroscopy (EIS) with a micro-reference electrode to understand the oxidative (in-)stability of VC and its effect on the interfacial resistances of both anode and cathode. We herein compare different VC concentrations corresponding to VC to graphite surface area ratios typically used in commercial-scale cells. At low VC concentrations (0.09 wt%, corresponding to 1 wt% in commercial-scale cells), an impedance increase exclusively on the anode and an improved capacity retention is observed, whereas higher VC concentrations (0.17 wt – 2 wt%, corresponding to 2 wt - 23 wt% in commercial-scale cells) show an increase in both cathode and anode impedance as well as worse cycling performance and overcharge capacity during the first cycle. By considering the onset potentials for VC reduction and oxidation in graphite/LNMO cells, we demonstrate that low amounts of VC can be reduced before VC oxidation occurs, which is sufficient to effectively passivate the graphite anode.

Manuscript submitted June 26, 2017; revised manuscript received August 16, 2017. Published August 31, 2017. This was Paper 567 presented at the Honolulu, Hawaii, Meeting of the Society, October 2–7, 2016.

During the first charge of a lithium ion battery (LiB), the so called solid electrolyte interphase (SEI)[1] is formed on the surface of the negative electrode. The standard electrolyte for LiBs consists of a mixture of cyclic and linear carbonates, e.g., ethylene carbonate (EC) and ethyl methyl carbonate (EMC), typically with lithium hexafluorophosphate ($LiPF_6$) as salt. Starting from a potential of ~0.8 V vs. Li/Li^+, EC is reduced electrochemically into ethylene gas and lithium ethylene dicarbonate (LEDC), which is a key component of the SEI.[2,3] Vinylene carbonate (VC) is one of the most effective additives to modify the SEI on graphite anodes, as it is reduced at potentials more positive than 1.0 V vs. Li/Li^+ and hence suppresses the reduction of EC.[4,5] Aurbach et al. have used VC as electrolyte additive in an EC/DMC (dimethyl carbonate) based electrolyte and that time reported a reduction of the irreversible capacity in the first cycles and an improved cycling stability at elevated temperatures for graphite anodes. The SEI resulting from the reduction of VC consists mainly of poly (vinylene carbonate) (poly(VC)).[4,6]

Important studies on the impact of different VC concentrations in graphite/NMC pouch cells have been carried out by the Dahn group. For example, Burns et al.[7] investigated the effect of different concentrations of VC (0, 1 and 2 wt%) on cycle life and impedance growth of full-cells with graphite anodes and either LCO ($LiCoO_2$) or NMC ($Li(Ni_{0.42}Mn_{0.42}Co_{0.16})O_2$) cathodes, employing galvanostatic cycling experiments coupled with high precision coulombic efficiency and electrochemical impedance spectroscopy (EIS) measurements. For cells with VC additive, they observed higher coulombic efficiencies and reduced capacity fading, whereby a notable increase in cell impedance was observed for cells with 2 wt% VC, which they attributed to a thicker SEI-film at the surface of the anode. However, since it is known that LCO cathodes can also form a resistive surface film in the presence of VC additive (presumably consisting of poly(VC)[8,9]), an assignment of the overall cell impedance growth to the individual contributions from anode and cathode requires more advanced techniques, like the symmetric cell approach.[10] Thus, later on, Burns et al.[10] investigated the effect of VC (0 - 6 wt%) over extended charge/discharge cycling of graphite/NMC 18650 cells on anode and cathode impedance growth via symmetric cell measurements. They showed that indeed the impedance of the negative electrode increases nearly linearly with VC concentration, whereas the impedance of the positive electrode first decreases as the VC concentration is increased to 2 wt% and then only increases gradually at higher VC concentrations. The strong anode impedance growth suggests that VC is mostly consumed at the graphite anode, leading to SEI growth. This is consistent with a study by Petibon et al.,[11] who analyzed the consumption of vinylene carbonate in graphite/NMC pouch cells and showed that the additive is mainly consumed at the anode side (both during high temperature formation (50°C) and during a potential hold at 4.2 V cell voltage). In addition, they found that nearly 2 wt% VC were consumed during formation, so that little residual VC remained after formation for VC concentrations of ≤2 wt%. In a subsequent study, Petibon et al.[12] also showed that residual VC after formation leads to a fast decay in the open-circuit voltage during storage in cells charged to 4.4 V cell voltage, caused by the poor oxidative stability of VC.

In a recent study from our group,[13] we compared the effect of different VC concentrations on the impedance of graphite anodes in graphite/LFP ($LiFePO_4$) full-cells, using a Swagelok T-cell configuration with a reference electrode which enables the deconvolution of the overall cell impedance into the individual contributions from anode and cathode. There, we showed that the VC to active material ratio (expressed as the ratio of VC mass to graphite surface area in the cell), rather than the concentration of the additive in the electrolyte, is a key parameter when comparing results using different types of battery cell hardware. Basically, the cell hardware can roughly be categorized either into lab-scale-cells with a small total capacity (<10 mAh, i.e., <5 cm^2 electrode area), which due to design constraints require a high electrolyte/active material mass ratio in order to function properly (e.g., coin or Swagelok T-cells), or into commercial-scale cells with a high total capacity (>100 mAh, i.e., >20 cm^2 electrode area), which are assembled with much lower electrolyte/active material mass ratios (e.g., multi-layer pouch or 18650 cells with low electrolyte/active material mass ratio). Consequently, the electrolyte/active material mass ratio in the latter is ~12-fold lower compared to commonly used lab-scale cells, so that a concentration of 2 wt% VC in the study from Burns et al.[10] based on 18650 cells would corresponds to ~0.17 wt% VC in a typical lab-scale cell. This scaling factor between commonly used lab-scale cells and commercial-scale cells needs to be considered when using lab-scale cells to evaluate the effect of additives.

*Electrochemical Society Member.
**Electrochemical Society Fellow.
zE-mail: daniel.pritzl@tum.de

While the above discussed studies show that the cathode impedance growth with VC additive is generally small for graphite/LCO and graphite/NMC cells operating at cell voltages up to 4.4 V, this is not the case when higher voltage cathode active materials such as high-voltage spinel $LiNi_{0.5}Mn_{1.5}O_4$ (LNMO) are used. Li et al.[14] have shown that the cell performance of graphite/LNMO cells drastically decreases when 1 or 2 wt% of VC are added to the electrolyte, consistent with studies by Lee et al.[15] and Song et al.,[16] which demonstrated that the oxidative stability of VC is insufficient for operation with an LNMO cathode. The oxidative instability of VC was examined in more detail in a recent study from the group of Brett Lucht:[17] By means of ex-situ surface analysis (XPS and FT-IR) they showed that the oxidation of VC starts at already ~4.5 V vs. Li/Li^+, leading to the formation of poly(VC) at the surface of the LNMO cathode. Even though these studies demonstrate that VC is not a suitable additive for cells with LNMO cathodes, they were all based on lab-scale cell setups with a high electrolyte/active material ratio, so that the ratio of VC mass over graphite surface area for the used VC concentrations of 1–2 wt% was roughly an order of magnitude higher than what would be present in commercial-scale cells.

The additive VC behaves very differently in high-voltage cells compared to fluorinated additives. Fluoroethylene Carbonate (FEC) is often used in this type of cells, leading to an overall increased battery performance. On the one hand both additives (VC and FEC) generate CO_2 during reduction,[5,18] thus improving the anode SEI. On the other hand, FEC is more stable towards oxidation[19] (compared to VC) and can thus be used in large concentrations/quantities even at high voltages (e.g., with LNMO or HE-NCM cathodes).

In the present study, we therefore want to investigate much lower VC concentrations in the electrolyte in lab-scale cell tests (0.09–0.52 wt% VC), which would correspond to VC concentrations of 1–6 wt% in commercial-scale cells for the same ratio of VC mass to graphite surface area. The first part of our investigation aims to understand the drastic decrease in cell performance when large amounts of VC are added to graphite/LNMO cells (i.e., at very high ratios of VC mass to graphite surface area). To this end, we will examine the anodic stability of VC via on-line electrochemical mass spectrometry (OEMS) using carbon black model electrodes and a VC-only electrolyte with 1 M $LiPF_6$. As a next step, we conduct impedance measurements in graphite/LNMO cells using a micro-reference electrode,[13] quantifying anode and cathode impedance after formation in electrolytes with different amounts of VC (0.09, 0.17, 0.52, and 2 wt%). In the second part, we examine the impact of different VC concentrations on the cycling behavior of graphite/LNMO cells and on anode/cathode impedance during cycling at 40°C. We also show that the additional capacity during the first charge correlates with the impedance of the LNMO cathode. Finally, by comparing the impedance growth of the graphite anode in cells with either an LNMO or an LFP cathode, we can clearly show that VC is consumed at the LNMO cathode, resulting in a lower impedance of the of the graphite anode in a graphite/LNMO vs. a graphite/LFP cell.

Experimental

Electrode preparation.—$LiNi_{0.5}Mn_{1.5}O_4$ (LNMO) electrodes were prepared by mixing LNMO (BASF SE, Germany), carbon black (Super C65, Timcal), and polyvinylene difluoride (PVDF, Kynar) at a mass ratio of 92/5/3 with NMP (N-methyl pyrrolidone, anhydrous, Sigma-Aldrich, Germany) in a planetary mixer (Thinky Corp.) for 15 min. The ink was coated onto aluminum foil (MTI, 18 μm) with a doctor blade coater and dried afterwards at 50°C in a convection oven for at least 3 h. The final LNMO coating had a loading of ~13.6 mg_{LNMO}/cm^2, corresponding to ~1.9 mAh/cm^2. Electrodes with a diameter of 11 mm (≡0.95 cm^2) were punched out and compressed to ~30% porosity with a KBr press. Graphite electrodes were prepared by mixing graphite (T311, SGL Carbon, Germany) and PVDF at a mass ratio of 95/5 with NMP by applying the same procedure as for the positive electrodes. The graphite ink was coated onto copper foil (MTI, ~12 μm) and dried in a convection oven at 50°C for 3 h. The loading of the graphite coating was ~7 $mg_{graphite}/cm^2$ corresponding to ~2.6 mAh/cm^2. The electrodes were punched out with a diameter of 11 mm and compressed to a porosity of ~30%. Both types of electrodes were dried under dynamic vacuum at 120°C for at least 12 h in a vacuum oven (Büchi, Switzerland) and then transferred into an Argon-filled glove box (MBraun, Germany) without exposure to air.

For OEMS measurements, isotopically labelled ^{13}C-electrodes were prepared by dispersing ^{13}C-carbon (BET ~140 m^2/g, 99% isotopic purity, Sigma-Aldrich, Germany) in NMP with an ultrasonication horn. PVDF was dissolved in NMP to yield a 10% wt solution. The PVDF solution was added to the ^{13}C-dispersion to yield a final mass ratio of 1:2 (PVDF:^{13}C), and stirred carefully. The ink was then coated onto a polyester separator (Freudenberg, Germany) with a wedge bar and dried in a convection oven at 50°C. Afterwards, electrodes with a diameter of 15 mm were punched out, dried under dynamic vacuum at 120°C over night and transferred into an argon-filled glove box. The final electrodes had a loading of ~1 mg_C/cm^2.

On-line electrochemical mass spectrometry.—The on-line electrochemical mass spectrometry (OEMS) setup has been described in more detail in a previous publication by our group.[20] For the experiments in this study, we used a recently developed sealed 2-compartment cell,[21] where working and counter electrode are separated by a sealed lithium-ion conductive glass ceramics (Ohara Corp., Japan). In this way, only gases coming directly from the working electrode are detected, and any gas evolution related to the lithium counter electrode or electrode crosstalk can be avoided. The cells were assembled with a lithium counter electrode (Ø 17 mm, 450 μm thickness, Rockwood Lithium, USA), a glassfiber separator soaked with 250 μL electrolyte in the lower compartment and a polyester separator soaked with 100 μL electrolyte in the upper compartment. The investigated electrolytes consisted only of EC or VC with 1 M $LiPF_6$ (all from BASF SE, Germany). To distinguish between electrolyte oxidation and carbon corrosion, we used isotopically labelled ^{13}C-carbon electrodes coated on a polyester separator as working electrodes (see above). The oxidative stability of the electrolytes was investigated by a linear potential sweep from OCV (~3 V vs. Li/Li^+) to 5.5 V vs. Li/Li^+ at a scan rate of 0.1 mV/s. The quantification of the OEMS signals in terms of moles of produced gas was described previously,[22] and gas evolution rates are reported in terms of μmol gas/m^2_{BET} of the ^{13}C-electrode.

Electrochemical characterization.—Swagelok T-cells with a Gold Wire Reference Electrode (GWRE)[13] were assembled in an argon filled glove box (O_2 and H_2O < 0.1 ppm, MBraun, Germany) using two glass fiber separators (11 mm diameter, 200 μm thickness, glass microfiber #691, VWR, Germany) and 60 μL of electrolyte. The electrolyte consisted of standard LP57 (1 M $LiPF_6$ in EC: EMC (3:7 wt/wt) < 10 ppm H_2O, BASF, Germany) without and with different amounts of vinylene carbonate (VC, BASF SE, Germany), which was added at concentrations of 0.09, 0.17 0.52 and 2 wt% to the electrolyte. The cells were assembled using a graphite anode, a LNMO cathode, and a gold wire reference electrode (GWRE). The detailed experimental procedure for the assembly can be found in Reference 13. For charge/discharge cycling, identical Swagelok T-cells without a reference electrode were assembled. Cell cycling was carried out in a climate chamber (25°C or 40°C, Binder, Germany) with a battery cycler (Series 400, Maccor, USA). The cycling protocol consisted of the following steps: i) two formation cycles with C/10 at 25°C, ii) charge/discharge cycling with 1C (20 cycles) at 40°C, and iii) charge/discharge cycling with 1C/3C (2 cycles) at 40°C. The steps ii) and iii) were repeated five times. All cycles were performed between 3.5 V – 4.8 V cell voltage, using a constant current constant voltage (CCCV) charge with a current limit of C/20 for the constant voltage phase and a constant current (CC) discharge. The C-rate is referenced to the theoretical capacity of the LNMO cathode (140 mAh/g_{LNMO}), i.e., 1C corresponds to 140 mA/g_{LNMO}. or ~1.9 mA/cm^2.

Electrochemical impedance spectroscopy (EIS) measurements on graphite/LNMO cells with GWRE were conducted after the first

formation cycle at 50% SOC (charged to 50% SOC with C/10) and after the 22nd, 66th and 102nd (charged to 50% SOC with 1C) using a potentiostat (VMP300, BioLogic, France). Prior to the impedance measurement, the cells were charged to 50% SOC, transferred to a climate chamber set to 10°C, and stored for 1 h in order to ensure a constant temperature of the cells. Galvanostatic electrochemical impedance spectroscopy (GEIS) was used in a frequency range from 100 kHz – 100 mHz with an amplitude of 0.6 mA.

In a previous study[13] we have demonstrated the stability of the GWRE reference potential (0.31 V vs. Li/Li^+) in graphite/LFP cells to be >500 h. By replacing the LFP electrode (upper cut off potential ~4.1 V vs. Li/Li^+) by a $LiNi_{0.5}Mn_{1.5}O_4$ electrode (upper cut off potential ~4.9 V vs. Li/Li^+), the long-term stability of the GWRE reference potential is limited. The potential drift observed in the latter case might be caused by oxidation products generated at the high-voltage positive electrode (LNMO) and their subsequent reduction at the exposed surface of the gold wire, leading to an oxidation of the lithium-gold alloy (i.e., to its gradual delithiation). To overcome this issue, relithiation of the GWRE (at 150 nA for 1 h, consuming <0.1% of the capacity of the LNMO electrode during each charge) is carried out before each impedance measurement. A similar observation is reported by Klett et al.,[23] who also relithiated their Li_xSn reference electrode prior to each impedance measurement.

Results

Anodic stability of vinylene carbonate (VC) investigated via on-line electrochemical mass spectrometry (OEMS).—Until now, the detrimental oxidation of VC is regarded as a major obstacle for the successful use of VC in LNMO cells.[14–17] In order to investigate the onset potential for VC oxidation and its products, we performed on-line electrochemical mass spectrometry on electrolytes based on only VC or EC mixed with 1 M $LiPF_6$. For these experiments, we used carbon black electrodes made from isotopically labelled ^{13}C-carbon, so that we can track the gas evolution from the unlabeled ^{12}C-electrolyte by monitoring the corresponding ^{12}C-related signals of CO_2 and CO.[22] As Jung et al.[24] recently showed that the onset and extent of electrolyte oxidation on LNMO and carbon black is identical, it is safe to transfer the results obtained from the ^{13}C-carbon model electrodes to real LNMO cathodes later on. To avoid crosstalk between oxidized species and the lithium counter electrode, we used our sealed 2-compartment cell setup.[21] In this way, only the direct oxidation of the pure electrolyte is observed. Figure 1 shows the current profile (a) and the gas evolution (b) of $^{12}CO_2$ (m/z = 44, solid lines) and ^{12}CO (m/z = 28, dotted lines) during an oxidative scan in either EC-only or VC-only electrolytes with 1 M $LiPF_6$ from OCV (~3 V vs. Li/Li^+) to 5.3 V vs. Li/Li^+. While the current signal includes processes like capacitive currents related to the electrode surface or PF_6^- intercalation into the graphitic domains of the conductive carbon, which is reported to start around 4.6 V vs. Li/Li^+,[25,26] we believe that the evolution of gaseous electrolyte oxidation products is a more meaningful indicator for the onset of electrolyte oxidation. As expected, Figure 1b shows that the oxidative CO_2-release of VC starts at significantly lower potentials (~4.3 V vs. Li/Li^+) compared to EC (~4.8 V vs. Li/Li^+). The small current starting at ~3.7 V vs. Li/Li^+ for VC is most likely related to the oxidation of the BHT stabilizer (butylated hydroxytoluene), as its integration between 3.67 V and 4.0 V yields a charge of 10.2 mAs compared to the 11.9 mAs theoretically needed for the 1-electron oxidation of the 200 ppm BHT contained in VC. Interestingly, there is no CO evolution resulting from the oxidation of VC (See red dotted line in Figure 1b); on the other hand, the electrooxidation of EC yields both CO_2 and small amounts of CO (see black dotted lines in Figure 1, bottom panel), as we had discussed previously.[27]

The lower anodic stability of VC compared to EC has already been demonstrated by previous experimental results[15,17,28] and calculations.[29,30] The CO_2 evolution from VC at potentials above ~4.3 V vs. Li/Li^+ (see Figure 1b), corresponding to ~4.2 V cell voltage in a full-cell with a graphite anode, fits well to the observation made by the Dahn group[11,31–33] that commercials cells containing VC

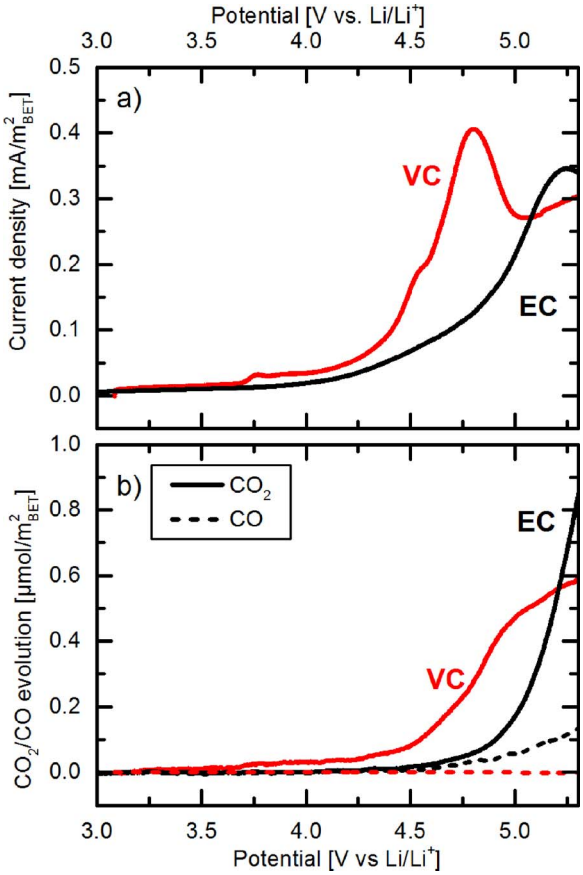

Figure 1. Anodic current (a) and evolution of $^{12}CO_2$ (b, solid lines) and ^{12}CO (b, dotted lines) from the electrolyte during a linear scan from OCV to 5.3 V vs. Li/Li^+ (0.1 mV/s) on a ^{13}C carbon electrode in electrolytes containing only EC (black lines) or VC (red lines) and 1M $LiPF_6$. The experiments were performed using on-line electrochemical mass spectrometry and a sealed 2-compartment cell[21] to avoid crosstalk with the lithium counter electrode.

evolve more gas when held at high potentials compared to the same cells without VC electrolyte. According to the EC oxidation mechanism proposed by Xing et al.[34] and Li et al.,[35] CO_2 is readily abstracted after ring opening of the EC radical cation (Scheme 1, black pathway 1a), while the evolution of CO from EC is energetically less favorable and only occurs with a simultaneous breaking of the CH_2-CH_2 bond after the intial ring opening (see blue pathway 1b in Scheme 1); for further discussion see Ref. 21). Although the decomposition mechanism of EC resulting in CO_2 can easily be applied to VC (see black pathway 2a in Scheme 1), the analogous pathway leading to CO is likely to present a very large barrier in the case of VC, as this would require breaking the much stronger CH=CH bond. Hence, our observation that no CO is produced during VC oxidation (Figure 1b) would be consistent with an analogous ring opening reaction as in the case of EC, which disagrees however with the early modeling predictions made by Zhang et al.[5] As poly(VC) has been found on electrodes cycled to high potentials in VC-containing electrolytes,[17] we assume that the radical cations formed in (2a) can trigger a radical polymerization reaction of VC to poly(VC) (see green pathway 2b in Scheme 1).[9,17]

Extracting the interfacial resistance from the impedance spectra.—As a next step, cells with different VC concentrations are assembled and impedance spectra are collected in order to understand the impact of the anodic decomposition of the additive in a graphite/LNMO full-cell. To extract the interfacial resistance from the anode Nyquist plots, the equivalent circuit shown in Figure 2a is used: i) the high frequency resistance (HFR) R_{HFR} represents the

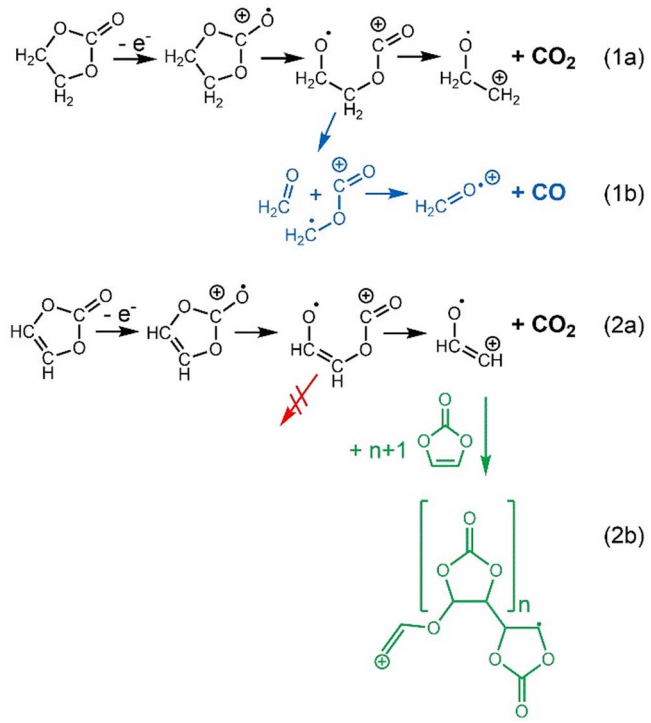

Scheme 1. Oxidation mechanism of EC leading to CO_2 (1a, black) and CO (1b, blue) as proposed by Xing et al.,[34] oxidation mechanism of VC leading to CO_2 (2a, black) and poly(VC) (2b, green).

contributions from the ionic conduction in the separator (between the GWRE and the respective electrode) and external electrical contact resistances; ii) up to three RQ-elements (resistor and constant-phase element in parallel) are used to determine the overall resistance of the anode, consisting of contributions from the charge transfer resistance, the solid-electrolyte interphase resistance, and one as yet unknown impedance contribution at low frequencies when high VC concentrations (0.52 and 2 wt%) are used (see Figure 3a); iii) the Warburg element (Z_W) mostly represents the diffusion of lithium in the liquid electrolyte phase as described in Reference 36. For the LNMO cathode, the equivalent circuit shown in Figure 2b is used, representing the analogous processes as in the case of the anode. Since the main focus of this study was to determine the individual impedance growth of anode and cathode during formation and extended charge/discharge cycling, only the overall anode and cathode impedance will be considered in the following ($R_{Anode} = R_1 + R_2 + R_3$, see Figure 2a; $R_{Cathode} = R_1 + R_2$ see Figure 2b). After the 22th cycle, a semi-circle at high frequencies appears in the cathode impedance spectra, which was shown to be due to the formation of a contact resistance at the interface between the cathode electrode and the cathode current collector,[36] and which will be omitted from the fitting process in this study. Unfortunately, a meaningful deconvolution/assignment of the individual impedance contributions to the overall impedance for each electrode would require more elaborate experiments, as we have shown in our recent work for the LNMO cathode impedance.[36] However, as explained above, the main objective of this study was to quantify the individual evolution of anode (R_{Anode}) vs. cathode ($R_{Cathode}$) impedance over extended charge/discharge cycling, for which a deconvolution into the various process is not necessary.

Figures 2c and 2d show exemplary Nyquist plots of a graphite anode and a LNMO cathode after one formation cycle in a graphite/LNMO full-cell with 0.09 wt% VC additive. The red points represent the experimental spectra (100 kHz - 100 mHz, current perturbation of 0.6 mA, 10°C), while the black line represents the fit to the equivalent circuit shown in Figures 2a and 2b. The values for the HFR of anode and cathode are ~4.0 and ~3.5 Ωcm^2, respectively;

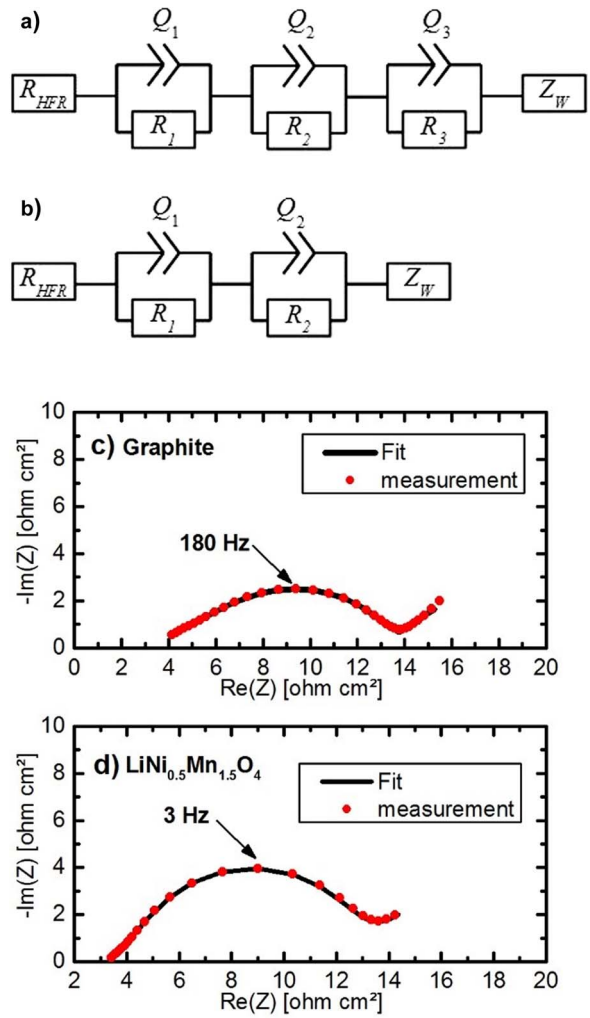

Figure 2. Equivalent circuit models for fitting the anode (a) and the cathode (b) impedance spectra. The Nyquist plots after one formation cycle and recharge to 50% SOC (at 0.1C and 40°C) of graphite/LNMO cells with LP57 electrolyte with 0.09 wt% VC are shown for both the graphite anode (c) and the LNMO cathode (d), whereby the experimental data (red points) are compared to the corresponding fit of the measurement (black line). The impedance is measured from 100 kHz to 100 mHz with an amplitude of 0.6 mA @ 10°C and 50% SOC.

the cause for the slight difference in these HFR values (which are expected to be identical for a symmetric placement of the GWRE) was described elsewhere.[13] The overall resistances of the anode (R_{Anode}) and the cathode ($R_{Cathode}$) are in both cases ~10 Ωcm^2.

Impedance analysis after the first formation cycle.—The OEMS measurement showed an onset for the anodic decomposition of VC at ~4.3 V vs. Li/Li^+, accompanied by the release of CO_2. To understand the effect of the VC decomposition products formed by VC oxidation on the cathode (e.g., poly(VC) and radicals, see Scheme 2a and 2b) and by VC reduction on the anode (discussed in Reference 5) on cathode and anode impedance growth, we conduct impedance measurements with the gold-wire reference electrode (GWRE) after one formation cycle at 25°C and recharge to 50% SOC (state-of-charge) in LP57 with different concentrations of VC (0, 0.09, 0.17, 0.52, and 2 wt%). The additive concentrations were chosen such that some of the VC concentrations in our lab-scale cells yield VC mass to graphite surface area ratios comparable to those tested in the commercial-scale pouch cell experiments by Burns et al.:[10] 0.09, 0.17, and 2 wt% VC in our lab-scale cells approximately corresponds to 1, 2, and 6 wt% VC in their

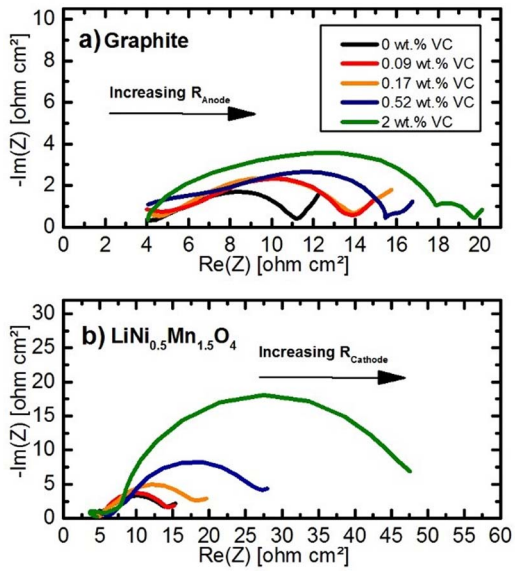

Figure 3. Anode and cathode impedances obtained from graphite/LNMO full-cell with GWRE after one formation cycle and recharge to 50% SOC at 25°C in LP57 with various VC additive concentrations. a) Impedance spectra of the graphite anode of cells containing 0 wt% VC (black lines), 0.09 wt% VC (red lines), 0.17 wt% VC (orange lines), 0.52 wt% VC (blue lines), and 2 wt% VC (green lines); b) analogous impedance spectra of the LNMO cathode. Impedance spectra were measured from 100 kHz to 100 mHz with a current amplitude of 0.6 mA at a temperature of 10°C and at 50% SOC.

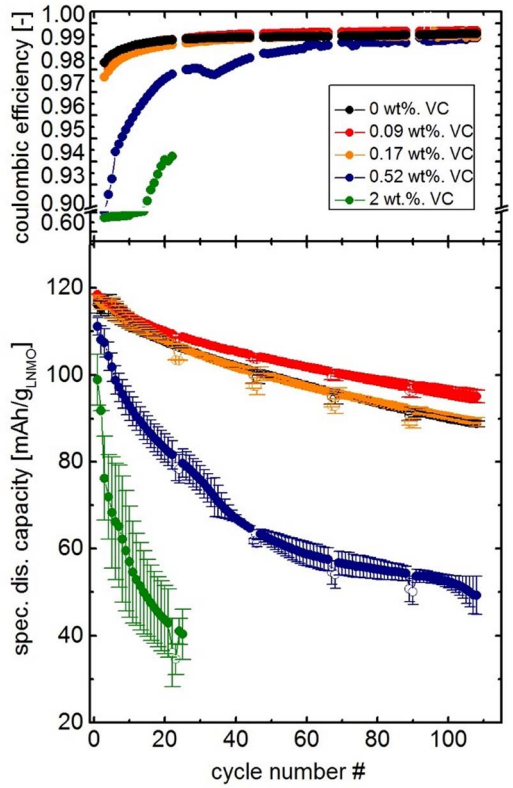

Figure 4. Coulombic efficiency (upper panel) and specific discharge capacity (mAh/g_{LNMO}) (lower panel) of graphite/LNMO cells (without GWRE) over extended charge/discharge cycling at 1C/1C (followed by two 1C/3C cycles after every 20 cycles) and 40°C between 3.5 and 4.8 V in LP57 electrolyte with different VC concentrations: 0 wt% VC (black points), 0.09 wt% VC (red points), 0.17 wt% VC (orange points), 0.52 wt% VC (blue points), and 2.0 wt% VC (green points). The formation of the cells was carried out at 25°C (2 cycles at C/10), while further cycling is done at 40°C. For clarity, the upper panel does not contain data of the two formation cycles and the 1C/3C cycles. The coulombic efficiencies of the two formation cycles (cycle 1 and 2) are given in Table I. Two cells were tested for each electrolyte composition; the figure shows the average of the two cells, with error bars representing the standard deviation. 3C discharge points are filled white for better visibility.

commercial-scale cells. In addition, to allow for a better comparison of the resulting anode and cathode impedance, we also conducted our impedance measurements at 10°C, as done in the latter study. Figures 3a and 3b show the Nyquist plots of the graphite and the LNMO electrodes recorded from a graphite/LNMO full-cell with GWRE.

Without VC additive (black lines), the fitted values for the overall resistance of the anode, R_{Anode}, are ~7 Ωcm² and ~9 Ωcm² for $R_{Cathode}$. When a small amount of VC (0.09 wt%, red lines) is added to the cells, the overall resistance of the anode increases to ~10 Ωcm², whereas the impedance of the cathode stays constant at ~9 Ωcm². When the concentration is increased to 0.17 wt% (orange lines), the impedance of the anode remains at ~10 Ωcm² while now the impedance of the cathode starts to increase to ~13 Ωcm². While the anode impedance only increases very little with a further rise in VC concentration, namely to ~15 Ωcm² for 0.52 wt% VC (blue lines) and to ~16 Ωcm² for 2 wt% VC (green lines), the cathode impedance increases substantially to ~22 Ωcm² for 0.52 wt% VC and to ~41 Ωcm² for 2 wt% VC.

Our interpretation of these observations is as follows: When small amounts of VC (0.09 wt%) are added to the graphite/LNMO cells, it will preferentially be reduced at the graphite anode, leaving no or little VC for oxidation at the LNMO cathode. On the other hand, when higher concentrations of VC are present in the electrolyte (0.17–2 wt%), residual VC remains in the electrolyte after anode SEI formation, allowing for oxidation of VC at the high-voltage LNMO cathode, ultimately leading to cathode impedance growth. As already suggested in previous studies[17] and shown in Scheme 1 (reactions 2a and 2b), the formation of a poly(VC) film on the LNMO cathode is the most likely explanation for the observed impedance increase of the positive electrode shown in Figure 3b. The very high cathode impedance of our lab-scale cell with 2 wt% VC after only one formation cycle indicates that the rapid oxidation of VC at the LNMO cathode potential (shown by OEMS data in Figure 1) leads to the formation of a highly resistive surface film. This would be consistent with the strong capacity fading reported for graphite/LNMO coin cells with 2 wt% VC[14] and will be further examined in the following. These results suggest that the ratio of (anode) additive to graphite surface is crucial for high-voltage lithium-ion cells, and that a successful use of SEI formers like VC will depend on the competition between additive reduction on the anode and its oxidation on the cathode, as will be explained in more detail in the Discussion section.

Cell cycling at elevated temperatures (40°C) with different concentrations of vinylene carbonate (VC).—As a next step, the influence of different VC concentrations on the cycling behavior at elevated temperatures (40°C) will be investigated. The two main questions are: i) can low concentrations of VC have a beneficial effect on the cycling performance of graphite/LNMO cells, despite the current understanding that VC has a detrimental effect; and, ii) how do the VC oxidation products affect the capacity retention of full-cells. To address these questions, graphite/LNMO cells with different VC concentrations are cycled at 40°C at 1C (CCCV charge, CC discharge; for details see Experimental section) after formation at 25°C (two C/10 cycles). After every twentieth 1C/1C charge/discharge cycle, two 1C/3C charge/discharge cycles are employed in order to gain information about the resistance buildup in the cells, which later on will be compared with the anode/cathode impedance data acquired in repeat experiments using T-cells equipped with a gold wire reference electrode. Figure 4 shows both the specific discharge capacity (in mAh/g_{LNMO}) versus the cycle number (bottom panel) and the coulombic efficiency (top panel) of graphite/LNMO cells with different VC concentrations. For clarity, each dataset shown in Figure 4 contains

the average value of two identical cells (error bars represent the standard deviations between the two cells). Starting from cells which contain no VC (0% VC, black dots), the first discharge capacity at C/10 is ∼117 (±2) mAh/g_{LNMO}, resulting in a first-cycle coulombic efficiency of ∼82%. After 80 cycles, the coulombic efficiency reaches a constant value of ∼99.5% while the discharge capacity remains at ∼88 (±1) mAh/g_{LNMO} after 108 cycles. When adding VC at a commonly used concentration of 2 wt% VC (Figure 4, green dots), the first-cycle discharge capacity at C/10 is only ∼99 (±6) mAh/g_{LNMO}, with a coulombic efficiency of ∼54%, i.e, dramatically lower than in cells with VC-free electrolyte. The capacity loss for cells with 2 wt% VC is very high (57 ±3 mAh/g_{LNMO} after 20 cycles), and the difference in capacity between the last 1C/1C (cycle 25) and the previous 3C/1C cycles amounts to ∼8 (±5) mAh/g_{LNMO} (in contrast to ∼1 (±1) mAh/g_{LNMO} for VC-free electrolyte at the same point), which indicates a dramatic increase in cell impedance. Owing to the already very low capacity after these initial 23 cycles, the test was discontinued here. The poor coulombic efficiency with 2 wt% VC can partly be explained by the early onset of VC oxidation at a cell voltage of ∼4.2 V (i.e., at ∼4.3 V vs. Li/Li^+), as evidenced by the OEMS data in Figure 1, since a parasitic oxidation reaction would reduce the coulombic efficiency.

When the concentration of VC is lowered to 0.52 wt% (Figure 4, blue points), the first discharge capacity is ∼111 (±2) mAh/g_{LNMO} and a first-cycle coulombic efficiency of ∼74% is obtained, which is much higher compared to cells with 2 wt% VC (see Table I). After 108 cycles, the discharge capacity is ∼49 (±4) mAh/g_{LNMO} and the coulombic efficiency increases up to 97.5% until cycle 30, where it shows an unexplained drop until cycle 40, and then gradually approaches 99% by the end of the test procedure. Also here, the low coulombic efficiency and capacity retention illustrate the negative impact of VC oxidation products on cell performance. When 0.17 wt% VC are added to the full-cell, a first-cycle discharge capacity of ∼118 (±2) mAh/g_{LNMO} with a first-cycle coulombic efficiency of 82% are observed, quite similar to the case without VC additive (see Table I). Thus, it is not surprising that after 108 cycles, the discharge capacity of ∼88 (±2) mAh/g_{LNMO} is essentially identical to that of the VC-free electrolyte, even though the coulombic efficiency up to cycle 30 is slightly lower (upper panel of Figure 4, orange points). The slightly larger difference between the 1C/1C and the 1C/3C discharge capacity suggests a somewhat higher cell resistance for the 0.17 wt% VC compared to the VC-free electrolyte, which we will correlate with the impedance data in the next section.

So far, the graphite/LNMO cell performance with VC-free electrolyte is clearly superior to VC-containing electrolyte. This observation, however, changes as the VC concentration is lowered to 0.09 wt% (Figure 4, red points), in which case we observe a higher 1st cycle coulombic efficiency (83%), an improved capacity retention (95 (±2) mAh/g_{LNMO} after 108 cycles) compared to cells without VC additive (88 (±1) mAh/g_{LNMO} after 108 cycles), as well as a better coulombic efficiency reaching 99.7% (vs. 99.6%) after 108 cycles.

As shown by Reaction 2a in Scheme 1, the oxidation of VC will release cations into the solution (presumably the cation radicals proposed in Reaction 2a) which will result in one or several of the following processes: i) electroneutrality in the electrolyte requires that lithium ions from the solution must intercalate into the graphite anode (under the reasonable assumption that no intercalation of the radical cations into graphite and/or the PF_6^- anions into LNMO can occur; this is a reasonable assumption, since the amount of C65 is small and as it is not fully graphitized), which would lead to a depletion of lithium ions in the electrolyte; ii) if the released radical cations stabilize by the release of a proton (as evidenced in our previous study[21]), the proton concentration in the electrolyte would increase (simultaneously decreasing the lithium ion concentration), unless proton intercalation into graphite (during charge) and/or LNMO (during discharge) can occur to a significant degree; iii) VC oxidation and the formation of protons could lead to enhanced dissolution of transition metal ions (as this process is known to correlate with the electrolyte oxidation potential),[37] which – together with oxidation products like HF themselves – could damage the SEI and lead to additional irreversible lithium loss at the anode; and, iv) VC oxidation could lead to impedance growth on anode and/or cathode due to reactions involving VC oxidation products. Regarding the latter, we will see in the following that while the observed impedance growth is substantial, it seems too low to explain the dramatic observed capacity fading. Figure 5 shows the full-cell voltage profiles (E_{WE}-E_{CE}) for cells with 0 wt% and 0.52 wt% VC after the 30th and 100th cycle. For cells containing 0 wt% VC one can clearly see that the increase in the overpotential during cycling is minor (black solid line vs. black dotted line) and therefore the loss of active lithium is the most likely reason for the capacity fade. Cells with 0.52 wt% VC show an increased polarization, which increases slightly during cycling (blue line vs. blue dotted line). However, as i) the capacity obtained during the constant voltage (CV) step does not increase significantly between cycle 30 and 100 for cells with 0.52 wt% VC, and ii) the voltage profiles for cells with 0.52 wt% VC at the end of the of the constant-current charge still bend upwards, indicating that the cathode is close to complete delithiation, the capacity loss is most likely connected to a loss of active lithium and cannot be solely explained by an increased polarization.

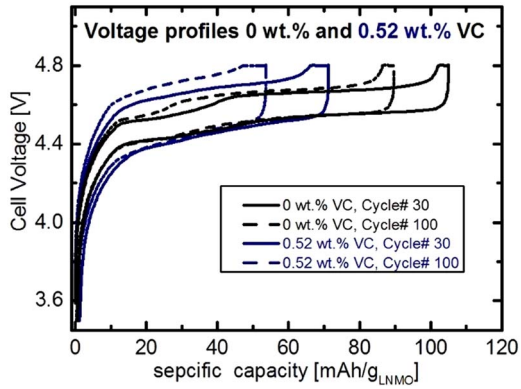

Figure 5. Full cell voltage profiles (E_{WE}-E_{CE}) for cells with 0 wt% and 0.52 wt% VC in graphite/LNMO cells (cycled at 40°C) after cycle 30 and cycle 100.

Thus, we believe that the first two mechanisms are the most likely explanation for the observed rapid capacity fading of cells with high concentrations of VC, even though it is currently unclear which one of these processes might be predominant: according to the first mechanism (i), lithium plating would eventually have to occur at the graphite anode and the lithium ion concentration in the electrolyte would get depleted due to a buildup of cationic oxidation products in the electrolyte; according to the second mechanism (ii), protons formed and accumulated in the electrolyte would be expected to corrode the LNMO cathode, resulting in transition metal dissolution and their

Table I. Coulombic efficiency of graphite/LNMO cells of the first two formation cycles at C/10 (25°C) for cells with 0, 0.09, 0.17, 0.52, and 2 wt% VC in LP57.

Concentration	0 wt% VC	0.09 wt% VC	0.17 wt% VC	0.52 wt% VC	2 wt% VC
1st cycle	82%	83%	80%	74%	54%
2nd cycle	95%	96%	94%	85%	59%

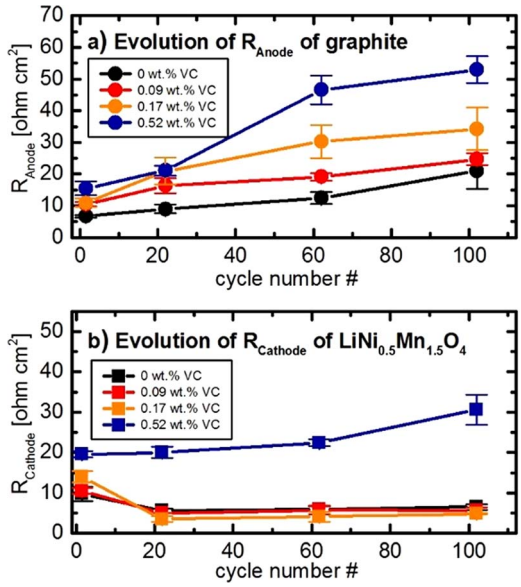

Figure 6. Evolution of the interfacial electrode resistances (R_{Anode} and $R_{Cathode}$) of graphite/LNMO cells (measured with GWRE) over extended charge/discharge cycling at 1C/1C and 40°C between 3.5 and 4.8 V in LP57 electrolyte with different VC concentrations. a) R_{Anode} of the graphite anode over cycling with 0 wt% VC (black line), 0.09 wt% VC (red line), 0.17 wt% VC (orange line), and 0.52 wt% VC (blue line); b) $R_{Cathode}$ of the LNMO cathode for the same electrolytes. Note that the impedance obtained after the first formation cycle at 25°C and C/10 at are included in this figure as cycle 1 (see data shown in Figure 3). Impedance spectra were recorded at 50% SOC and 10°C from 100 kHz to 100 mHz with an amplitude of 0.6 mA. Two cells were tested for each electrolyte composition; the data points show the average of the two cells, with error bars representing the standard deviation.

deposition on the graphite anode. Further studies are currently underway to prove/disprove these hypotheses.

Analysis of the impedance of anode and cathode during cycling.—In this section, we want to investigate the effect of different VC concentrations on the impedance of anode and cathode during cycling. Therefore, the T-cells with GWRE used for the examination of anode and cathode impedance vs. VC concentration after the first formation cycle at 25°C (data shown in Figure 3) were transferred to a 40°C climate chamber where they were was cycled at 1C/1C charge/discharge, The cycling protocol was identical to that used for the cell cycling shown in Figure 4, except that the two 1C/3C charge/discharge cycles after every 20th cycle were omitted. This, however, did not significantly alter the cycle-life: cells equipped with a GWRE and with VC-free electrolyte had a capacity of 87 (±2) mAh/g_{LNMO} after 102 cycles, which is comparable to a capacity of 89 (±1) mAh/g for the cells with the same electrolyte but without reference electrodes (see black symbols in Figure 4). Impedance was measured after the 22nd, 62nd, and 102nd cycle at 50% SOC and 10°C.

Figures 6a and 6b show the overall interfacial resistance of the graphite anode and the LNMO cathode versus cycle number. Note that the data from the first formation cycle are included, where cells were cycled at 25°C.

The anode impedance (Figure 6a) increases roughly linearly with cycle number for cells without VC (black line) and those with 0.09 wt% (red line) and 0.17 wt% VC additive (orange line). For cells with 0 wt% VC, the anode impedance increases from ∼7 Ωcm^2 (first cycle) to ∼20 Ωcm^2 (102nd cycle). Cells containing 0.09 wt% and 0.17 wt% VC show a similarly gradual impedance increase. For cells with a concentration of 0.17 wt% VC, the impedance increase is slightly higher compared to cells with 0.09 wt% VC, although the initial values for the anode impedance are identical (∼10 Ωcm^2). The anode impedance of cells with 0.52 wt% VC increases substantially during cycling, namely up to ∼55 Ωcm^2 after the 102nd cycle. An analogous increase of the graphite anode impedance with increasing VC concentrations was also observed by Burns et al.[10] in commercial-scale graphite/LCO cells for >1 wt.%VC. As will be discussed later, the difference in the VC threshold concentration is due to differences in the electrolyte to graphite surface ratio in commercial-scale vs. lab-scale cells.

Figure 6b shows the interfacial resistance versus cycle number for the LNMO cathode. For cells with 0, 0.09, and 0.17 wt% VC, the impedance decreases after the formation cycle, reaching a constant value of ∼5 Ωcm^2 after 20 cycles. In contrast, the LNMO cathode interfacial impedance starts out with a significantly higher value after the first formation cycle (∼22 Ωcm^2) for the cells with 0.52 wt% VC and increases with cycle number to ∼30 Ωcm^2. We believe that the most likely explanation for the LNMO cathode impedance decrease for low VC concentrations is related to the different temperatures during the first formation cycle (25°C) and the subsequent extended charge/discharge cycling (40°C). During cycling at elevated temperatures, the electrolyte/LNMO interface initially formed at 25°C might be restructured at 40°C by the enhanced solubility of some of the interfacial species (e.g., dissolution of organic interfacial species like poly(VC) or of manganese fluoride produced by reaction with HF traces in the original electrolyte), leading to an impedance decrease. For the cells with 0.52% VC, one could imagine that the relatively high VC concentration has led to a thicker cathode surface film, which cannot be dissolved due to a change in temperature. Further, the ongoing cathode impedance growth during cycling could mean that not all VC has been consumed during the initial cycles.

It should be noted that if the content of conductive carbon in the LNMO electrodes is decreased from 5 wt% (used here) to 2 wt%, an increase in LNMO cathode impedance during cycling can be observed even for low VC concentrations. This effect can clearly be attributed to a growing contact resistance at the current collector/electrode interface, as we will show in a future study.[38] However, when 5% carbon black are added to the electrodes (see this study), the increase of the contact resistance is significant.

Discussion

In the following, we will seek to examine why the very low VC concentration of 0.09 wt% in our lab-scale graphite/LNMO cells leads to a clearly improved capacity retention (see Figure 5). This could be understood if these low concentrations of VC are sufficient to form a protective SEI, and if during the first formation cycle, VC reduction at the graphite anode can be completed prior to its oxidation at the LNMO cathode. We will also show that high VC concentrations result in significantly overcharge capacity in the first charging cycle, consistent with the oxidation of the majority of remaining VC at the LNMO cathode. Finally, based on the here observed effect of VC concentration on graphite/LNMO lab-scale cell performance, we will project the VC concentration levels in the electrolyte of commercial-scale cells which would lead to an improved cycling performance of graphite/LNMO cells compared to VC-free electrolyte.

Estimated coverage of VC derived SEI on graphite surface with 0.09 wt% VC additive.—In the following, we want to estimate how many monolayers of poly(VC) can be deposited on the graphite surface by the reduction of all VC contained in the electrolyte with 0.09 wt% VC, i.e., for the concentration which showed the best capacity retention in Figure 4. The purpose of this estimate is to evaluate whether the amount of VC-derived SEI (consisting largely of poly(VC)) at this low VC concentration could yield monolayer thick films, which would be required for surface passivation.

First, we approximate the surface area that can be occupied by one repeat unit of poly(VC), corresponding to the reductive decomposition of one VC molecule.[39] Analogous to Jung et al.,[18] we assume that one adsorbed decomposition product of VC consists of eight atoms (total amount of atoms per poly(VC) repeat unit) and that every atom occupies a square with an average length of a carbon-carbon single

bond of 0.15 nm. Thus, the corresponding area that would be covered by one poly(VC) unit equals to $8 \times (0.15\ \text{nm}^2)^2 = 0.18\ \text{nm}^2$. Taking into account the Avogadro constant ($N_A = 6.022 \cdot 10^{23}$ atoms/mol) and the total surface area of the graphite anodes used in this study (0.033 $m^2_{Graphite}$, based on a BET surface area of ~5 m^2/g, a loading of ~7 $mg_{Graphite}/cm^2_{electrode}$, and a geometric surface area of 0.95 cm^2), we can now estimate how many moles of VC are required to form one monolayer n_{ML} of poly(VC) on the graphite surface:

$$n_{ML} = \frac{0.033\ \text{m}^2}{N_A \times 0.18\ \text{nm}^2} = 0.307\ \mu\text{mol/ML} \quad [1]$$

To obtain the effective number of monolayers of poly(VC) produced on the graphite anode during the first formation cycles, one would need to estimate the fraction of the added moles of VC which are reduced at the anode compared to the fraction which might be oxidized at the cathode. Based on the impedance data in Figure 3b, the LNMO impedance after formation increases only in the cases where the VC concentration is ≥0.17 wt%, so that it is reasonable to assume that for cells with 0.09 wt% VC, all VC in the electrolyte is only reduced at the anode, since the oxidation of excess VC on the cathode obviously leads to a highly resistive film (presumably also poly(VC)[17]) on the LNMO cathode. Hence, it should be a reasonable estimate that the total amount of VC in the 0.09 wt% VC electrolyte ($n_{VC} = 0.73\ \mu\text{mol}_{VC}$ in 60 μL electrolyte) will be reduced at the anode within the first formation cycle to form an SEI layer. In this case, the total number of deposited poly(VC) monolayers N_{ML} in the anode SEI can be estimated as:

$$N_{ML} = \frac{n_{VC}}{n_{ML}} = \frac{0.73\ \mu\text{mol}_{VC}}{0.307\ \mu\text{mol/ML}} = 2.4\ \text{ML} \quad [2]$$

The resulting value on the order of 2–3 monolayer equivalents of poly(VC) could in principle be sufficient to build a passivating VC-derived SEI on the graphite anode. The thickness of this layer, d_{SEI}, can be estimated by assuming that the average monolayer thickness d_{ML} will roughly be the length of a carbon-carbon single bond (0.15 nm):

$$d_{SEI} = N_{ML} \times d_{ML} = 2.4\ \text{ML} \times 0.15\ \text{nm/ML} = \sim 0.4\ \text{nm} \quad [3]$$

In view of the superior cycling performance with 0.09 wt% VC compared to VC-free electrolyte or electrolyte with higher VC concentrations (see Figure 4) and considering the above estimates, we can finally conclude that a VC concentration of 0.09 wt% is on the one hand sufficiently small to be completely reduced within the first cycle, thus avoiding any detrimental side reactions during subsequent oxidation at the LNMO cathode, and on the other hand still large enough to accomplish adequate passivation of the graphite anode with an average SEI thickness of ~0.4 nm. The overall SEI will be thicker than ~0.4 nm as also EC and the PF_6^- anion can be reduced after the initial cycles, however a sufficient fraction of the SEI consists of poly(VC) leading to enhanced stability.

Reduction and oxidation of VC considering the half-cell potentials of graphite and LNMO.—The above analysis tacitly assumed that the quantity of VC in the 0.09 wt% electrolyte can be reduced at the graphite anode prior to the onset of VC oxidation at the LNMO cathode during the first formation cycle. That this is indeed feasible can be shown by examining the graphite and LNMO half-cell potentials during the first charging of graphite/LNMO cells. To follow the half-cell potentials during the first charge, a graphite/LNMO cell with 0 wt% VC and a lithium metal reference electrode was used. Figure 7 shows the potential of the graphite anode vs. Li/Li^+ and of the LNMO cathode vs. Li/Li^+ during the first part of the formation (up to a first charge capacity of 13 mAh/g_{LNMO}, which correspond to ~1 h of charge at C/10). The dark blue line represents the graphite half-cell potential, while the vertical dashed lines indicate the onset for the VC reduction at ~1.8 V vs. Li/Li (blue line) and the reduction of EC at ~0.8 V vs. Li/Li^+ (red line) taken from References 4 and 5. After a charge capacity of only ~0.5 mAh/g_{LNMO} (~2 minutes at C/10), the onset potential for the reduction of VC is reached, whereas after a

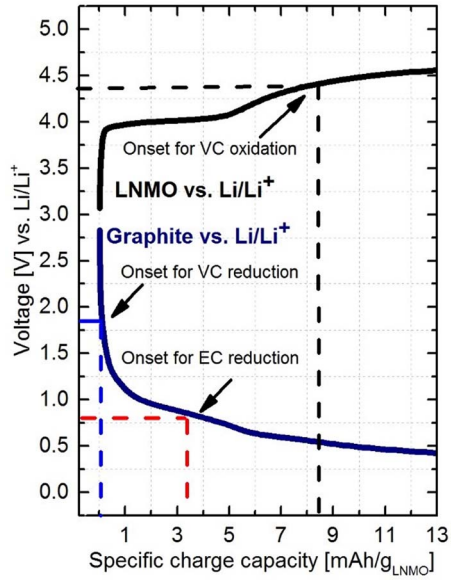

Figure 7. Half-cell potentials of LNMO (black line) and graphite (blue line) vs. Li/Li^+ during the first formation cycle at C/10 and 25°C in an VC-free LP57 electrolyte. The vertical dashed lines mark the onset potentials for VC reduction (blue), EC reduction (red), and VC oxidation (black).

total capacity of ~4.5 mAh/g_{LNMO} (~18 minutes at C/10), the onset potential for EC reduction is reached. At the same time, the half-cell potential of the LNMO cathode (Figure 7, black line) shows a short plateau around ~4.0 V vs. Li/Li^+ for ~6 mAh/g_{LNMO}, corresponding to the Mn^{3+}/Mn^{4+} redox couple. Upon further charging, the LNMO potential gradually increases toward its main voltage plateau at ~4.7 V vs. Li/Li^+, which belongs to the Ni^{2+}/Ni^{3+} redox couple (due to the zoomed-in view of the capacity axis, only the onset for the plateau at 4.7 V vs. Li/Li^+ is visible).[40] An potential of ~4.3 V vs. Li/Li^+, which corresponds to the onset potential for VC oxidation (black vertical line), is reached by the LNMO cathode after ~8.5 mAh/g_{LNMO} (i.e., ~34 minutes) in this first charge of the graphite/LNMO cell. This means that there are ~8 mAh/g_{LNMO} or ~30 minutes during the first charge where the graphite potential is already low enough to reduce VC, but where the LNMO potential is still too low to oxidize VC (illustrated by the difference between the vertical blue and black lines in Figure 6). The capacity of ~8 mAh/g_{LNMO} can now be compared to the theoretical capacities required for the reduction of different amounts of VC in the electrolyte.

Based on a previous study,[5] the first step in the formation of poly(VC) is most likely the one-electron reduction of VC to the radical anions •CH = CH-O-COO⁻ or •CH = CH-O⁻ (upon release of CO_2), both of which can react with VC to poly(VC). Thus, the formation of poly(VC) would require ≤0.5 electrons per VC molecule (depending on the number of repeat units in the poly(VC) product). This implies that the reduction of 0.73 μmol VC in the 0.09 wt% VC electrolyte would require a reductive charge of ≤0.010 mAh or, if referenced to the mass of LNMO in the cell (12.9 mg, based on a loading of 13.6 mg_{LNMO}/cm^2 and an electrode area of 0.95 cm^2), a charge of ≤0.76 mAh/g_{LNMO}. Thus, for the 0.09 wt% VC electrolyte, the total amount of VC in the electrolyte can easily be reduced at the graphite anode before the LNMO cathode potential reaches the onset potential for VC oxidation (which occurs at ~8 mAh/g_{LNMO} after the VC reduction onset, as discussed before). The same analysis would suggest that even for our VC concentration of 0.52 wt%, the required reductive charge of ≤4.5 mAh/g_{LNMO} would still be available prior to reaching an LNMO potential of ~4.3 V, which is required to oxidize VC; on the other hand, for 2 wt% VC, the reductive charge which can be passed before the LNMO cathode reaches ~4.3 V would likely not suffice to reduce all of the VC in the electrolyte (which would require

≤17.3 mAh/g_{LNMO}). While these estimates show that even 0.52 wt% VC in our electrolyte could in principle be reduced at the graphite anode before the LNMO cathode potential is high enough to oxidize VC, the LNMO cathode impedance data after the first formation cycle (see Figure 3b) clearly shows a substantial LNMO impedance increase with VC concentrations ≥0.17 wt%, indicating that there is residual VC left in cells with ≥0.17 wt% VC after the initial 8.5 mAh/g_{LNMO} charge. These observations fit well to a study by Petibon et al.,[11] who showed that in commercial-scale NMC/graphite pouch cells with 1% wt.VC (corresponding to 0.09 wt% VC in our cells in terms of VC to graphite surface ratio), more than 80% of the initial VC is already consumed after ∼50% of the first charge, whereas at the same point, about 4.2 wt% VC is left if the cell originally contained 6 wt% VC (i.e., 0.52 wt% VC in our study). Our results suggest that for the formation of a passivating anode SEI, VC concentrations between 0.09 wt% (no LNMO impedance increase compared to 0 wt% VC, see Figure 3b) and 0.17 wt% (LNMO impedance increase, see Figure 3b) are sufficient. Assuming that the reduction of VC is substantially slowed down once this passivation has been reached, any excess VC would be oxidized at the LNMO cathode once it exceeds a potential of ∼4.3 V, as seen in the LNMO impedance for cells with ≥0.17 wt% VC.

Overcharge capacities from the anodic decomposition of VC.— The impedance data in Figure 3b suggest that in the case of higher VC concentrations (≥0.17 wt%), a significant fraction of the VC present in the electrolyte must be oxidized in the first cycle at the LNMO cathode. In this case, the additional oxidative current used for the oxidation of VC should increase the first cycle charge capacity.[16,17] Therefore, we want to analyze the first cycle overcharge capacities in graphite/LNMO cells with different amounts of VC. The formation protocol consists of two C/10 charge (CCCV)/discharge (CC) cycles between 3.5 V – 4.8 V cell voltage with a current limit of C/20 for the CV step. Figure 8a shows the first charge of cells with different VC concentrations. For the cells with a concentration of 0 wt% VC and 0.09 wt% VC, the first charge capacities are ∼140 mAh/g_{LNMO} and ∼141 mAh/g_{LNMO} (black line and red line in Figure 8a). These values correspond to the theoretical capacity of the LNMO electrode, consistent with our above assumption that no VC oxidation occurs in cells with 0.09 wt% VC. When the concentration of VC is increased to 0.17 wt% VC, the capacity increases to ∼144 mAh/g_{LNMO} (yellow line in Figure 8a), indicating that the now occurring electrochemical oxidation of VC causes an additional charge capacity. This is further supported when the concentrations of 0.52 wt% and 2 wt% are taken into account, for which the first charge capacity increases to ∼151 mAh/g_{LNMO} and to ∼183 mAh/g_{LNMO}, respectively (see blue line and green line in Figure 8a).

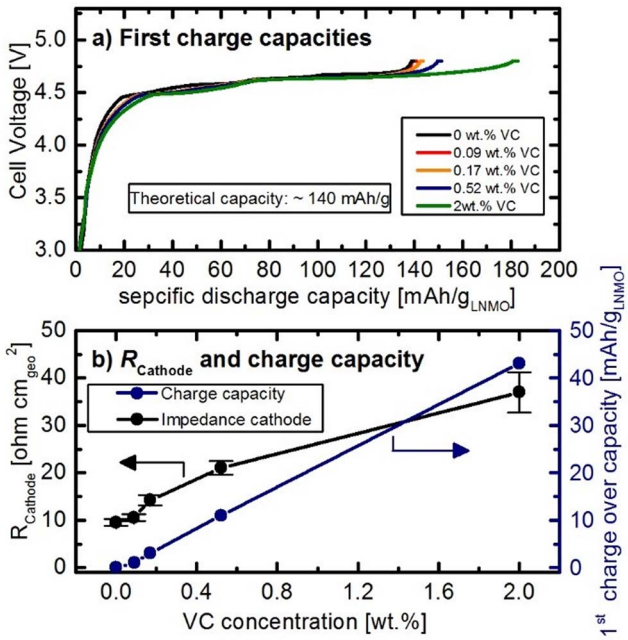

Figure 8. a) First charge of graphite/LNMO cells with 0 wt% VC (black line), 0.09 wt% VC (red line), 0.17 wt% VC (orange line), 0.52 wt% VC (blue line), and 2 wt% VC (green line). The charge is carried out in a constant current constant charge mode (CCCV) with a current limit of C/20 for the CV step. b) First charge capacities of the graphite/LNMO cell and LNMO cathode interfacial impedance, $R_{Cathode}$, after first charge/discharge (data from Figure 3b) vs. VC concentration.

In the following, we want to correlate the overcharge capacities arising from VC oxidation (i.e., the first charge capacity minus 140 mAh/g_{LNMO}, which is the first charge capacity of a cell with VC-free electrolyte) to the impedance of the LNMO electrode. In Figure 8b, the first charge capacities (blue symbols, right y-axis) are plotted vs. VC concentration. It is apparent that for VC concentrations ≥0.17 wt%, the charge capacity increases proportionally with the VC concentration (i.e., doubling the VC concentration leads to a doubling of the overcharge capacity), which is a clear evidence that excess VC is being oxidized quantitatively during the first charge. The lower than predicted overcharge for the cells with 0.09 wt% VC is in agreement with our assumption that in cells with 0.09 wt% VC, nearly all VC is consumed at the anode before its oxidation can occur. This overall trend fits very well with the LNMO impedance data obtained after the first cycle (see Figure 3b), which are re-plotted in Figure 8b (black symbols, left y-axis), demonstrating that the overcharge capacity and the impedance of the LNMO cathode are correlated. As mentioned before, the impedance increase at the positive electrode can be explained by the formation of poly(VC), which can also be formed during oxidation (see reactions 2a and 2b in Scheme 1). In contrast to the first charge capacity, the cathode impedance grows less severely at high VC concentrations. An explanation for this behavior could be the structural or morphological changes in the poly(VC) layer once a certain thickness has been reached, which might affect the cathode impedance.

The slope of the overcharge capacity vs. VC concentration (see blue line in Figure 8a) corresponds to ∼2.4 electrons per VC molecule. However, so far only a ≤1 electron per oxidized VC molecule has been proposed (see reactions 2a and 2b in Scheme 1).[17] We thus propose that the larger number of electrons per VC could arise from a further oxidation of the initially produced radical cation (see reaction 2a in Scheme 2), following its stabilization through the release of a proton (see reaction 2c, Scheme 2). The analogous formation of protons during the oxidation of EC/EMC electrolyte has been proposed by Metzger et al.,[21] based on the observation that H_2 is evolved on the

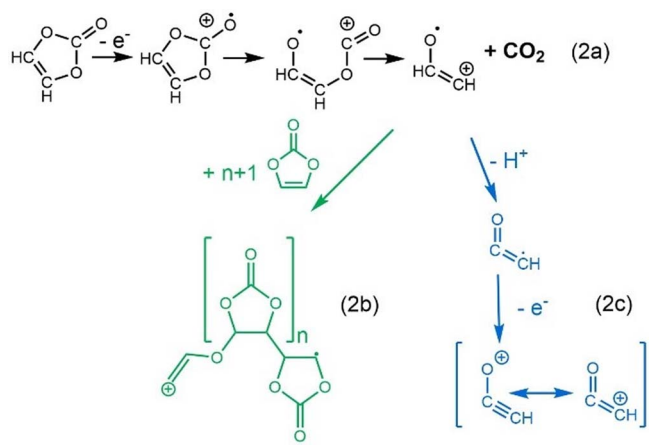

Scheme 2. Extension of the VC oxidation mechanism from Scheme 1 including proton abstraction and a second oxidation step.

anode during electrolyte oxidation, presumably due to the reduction of released protons. After the release of a proton, the intermediate could then be oxidized again, resulting in a mesomerically stabilized cation. Further, this end product of path 2c could again abstract a proton, which would lead to the formation of dicarbon monoxide, a very reactive gas. The so far unexplained 0.4 electrons per molecule VC could be explained by a crosstalk mechanism: oxidation products can diffuse to the anode, where they will be reduced and can then again be oxidized at the cathode, leading to an apparently higher number of electrons per VC. Besides, it is possible that also poly(VC) can be oxidized at high potentials, most likely leading to proton abstraction and additional crosslinking.

Dependence of the graphite anode impedance on the positive electrode (LNMO vs. LFP).—As a next step, we want to understand how the positive electrode affects the impedance of the graphite anode. Therefore, the data of this study is compared with our previous study,[13] where we have investigated the effect of different VC concentrations (0.17 wt% VC and 0.52 wt% VC) on the impedance in graphite/LFP cells. As the upper cutoff potential of the LFP cathode is ~4.1 V vs. Li/Li^+ (compared to ~4.9 V vs. Li/Li^+ for LNMO), the oxidative decomposition of VC does not occur in graphite/LFP cells, which is in accordance with the LFP cathode impedance being independent from VC concentration (see Figure 8 in Reference 13). To compare the anode impedance data of the graphite/LFP cells from our previous study[13] and the graphite/LNMO cells from the present work, we recalculate the VC concentrations used for both cell chemistries in units of $mg_{VC}/m^2_{Graphite}$.

Figure 9 shows graphite anode impedances (R_{Anode}) after the first formation cycle in graphite/LNMO cells (black symbols; data from Figure 3a) and those in graphite/LFP cells (red symbols) vs. the VC concentration in $mg_{VC}/m^2_{Graphite}$. As one would expect, the graphite anode impedances for cells with 0 wt% VC are very similar, with a value of ~7 Ωcm^2 for the graphite/LNMO cells and ~5 Ωcm^2 for the graphite/LFP cells. When VC is added to the graphite/LFP cells, the graphite anode impedances increases linearly with VC concentration (to ~16 and ~47 Ωcm^2 for 0.17 and 0.52 wt% VC, respectively), as described previously.[13] Interestingly, the increase of anode impedance between 0 wt% and 0.09 wt% VC in graphite/LNMO cells matches precisely to the linear slope of the graphite/LFP cells. However, at VC concentrations ≥0.17 wt%, a deviation from the linear trend is observed for graphite/LNMO cells (to ~10 and ~14 Ωcm^2 for 0.17 and 0.52 wt% VC, respectively), i.e., the graphite anode impedance at high VC concentrations is much lower for graphite/LNMO compared to graphite/LFP cells. This effect can be explained by considering the competing reactions at the respective cathode: In graphite/LFP cells, no VC is consumed by the cathode, and the only reaction to occur is the reductive polymerization of VC on the anode, whereas the oxidation of VC on the cathode competes with its reduction in graphite/LNMO cells. Hence, less VC is available for reduction, leading to a lower anode impedance at similar $mg_{VC}/m^2_{Graphite}$ amounts. At this point, we would like to mention that the formation of the graphite/LFP cells was carried out at 40°C, while the graphite/LNMO cells were formed at 25°C, which might also affect the resulting anode impedance (measured at 10°C in both cases); however, as the anode impedance for 0 wt% VC is identical for both cell chemistries, and the graphite/LNMO anode impedance with 0.09 wt% VC fits well to the linear relationship between VC concentration and anode impedance in graphite/LFP cells, we believe that the oxidation of VC at the cathode is the major cause for the observed differences between graphite/LNMO and graphite/LFP cells.

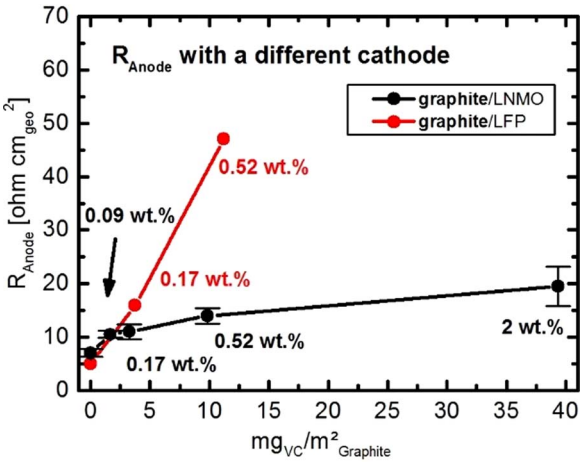

Figure 9. Interfacial resistance of graphite anodes after formation at 25°C in graphite/LNMO cells (this study) compared to graphite anodes in graphite/LFP cells from our earlier study.[13] The VC concentration is recalculated in units of $mg_{VC}/m^2_{Graphite}$ to assess for the slightly different areal loadings (namely ~2.6 mAh/cm^2_{geo} in the graphite/LNMO cells and ~2.2 mAh/cm^2_{geo} in the graphite/LFP cells, based on 340 $mAh/g_{graphite}$). The error bars represent the standard deviation between two measurements. All corresponding impedance spectra were recorded at 10°C from 100 kHz to 100 mHz.

Projected performance of graphite/LNMO commercial-scale cells.—The present study clearly proves that VC can enhance the cycling stability of graphite/LNMO cells, in contrast to previous reports. Yet, it also demonstrates that the concentration of VC in graphite/LNMO cells has to be carefully tuned, as the oxidation of only low amounts of VC can already lead to a deterioration of the capacity retention. The optimal VC concentration, corresponding to the amount of VC that can be reduced before the cathode reaches a potential >4.2 V vs. Li/Li^+, depends on the ratio of electrolyte to graphite surface area as well as the formation procedure (i.e., the time at potentials where VC reduction, but no oxidation can occur). In our case, the best performance in lab-scale cells is achieved with a concentration of 0.09 wt% VC, which corresponds to ~1 wt% VC in commercial-scale cells as used by Dahn's group (for details on this conversion please refer to Ref. 13). While Burns et al.[7] have shown that already 1 wt% VC leads to a significantly better capacity retention in commercial-scale graphite/LCO and graphite/NMC cells, the cycle life of commercial-scale graphite/NMC cells depends strongly on the amount of VC available.[10] Hence, 1 wt% VC by its own might not be sufficient to achieve an outstanding cycling performance with graphite/LNMO cells. Therefore, a combination of 1 wt% VC with other additives, which are either oxidatively stable or whose oxidation products are not detrimental to cell performance, and which can act as "repair additives" for the VC-derived SEI, would be a feasible combination for commercial-scale graphite/LNMO cells. To assure that diffusion of VC in a lab-scale cell is not the limiting factor when these type of cells are compared to commercial-scale cells we estimate the diffusion times for these two cell types: The diffusion time can be estimated as follows:

$$t = \frac{(x \cdot \tau)^2}{D} \quad [4]$$

where t is the characteristic diffusion time, x is the length of the diffusion path, τ is the tortuosity of the separator, and D is the diffusion coefficient. A typical value for the liquid diffusion is in the order of 10^{-6} cm^2/s (J. Landesfeind et al.[40]). In our lab test cells, two glass fiber separators have been used ($x \approx 2 \cdot 200\ \mu m$, $\tau \approx 1$), yielding a diffusion time on the order of:

$$t = \frac{(400\,\mu m)^2}{10^{-6}\,\frac{cm^2}{s}} = 1600\,s \quad [5]$$

In a commercial cell the distance between anode and cathode is ~25 μm with an average tortuosity of $\tau \approx 4$ (see, e.g., J. Landesfeind et al.[41]), yielding an approximate diffusion time constant of:

$$t = \frac{(25\,\mu m \cdot 4)^2}{10^{-6}\,\frac{cm^2}{s}} = 100\,s \quad [6]$$

As the oxidation of VC would only become possible after ≈34 minutes of charge, the rate of VC diffusion to the anode electrode is not limiting. During that initial time period, we believe that VC will be reduced preferentially at the anode, since its reduction potential is substantially higher than that of the EC and EMC solvents in LP57 (≈1.7 V vs. Li/Li^+ for VC compared to ≈0.9 V for LP57).[5]

Conclusions

In this study, we use a combined on-line electrochemical mass spectrometry (OEMS) and impedance analysis with a micro-reference electrode (GWRE), in order to i) understand the oxidative (in-)stability of the additive vinylene carbonate (VC), and, ii) to investigate the impact of the additive in graphite/$LiNi_{0.5}Mn_{1.5}O_4$ cells on the interfacial resistance of both anode and cathode. We have shown that the oxidation of VC occurs at an onset potential of ∼4.3 V vs. Li/Li^+ (by OEMS), which leads to a significant impedance buildup on the LNMO cathode in graphite/LNMO cells. This was shown by monitoring the graphite anode and the LNMO cathode impedance after formation and during extended charge discharge cycling using a micro-reference electrode.

Based on these data, we could conclude that VC oxidation on the cathode is competing with VC reduction on the anode. During the initial charge of graphite/LNMO cells, a charge of ∼8 mAh/g_{LNMO} can be passed before the LNMO cathode potential reaches 4.3 V vs. Li/Li^+ while the anode potential is already low enough to reduce VC to form an anode SEI. As a consequence, if the total amount of VC in the electrolyte is high enough to form a passivating anode SEI during this initial part of the first charge, but low enough so that all VC is being consumed during the initial anode SEI formation, the capacity retention of cells with a VC-containing electrolyte is superior compared to VC-free electrolyte. In our lab-scale cells, this corresponds to the lowest tested VC concentration of 0.09 wt%. Based on our previously discussed metrics for comparing additives in lab-scale vs. commercial-scale cells, this would translate into a ∼1 wt% VC concentration for commercial-scale cells.

Acknowledgment

Financial support by the BASF SE through its Network on Electrochemistry and Batteries is gratefully acknowledged. M. W. acknowledges funding by The German Federal Ministry for Economic Affairs and Energy (funding number 03ET6045D).

References

1. E. Peled, *J. Electrochem. Soc.*, **126**, 2047 (1979).
2. R. Imhof and P. Novák, *J. Electrochem. Soc.*, **145**, 3313 (1998).
3. M. Nie, D. Chalasani, D. P. Abraham, Y. Chen, A. Bose, and B. L. Lucht, *J. Phys. Chem. C*, **117**, 1257 (2013).
4. H. Ota, Y. Sakata, A. Inoue, and S. Yamaguchi, *J. Electrochem. Soc.*, **151**, A1659 (2004).
5. B. Zhang, M. Metzger, S. Solchenbach, M. Payne, S. Meini, H. A. Gasteiger, A. Garsuch, and B. L. Lucht, *J. Phys. Chem. C*, **119**, 11337 (2015).
6. M. Nie, J. Demeaux, B. T. Young, D. R. Heskett, Y. Chen, A. Bose, J. C. Woicik, and B. L. Lucht, *J. Electrochem. Soc.*, **162**, 7008 (2015).
7. J. C. Burns, N. N. Sinha, D. J. Coyle, G. Jain, C. M. VanElzen, W. M. Lamanna, A. Xiao, E. Scott, J. P. Gardner, and J. R. Dahn, *J. Electrochem. Soc.*, **159**, A85 (2012).
8. A. Würsig, H. Buqa, M. Holzapfel, F. Krumeich, and P. Novaǵk, *Electrochem. Solid-State Lett.*, **8**, A34 (2005).
9. L. El Ouatani, R. Dedryvère, C. Siret, P. Biensan, S. Reynaud, P. Iratçabal, and D. Gonbeau, *J. Electrochem. Soc.*, **156**, A103 (2009).
10. J. C. Burns, R. Petibon, K. J. Nelson, N. N. Sinha, A. Kassam, B. M. Way, and J. R. Dahn, *J. Electrochem. Soc.*, **160**, A1668 (2013).
11. R. Petibon, J. Xia, J. C. Burns, and J. R. Dahn, *J. Electrochem. Soc.*, **161**, A1618 (2014).
12. R. Petibon, J. Xia, L. Ma, M. K. G. Bauer, K. J. Nelson, and J. R. Dahn, *J. Electrochem. Soc.*, **163**, A2571 (2016).
13. S. Solchenbach, D. Pritzl, E. J. Y. Kong, J. Landesfeind, and H. A. Gasteiger, *J. Electrochem. Soc.*, **163**, A2265 (2016).
14. J. Hoffmann, M. Payne, and J. Li, *ECS Meet. 224, Abstr*, #1106 (2013).
15. H. Lee, S. Choi, H. Kim, Y. Choi, S. Yoon, and J.-J. Cho, *Electrochem. commun.*, **9**, 801 (2007).
16. Y.-M. Song, J.-G. Han, S. Park, K. Lee, and N.-S. Choi, *J. Mater. Chem. A*, **2**, 9506 (2014).
17. Y. Dong, J. Demeaux, and B. L. Lucht, *J. Electrochem. Soc.*, **163**, A2413 (2016).
18. R. Jung, M. Metzger, D. Haering, S. Solchenbach, C. Marino, N. Tsiouvaras, C. Stinner, and H. A. Gasteiger, *J. Electrochem. Soc.*, **163**, A1705 (2016).
19. E. Markevich, G. Salitra, K. Fridman, R. Sharabi, G. Gershinsky, A. Garsuch, G. Semrau, M. Schmidt, and D. Aurbach, *Langmuir*, **30**, 7414 (2014).
20. N. Tsiouvaras, S. Meini, I. Buchberger, and H. A. Gasteiger, *J. Electrochem. Soc.*, **160**, A471 (2013).
21. M. Metzger, B. Strehle, S. Solchenbach, and H. A. Gasteiger, *J. Electrochem. Soc.*, **163**, A798 (2016).
22. M. Metzger, C. Marino, J. Sicklinger, D. Haering, and H. A. Gasteiger, *J. Electrochem. Soc.*, **162**, A1123 (2015).
23. M. Klett, J. A. Gilbert, S. E. Trask, B. J. Polzin, A. N. Jansen, D. W. Dees, and D. P. Abraham, *J. Electrochem. Soc.*, **163**, A875 (2016).
24. R. Jung, M. Metzger, F. Maglia, C. Stinner, and H. A. Gasteiger, *J. Electrochem. Soc.*, **164**, A1361 (2017).
25. J. A. Seel and J. R. Dahn, *J. Electrochem. Soc.*, **147**, 892 (2000).
26. W. Märkle, N. Tran, D. Goers, M. E. Spahr, and P. Novák, *Carbon.*, **47**, 2727 (2009).
27. M. Metzger, J. Sicklinger, D. Haering, C. Kavakli, C. Stinner, C. Marino, and H. A. Gasteiger, *J. Electrochem. Soc.*, **162**, A1227 (2015).
28. M. Itagaki, N. Kobari, S. Yotsuda, K. Watanabe, S. Kinoshita, and M. Ue, *J. Power Sources*, **148**, 78 (2005).
29. X. Zhang, J. K. Pugh, and P. N. Ross, *J. Electrochem. Soc.*, **148**, E183 (2001).
30. O. Borodin, W. Behl, and T. R. Jow, *J. Phys. Chem. C*, **117**, 8661 (2013).
31. J. Self, C. P. Aiken, R. Petibon, and J. R. Dahn, *J. Electrochem. Soc.*, **162**, A796 (2015).
32. C. P. Aiken, J. Self, R. Petibon, X. Xia, J. M. Paulsen, and J. R. Dahn, *J. Electrochem. Soc.*, **162**, A760 (2015).
33. L. E. Downie, S. Hyatt, and J. R. Dahn, *J. Electrochem. Soc.*, **163**, A35 (2016).
34. L. Xing, W. Li, C. Wang, F. Gu, M. Xu, C. Tan, and J. Yi, *J. Phys. Chem. B*, **113**, 16596 (2009).
35. T. Li, L. Xing, W. Li, Y. Wang, M. Xu, F. Gu, and S. Hu, *J. Power Sources*, **244**, 668 (2013).
36. J. Landesfeind, D. Pritzl, and H. A. Gasteiger, *J. Electrochem. Soc.*, **164**, A1773 (2017).
37. D. H. Jang and S. M. Oh, *J. Electrochem. Soc.*, **144**, 3342 (1997).
38. D. Pritzl, A. Bumberger, M. Wetjen, S. Solchenbach, J. Landesfeind, and H. A. Gasteiger, *Manuscr. prep.*.
39. A. L. Michan, B. S. Parimalam, M. Leskes, R. N. Kerber, T. Yoon, C. P. Grey, and B. L. Lucht, *Chem. Mater.*, **28**, 8149 (2016).
40. B. Li, L. Xing, M. Xu, H. Lin, and W. Li, *Electrochem. commun.*, **34**, 48 (2013).
41. A. Ehrl, J. Landesfeind, W. A. Wall, and H. A. Gasteiger, *J. Electrochem. Soc.*, **164**, A826 (2017).

3.2 The effect of CO_2 in Li-ion batteries

As described in chapter 1.3, CO_2 is a long-known additive for Li-ion cells and has been investigated in combination with lithium metal, graphite and silicon anodes. Being produced by numerous electrolyte decomposition reactions, its evolution and consumption is omnipresent in Li-ion cells. In the first part of this section, the effect of CO_2 from lithium oxalate as a "sacrificial salt" on LNMO/graphite and LNMO/SiG cells is investigated (see chapter 3.2.1). Chapter 3.2.2 takes a closer look at the trans-esterification reaction that occurs during the reduction of ethylmethyl carbonate (EMC), and the suppression of this reaction by CO_2 and other additives. Lastly, the reduction products of CO_2 as well as VC and FEC on graphite electrodes are thoroughly studied by ATR-FTIR, XPS, NMR and OEMS in the study presented in chapter 3.2.3. To deconvolute between electrolyte and CO_2 reduction products, this study employed isotopically enriched $^{13}CO_2$.

3.2.1 Lithium oxalate as capacity and cycle-life enhancer in LNMO/graphite and LNMO/SiG full cells

The publication "Lithium oxalate as capacity and cycle-life enhancer in LNMO/graphite and LNMO/SiG full cells" was submitted in January 2018 to the *Journal of the Electrochemical Society* and published online in February 2018. The results of this study were presented by Sophie Solchenbach at the 232nd Meeting of the Electrochemical Society in National Harbor, Maryland in October 2017 (Abstract Number 393). The article was published "open access" under the Creative Commons Attribution 4.0 License (CC BY). A permanent link to this article can be found under: http://jes.ecsdl.org/content/165/3/A512.

The concept of "sacrificial salts" was originally investigated by Shanmukaraj et al.[176] as a method to compensate for SEI formation losses during the first cycle of a Li-ion battery: A lithium salt, integrated into the composite cathode, is oxidized during the first charge while the lithium cation is released into the electrolyte, effectively increasing the cathode's charge capacity. In the study presented here, lithium oxalate was incorporated as a sacrificial salt into LNMO cathodes, and its effect on LNMO/graphite and LNMO/silicon-graphite (SiG) full cells was examined. As expected, the first charge capacity of all cells increased according to the amount of lithium oxalate used. LNMO/graphite cells with lithium oxalate showed a slightly improved coulombic efficiency, which we attributed to the presence of CO_2 from lithium oxalate decomposition. In LNMO/SiG cells, this effect was even more pronounced; surprisingly, we also found an improved capacity retention for LNMO/SiG cells with lithium oxalate in electrolytes containing FEC, which is already an effective SEI former for silicon-based anodes. Post-mortem ^{19}F-NMR analysis of the electrolyte solution from LNMO/SiG cells with and without lithium oxalate revealed a reduced FEC consumption in cells with lithium oxalate, demonstrating that the combination of CO_2 and FEC delivers more capacity per mol of consumed additive than either of the two additives alone.

Author contributions

S. S. and K. U. S. investigated the effect of lithium oxalate particle size and established the ball-milling procedure. S. S., D. P. and M. W. prepared the electrodes. S. S. performed and evaluated the electrochemical testing and the OEMS measurements. S. S. and M. W. performed the ^{19}F-NMR analysis. S. S. and H. A. G. wrote the manuscript. All authors commented on the data and discussed the manuscript.

Lithium Oxalate as Capacity and Cycle-Life Enhancer in LNMO/Graphite and LNMO/SiG Full Cells

Sophie Solchenbach,*,z Morten Wetjen,* Daniel Pritzl,* K. Uta Schwenke, and Hubert A. Gasteiger**

Chair of Technical Electrochemistry, Department of Chemistry and Catalysis Research Center, Technical University of Munich, Garching, Germany

In the present study, we explore the use of lithium oxalate as a "sacrificial salt" in combination with lithium nickel manganese spinel (LNMO) cathodes. By online electrochemical mass spectrometry (OEMS), we demonstrate that the oxidation of lithium oxalate to CO_2 (corresponding to 525 mAh/g) occurs quantitatively around 4.7 V vs. Li/Li^+. LNMO/graphite cells containing 2.5 or 5 wt% lithium oxalate show an up to ∼11% higher initial discharge capacity and less capacity fade over 300 cycles (12% and 8% vs. 19%) compared to cells without lithium oxalate. In LNMO/SiG full-cells with an FEC-containing electrolyte solution, lithium oxalate leads to a better capacity retention (45% vs 20% after 250 cycles) and a higher coulombic efficiency throughout cycling (∼1%) compared to cells without lithium oxalate. When CO_2 from lithium oxalate oxidation is removed after formation, a similar capacity fading as in LNMO/SiG cells without lithium oxalate is observed. Hence, we attribute the improved cycling performance to the presence of CO_2 in the cells. Further analysis (e.g., FEC consumption by ^{19}F-NMR) indicate that CO_2 is an effective SEI-forming additive for SiG anodes, and that a combination of FEC and CO_2 has a synergistic effect on the lifetime of full-cells with SiG anodes.
 [DOI: 10.1149/2.0611803jes]

Manuscript submitted January 12, 2018; revised manuscript received February 14, 2018. Published February 22, 2018. This was Paper 393 presented at the National Harbor, Maryland Meeting of the Society, October 1–5, 2017.

Lithium nickel manganese spinel ($LiNi_{0.5}Mn_{1.5}O_4$, LNMO) is a promising cathode material for high energy lithium ion batteries due to its high operating potential around 4.7 V vs. Li/Li^+, its high rate capability, structural stability and the absence of cobalt. However, its lower specific capacity (146 mAh/g_{LNMO}) compared to layered oxide materials (e.g. lithium nickel manganese cobalt oxide (NMC), specific capacity 150–250 mAh/g_{NMC})[1] is regarded as a major drawback. In full-cells, the practically achievable capacity of LNMO is even lower, as the formation of the solid-electrolyte interphase (SEI) on the graphite anode consumes active lithium. For many layered oxide cathodes, however, the first cycle irreversible capacity of the cathode is similar to the capacity needed for SEI formation (∼20 mAh/g_{NMC}), and hence the practical discharge capacity of the cathode and the remaining active lithium are more or less balanced again.[2,3] In contrast, the first cycle irreversible capacity of LNMO (∼6 mAh/g_{LNMO}) is much lower than the capacity needed for SEI formation. This leads to a mismatch between active lithium and practical cathode capacity, i.e., there is not enough active lithium available to fully discharge the LNMO cathode during subsequent cycling.

In cells with silicon-based anodes, active lithium losses on the anode are even higher compared to graphite, as the expansion of the silicon particles during the first lithiation leads to a continuous exposure of fresh, unpassivated silicon surface.[4] On this new surface, electrolyte reduction occurs instantaneously, which reduces the total lithium reservoir in the cell. Therefore, different ideas to increase the amount of active lithium in lithium ion full-cells have been suggested, for example via prelithiation of silicon anodes with metallic lithium.[5–8] Recently, Gabrielli et al.[9] successfully used LNMO that had been chemically overlithiated to compensate for the initial lithium loss in LNMO/silicon-carbon full cells. Alternatively, Shanmukaraj et al.[10] proposed "sacrificial salts" as an additional source of lithium ions: A lithium salt is incorporated in the active material/carbon black matrix of the cathode. During the initial charge, the anion of the sacrificial salt is oxidized yielding mostly gaseous products, while the corresponding lithium cation is intercalated into the graphite anode; the gas can then be removed after formation. Lithium oxalate has a high specific charge capacity of 525 mAh/g (based on $Li_2C_2O_4 \rightarrow 2\,Li^+ + 2\,e^- + 2\,CO_2$), but was disregarded as a sacrificial salt for typical 4 V cell chemistries due to its high oxidation potential around 4.6–4.7 V vs. Li/Li^+.[10] However, this potential matches well with the charging plateau of LNMO. Additionally, lithium oxalate releases only CO_2 during oxidation, which is considered to improve the interfacial stability of graphite as well as of lithium metal anodes.[11–15] Strehle et al.[16] showed that the presence of CO_2 can suppress the formation of soluble lithium alkoxides and the follow-up electrolyte transesterification reactions. CO_2 can act further as a scavenger for detrimental trace water and protons.[17] Recently, Krause et al.[18] demonstrated that CO_2 is also an effective additive for silicon-based cells, increasing their capacity retention and coulombic efficiency.

In the present study, we use lithium oxalate as a capacity enhancer in LNMO/graphite and LNMO/silicon-graphite (SiG) full cells. First, we investigate the electrochemical oxidation of lithium oxalate and the resulting gas evolution by online electrochemical mass spectrometry (OEMS) in order to quantify its decomposition reaction and potential. As a next step, we test the addition of 2.5 or 5 wt% of lithium oxalate to LNMO composite electrodes in half cells, which increases the theoretical capacity of the initial charge by about 10% or 20%, respectively. To investigate the effect of the increased lithium inventory in full-cells, we cycle LNMO composite electrodes containing 0, 2.5, or 5 wt% lithium oxalate in full-cells against graphite anodes. We further test LNMO composite electrodes with 0 or 5 wt% lithium oxalate with silicon-graphite electrodes (SiG, 35 wt% silicon, 45 wt% graphite) in an electrolyte solution containing fluoroethylene carbonate (FEC). This additive is known to improve the cycling stability of silicon-based electrodes[19–25] and is commonly employed for cell chemistries containing silicon. As the LNMO/SiG cells with lithium oxalate showed less capacity fade and a higher coulombic efficiency throughout cycling than their counterparts without lithium oxalate, we investigate the effect of CO_2 on cycling performance and FEC consumption in LNMO/SiG cells. Lastly, we discuss the opportunities and challenges associated with the use of lithium oxalate as a sacrificial salt in LNMO/graphite and LNMO/SiG cells.

Experimental

Lithium oxalate/carbon black electrode preparation.—2 g Commercial lithium oxalate (99% purity, average particle size ∼40 µm, Alfa Aesar, United States) was ballmilled with zirconia balls (Ø 3 mm, 30 g) at 400 rpm for 1 h without solvent (dry), then for 1.5 h in 2 mL N-methyl pyrrolidone (NMP, anhydrous, Sigma-Aldrich, United States) until an average particle size of 0.2 µm was reached. The particle sizes before and after ballmilling were quantified by

*Electrochemical Society Student Member.
**Electrochemical Society Fellow.
zE-mail: sophie.solchenbach@tum.de

Table I. Electrode composition and properties of cathodes and anodes used for LNMO/Li half-cells and LNMO/graphite and LNMO/SiG full-cells. Theoretical capacities for LNMO, lithium oxalate (LO), graphite, and silicon were taken as 146 mAh/g_{LNMO}, 525 mAh/g_{LO}, 372 mAh/$g_{graphite}$, and 3579 mAh/g_{Si}. Practical 1st charge/discharge capacities for LNMO and graphite electrodes were determined at a C-rate of 0.1 h^{-1} in lithium half-cells, while the practical capacities for SiG electrodes were taken from Ref. 25. For simplicity, all cathode capacities are given per gram of LNMO, neglecting the weight of lithium oxalate. Mass loadings refer to LNMO for the cathode and graphite or graphite+silicon for the anode. Areal capacities are based on practical 1st charge/discharge capacities.

Electrode/cell properties	Units	LNMO	+ 2.5 wt% LO	+ 5 wt% LO	graphite	SiG
LNMO	wt%	90.0	87.80	85.72	–	–
Lithium oxalate	wt%	–	2.44	4.76	–	–
Graphite	wt%	–	–	–	95.0	45.0
Silicon	wt%	–	–	–	–	35.0
Carbon black (C65)	wt%	5.0	4.88	4.76	–	–
PVDF	wt%	5.0	4.88	4.76	5.0	–
Carbon fibers	wt%	–	–	–	–	9.0
LiPAA	wt%	–	–	–	–	11.0
Theoretical 1st charge capacity	mAh/g	146	161 (146 + 15)	175 (146 + 29)	372	1420
Practical 1st charge capacity	mAh/g	145	160	173	353	1466
Practical 1st discharge capacity	mAh/g	140	140	140	332	1265
LNMO / lithium half cells						
LNMO mass loading	mg/cm^2	10.8 ± 0.1	11.2 ± 0.1	13.1 ± 0.1	–	–
1st charge areal capacity	mAh/cm^2	1.6 ± 0.0	1.8 ± 0.0	2.3 ± 0.0	–	–
1st discharge areal capacity	mAh/cm^2	1.5 ± 0.0	1.6 ± 0.0	1.8 ± 0.0	–	–
LNMO / graphite full-cells						
LNMO / graphite mass loading	mg/cm^2	11.4 ± 0.4	11.1 ± 0.1	13.1 ± 0.1	6.8 ± 0.9	–
1st charge areal capacity	mAh/cm^2	1.7 ± 0.1	1.8 ± 0.0	2.3 ± 0.0	2.4 ± 0.3	–
1st discharge areal capacity	mAh/cm^2	1.6 ± 0.1	1.5 ± 0.0	1.8 ± 0.0	2.3 ± 0.3	–
LNMO / SiG full-cells						
LNMO / SiG mass loading	mg/cm^2	15.7 ± 1.8	11.3 ± 0.1	15.5 ± 1.7	–	1.9 ± 0.3
1st charge areal capacity	mAh/cm^2	2.3 ± 0.3	1.8 ± 0.0	2.7 ± 0.3	–	2.8 ± 0.4
1st discharge areal capacity	mAh/cm^2	2.2 ± 0.3	1.6 ± 0.0	2.2 ± 0.2	–	2.4 ± 0.4

dynamic light scattering (LA-950, Horiba, Japan) with NMP as dispersion media. To investigate the oxidation of lithium oxalate and the associated gas evolution, lithium oxalate/carbon black electrodes were prepared by mixing 200 mg ballmilled lithium oxalate with 200 mg Super C65 (Timcal, Imerys, Switzerland) and 3.2 g NMP, and dispersing the mixture with an ultrasonication horn. Polyvinylene difluoride (PVDF, Kynar HSV 900, Arkema, France) was dissolved in NMP at a weight ratio of 1:9, and then 490 mg of this PVDF solution was added to the lithium oxalate / carbon dispersion, followed by mixing in a planetary mixer (Thinky mixer, 2000 rpm, 5 min) to create a homogeneous ink. The resulting ink was coated onto Celgard trilayer separator foil (polypropylene (PP)-polyethylene (PE)-polypropylene (PP), C480, Celgard, United States) using a Mayer rod technique (100 μm wire thickness), and dried at 50°C for 6 hours. Afterwards, electrodes with a diameter of 15 mm were punched out, dried under dynamic vacuum at 95°C for at least 12 h, and then transferred into an argon-filled glove box (MBraun, Germany) without exposure to air. The final electrodes had a weight composition of 45:45:10 (lithium oxalate:carbon:PVDF) and a lithium oxalate loading of 0.4 mg/cm^2.

Lithium oxalate/LNMO electrode preparation.—Lithium manganese nickel spinel electrodes ($LiMn_{1.5}Ni_{0.5}O_4$, LNMO, 0.9 $m^2{}_{BET}$/g, BASF SE, Germany) with 2.5 or 5 wt% lithium oxalate were prepared by first dispersing C65 carbon and lithium oxalate (1:1 by weight) in NMP with an ultrasonication horn as described above. LNMO, PVDF and C65 were added to the dispersion according to the compositional ratios given in Table I. The compositions were chosen in order to keep a fixed weight ratio of LNMO:C65:PVDF of 90:5:5 in all electrodes once all lithium oxalate would be oxidized. NMP was added to yield a solid content of 40%, and the slurry was mixed in a planetary mixer (2000 rpm, 15 min). LNMO electrodes without lithium oxalate were prepared by combining LNMO, C65, and PVDF in ratios according to Table I (using the same mixing procedure). The slurries were then coated onto aluminum foil (15 μm, MTI, United states) using a gap bar (300 μm wet film thickness, ∼11–13 mg_{LNMO}/cm^2). To match the higher areal capacities of the SiG electrodes, additional LNMO coatings with 0 and 5 wt% lithium oxalate were prepared with a wet film thickness of 450 μm (∼14–16 mg_{LNMO}/cm^2). For OEMS measurements with LNMO or LNMO + 5 wt% lithium oxalate electrodes, the corresponding slurries were coated onto perforated aluminum foil (Microgrid Al 25, Dexmet, United States; ∼25 μm thickness). All LNMO coatings were dried at 50°C for 6 h in a convection oven. Electrodes with a diameter of 14 mm were punched out and compressed with 150 MPa, which resulted in electrode thicknesses ∼55 μm and ∼75 μm, respectively, and a porosity of 35%.

Graphite and silion-graphite (SiG) electrode preparation.—Graphite electrodes were prepared by mixing graphite (T311, BET surface area 5 m^2/g, SGL Carbon, Germany) and PVDF according to the ratio given in Table I with NMP in a planetary mixer (2000 rpm, 10 min). The ink (50% solid content) was coated onto copper foil (MTI, United States) using a 150 μm gap bar and dried at 50°C for 6 h in a convection oven. Silicon-graphite electrodes were prepared from silicon nanoparticles (∼200 nm, Wacker Chemie AG, Germany), graphite, vapor grown carbon fibers (VCGF-H, Showa Denko, Japan) and lithium poly(acrylate) (LiPAA, Sigma-Aldrich, Germany) by a ballmilling routine as described in Wetjen et al.[25] Graphite and SiG coatings were punched into 15 mm electrodes. The final loadings and compositions for all electrodes are given in Table I. Prior to cell assembly, all electrodes were dried under dynamic vacuum at 120°C for at least 12 h and then transferred into an argon-filled glove box (MBraun, Germany) without exposure to air.

Cell assembly and cycling.—2032 coin cells were assembled in an Ar-filled glove box (MBraun, H_2O, O_2 < 0.1 ppm) with LNMO (with or without lithium oxalate) as cathodes (Ø 14 mm) and either graphite or SiG electrodes as anodes (Ø 15 mm). Individual anodes and cathodes were paired in a such a way that the anode/cathode areal capacity balancing for all cells was ∼1.2–1.3 (based on their practical 1st discharge capacity, see Table I), in order to accommodate any excess

lithium from the lithium oxalate oxidation. The electrodes were separated by 2 glass fiber separators (Whatman, Ø 16 mm) and wetted with 80 μL LP57 electrolyte solution (30 wt% ethylene carbonate (EC), 70 wt% ethyl methyl carbonate (EMC), 1 M lithium hexafluorophosphate ($LiPF_6$), Selectilyte, BASF SE) or 80 μL LP57 + 5 wt% fluoroethylene carbonate (FEC, BASF SE). LNMO/graphite cells were cycled galvanostatically between 3.5–4.8 V at 1C (≈1.7 mA/cm^2) after 2 formation cycles at a rate of C/10. LNMO/SiG cells were cycled galvanostatically between 4.0–4.8 V at C/2 (≈1.1 mA/cm^2) after 3 formation cycles at a rate of C/10. The lower cutoff voltage of 4.0 V was chosen, as Si-based cells have shown better cycling stability when high anode potentials were omitted.[21] Note that due to the lower potential of silicon during its first lithiation, the upper cutoff voltage was set to 4.9 V in the first cycle of the LNMO/SiG cells. For both cell chemistries, a constant voltage (CV) step was performed with a current limit of C/20 after each galvanostatic charging step. All cells were cycled with a battery cycler (Series 4000, Maccor, USA, coulombic efficiency accuracy ∼300 ppm[26]) in a climate chamber (Binder, Germany) at 25°C. Specific capacities and coulombic efficiencies are given as the average of two duplicate cells, whereas error bars represent the deviation of these cells from the average. Note that the Maccor coulombic efficiency accuracy is not included in the error bars, because the focus of this study lies on comparing different cell configurations and not on an exact estimate of the cells' lifetime.

On-line electrochemical mass spectrometry (OEMS).—The cell design of the on-line electrochemical mass spectrometry (OEMS) system has been described in previous publications.[27] To study the oxidation of lithium oxalate, a lithium oxalate / carbon black electrode was charged galvanostatically vs. a lithium metal counter electrode (Ø 17 mm, 450 μm thickness, Rockwood Lithium, United States) with a nominal rate of C/10 (≈0.02 mA/cm^2, based on the theoretical capacity of 525 mAh/g for lithium oxalate). To avoid reactions of CO_2 with the lithium anode, a sealed 2-compartment setup[28] where the cathode and anode compartment are separated by an aluminum-sealed lithium-ion conductive glass ceramics (LICGC, Ohara Corp., Japan) was used, with a glass fiber separator soaked with 250 μL LP57 in the lithium anode compartment, and a Celgard trilayer separator (H2013) soaked with 80 μL LP57 in the lithium oxalate/carbon black cathode compartment, respectively.

OEMS measurements on LNMO/SiG full-cells were performed in 1-compartment OEMS cells (i.e., without barrier between anode and cathode compartment) using LNMO electrodes (∼11.4 mg$_{LNMO}$/cm^2) without or with 5 wt% lithium oxalate coated onto perforated aluminum foil as cathodes in combination with SiG anodes, and using 150 μL of electrolyte solution (LP57 pure or with 5 wt% FEC) and two Celgard separators (H2013, Ø 28 mm). To eliminate the effect of the SiG electrode, we also performed an OEMS measurement using the same cathode, separator and electrolyte solution, but a Ø 15 mm delithiated $LiFePO_4$ electrode (LFP, 3.5 mAh/cm^2, Custom Cells, Itzehoe) as anode. Prior to the OEMS measurement, the LFP electrode was cycled once at a rate of C/10 vs. a lithium metal electrode between 2 V and 4 V, and then electrochemically delithiated to a lithium content of 0.15 by a galvanostatic charge at C/10 with a capacity cutoff at 3 mAh/cm^2. The cell was then disassembled inside an Ar-filled glove box and the LFP electrode directly transferred to the OEMS cell. All OEMS experiments were performed in a climate chamber (Binder, Germany) at 25°C.

FEC quantification by NMR.—The consumption of fluoroethylene carbonate (FEC) during cycling of LNMO/SiG cells with and without lithium oxalate was investigated by ^{19}F-NMR of the recovered electrolyte solutions from full-cells. To this purpose, LNMO/SiG full-cells with or without lithium oxalate and LP57 + 5 wt% FEC were cycled as described above, and carefully disassembled after 50 cycles or 250 cycles. One of the glass fiber separators was removed and immersed into 700 μL deuterated dimethyl sulfoxide (DMSO-d6, anhydrous, Sigma-Aldrich, USA). The solutions were then filled into air-tight NMR tubes and ^{19}F-NMR spectra were measured on a Bruker Ascend 400 (400 MHz). As the obtained ^{19}F-NMR spectra show only peaks that can either be ascribed to PF_6^- or FEC, and assuming that changes in the PF_6^- concentration in the electrolyte solution during cycling are negligible, the PF_6^- anion can be used as an internal standard.[22] The amount of FEC remaining in the electrolyte solution can thus be determined by the ratio of PF_6^- and FEC peak integrals. A more detailed description of this method can be found in a recent publication by Jung et al.[22]

Results

Electrochemical characterization of lithium oxalate/carbon and lithium oxalate/LNMO electrodes.—To investigate the electrochemical oxidation of lithium oxalate within the potential window of an LNMO cathode, we first tried to understand the electrochemical oxidation of lithium oxalate by itself, i.e., in the absence of any active material. Therefore, we fabricated model electrodes that contain only lithium oxalate in a conductive carbon matrix, similar to the ones used by Meini et al.,[29,30] who studied the anodic decomposition of lithium salts (Li_2O_2, Li_2CO_3, LiOH, and Li_2O). Figure 1a shows the potential during the galvanostatic charge of an electrode consisting of 45 wt% sub-micron lithium oxalate, 45 wt% carbon black and 10 wt% binder, with a nominal rate of C/10 (based on its theoretical decomposition capacity of 525 mAh/g$_{LO}$; see reaction 1 below). The potential profile shows a flat plateau around 4.7 V vs. Li/Li$^+$ until ∼90% of the

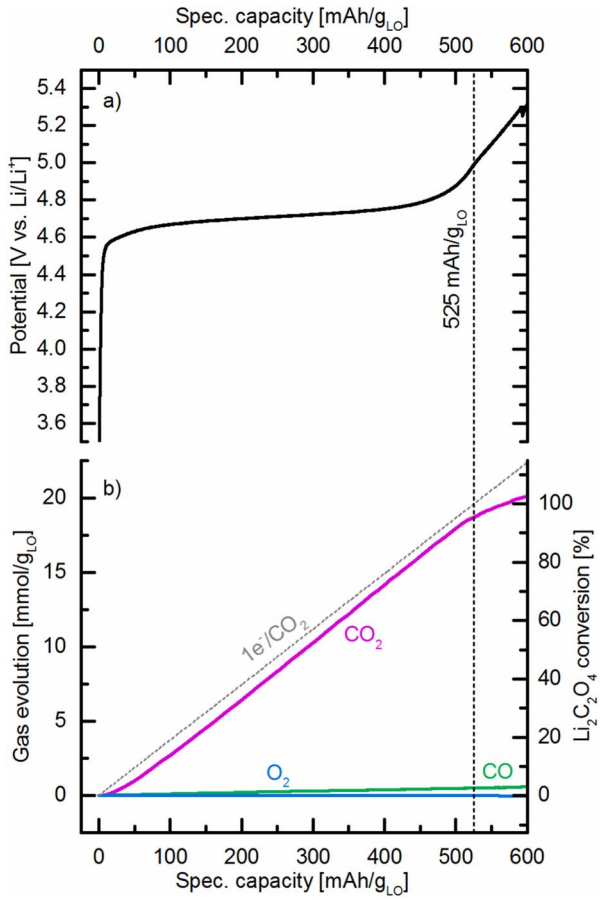

Figure 1. a) Potential vs. specific capacity during the oxidation of a lithium oxalate/carbon electrode with a nominal rate of C/10 in LP57 (EC:EMC 3:7 by weight, 1 M $LiPF_6$) at 25°C. The black dashed vertical line corresponds to the theoretical specific oxidation capacity of lithium oxalate (525 mAh/g$_{LO}$; see reaction 1). b) Gas evolution during the electrochemical oxidation of lithium oxalate either normalized to the mass of lithium oxalate (left y-axis) or referenced to the theoretical amount predicted by reaction 1 (right y-axis). The gray dashed line marks the theoretically expected 1e$^-$/CO_2 slope.

theoretical capacity (~470 mAh/g_{LO}) is reached, from which point on the potential rises continuously. The concomitant gas evolution, as measured by on-line electrochemical mass spectrometry (OEMS) during this first charge, is shown Figure 1b. Here it is important to note that this experiment was conducted in a sealed 2-compartment cell,[28] so that there are no contributions to the measured gas evolution from the lithium metal counter electrode nor any consumption of the gas evolved at the working electrode by the lithium metal electrode. During charge, a linear increase of the CO_2 (m/z = 44) concentration in the cell headspace is observed (pink line in Figure 1b), indicating a constant gas evolution of CO_2. Carbon monoxide (m/z = 28, green line) and particularly oxygen (m/z = 32, blue line) are only detected in negligible trace amounts throughout the entire measurement. The slope of the CO_2 evolution vs. charge during the bulk oxidation of lithium oxalate is close to the 1 e^-/CO_2 line (gray dashed line in Figure 1b), suggesting a 1-electron process. As the CO_2 evolution from electrolyte oxidation is negligible at potentials ≤ 5 V vs. Li/Li^+ on a carbon black electrode at room temperature,[31] we can attribute the CO_2 evolution entirely to the oxidation of lithium oxalate. Once the theoretical charging capacity of $Li_2C_2O_4$ has been reached (black dashed line in Figure 1), the CO_2 evolution slows down. This indicates that lithium oxalate is quantitatively oxidized around 4.7 V vs. Li/Li^+ according to reaction 1:[32]

$$Li_2C_2O_4 \rightarrow 2Li^+ + 2e^- + 2CO_2 \quad [1]$$

The slight deviation downwards from the 1 e^-/CO_2 line can be explained by two effects: i) the lithium oxalate used here contains about 1% Li_2CO_3 as impurity, whose oxidation also gives CO_2, but in a ≥ 2 e^-/CO_2 process;[29] and ii) about 2.5% of the total CO_2 remain dissolved in the electrolyte solution and are thus not detectable by OEMS (for details see Discussion section of this paper).

The oxidation potential of 4.7 V vs. Li/Li^+ for lithium oxalate lies well within the plateaus of the Ni^{2+}/Ni^{3+} and Ni^{3+}/Ni^{4+} redox couple of high-voltage lithium nickel manganese spinel ($LiNi_{0.5}Mn_{1.5}O_4$, LNMO) at 4.7 V and 4.75 V vs. Li/Li^+, respectively.[33] In the following, we explore the use of lithium oxalate as a sacrificial salt in combination with LNMO cathodes. Figure 2a shows the first charge/discharge profile of a LNMO cathode vs. Li at C/10 with 0 wt% (black line), 2.5 wt% (purple line) or 5 wt% lithium oxalate (pink line) added to the cathode slurry during electrode fabrication. The ratios of LNMO to binder and conductive carbon were kept constant in all electrode compositions (see Table I). During charge, the LNMO cathode without lithium oxalate (black lines in Figure 2a) can be delithiated to a capacity of 145 mAh/g_{LNMO}, which is essentially identical with the theoretical capacity of 146 mAh/g_{LNMO} (black dashed line in Figure 2). LNMO cathodes with 2.5 wt% lithium oxalate (purple lines in Figure 2a) deliver ~160 mAh/g_{LNMO} charge capacity, which also comes close to the theoretically expected 161 mAh/g_{LNMO} for these electrodes based on the combined capacity of LNMO and lithium oxalate (see Table I and purple dashed line in Figure 2). Accordingly, the charge capacity of the cathode with 5% lithium oxalate (pink lines in Figure 2) is about 173 mAh/g_{LNMO} (theoretical capacity: 175 mAh/g_{LNMO}, see pink dashed line). Note that all capacities are given per gram of LNMO, neglecting the weight of the lithium oxalate, as the latter is virtually completely oxidized to CO_2 and Li^+-ions during the first charge. Considering the potential profiles, one can see that the transition between the Ni^{2+}/Ni^{3+} and the Ni^{3+}/Ni^{4+} plateaus is gradually shifted toward higher specific capacities with increasing lithium oxalate content. This indicates that a large fraction (but not all) of the lithium oxalate is already oxidized during the Ni^{2+}/Ni^{3+} plateau. The subsequent discharge is equally long for all three electrode compositions, i.e., amounting to the same first discharge capacity of 140 mAh/g_{LNMO} (see Table I). Furthermore, the charge/discharge capacities as well as the potential profiles of the second cycle at C/10 are identical for the three different compositions (see Figure 2b). Theoretically, the oxidation of all lithium oxalate will increase the LNMO electrode porosity from ~35% to ~38% or ~40% for electrodes containing 2.5 wt% or 5 wt% lithium oxalate, respectively. However, based on the capacities and potential profiles

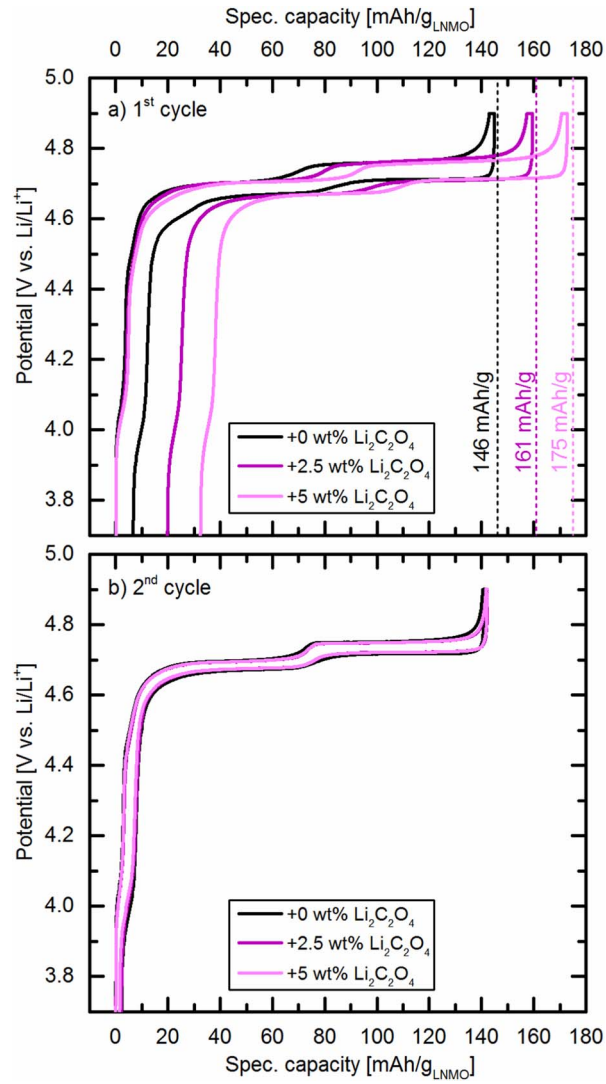

Figure 2. a) First charge/discharge and b) second charge/discharge of LNMO electrodes with 0 wt% (black line), 2.5 wt% (purple line) and 5 wt% (pink line) lithium oxalate in the composite cathode vs. Li metal in LP57 at a rate of C/10 between 3.5-4.9 V at 25°C. The dashed lines mark the respective theoretical first charge capacities listed in Table I. For LNMO loadings, see Table I.

obtained during the second cycle (see Figure 2b), we can conclude that the effect of this porosity change is only minor, and the oxidation of lithium oxalate within the cathode has not altered the subsequent electrochemical behavior.

The effect of lithium oxalate in LNMO/graphite full cells.—In the above shown LNMO/Li half-cells, the anode consisted of a massive lithium reservoir, meaning that at least with regards to the availability of active lithium, the LNMO cathode could be fully relithiated in all cases. However, in full-cells with a graphite anode, the amount of active lithium in the cell is limited, and the relithiation capacity of the cathode depends on the amount of lithium still available, i.e., lithium that has not been consumed for SEI formation. Therefore, we expect higher discharge capacities for cathode compositions that have shown higher capacities in their first charge in LNMO/graphite cells, i.e., for those cells which have a higher lithium oxalate content in the cathode. Figure 3a shows the discharge capacities (closed symbols) and 1st cycle charge capacities (open symbols) for LNMO/graphite full-cells with different lithium oxalate contents (0, 2.5, and 5 wt%) in the LNMO cathode for two formation cycles at C/10 and further cycling at 1C (all at 25°C). The areal capacity of the graphite anodes was kept

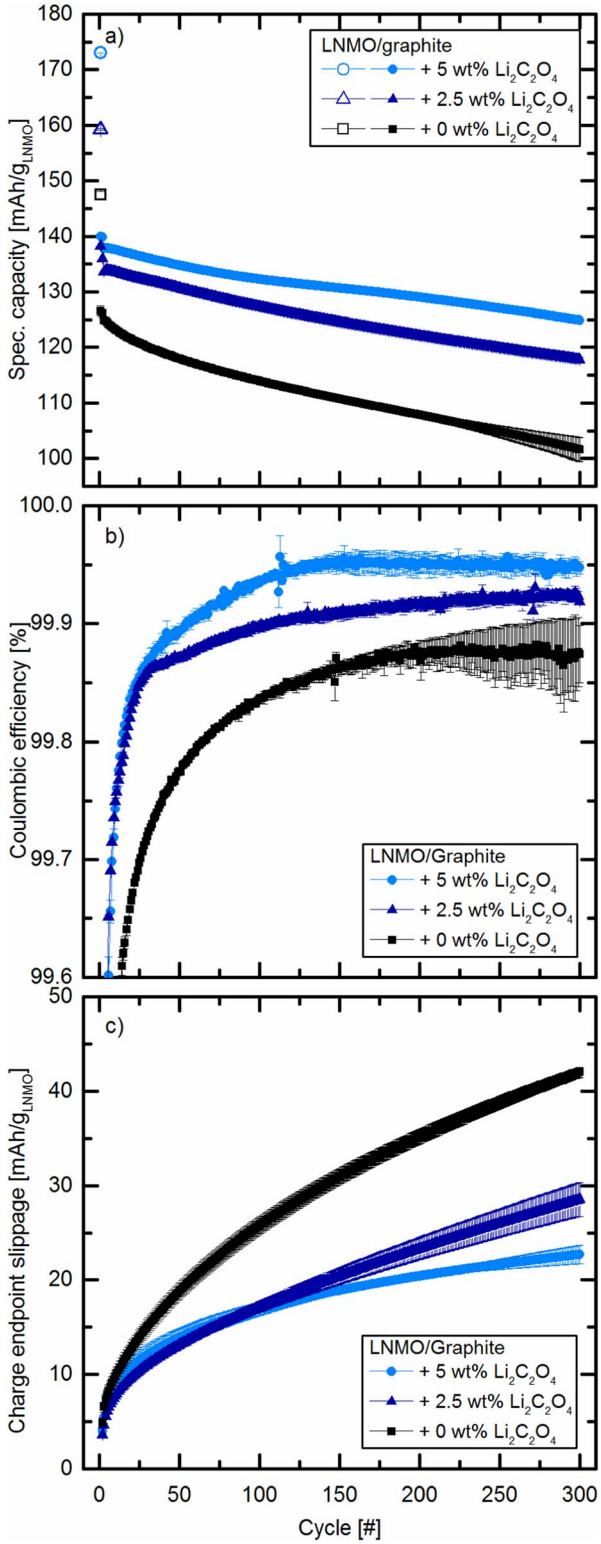

Figure 3. a) Specific discharge (closed symbols) and 1st cycle specific charge (open symbols) capacities, b) coulombic efficiencies and c) charge end point slippage of LNMO/graphite cells with 0 wt% (black squares), 2.5 wt% (dark blue triangles) and 5 wt% (light blue circles) lithium oxalate in the cathode composite during cycling in LP57 at 1C between 3.5-4.8 V and 25°C. The first two cycles were performed at C/10. All symbols represent the average of two replicate cells, whereas error bars represent the deviation between the replicates. The LNMO and graphite loadings are given in Table I.

constant in order to have a comparable first cycle irreversible capacity for all cells. Similar to the LNMO/Li half cells, the first charge capacity is 146 mAh/g_{LNMO}, 159 mAh/g_{LNMO}, and 173 mAh/g_{LNMO} for cells with 0, 2.5, and 5 wt% lithium oxalate in the cathode (closed symbols in Figure 3a). The discharge capacity is now however different for the three compositions: while the cells without lithium oxalate reach a first cycle discharge capacity of 125 mAh/g_{LNMO}, the cells with 2.5 wt% lithium oxalate have a first cycle discharge capacity of 138 mAh/g_{LNMO}, which means that the first irreversible capacity of these different cells is in both cases ~21 mAh/g_{LNMO}. The cells with 5 wt% lithium oxalate have a first cycle discharge capacity of around 139 mAh/g_{LNMO}. Assuming a similar irreversible capacity as for the cells with 0 wt% and 2.5 wt% lithium oxalate, one would expect a discharge capacity of around 152 mAh/ g_{LNMO}; however, this is above the practical reversible capacity of LNMO of 140 mAh/g (as shown in Figure 2). The additional lithium (corresponding to ~12 mAh/g_{LNMO}) thus remains as a reservoir in the graphite anode.

During the subsequent cycles at 1C, the difference in discharge capacity between the three different cathode compositions is retained up to 300 cycles. Interestingly, the cells with lithium oxalate also show better capacity retention: While cells without lithium oxalate drop about 19% in capacity between cycle 3 (i.e., the first cycle at 1C) and cycle 300, the cells with 2.5 and 5 wt% lithium oxalate lose only about 12% and 8% capacity, respectively. These cells also show an improved average coulombic efficiency between cycles 3–300 of 99.88% (2.5 wt% lithium oxalate) and 99.92% (5 wt% lithium oxalate), compared to 99.81% for cells without lithium oxalate (see Figure 3b). This phenomenon could be explained by i) the additional lithium reservoir and its effect on the graphite potential at the end of discharge, and/or, ii) by the effect of CO_2 as an SEI-forming additive. In the cells with 5 wt% lithium oxalate, some lithium remains in the graphite after formation. Hu et al.[34] have shown that LNMO/graphite cells show an improved cycling behavior as long as the cells contain an excess of active lithium (added in their case as metallic lithium or by ex-situ pre-lithiation of the graphite anode). However, the amount of additional lithium in our case is much lower compared to Hu et al.[34] (~10% vs. ~100% of the initial LNMO capacity) and should therefore only affect the very first cycles (i.e., until the additional capacity of ~12 mAh/g has been consumed). Still, if lithium is remaining in the graphite anode at the end of a discharge, the maximum graphite potential is lower compared to cells with less or without lithium oxalate. It has been shown that enhanced gas evolution related to SEI damage can occur when graphite is polarized to high potentials (>1.2 V vs. Li/Li^+).[35] Although a precise determination of the anode potential without a reference electrode is hardly possible, we can use following approximation: If we assume a maximum potential of 4.7 V vs. Li/Li^+ for LNMO at the end of discharge and consider that the difference between cathode and anode potential has to be at least 3.5 V (which is our lower cutoff penalty), the graphite potential is limited to a maximum of 1.2 V vs. Li/Li^+; hence, SEI damage should be avoided. Furthermore, the observed improvements in cycling stability of cells with 2.5 wt% lithium oxalate cannot be explained by different maximum potentials for graphite, as in this case, no lithium is remaining in the graphite and the upper cutoff potential during graphite delithiation should be very similar to cells without lithium oxalate.

Consequently, this brings us back to the effect of CO_2 as an SEI additive. In general, SEI instability and the consequent active lithium loss is regarded as a major fading mechanism in LNMO/graphite cells.[34–36] Pritzl et al.[37] recently showed that the cycling stability of LNMO/graphite cells can be improved by very small amounts of VC, an effective SEI former; however, if the amount of VC gets too large, the competitive oxidation of VC on LNMO counteracts its beneficial effect on the anode.[37,38] CO_2 has long been known to improve SEI properties on both lithium metal[14,15] and graphite.[12,13,39] Xiong et al. found that almost all CO_2 generated on the cathode can be consumed on the graphite anode in commercial-scale NMC422/graphite full-cells, given that no other strong SEI-forming additives are present.[40] Krause et al. showed that CO_2 can have a similar effect on the cycling stability of graphite electrodes in EC-free electrolyte solutions as

VC.[18] Recently, our group demonstrated that CO_2 can stop the transesterification reactions occurring from alkoxides generated through the reduction of linear carbonates.[16] Furthermore, the CO_2^- radical from the reduction of CO_2 on graphite can act as an H_2O/H^+ scavenger, yielding lithium formate and lithium carbonate as SEI products.[17] As protons are a possible product of electrolyte oxidation,[28] this effect would be especially relevant for high-voltage lithium ion cell chemistries like the LNMO/graphite system.

Sloop et al.[41] suggested that the reduction of CO_2 could lead to lithium oxalate formation at the anode, which could dissolve and be re-oxidized at the cathode, generating a shuttling current followed by self-discharge. To assess whether the presence of CO_2 indeed leads to enhanced side reactions, we calculated the charge end point slippage (the cumulative irreversible charge capacity, i.e., the charge capacity of each cycle subtracted by the previous discharge, summed up over all cycles), which is an indicator for oxidative or shuttling side reactions.[42] The charge end point slippage for LNMO/graphite cells with 0, 2.5, or 5 wt% lithium oxalate is shown in Figure 3c. As a CO_2/oxalate shuttle mechanism would contribute to the charge capacity but not the discharge capacity, cells with lithium oxalate should show a higher charge end point slippage compared to cells which do not contain lithium oxalate or CO_2. However, it becomes clear from Figure 3c that the charge end point slippage for cells with lithium oxalate is lower compared to cells without lithium oxalate. Hence, under the present conditions, the CO_2/oxalate shuttle effect is either negligible or nonexistent and does not contribute to the side reactions in the cell. This is in agreement with Xiong et al.,[40,43] who showed that there is no re-generation of CO_2 from a lithium oxalate/CO_2 shuttle detectable in NMC422/graphite cells.

The effect of lithium oxalate in LNMO/SiG full cells.—The use of a sacrificial salt to compensate for SEI losses is even more relevant if LNMO cathodes are combined with silicon or silicon/graphite anodes, which typically have much higher SEI losses due to i) the high specific surface area of the nanometer-sized silicon particles, and, ii) the expansion of the silicon particles during their lithiation, creating fresh surface area in every cycle that triggers further SEI growth. Hence, we investigate the use of lithium oxalate as capacity enhancer in combination with silicon/graphite (SiG) electrodes containing 35 wt% nano-Si and 45 wt% graphite. These electrodes, which have been investigated in more detail in a previous study by our group,[25] show a typical first cycle coulombic efficiency of ∼85%. Therefore, we combine them with LNMO cathodes containing 5 wt% lithium oxalate, as the amount of lithium oxalate in these electrodes should largely compensate the irreversible loss during the first cycle. As electrolyte solution, we use LP57 + 5 wt% fluoroethylene carbonate (FEC), as this additive is known to improve the capacity retention of silicon-based electrodes.[19–25] The capacity retention and the coulombic efficiency of the LNMO/SiG cells with 5 wt% (green symbols) and without lithium oxalate (black symbols) in the cathode are shown in Figures 4a and 4b, respectively. The first charge capacities are 145 mAh/g_{LNMO} for cells without lithium oxalate and 173 mAh/g_{LNMO} for cells with 5 wt% lithium oxalate (open symbols), similar to the corresponding cells with graphite anodes. The first discharge capacities of 128 mAh/g_{LNMO} for cells with 5 wt% lithium oxalate and 109 mAh/g_{LNMO} without lithium oxalate are however lower compared to the corresponding LNMO/graphite cells. This was expected due to the higher irreversible capacity of the SiG anodes. It is to note that the first cycle irreversible capacity of cells with 5% lithium oxalate is slightly higher compared to the cells without lithium oxalate (45 mAh/g_{LNMO} vs. 36 mAh/g_{LNMO}); this effect can be explained as the 20% larger charge capacity results in a ∼17% higher degree of lithiation (considering the balancing factor of ∼1.3) The stronger expansion of the silicon particles creates more fresh surface and requires a higher irreversible capacity to passivate the selfsame.

During cycling, all SiG-based cells show a much stronger capacity fade compared to the LNMO/graphite cells (Figure 3). Yet, also for the LNMO/SiG system, the cells with lithium oxalate show a more stable cycling behavior and a higher coulombic efficiency compared to their

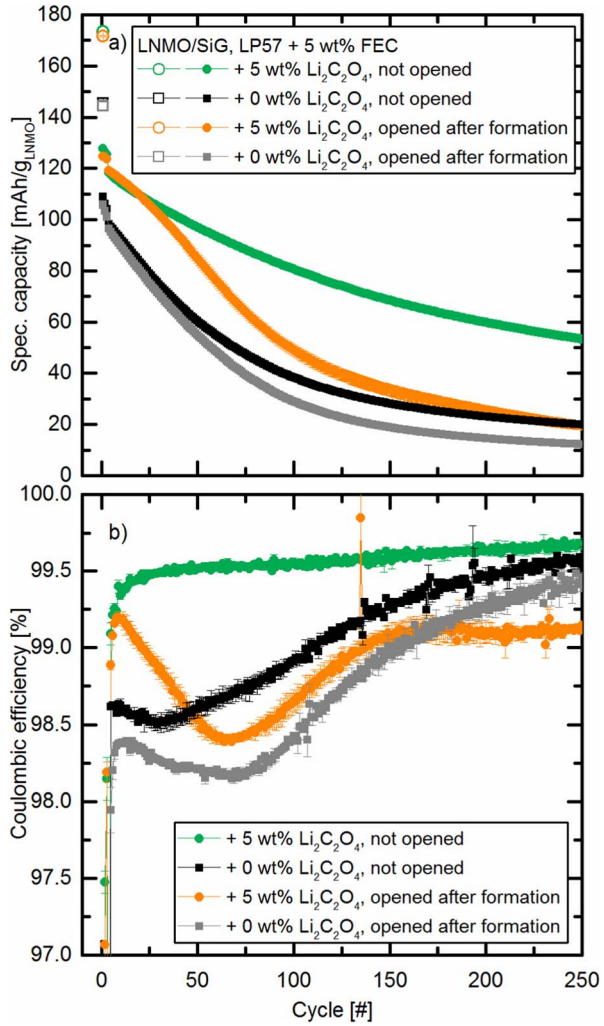

Figure 4. a) Specific discharge (closed symbols) and 1st cycle charge (open symbols) capacities and b) coulombic efficiencies of LNMO/SiG cells with 0 wt% (black and gray squares) or 5 wt% (green and orange circles) lithium oxalate in the cathode matrix during cycling in LP57 + 5 wt% FEC at C/2 and 25°C between 4.0–4.8 V. The first three cycles were performed at C/10. Cells represented by black and green symbols ("not opened") were then cycled at C/2. Cells represented by gray and orange symbols ("opened after formation") were reopened after the third cycle inside an Ar-filled glove box and both electrodes of each cell were transferred to a new cell with fresh separators and electrolyte solution. Cycling was then continued at C/2. All symbols represent the average of two replicate cells, whereas error bars represent the deviation between the replicates. The LNMO and SiG loadings are given in Table I.

counterparts without lithium oxalate. While this difference was rather small in the LNMO/graphite cells, in the case of the LNMO/SiG cells, the average coulombic efficiency is almost 1% point higher during the first 50 cycles for cells containing 5 wt% lithium oxalate (black vs. green symbols in Figure 4b). At the same time, the capacity retention after 250 cycles is ∼45% for cells with 5 wt% lithium oxalate and only ∼20% for cells without lithium oxalate (referenced to the discharge capacity of cycle 4, i.e., the first cycle at C/2). Again, this effect could be attributed to either the additional lithium, or the CO_2 present in the cell. Markevich et al.[21] reported that the cycling stability of silicon is improved if complete delithiation is omitted; and similar to LNMO/graphite cells, LNMO/Si cells show a stable cycling performance if a sufficiently large lithium reservoir is available.[44] However, in both cell types used here (i.e., LNMO/SiG with and without lithium oxalate), the discharge capacity is always at least 20 mAh/g_{LNMO} lower than the maximum relithiation capacity of the LNMO cathode, which means that the potential of the LNMO cathode

is still around ∼4.7 V when the cells reaches the lower cutoff voltage (compare the half-cell potentials from Figure 2). As the lower cell cutoff is limited to 4.0 V, this corresponds to a maximum voltage of ∼0.7 V at the anode for both cells, where structural damage due to complete delithiation is unlikely.

In the LNMO/graphite cells, we have attributed the clearly improved cycling performance of cells with lithium oxalate to the effect of CO_2 as an SEI-forming additive. In contrast, in the LNMO/SiG cells there is already an SEI-forming additive (namely FEC), yet the differences between cells with and without lithium oxalate are much more pronounced for SiG anodes. In order to understand whether the additional lithium or CO_2 leads to the improved capacity retention, we repeated the cycling experiments with SiG anodes and LNMO cathodes containing either 0 or 5 wt% of lithium oxalate. This time, however, we stopped the cells after formation (i.e., after the initial 3 cycles at C/10) in the discharged state and disassembled them inside an Ar-filled glove box. The electrodes were then reassembled in new coin cells with fresh electrolyte solution and separators. In this way, all CO_2 was removed from the void space in the cell body and from the electrolyte solution, while the amount of active lithium was not altered. The gray and orange symbols in Figure 4 show the capacity retention and coulombic efficiency of these reassembled cells. The capacities of the first three cycles of both cell types look identical to Figure 4, as expected. After reassembly, the performance of the cells without lithium oxalate (gray symbols in Figure 4a) is slightly worse than the same cells which had not been opened (black symbols in Figure 4a), which can be attributed to a partial re-dissolution of the SEI in the fresh electrolyte solution. The minor differences however indicate that the reassembly procedure did not alter the cell performance substantially. The cells with lithium oxalate (orange symbols in Figure 4a) show the same discharge capacity directly after reassembly as before the reopening procedure, which also indicates that they were not damaged during the reassembly. However, from cycle 20 onwards, these cells show a much stronger capacity decrease compared to the cells with lithium oxalate that had not been opened (green symbols in Figure 4a). From cycle 10 on (i.e., almost directly after the reassembly), the coulombic efficiency of the reassembled cells with lithium oxalate (orange symbols in Figure 4b) starts to decline, while it is continuously rising in the cells with lithium oxalate that have not been opened (green symbols in Figure 4b). Around cycle 50, the coulombic efficiency of the reassembled cells with lithium oxalate (orange symbols) has reached the level of the cells without lithium oxalate (black and gray symbols). Apparently, the removal of CO_2 leads to an increase in irreversible reactions, which lowers the coulombic efficiency and depletes the active lithium, ultimately causing a drop in capacity.

FEC consumption in LNMO/SiG full cells with and without lithium oxalate.—To understand to which extent CO_2 participates in SEI formation when FEC is present, we conducted a post-mortem analysis of the electrolyte solution of aged LNMO/SiG cells without lithium oxalate and with 5 wt% lithium oxalate after 50 and 250 cycles, quantifying the amount of residual FEC by ^{19}F-NMR (for more details see Jung et al.[22]). The upper x-axis of Figure 5 shows the amount of residual FEC found in the electrolyte solution. As more remaining FEC is found in the cells with lithium oxalate (green symbols) compared to their counterparts without lithium oxalate that underwent the same number of cycles (black symbols), it is apparent that the FEC consumption per cycle for cells containing both FEC and lithium oxalate is lower. Previous studies have shown that the amount of consumed FEC correlates linearly with the cumulative irreversible discharge capacity (i.e., the sum of the differences between discharge and charge capacity over a certain amount of cycles),[22] which has recently also been demonstrated for SiG anodes with identical composition.[25] Therefore, the cumulative irreversible discharge capacity for each of the analyzed cells is shown on the y-axis of Figure 5, while the amount of consumed FEC in μmol is shown on the lower x-axis. The dashed lines show different e^-/FEC ratios, among them the empirically found 4 e^-/FEC (= 0.107 mAh_{irr}/μmol) relationship

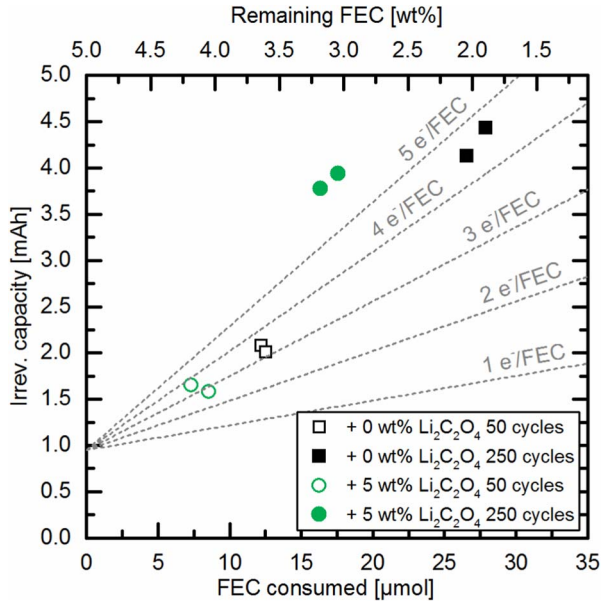

Figure 5. Cumulative irreversible discharge capacity vs. remaining FEC (upper x-axis) and consumed FEC (lower x-axis) in LNMO/SiG cells with 5 wt% (green circles) or 0 wt% lithium oxalate (black squares) in the cathode composite during cycling in LP57 + 5 wt% FEC at C/2 and 25°C between 4.0–4.7 V after 50 cycles (open symbols) or 250 cycles (closed symbols). The two identical symbols represent results from two replicate cells.

observed by Jung et al.[22] The offset of the e^-/FEC ratios on the y-axis in Figure 5 can be explained by considering the following: As the lower cell cutoff potential is restricted to 4.0 V, the potential of the SiG anode is limited to a maximum of ∼0.7 V vs. Li/Li^+ (assuming a maximum cathode potential of 4.7 V vs Li/Li^+). At this potential, only about 85% of all lithium is extracted from the SiG electrode during discharge,[25] leading to an apparently higher irreversible capacity for the first cycle, which is however not related to FEC consumption.

It is to note that in contrast to References 22 and 25, in the present study the silicon-based anode is not the capacity-limiting electrode, and side reactions occurring at the LNMO cathode may not be negligible, which makes an analysis of the cumulative irreversible capacity less obvious. Still, the cells without lithium oxalate (black symbols) lie reasonably close to the previously found 4 e^-/FEC linear correlation, which holds also true for the cells with 5 wt% lithium oxalate after 50 cycles (open green circles). After 250 cycles, however, the irreversible capacity is about 1 mAh higher (or the FEC consumption is 10 μmol lower) than the 4 e^-/FEC correlation for cells with 5 wt% lithium oxalate (closed green circles in Figure 5). This indicates that there is an additional process related to the irreversible discharge capacity, which does not consume FEC. It is likely that this additional process is the electrochemical reduction of CO_2 on the SiG anode, as this reaction would contribute to the cumulative irreversible capacity, but not the FEC consumption.

Consumption of carbon dioxide in LNMO/SiG full cells.—To investigate the consumption of CO_2 on the SiG anode, we performed 1-compartment OEMS measurements on the first cycle of LNMO/SiG full-cells. If a significant amount of the CO_2 from lithium oxalate oxidation were to be consumed on the SiG anode during this first formation cycle, the overall CO_2 evolution should be lower than expected for the essentially complete lithium oxalate oxidation in the first cycle. As a benchmark for the maximum CO_2 evolution that can be practically achieved from our LNMO/lithium oxalate cathodes, we also measured a LNMO electrode containing 5 wt% lithium oxalate vs. an oversized delithiated LFP electrode. Due to the high potential of the LFP (∼3.4 V vs. Li/Li^+), we do not expect any reductive consumption of CO_2 in this system. The yellow line in Figure 6a shows

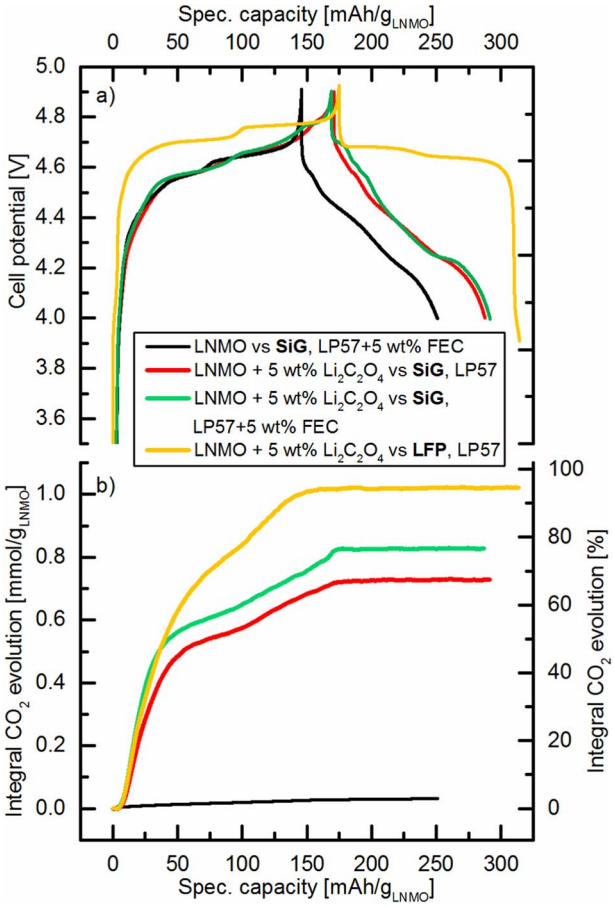

Figure 6. a) Potential profile and b) CO_2 evolution during the first charge/discharge cycle of an LNMO/SiG cell with 0 wt% lithium oxalate in LP57 + 5 wt% FEC (black lines), an LNMO/SiG cell with 5 wt% lithium oxalate in LP57 (red lines), an LNMO/SiG cell with 5 wt% lithium oxalate in LP57 + 5 wt% FEC (green lines), and an LNMO/LFP cell with 5 wt% lithium oxalate in LP57 (yellow lines). Cycling was done at C/5 and 25°C in a 1-compartment OEMS cell.

the potential profile of an LNMO/LFP cell with 5 wt% lithium oxalate (the cell potential was converted to the Li/Li^+ scale by adding 3.42 V, the equilibrium potential of LFP[45]), whereas the yellow line in Figure 6b shows the corresponding CO_2 evolution. The first charge capacity (174 mAh/g_{LNMO}) in the LNMO/LFP + 5 wt% lithium oxalate OEMS cell is similar to the capacity achieved in LNMO half cells containing 5 wt% lithium oxalate vs. lithium (compare Figure 2). The CO_2 evolution in the LNMO/LFP + 5 wt% lithium oxalate OEMS cell rises to 1.02 mmol/g_{LNMO}, which corresponds to ∼95% of the theoretical amount of CO_2 based on conversion of all lithium oxalate (see right y-axis in Figure 6b). The deviation from 100% is likely due to Li_2CO_3 impurities as well as partial dissolution of CO_2 in the electrolyte solution, as discussed previously.

As a next step, we repeated this experiment but replaced the LFP counter electrode with a SiG anode, while the cathode (LNMO + 5 wt% lithium oxalate) and the electrolyte solution (LP57 + 5 wt% FEC) remained identical (green lines in Figures 6a and 6b). With the SiG anode, the total CO_2 evolution was significantly lowered to 0.83 mmol/g_{LNMO} (∼77% of the theoretical CO_2). In the absence of FEC (i.e., in pure LP57), the total CO_2 evolution of the LNMO/SiG cells with 5 wt% lithium oxalate (red lines in Figures 6a and 6b) is further decreased to 0.73 mmol/g_{LNMO}, i.e., to ∼68% of the theoretical CO_2. These results indicate that a significant amount of the practically available CO_2 (∼19% for cell with LP57 + 5 wt% FEC or ∼28% for cells with LP57) is already reduced in the first cycle of LNMO/SiG cells. To evaluate whether the apparently lower CO_2 consumption in FEC-containing vs. FEC-free electrolyte solutions may not simply be due to the additional release of CO_2 by the reduction of FEC,[22,46] we also investigated an LNMO/SiG cell without lithium oxalate in LP57 + 5 wt% FEC by OEMS (black lines in Figures 6a and 6b). While a minor extent of CO_2 is formed in this case, it amounts to only 0.03 mmol/g_{LNMO}, which is small compared to the ∼0.10 mmol/g_{LNMO} difference between the lithium oxalate containing LNMO/SiG cells with and without FEC. These observations are consistent with the findings by Krause et al.,[18] who showed that CO_2 dosed to cells with silicon anodes gets consumed at the silicon anode, and that its consumption rate is reduced in the presence of FEC.

In contrast to FEC, where the consumed amount can be easily determined by ^{19}F-NMR, a quantification of the remaining CO_2 after extended cycling is not easily possible from the coin cells used in this study. However, Krause et al.[18] showed that once all added CO_2 is consumed, Si alloy-based cells suffer from a severe drop in coulombic efficiency and capacity retention, analogously to what both Jung et al.[22] and Petibon et al.[24] demonstrated for the complete consumption of FEC from Si-based cells. Additionally, also the significantly different coulombic efficiencies from LNMO/SiG cells where CO_2 was either left in the cells (green symbols in Figure 4) or purposely removed (orange symbols in Figure 4) indicate that a drop in coulombic efficiency can be expected at the point where all CO_2 is depleted. Therefore, we repeated the cycling experiment from Figure 4 with LNMO/SiG cells containing different amounts of lithium oxalate (namely 0, 2.5, and 5 wt%) in pure LP57, i.e., without FEC in the electrolyte solution. Furthermore, with this experiment we investigate the effectiveness of CO_2 by itself as an SEI-forming additive for silicon-based anodes. Figure 7 shows the capacity retention for LNMO/SiG cells with LP57 and 0, 2.5, and 5 wt% lithium oxalate in the LNMO cathode. The initial charge/discharge capacities for cells with 0 wt% and 5 wt% lithium oxalate are similar to the cells with the same electrodes in FEC-containing electrolyte solution (see Figure 4), namely 145/110 mAh/g_{LNMO} and 173/123 mAh/g_{LNMO}, respectively, whereas the first cycle charge/discharge capacity of cells with 2.5 wt% lithium oxalate lies in between these two (160/112 mAh/g_{LNMO}). During cycling, the cells with 0 wt% lithium oxalate decline dramatically in capacity, while their coulombic efficiency drops to <90% (black symbols). After 100 cycles, there is essentially zero capacity left in these cells. Comparing the cells without lithium oxalate (i.e., without CO_2) from Figure 4 and Figure 7 (both black symbols), once again illustrates how important SEI-forming additives like FEC are for silicon-based anodes to achieve a minimum of stable cycling.

The LNMO/SiG cells with pure LP57 and 5 wt% lithium oxalate (red spheres in Figure 7), however, show initially a much improved cycling stability and a coulombic efficiency of around 99.5%, which is much higher than the ∼98.5% of the cells with FEC but without lithium oxalate (i.e., without CO_2; black symbols in Figure 4) and essentially identical with that of the cells with FEC and 5 wt% lithium oxalate (i.e., with CO_2; green symbols in Figure 4). This comparison clearly demonstrates that CO_2 forms an even more effective SEI than FEC. The cells with 2.5 wt% lithium oxalate (brown triangles in Figure 7) show a ∼9 mAh/g lower capacity compared to their counterparts with 5 wt% lithium oxalate, which we ascribe to the lower amount of additionally available active lithium in the former. However, their coulombic efficiencies in the first tens of cycles are essentially identical due to the presence of CO_2. Around cycle 36 and 89, respectively, the cells with 2.5 wt% and 5 wt% lithium oxalate show a distinct decline in coulombic efficiency from ∼99.5% to ∼94% (for cells with 2.5 wt% lithium oxalate) or 97% (for cells with 5 wt% lithium oxalate), which in both cases is followed by a rapid decay in capacity.

In analogy to the rapid capacity fade and coulombic efficiency loss which was observed for silicon electrodes in FEC containing electrolye (without CO_2) once all FEC was being consumed,[22,24] and the observations made by Krause et al.,[18] it is very likely that it is the complete consumption of CO_2 which leads to the onset of the decline in coulombic efficiency around cycle 36 and 89 in cells with lithium oxalate (i.e., with CO_2) in the FEC-free electrolyte solution

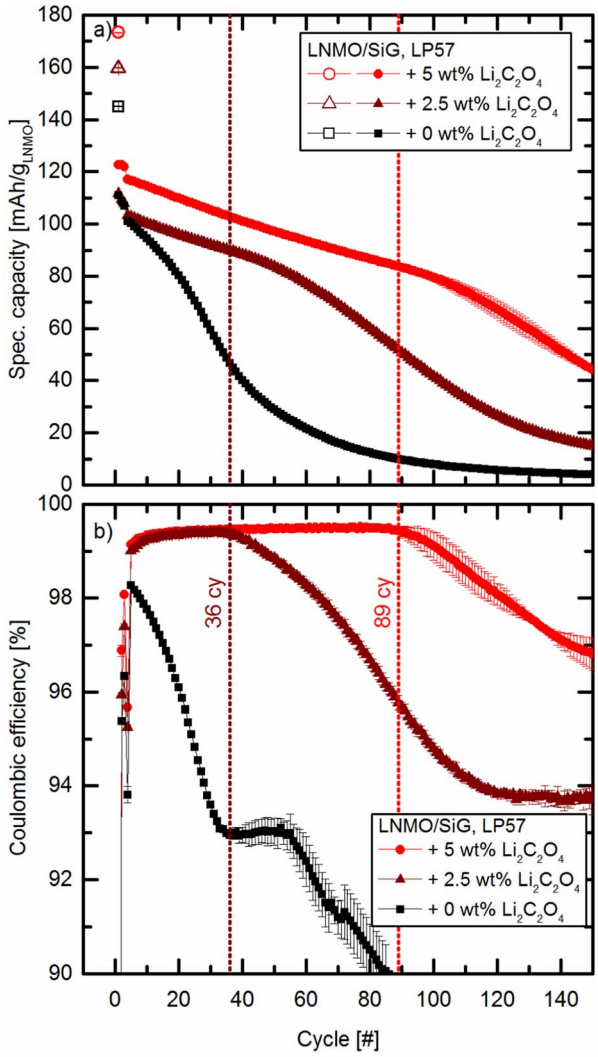

Figure 7. Specific charge (closed symbols) and discharge (open symbols) capacities (upper panel) and coulombic efficiencies (lower panel) of LNMO/SiC cells with 0 wt% (black squares), 2.5 wt% (brown triangles), and 5 wt% (red circles) lithium oxalate in the cathode composite during cycling in pure LP57 at C/2 and 25°C between 4.0–4.8 V. The first three cycles were performed at C/10. All symbols represent the average of two replicate cells, whereas error bars represent the deviation between the replicates. The LNMO and SiG loadings are given in Table I.

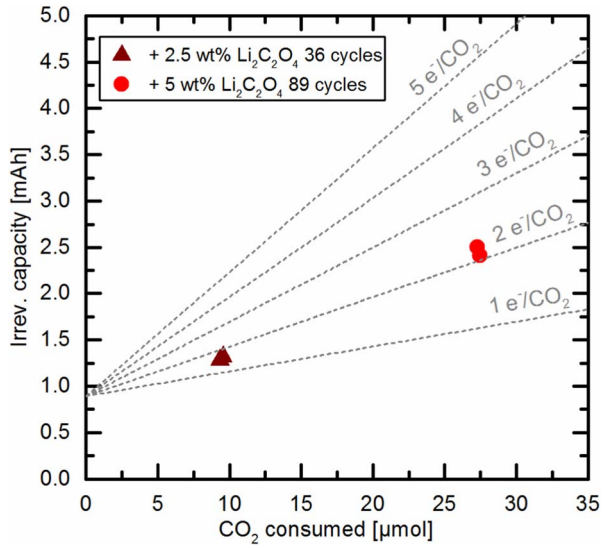

Figure 8. Cumulative irreversible discharge capacity vs. consumed CO_2 in LNMO/SiG cells with 5 wt% (red circles) or 2.5 wt% lithium oxalate (brown triangles) in the cathode composite during cycling in LP57 at C/2 and 25°C between 4.0–4.7 V after 36 cycles (2.5 wt% lithium oxalate) or 89 cycles (5 wt% lithium oxalate). These data are derived from Figure 7.

(see Figure 7). Under this assumption, we can examine whether there is a similar correlation between consumed CO_2 and cumulative irreversible capacity as we had done for FEC-containing electrolyte solution (see Figure 5), by taking the cumulative irreversible discharge capacity after cycle 36 (for cells with 2.5 wt% lithium oxalate) and cycle 89 (for cells with 5 wt% lithium oxalate) and the total theoretical amount of CO_2 that was available from lithium oxalate oxidation (see reaction 1) in these cells. Note that due to the ∼30% lower loading of the LNMO electrodes with 2.5 wt% lithium oxalate (see Table I), the total theoretical amount of CO_2 in these cells is not 50% of the amount in the cells with 5 wt% lithium oxalate, but somewhat lower. The resulting correlation is shown in Figure 8; interestingly, the points lie close to a 2 e^-/CO_2 linear slope, whereas the often assumed reduction of CO_2 to carbonate and CO (acc. to: $2\ CO_2 + 2\ e^- \rightarrow CO_3^{2-} + CO$)[47–49] as well as the reduction of CO_2 to oxalate (acc. to: $2\ CO_2 + 2\ e^- \rightarrow C_2O_4^{-2}$)[49–51] both would correspond to 1 e^-/CO_2. Apparently, a more complex reduction mechanism is taking place. One possible pathway is the formation of formate anions from CO_2 and protic species (i.e., protons from trace HF or electrolyte oxidation products), which would correspond to a total of 2 e^-/CO_2 (acc. to: $CO_2 + 2\ e^- + H^+ \rightarrow HCOO^-$).[47,51] Furthermore, it may be possible that a fraction of the cumulative irreversible capacity is related to decomposition reactions of the electrolyte solvent. A more detailed analysis of the possible reduction reactions of CO_2 on lithium ion battery anodes is currently under investigation.[17]

In the LNMO/SiG cells with pure LP57 and 5 wt% lithium oxalate (red spheres in Figure 7) as well as in the reassembled LNMO/SiG cells with 5 wt% lithium oxalate, i.e., after the removal of CO_2 (orange spheres in Figure 4), we have observed a rapid drop in coulombic efficiency (to a less pronounced degree also in capacity) at the point where no CO_2 was left. However, such a coulombic efficiency drop is not observable for the cells with 5 wt% lithium oxalate with LP57 + 5 wt% FEC (green spheres in Figure 4). To our current understanding, this would indicate that CO_2 has not been completely consumed in these cells even after 250 cycles. To estimate the amount of remaining CO_2 in these cells, we again consider the irreversible capacity vs. FEC consumption relationship shown in Figure 5. As previously discussed, the irreversible capacity for the cells with 5 wt% lithium oxalate is higher compared to the experimentally found 4 e^-/FEC (= 0.107 mAh/μmol_{FEC}) line (green circles in Figure 5). If we assume that this additional irreversible capacity (∼1 mAh) is associated with the reduction of CO_2, we can use the empirically found correlation of 2 e^-/CO_2 (= 0.0536 mAh/μmol_{CO2}) from Figure 8 to estimate that ∼18.6 µmol of CO_2 have been consumed after 250 cycles. The fact that this amount is still lower than the available amount of CO_2 (28.2 µmol) suggests that CO_2 is still remaining in these cells after 250 cycles, which would explain why no rapid coulombic efficiency drop has occurred until this point for the cells with 5 wt% lithium oxalate in FEC-containing electrolyte solution (green circles in Figure 4). For the same cells after 50 cycles, the irreversible capacity lies close to the 4 e^-/FEC line, which means that an assessment of the CO_2 consumption through the irreversible capacity cannot be undertaken. We believe that due to both the low consumption of FEC after 50 cycles as well as the low irreversible capacity, a definitive correlation cannot be made. Nevertheless, it is possible that a fraction of the irreversible capacity is used for the reduction of CO_2; the large differences in coulombic efficiency between cells with and without lithium oxalate (see Figure 4) as well as the results from OEMS measurements

(see Figure 6) suggest that CO_2 is modifying the SEI already during early cycles.

Discussion

Implications for the deliverable capacity of LNMO / SiG cells.— Besides the continuous loss of active lithium, the lifetime of cells with Si-based anodes is largely dependent on the amount of SEI-forming additives available.[18,22,24,25] The experiments in the present study have shown that LNMO/SiG cells with lithium oxalate show a better capacity retention and coulombic efficiency compared to their counterparts without lithium oxalate even in the presence of FEC, and that the co-reduction of CO_2 and FEC occurs simultaneously. However, the question remains how "efficient" the combination of FEC and CO_2 is in terms of additive consumption and active lithium loss. To elucidate this, Figure 9a shows the cumulative delivered discharge capacity, i.e., the sum of discharge capacities over all cycles up to a certain point, per cumulative irreversible discharge capacity for cells with only FEC (gray bars), only CO_2 (red bars) or both additives (green bars). While for cells containing FEC, the data after 50 and 250 cycles (gray solid and dashed bars) are shown, we plotted the data from cycle 36 and 89 for cells without FEC and only CO_2, as these are the cycles for which there is strong evidence that all CO_2 has been consumed. Comparing only FEC- or only CO_2-containing cells (gray and red bars in Figure 9a) , it becomes clear that CO_2 improves the delivered capacity per irreversible capacity. The largest impact, however, has the combination of FEC and CO_2 (green bars in Figure 9a), which leads to a doubling of the delivered capacity per irreversible capacity after 50 and 250 cycles compared to FEC by itself.

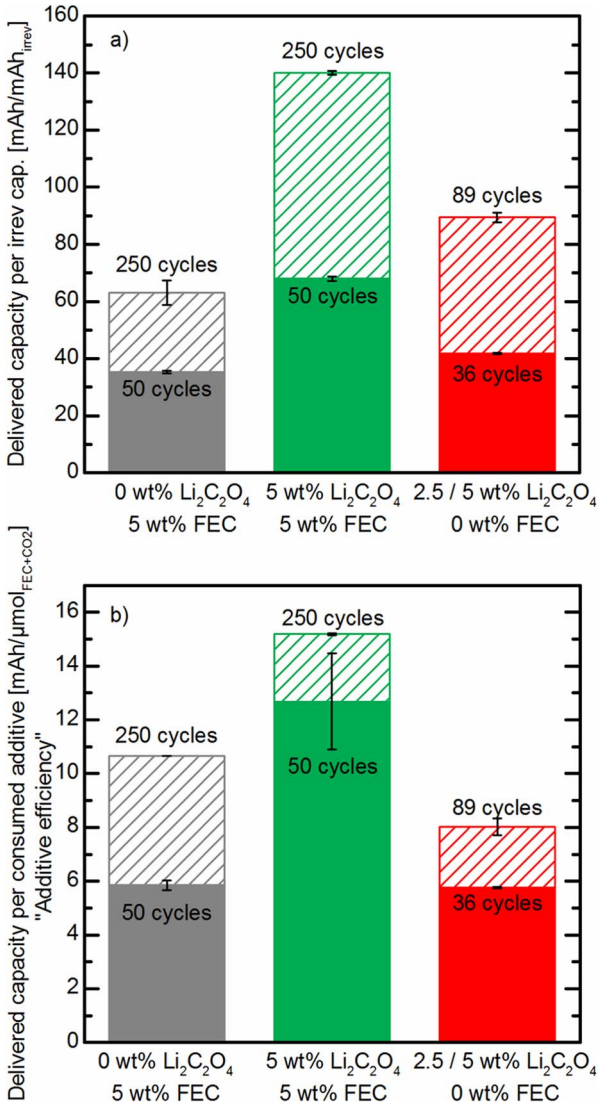

Figure 9. Cumulative delivered discharge capacity a) per cumulative irreversible discharge capacity, and, b) per µmol of additives (FEC+CO_2) for LNMO/SiG cells without lithium oxalate and LP57 + 5 wt% FEC (gray bars), cells with 5 wt% lithium oxalate and LP57 + 5 wt% FEC (green bars), and cells with 2.5 or 5 wt% lithium oxalate and LP57 (red bars). The solid bars represent the delivered capacity after 50 (36 for cells without FEC) cycles, while the dashed bars represent the delivered capacity after 250 (89 for cells without FEC) cycles. Bars represent the average result from two replicate cells, whereas error bars represent the deviation between the replicates.

Figure 9b shows the cumulative delivered discharge capacity per µmol of consumed additive (i.e., the sum of CO_2 and FEC), for the same points as in Figure 9a. To estimate the amount of CO_2 consumed in the LNMO/SiG cells with both lithium oxalate and FEC, we used the above described approximation based on the additional irreversible capacity. From Figure 9b, it is apparent that the combination of CO_2 and FEC (green bars) in LNMO/SiG cells leads to an improved additive efficiency (i.e., delivered capacity per mol of additive) compared to the use of single additives (gray and red bars). This effect is especially pronounced during the early stage of cycling ($\leq$50 cycles), where the additive efficiency for cells with lithium oxalate and FEC is more than two times higher compared to the cells with only FEC (13.1 mAh/µmol vs 5.9 mAh/µmol, respectively). Interestingly, the additive efficiency of only FEC cells (gray bars) is similar to only CO_2 cells (red bars), whereas the delivered capacity per irreversible capacity is clearly lower for cells containing only FEC than for only CO_2 cells (gray and red bars in Figure 9a). However, this agrees with the lower number of electrons required for the reduction of CO_2 in contrast to FEC (compare Figure 5 and Figure 8). For all cells, the additive efficiency grows for a higher number of cycles, which fits well to the observation that coulombic efficiencies also tend to increase during cycling as long as FEC and/or CO_2 have not been consumed (see Figure 4 and Figure 7 as well as Reference 25). In the case of graphite anodes (see Figure 3), this is related to the formation of a gradually more passivating and thicker SEI; in the case of silicon anodes, the additional effect leading to an improvement of the coulombic efficiency is the fact that as the capacity fades, the state-of-charge change per cycle becomes lower, which causes less volume expansion/contraction and thus less and less SEI rupture.

Implications for the energy density of LNMO/graphite cells.— To consider the effect of lithium oxalate on commercial-scale cells, we take a step back to the LNMO/graphite cells that were shown in Figure 3. Figure 10 shows the specific energy density (using the charge-averaged discharge voltage) during cycle 5 and cycle 300 of the LNMO/graphite cells with different amounts of lithium oxalate from Figure 3 at 1C discharge. The addition of 2.5 wt% lithium oxalate increases the initial (5th cycle) cathode specific energy density from 555 Wh/kg$_{LNMO}$ to 600 Wh/kg$_{LNMO}$; the addition of 5 wt% lithium oxalate does not improve the energy density much further in the 5th cycle (to 615 Wh/kg$_{LNMO}$). These values are ~5-10% lower than the energy density of NMC622/graphite cells cycled at the same conditions to 4.4 V, the highest possible cutoff potential which still shows stable performance.[52] After 300 cycles, the cathode specific energy density of the LNMO/graphite cells without lithium oxalate drops to 453 Wh/kg$_{LNMO}$ ($\equiv$82% energy density retention), while ~16% higher specific energies of 527 Wh/kg$_{LNMO}$ ($\equiv$88% energy density retention) are observed for cells with 2.5 wt% lithium oxalate; at the higher level of 5 wt% lithium oxalate, the specific energies of 555 Wh/kg$_{LNMO}$ are ~23% higher than without oxalate and the energy density retention is 90%. These energy retentions are very comparable to that of the above mentioned NMC622/graphite cells.[52] While the lithium oxalate containing LNMO/graphite cells do have a ~5-10% lower energy density, they are an interesting option for cobalt-free lithium ion battery cells, which may become critical in the future due to the rising cost and geographic concentration of cobalt.[53,54]

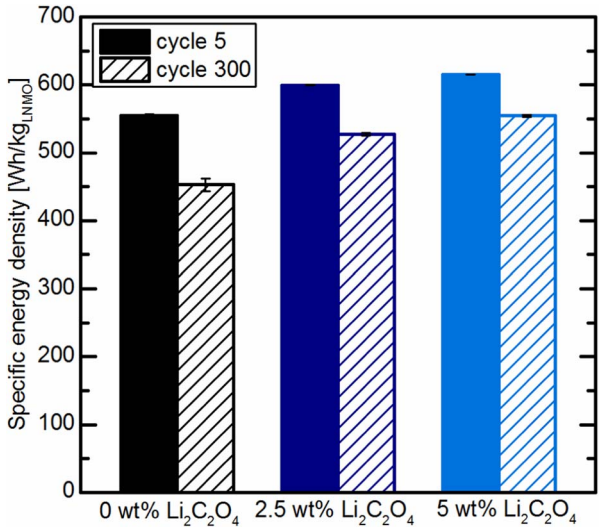

Figure 10. Cathode specific energy density during 1 C discharge of LNMO/graphite cells with 0 wt% (black bars), 2.5 wt% (dark blue bars), and 5 wt% lithium oxalate (light blue bars) at cycle 5 (solid bars) and cycle 300 (dashed bars) at 25°C. Bars represent the average result from two replicate cells, whereas error bars represent the deviation between the replicates. The data are based on Figure 3.

Assuming all electrodes used here have the same initial porosity of 35%, the specific volume of electrode (including voids) per gram LNMO increases from 0.44 cm^3/g_{LNMO} to 0.46 cm^3/g_{LNMO} or 0.48 cm^3/g_{LNMO} by adding 2.5 wt% or 5 wt% lithium oxalate, respectively (calculated from electrode compositions given in Table I and bulk densities of 4.4 g/cm^3 for LNMO, 1.8 g/cm^3 for PVDF, 2.2 g/cm^3 for C65 and 2.1 g/cm^3 for lithium oxalate).[55] Accordingly, the oxidation of lithium oxalate leads to a porosity increase from 35% to 38% in the electrodes with 2.5 wt% and to 40% in the electrodes with 5 wt% lithium oxalate. The resulting volumetric energy density, here defined as energy per entire electrode volume including voids, is around 1272 $Wh/L_{electrode}$ at cycle 5 for cells without lithium oxalate and rises about 3% to 1315 $Wh/L_{electrode}$ for cells containing 2.5 wt% lithium oxalate. Cells with 5 wt% lithium oxalate deliver only 1291 $Wh/L_{electrode}$ at cycle 5, as the higher porosity now counteracts the slight increase in gravimetric energy density. This effect can be avoided if electrodes with lithium oxalate are calendered to initial porosities of 32% (2.5 wt% lithium oxalate) or 30% (5 wt% lithium oxalate). In this way, the porosity reaches 35% after lithium oxalate oxidation for all electrodes, and the resulting volumetric energy densities at cycle 5 for electrodes containing 0, 2.5 or 5 wt% lithium oxalate are 1272 $Wh/L_{electrode}$, 1376 $Wh/L_{electrode}$ or 1412 $Wh/L_{electrode}$.

Gas evolution in large-format cells.—As for LNMO/graphite cells, the use of more than 2.5 wt% lithium oxalate shows the biggest improvement factor and perhaps is the best compromise between the amount of electrode additive and specific energy retention. Therefore, the following considerations are all based on electrodes containing 2.5 wt% lithium oxalate. The CO_2 evolution from the oxidation of lithium oxalate during formation could be an issue in commercial-scale cells due to swelling (in pouch cells) or pressure buildup (in hard-case cells). This is largely related to the fact that in commercial-scale cells, the ratio of active materials to electrolyte solution and void volume is typically ~10 times higher compared to the lab-scale cells used here.[37,56] Strehle et al.[16] recently showed that under these conditions, the majority of CO_2 released from VC reduction would remain dissolved in the electrolyte solution instead of being released into the gas headspace of the cell. This is illustrated by first estimating the amount of dissolved CO_2 by Henry's law 2:

$$\frac{p_{CO_2(gas)}}{K_H} = \frac{n_{CO_2(el)}}{V_{el}\ c_{el} + n_{CO_2(el)}} \quad [2]$$

Table II. Expected pressure buildup for coin or 18650 cells or volume expansion for pouch cells as well as the fraction of CO_2 dissolved in the electrolyte solution for a cathode electrode with 2.5 wt% lithium oxalate at room temperature (25°C) and a surrounding pressure of 1 bar. Note that CO_2 consumption at the anode is not taken into account here.

Cell type	2023 coin cell (2.6 mAh)	pouch cell (180 mAh)	18650 cell (3 Ah)
Cell headspace V_{gas} [mL]	0.5	–	1
Electrolyte solution V_{el} [mL]	0.08	0.75	7.6
Cathode material [g]	0.017	0.9	20.4
Total CO_2 $n_{CO2(total)}$ [μmol]	9.3	460	10 400
Fraction of CO_2 in the electrolyte solution [%]	30.3	17.9	95.4
Pressure buildup Δp [MPa]	0.032	–	1.19
Volume expansion ΔV [mL]	–	9.3	–

where $n_{CO2(el)}$ is the amount of CO_2 dissolved in the liquid electrolyte solution, V_{el} is the volume of the electrolyte solution, c_{el} is the total molar concentration of the electrolyte solution (i.e., solvent and salt) and K_H is the Henry constant of CO_2 in the electrolyte solution in units of pressure. Combining this with the ideal gas law and the assumption that $V_{el}\ c_{el} + n_{CO2(el)} \approx V_{el}\ c_{el}$, the fraction of CO_2 dissolved in the electrolyte solution can now be given as 3:

$$\frac{n_{CO_2(el)}}{n_{CO_2(total)}} = \frac{V_{el}\ RTc_{el}}{V_{el}RTc_{el} + V_{gas}K_H} \quad [3]$$

where $n_{CO2(total)}$ is the total amount of CO_2 present in the system and V_{gas} is the volume of the cell's gas headspace. Assuming a constant gas volume, as would be the case for a hard-case cell, the pressure buildup can be expressed as 4:

$$\Delta p = n_{CO_2(total)} \frac{K_H RT}{V_{el}RTc_{el} + V_{gas}K_H} \quad [4]$$

On the other hand, in soft pouch cells, gas evolution would typically lead to expansion (or bulging) of the cell. This volume expansion at a given pressure can be calculated by 5:

$$\Delta V = RT\left(\frac{n_{CO_2(total)}}{p} - \frac{V_{el}c_{el}}{K_H}\right) \quad [5]$$

To assess how much pressure buildup or volume expansion would actually occur in a commercial-scale cell containing 2.5 wt% lithium oxalate in the cathode electrode, we use a similar approximation for a commercial-scale 3 Ah cell as shown in ref. 16, where the weight for cathode active material and electrolyte solution were taken from Wagner et al.[57] Furthermore, we also calculate the expected volume expansion for a 180 mAh pouch cell containing ~ 0.75 mL electrolyte solution as used by Xia et al.,[58] assuming a constant pressure of 1 bar in the cell. In both cases, the composite cathode is approximated to consist of 96% active material and 2.5 wt% lithium oxalate. For comparison, the 2032-type coin cells used in this study are also included in this assessment.

Table II summarizes the expected pressure buildup and volume expansion for the respective cells. The pressure increase in coin cells is low (~0.03 MPa), due to the relatively large void space compared to electrolyte solution and cathode active material volume. In a 180 mAh pouch cell, the estimated gas evolution would be ~9.3 mL at 1 bar, which is about 5 times larger than the gas evolution normally expected for these cells during formation.[58] The pressure buildup in the hard case 18650 cell is ~1.2 MPa; this causes that 95% of the CO_2 remains dissolved in the electrolyte solution. However, the oxidation of lithium oxalate is completed after the first charge, which means that the gas evolution will stop thereafter. As many commercial-scale cells are vented during or after formation, the high pressure/volume increase is only a matter of the very first cycles. We have further not considered the consumption of CO_2 on the graphite or silicon/graphite

anode: Strehle et al.[16] showed that up to 40 μmol (≈1 mL) CO_2 can be consumed per square meter graphite surface area during the first formation cycle, which agrees well with previous reports by Xiong et al.[40] The graphite electrodes used in the present study have a specific surface area of 0.034 m_{BET}^2/cm_{geom}^2, hence 40 μmol/m_{BET}^2 would correspond to a CO_2 consumption of 1.4 μmol/cm_{geom}^2, which is about ∼20% of the evolved CO_2 (6 μmol/cm_{geom}^2). As long as the ratio of lithium oxalate to graphite or the specific surface area of the graphite do not change drastically, the same fraction of CO_2 would also be consumed during formation in other cell formats. For silicon-based anodes, the previous OEMS measurements have shown that the CO_2 consumption of SiG anodes during the first charge can be about 19–28% of the theoretically available CO_2 (see Figure 6). Assuming a consumption of 25% CO_2 in the first cycle, the volume expansion in pouch cells would be decreased to ∼6.5 mL, while the pressure rise in 18650 cells would be limited to ∼0.89 MPa. Although a venting of some of the excess gas is probably still required in this case, a complete removal of CO_2 after formation is not desirable, as the amount of CO_2 within the cell should remain high during cycling to benefit from its properties as an SEI-forming additive, as was shown here and in Reference 18.

Conclusions

In this paper, we assessed the use of lithium oxalate as a "sacrificial salt", i.e., a lithium ion donor, in combination with LNMO cathodes. We have shown that the incorporation of 2.5 wt% or 5 wt% lithium oxalate into the cathode electrode increases the first cycle charge capacity by about 10% and 20%, respectively, without affecting the electrochemical performance of the cathode during subsequent cycles. The effect of lithium oxalate and CO_2 released from its oxidation was investigated in LNMO/graphite and LNMO/silicon-graphite (SiG) cells. The former showed increased initial capacity according to the increased pool of active lithium, as well as a higher coulombic efficieny and capacity retention, when lithium oxalate was added to the cathode matrix. For LNMO/SiG cells, a significantly improved cycling stability and coulombic efficiency was found for cells containing lithium oxalate and FEC compared to cells with only FEC but no lithium oxalate, which we ascribe to the beneficial effect of CO_2 on the cycling stability of silicon-based anodes.

By OEMS measurements and analysis of the cumulative irreversible discharge capacity, we can conclude that CO_2 and FEC are simultaneously reduced, following and overall ∼4 e^-/FEC and ∼2 e^-/CO_2 process. Furthermore, the combination of these two additives is more efficient in terms of deliverable capacity per irreversible capacity and per mol of consumed additive than either of them alone. In this context, the use of lithium oxalate in the cathode matrix is not limited to its use as a "sacrificial salt" in the original sense, but also displays an easy and controllable way to introduce defined amounts of CO_2 into lithium ion cells with graphite or silicon-based anodes.

Acknowledgments

Sophie Solchenbach and Daniel Pritzl gratefully acknowledge the BASF Battery Research Network for financial support. Funding for Morten Wetjen was provided by the German Federal Ministry for Economic Affairs and Energy (BMWi; funding number 03ET6045D). Wacker Chemie AG is kindly acknowledged for providing the silicon nanoparticles. Furthermore, the authors want to thank Dr. Stefano Meini for fruitful discussions.

ORCID

Sophie Solchenbach https://orcid.org/0000-0001-7142-452X

References

1. D. Andre, S.-J. Kim, P. Lamp, S. F. Lux, F. Maglia, O. Paschos, and B. Stiaszny, *J. Mater. Chem. A*, **3**, 6709 (2015).
2. I. Buchberger, S. Seidlmayer, A. Pokharel, M. Piana, J. Hattendorff, P. Kudejova, R. Gilles, and H. A. Gasteiger, *J. Electrochem. Soc.*, **162**, A2737 (2015).
3. M. Klett, J. A. Gilbert, K. Z. Pupek, S. E. Trask, and D. P. Abraham, *J. Electrochem. Soc.*, **164**, A6095 (2017).
4. J. C. Arrebola, A. Caballero, H. Göhr, L. Hernán, J. Morales, and L. Sánchez, *Electrochem. commun.*, **11**, 1061 (2009).
5. C. R. Jarvis, M. J. Lain, M. V. Yakovleva, and Y. Gao, *J. Power Sources*, **162**, 800 (2006).
6. I. W. Seong, K. T. Kim, and W. Y. Yoon, *J. Power Sources*, **189**, 511 (2009).
7. N. Liu, L. Hu, M. T. McDowell, A. Jackson, and Y. Cui, *ACS Nano*, **5**, 6487 (2011).
8. M. Marinaro, M. Weinberger, and M. Wohlfahrt-Mehrens, *Electrochim. Acta*, **206**, 99 (2016).
9. G. Gabrielli, M. Marinaro, M. Mancini, P. Axmann, and M. Wohlfahrt-Mehrens, *J. Power Sources*, **351**, 35 (2017).
10. D. Shanmukaraj, S. Grugeon, S. Laruelle, G. Douglade, J.-M. Tarascon, and M. Armand, *Electrochem. commun.*, **12**, 1344 (2010).
11. J. O. Besenhard, M. W. Wagner, M. Winter, A. D. Jannakoudakis, P. D. Jannakoudakis, and E. Theodoridou, *J. Power Sources*, **44**, 413 (1993).
12. Y. Ein-Eli, B. Markovsky, D. Aurbach, Y. Carmeli, H. Yamin, and S. Luski, *Electrochim. Acta*, **39**, 2559 (1994).
13. D. Aurbach, Y. Ein-Eli, O. Chusid, Y. Carmeli, M. Babai, and H. Yamin, *J. Electrochem. Soc.*, **141**, 603 (1994).
14. T. Osaka, T. Momma, T. Tajima, and Y. Matsumoto, *J. Electrochem. Soc.*, **142**, 1057 (1995).
15. D. Aurbach and Y. S. Cohen, *J. Electrochem. Soc.*, **144**, 3355 (1997).
16. B. Strehle, S. Solchenbach, M. Metzger, K. U. Schwenke, and H. A. Gasteiger, *J. Electrochem. Soc.*, **164**, A2513 (2017).
17. K. U. Schwenke, S. Solchenbach, J. Demeaux, B. L. Lucht, and H. A. Gasteiger, Manuscript in preparation.
18. L. J. Krause, V. L. Chevrier, L. D. Jensen, and T. Brandt, *J. Electrochem. Soc.*, **164**, A2527 (2017).
19. H. Nakai, T. Kubota, A. Kita, and A. Kawashima, *J. Electrochem. Soc.*, **158**, A798 (2011).
20. V. Etacheri, O. Haik, Y. Goffer, G. A. Roberts, I. C. Stefan, R. Fasching, and D. Aurbach, *Langmuir*, **28**, 965 (2012).
21. E. Markevich, K. Fridman, R. Sharabi, R. Elazari, G. Salitra, H. E. Gottlieb, G. Gershinsky, A. Garsuch, G. Semrau, M. A. Schmidt et al., *J. Electrochem. Soc.*, **160**, A1824 (2013).
22. R. Jung, M. Metzger, D. Haering, S. Solchenbach, C. Marino, N. Tsiouvaras, C. Stinner, and H. A. Gasteiger, *J. Electrochem. Soc.*, **163**, A1705 (2016).
23. E. Markevich, G. Salitra, and D. Aurbach, *ACS Energy Lett.*, **2**, 1337 (2017).
24. R. Petibon, V. Chevrier, C. P. Aiken, D. S. Hall, S. Hyatt, R. Shunmugasundaram, and J. R. Dahn, *J. Electrochem. Soc.*, **163**, 1146 (2016).
25. M. Wetjen, D. Pritzl, R. Jung, S. Solchenbach, R. Ghadimi, and H. A. Gasteiger, *J. Electrochem. Soc.*, **164**, A2840 (2017).
26. T. M. Bond, J. C. Burns, D. A. Stevens, H. M. Dahn, and J. R. Dahn, *J. Electrochem. Soc.*, **160**, A521 (2013).
27. N. Tsiouvaras, S. Meini, I. Buchberger, and H. A. Gasteiger, *J. Electrochem. Soc.*, **160**, A471 (2013).
28. M. Metzger, B. Strehle, S. Solchenbach, and H. A. Gasteiger, *J. Electrochem. Soc.*, **163**, A798 (2016).
29. S. Meini, N. Tsiouvaras, K. U. Schwenke, M. Piana, H. Beyer, L. Lange, and H. A. Gasteiger, *Phys. Chem. Chem. Phys.*, **15**, 11478 (2013).
30. S. Meini, S. Solchenbach, M. Piana, and H. A. Gasteiger, *J. Electrochem. Soc.*, **161**, A1306 (2014).
31. R. Jung, M. Metzger, F. Maglia, C. Stinner, and H. A. Gasteiger, *J. Phys. Chem. Lett.*, **8**, 4820 (2017).
32. A. A. Isse, A. Gennaro, and F. Maran, *Acta Chem. Scand.*, **53**, 1013 (1999).
33. B. Li, L. Xing, M. Xu, H. Lin, and W. Li, *Electrochem. commun.*, **34**, 48 (2013).
34. L. Hu, K. Amine, and Z. Zhang, *Electrochem. commun.*, **44**, 34 (2014).
35. B. Michalak, B. B. Berkes, H. Sommer, T. Brezesinski, and J. Janek, *J. Phys. Chem. C*, **121**, 211 (2017).
36. B. Michalak, B. B. Berkes, H. Sommer, T. Bergfeldt, T. Brezesinski, and J. Janek, *Anal. Chem.*, **88**, 2877 (2016).
37. D. Pritzl, S. Solchenbach, M. Wetjen, and H. A. Gasteiger, *J. Electrochem. Soc.*, **164**, A2625 (2017).
38. Y. Dong, J. Demeaux, and B. L. Lucht, *J. Electrochem. Soc.*, **163**, 2413 (2016).
39. Y. Zhang, L. Wang, H. Feng, A. Zhang, C. Zhang, and P. Zhang, *Ionics (Kiel).*, **17**, 677 (2011).
40. D. J. Xiong, L. D. Ellis, R. Petibon, T. Hynes, Q. Liu, and J. R. Dahn, *J. Electrochem. Soc.*, **164**, 340 (2017).
41. S. E. Sloop, J. B. Kerr, and K. Kinoshita, *J. Power Sources*, **119–121**, 330 (2003).
42. A. J. Smith, J. C. Burns, D. Xiong, and J. R. Dahn, *J. Electrochem. Soc.*, **158**, A1136 (2011).
43. D. J. Xiong, R. Petibon, M. Nie, L. Ma, J. Xia, and J. R. Dahn, *J. Electrochem. Soc.*, **163**, 546 (2016).
44. K. Fridman, R. Sharabi, R. Elazari, G. Gershinsky, E. Markevich, G. Salitra, D. Aurbach, A. Garsuch, and J. K. Lampert, *Electrochem. commun.*, **33**, 31 (2013).
45. A. Yamada, H. Koizumi, S.-I. Nishimura, N. Sonoyama, R. Kanno, M. Yonemura, T. Nakamura, and Y. Kobayashi, *Nat. Mater.*, **5**, 357 (2006).
46. M. E. Spahr, T. Palladino, H. Wilhelm, A. Würsig, D. Goers, H. Buqa, M. Holzapfel, and P. Novák, *J. Electrochem. Soc.*, **151**, A1383 (2004).
47. L. V Haynes and D. T. Sawyer, *Anal. Chem.*, **39**, 332 (1958).

48. D. Aurbach and O. Chusid, *Electrochem. Soc. Lett.*, **140**, L155 (1993).
49. A. Gennaro, A. A. Isse, M.-G. Severin, E. Vianello, I. Bhugunb, and J.-M. Saveant, *J. Chem. Soc. Faraday Trans.*, **92**, 3963 (1996).
50. U. Kaiser and E. Heitz, *Berichte der Bunsen-Gesellschaft*, **77**, 818 (1973).
51. C. Amatore and J.-M. Saveant, *J. Am. Chem. Soc.*, **103**, 5021 (1981).
52. R. Jung, M. Metzger, F. Maglia, C. Stinner, and H. A. Gasteiger, *J. Electrochem. Soc.*, **164**, A1361 (2017).
53. R. L. Moss, E. Tzimas, P. Willis, J. Arendorf, L. Tercero Espinoza, F. Marscheider-Weidemann, M. Soulier, A. Lüllmann, C. Sartorius, and K. Ostertag, *JRC Sci. Tech. Reports* (2013).
54. P. A. Nelson, K. G. Gallagher, I. Bloom, and D. W. Dees, *Argonne National Laboratory Report ANL-11/32* (2011).
55. E. J. Berg, C. Villevieille, D. Streich, S. Trabesinger, and P. Novák, *J. Electrochem. Soc.*, **162**, A2468 (2015).
56. S. Solchenbach, D. Pritzl, E. J. Y. Kong, J. Landesfeind, and H. A. Gasteiger, *J. Electrochem. Soc.*, **163**, 2265 (2016).
57. F. T. Wagner, B. Lakshmanan, and M. F. Mathias, *J. Phys. Chem. Lett.*, **1**, 2204 (2010).
58. J. Xia, R. Petibon, A. Xiao, W. M. Lamanna, and J. R. Dahn, *J. Electrochem. Soc.*, **163**, A1637 (2016).

3.2.2 The effect of CO_2 on alkyl carbonate trans-esterification during formation of graphite electrodes

The paper "The Effect of CO_2 on Alkyl Carbonate Trans-Esterification during Formation of Graphite Electrodes in Li-Ion Batteries" was submitted to the Journal of the Electrochemical Society in July 2017 and published in August 2017. The results of this paper were presented by Benjamin Strehle at the 228th Meeting of the Electrochemical Society in Phoenix, Arizona in October 2015 (Abstract Number 369). The article was published "open access" under the Creative Commons Attribution 4.0 License (CC BY). A permanent link to this article can be found under: http://jes.ecsdl.org/content/164/12/A2513.

In this study, the transesterification reaction of ethylmethyl carbonate (EMC) to dimethyl carbonate (DMC) and diethyl carbonate (DEC), triggered by alkoxide species, was studied by OEMS. Although there is no direct gaseous product of this reaction, relative changes of the electrolyte background due to the altered composition could be observed. Within the study, background mass traces unique for each of the linear carbonates were identified and in the following used to evaluate the effect of vinylene carbonate (VC), vinyl ethylene carbonate (VEC) and CO_2 on the transesterification reaction. While VC forms CO_2 upon reduction (s. chapter 1.3), we confirmed that VEC is reduced to butadiene in a mechanism similar to the EC reduction pathway.[177] CO_2 is known to react with lithium alkoxides to the corresponding lithium alkyl carbonates,[178] and thus could potentially be effective in suppressing the transesterification reaction by itself. It was found that all concentrations of VC stopped the EMC transesterification, whereas high concentrations of VEC (2 wt% vs. 0.2 wt%) and CO_2 (10 vol% vs. 1000 ppm in the cell headspace) were required to fully inhibit EMC decomposition. In this way, the transesterification of EMC can also serve as a marker for the ability of an additive to form a stable and effective SEI.

Author contributions

B. S. performed and evaluated the OEMS measurements. B. S., S. S. and M. M. developed and discussed all reduction/reaction mechanisms. B. S. and H. A. G. wrote the manuscript. All authors discussed the data and commented the manuscript.

The Effect of CO_2 on Alkyl Carbonate Trans-Esterification during Formation of Graphite Electrodes in Li-Ion Batteries

Benjamin Strehle,[*,z] Sophie Solchenbach,[*] Michael Metzger,[*,a] K. Uta Schwenke, and Hubert A. Gasteiger[**]

Chair of Technical Electrochemistry, Department of Chemistry and Catalysis Research Center, Technische Universität München, D-85748 Garching, Germany

Apart from the often-described formation of interphases between the electrodes and the electrolyte in Li-ion batteries, changes of the bulk electrolyte also occur during cycling. In this study, we use On-line Electrochemical Mass Spectrometry (OEMS) to measure the gas evolution associated with changes in the electrolyte during the initial cycles of graphite/lithium half-cells in an electrolyte composed of ethylene carbonate (EC), ethyl methyl carbonate (EMC), and the conducting salt $LiPF_6$. The reduction of the electrolyte at the graphite surface within the first cycle is accompanied by the release of lithium alkoxides (LiOR), which initiate the conversion of the co-solvent EMC into the linear carbonates dimethyl carbonate (DMC) and diethyl carbonate (DEC). This trans-esterification can be suppressed by the use of additives such as vinylene carbonate (VC) and vinyl ethylene carbonate (VEC). Upon reduction, VC generates CO_2, while VEC generates 1,3-butadiene. The beneficial impact of the additives arises from these gases, which scavenge the highly reactive LiOR species by forming non-reactive products. Furthermore, our results demonstrate the positive effect of CO_2 on the cell chemistry and the importance of adjusting the electrolyte volume and additive concentration with respect to the active material mass in Li-ion batteries.

Manuscript received July 17, 2017. Published August 24, 2017. This was Paper 369 presented at the Phoenix, Arizona, Meeting of the Society, October 11–15, 2015.

Li-ion batteries (LIBs) have been successfully used in electronic devices during the past 25 years. Recently, the expanding market of hybrid electric vehicles (HEVs), plug-in hybrid electric vehicles (PHEVs), and battery electric vehicles (BEVs) powered by LIBs has pushed the requirements on this technology even further.[1–4] However, the application of LIBs particularly in PHEVs and BEVs is still hampered by their limited safety, thermal stability, and cycle life. Although the applied electrolyte solutions are prone to thermal decomposition, mixtures of cyclic and linear organic carbonate solvents in combination with the conducting salt $LiPF_6$ are widely used for LIBs. They represent an optimum between low viscosity, low vapor pressure, good salt solubility, and high conductivity. The electrolyte composition plays an important role in terms of cycle life. During the initial cycles, the electrolyte is reduced at the anode and forms a passivating layer, the so-called solid electrolyte interphase (SEI). The SEI prevents the further reduction of the bulk electrolyte by blocking the electron transport while allowing Li-ions to pass through. Its stability is thus critical for attaining long LIB cycle and storage life,[5,6] whereby electrolyte additives have been shown to substantially alter the composition of the SEI and to improve its effectiveness.[7]

Besides the formation of electrode interphases, also changes of the bulk electrolyte can occur during the cycling of a cell. These processes can be induced either by thermal reactions or by the dissolution and/or further reaction of reduced or oxidized electrolyte species from the anode or cathode, respectively. For example, the thermal decomposition products of $LiPF_6$ can react with the electrolyte solvents or impurities to form phosphate esters and POF_3.[8–10] Furthermore, organic carbonates can undergo an ester exchange reaction. This trans-esterification has been observed for both linear and cyclic carbonates and is triggered by strong nucleophiles attacking the carbonyl carbon atom.[11–15] In Li-ion batteries, these nucleophilic species are typically lithium alkoxides (LiOR, dissociated into Li^+ and RO^-), generated through the reduction of the electrolyte solvents.[16] While linear carbonates thus convert to other linear carbonates, the dimerization with cyclic carbonates such as EC results in the formation of soluble ethylene glycol bis-(alkyl carbonates). These products are generally unwanted, because they deteriorate the properties of an optimized electrolyte formulation.[17] The extent of trans-esterification can be affected by a number of parameters, including the effectiveness of the passivation of the anode surface by the SEI as well as the operating potential of the cathode.[12,18] While it is well known that electrolyte additives can suppress the trans-esterification reaction,[19,20] it still remains unclear by which mechanism this is accomplished. For example, additives could either prevent the generation of alkoxide species in the first place, i.e., by being reduced preferentially and by resulting in a superior passivation of the anode, or they could scavenge initially formed alkoxides by direct chemical reactions.

In this paper, we investigate the effect of electrolyte additives and CO_2 on the trans-esterification reaction of the electrolyte in contact with a lithiated graphite electrode via On-line Electrochemical Mass Spectrometry.[21] By using a 2-compartment cell design which enables the separation of anode and cathode by a Li-ion conducting diffusion barrier,[22] the effect of species produced at the metallic lithium counter-electrode can be excluded. While the trans-esterification products of EC are not sufficiently volatile to be detected by OEMS, we will show that the conversion of the linear carbonate EMC into DMC and DEC is clearly detectable due to the higher vapor pressure of linear carbonates. Since the reduction of both cyclic and linear carbonates to alkoxides is accompanied by the evolution of CO,[23–25] we will use CO as an indicator for the generation of LiOR species. Based on these results, we study the extent of trans-esterification in the presence of VC and VEC at different concentrations. Both additives have been investigated in the literature with regards to their ability to suppress the trans-esterification reaction.[15,19,20] As the reduction of VC leads to a substantial evolution of CO_2,[26,27] we take a closer look at the effect of CO_2 on the trans-esterification reaction.

Experimental

Electrodes and electrolytes.—Graphite electrodes were made from SLP30 graphite powder (BET surface area of 7 $m^2\ g^{-1}$, TIMCAL, Switzerland). The electrode slurries were prepared by adding 10 wt% of polyvinylidene fluoride binder (PVDF, Kynar HSV 900, Arkema, France) to the graphite powder and mixing both components with *N*-methyl-2-pyrrolidinone (NMP, anhydrous, 99.5%, Sigma-Aldrich, Germany; solid content 30 wt%) for 10 min at 2000 rpm

*Electrochemical Society Student Member.
**Electrochemical Society Fellow.
[a]Present address: Robert Bosch LLC, Research and Technology Center, Palo Alto, California 94304, USA.
[z]E-mail: benjamin.strehle@tum.de

and 50 mbar in a planetary orbital mixer (Thinky, USA). The resulting slurries were blade-coated onto a porous polyolefin separator (thickness 21.5 μm, porosity 50%, C480, Celgard, USA) at a wet-film thickness of 250 μm using an automatic coater (RK PrintCoat Instruments, UK). After drying on a hot plate at 55°C over night in ambient air, electrodes with a diameter of 15 mm were punched out from the coating. The electrodes were further dried at 95°C for at least 12 h under dynamic vacuum in a glass oven (Büchi, Switzerland) and then directly transferred into an argon-filled glove box (O_2 and H_2O <0.1 ppm, MBraun, Germany). The graphite loading of the utilized electrodes ranges in between 6.4 ± 0.3 mg_C cm^{-2}, the electrode thickness is ≈70 μm, and the porosity is ≈50%.

The investigated electrolytes and additives were provided by BASF (Germany), except for $LiPF_6$ (battery grade, ≥99.99% trace metal basis; supplied from Sigma-Aldrich) and the pure linear carbonates (DMC and DEC: anhydrous, >99%; EMC: 99%; also supplied from Sigma-Aldrich), which were stored over a molecular sieve (0.3 nm, Merck, Germany). The standard electrolyte LP57 (1 M $LiPF_6$ in EC:EMC 3:7 by weight) and LP57-2 (LP57 + 2 wt% VC) were received ready-to-use. LP57 contained <20 ppm water as determined by Karl-Fischer titration (Titroline KF, Schott Instruments, Germany). All other electrolyte solutions were prepared and stored in aluminum bottles in the glove box. The additives VC and VEC were directly used without any purification or drying step and their amount is specified in terms of weight percent.

Cell assembly.—In order to investigate the direct and exclusive effect of different electrolyte additives on the graphite anode in Li-ion batteries, a recently developed 2-compartment cell was applied in this study.[22] In this cell setup, the graphite working-electrode (WE) and the lithium counter-electrode (CE) compartment are separated by a Li-ion conductive glass ceramic (LICGC, diameter 1 inch, thickness 150 μm, conductivity 10^{-4} S cm^{-1} at 25°C, Ohara, Japan), which is referred to as "Ohara glass" in the following text. The Ohara glass was laminated with several polypropylene (PP) sheets and an additional aluminum foil, all cut to annuli, in order to enable an effective edge-sealing (see Figure 1 in Ref. 22). In contrast to the former sealing by PP only,[28] the new PP/Al/PP sealing ensures a gastight separation between both compartments, so that the recorded OEMS signals from the WE compartment derive solely from reactions at the graphite electrode and the electrolyte in this compartment, without interference from the lithium counter-electrode.

In order to protect the Ohara glass from unwanted reactions with metallic lithium (diameter 17 mm, thickness 0.45 mm, 99.9%, Rockwood Lithium, USA), one sheet of C480 separator was placed between the lithium metal and the Ohara glass as well as between the SLP30 graphite electrode and the Ohara glass. A stainless steel mesh placed on top of the separator-coated graphite electrode serves as current collector (SS316, aperture 1 mm, wire diameter 0.22 mm, Spörl, Germany). This approach allows electrolyte access from both sides of the electrode, and gases evolved on the graphite surface can diffuse without significant time delay into the head space of the cell, from where they are fed into the mass spectrometer. The total amount of electrolyte is 120 μl (80 μl in the WE compartment and 40 μl in the CE compartment).

All pieces of cell hardware were dried for at least 12 h at 70°C in a vacuum oven (Thermo Fisher Scientific, USA) before usage. The single separator sheets were dried just as the electrodes for 12 h at 95°C under dynamic vacuum in a glass oven (Büchi, Switzerland).

On-line Electrochemical Mass Spectrometry (OEMS).—After assembly and sealing in the glove box, the cell was placed into a temperature-controlled chamber (Binder, Germany) held at 25°C. A crimped capillary leak (Vacuum Technology Inc., USA) connects the head space of the WE compartment to the mass spectrometer system (QMA 410, Pfeiffer Vacuum, Germany), permitting a defined gas flow of ≈1 μl min^{-1} from the cell head space to the crossbeam ionization source of the mass spectrometer. Furthermore, our OEMS setup is equipped with a quadrupole mass analyzer and a secondary electron multiplier (SEM), detecting mass-to-charge ratios between 1 and 90 amu within the scope of this study. For more details see our previous work.[21]

In order to remove any gas traces from the glove box atmosphere (under which the cell was assembled) and to obtain a stable background of the mass signals, the cell was purged initially with Ar for approximately 5 min and then held at open circuit voltage (OCV ≈ 3.2 V vs. Li/Li^+) for 4 h. Considering the gas flow of 0.05 l min^{-1} and the cell's head space volume of 8.5 ml, the atmosphere in the cell's head space is exchanged ≈30x during the purging step. Subsequently, a cyclic voltammetric (CV) formation was applied at a scan rate of 0.4 or 0.5 mV s^{-1} (Series G 300 Potentiostat, Gamry Instruments, USA). In contrast to a galvanostatic procedure, the potentiodynamic scan allows a more precise identification of the potential dependence of the observed mass spectrometric changes at the graphite WE, especially in the potential window above 0.5 V vs. Li/Li^+. In addition, it prevents an early cutoff of the graphite lithiation which can occur due to the significant iR-drop caused by the limited conductivity of the Ohara glass, as was shown previously.[29] The potential of the graphite electrode was ramped from OCV to 0 V vs. Li/Li^+ in the reduction (lithiation) step and from 0 to 1.5 V vs. Li/Li^+ in the oxidation (delithiation) step. Three such CV formation cycles were performed (whereby the last positive-going scan was let to continue up to the initial OCV value) and the gas phase was sampled continuously by OEMS. Conversion of the recorded ion currents into concentrations was done for hydrogen, ethylene, carbon monoxide, and carbon dioxide using two different calibration gases (gas I: Ar with 2000 ppm H_2, CO, O_2, and CO_2; gas II: Ar with 2000 ppm H_2, C_2H_4, O_2, and CO_2; Westfalen AG, Germany). The fragmentation pattern of CO_2 was determined independently from 1000 ppm CO_2 in Ar. When VEC was deployed as additive, 1,3-butadiene was quantified additionally with a calibration gas containing 1000 ppm C_4H_6 in Ar. Important parameters of the calibration are summarized in Table I. To avoid signal fluctuations due to minor pressure/temperature changes, all mass signal currents (I_Z) are normalized to the ion current of the ^{36}Ar isotope (I_{36}, referred to as I_Z/I_{36}).

Table I. Typical values of the calibration factors and fragmentation patterns determined for our OEMS system, referenced to gas concentrations of 2000 ppm in Ar. The mass signals provided with an asterisk are the standard m/z signals used for the quantification of the respective gas.

Gas	Mass signal m/z	Calibration factor[a]	Fragmentation[b]
H_2	2*	0.15	100%
C_2H_4	28	0.60	100%
	27	0.36	60%
	26*	0.38	63%
	25	0.08	13%
CO	28*	0.64	100%
	12	0.03	5%
CO_2	44*	0.58	100%
	28	0.08	14%
	12	0.07	12%
C_4H_6	54	0.25	49%
	53	0.19	37%
	51	0.09	17%
	50	0.10	20%
	39*	0.52	100%
	28	0.33	63%
	26	0.17	33%

[a]The calibration factor corresponds to the averaged increase of the respective ion current ratio I_Z/I_{36} when the cell is flushed with the calibration gases.
[b]The fragmentation is stated in percentage terms relative to the strongest signal for the given gas.

Table II. Overview of the performed OEMS measurements in this study. All measurements were conducted in a 2-compartment cell, in which anode and cathode compartments are sealed hermetically from each other.

#	Electrolyte	Loading [$mg_C\ cm^{-2}$]	Scan rate [$mV\ s^{-1}$]	Figures
1	LP57	5.9	0.5	1, 2, 4
2	+ 2% VC	6.4	0.5	1, 4
3	+ 1000 ppm CO_2	5.9	0.4	1, 4
4	1 M $LiPF_6$ in EMC	6.7	0.4	5, 6, 7
5	+ 1000 ppm CO_2	6.2	0.4	6, 7
6	+ 10% CO_2	6.7	0.4	6, 7
7	LP57 + 2% VEC	6.7	0.5	8, 9
8	LP57 + 0.2% VEC	6.6	0.4	10, 11
9	LP57 + 0.2% VC	6.6	0.5	10, 11

Since the main signal of CO at m/z = 28 is superimposed by signals from C_2H_4 and/or CO_2, determination of the CO signal $I_{28\,(CO)}$ requires that the contributions to I_{28} from C_2H_4 and from CO_2 have to be subtracted. Based on the mass signals at m/z = 26 (unique to C_2H_4) and 44 (unique to CO_2), their contribution to I_{28} is calculated using the measured fragmentation of C_2H_4 and CO_2 in our mass spectrometer system (see Table I). Consequently, CO can be quantified on the mass signal at m/z = 28 as follows: $I_{28\,(CO)} = I_{28} - 1/0.63 \cdot I_{26} - 0.14 \cdot I_{44}$. In experiments with the model electrolyte 1 M $LiPF_6$ in EMC in the presence of CO_2, the amount of CO was also calculated from the mass signal at m/z = 12: $I_{12\,(CO)} = I_{12} - 0.12 \cdot I_{44}$. When VEC was added to the electrolyte, the intensity of 1,3-butadiene was subtracted analogously from channel m/z = 26 to quantify C_2H_4: $I_{26\,(C2H4)} = I_{26} - 0.33 \cdot I_{39}$.

While the calibration is only valid for a pure Ar gas phase in the cell's head space, the vapor pressure of the electrolyte (4.3 kPa for LP57 at 25°C, i.e., contributing to ≈4% of the gas phase in the cell) and the presence of other gases at the level of up to several thousands of ppm (<1%) do not cause any notable deviation. When studying the effect of CO_2 in combination with the model electrolyte 1 M $LiPF_6$ in EMC, however, the cell was purged initially with a 10% CO_2 in Ar gas. In this case, the concentrations have to be corrected by the factor 0.90, because the gas phase consists only to 90% of Ar and thus, the ion current of the ^{36}Ar isotope used for normalization is smaller. The original intensity of the pure 10% CO_2 in Ar gas is $I_{44}/I_{36} = 31.0$. If this factor is referenced to 2000 ppm (as was done for the calibration gases, see Table I), it equates to $31.0 \cdot 0.02 = 0.62$, which after correction for the reduced Ar pressure results in $0.62 \cdot 0.90 = 0.56$. The calibration factor obtained from the 10% CO_2 in Ar gas differs by only 3% from that obtained for the calibration gases containing 2000 ppm CO_2 (determined as 0.58, see Table I), demonstrating that the mass spectrometer has a sufficiently linear response between ca. 10^3 to 10^5 ppm. Gas concentrations are converted in gas moles by using the ideal gas law and the volume of the cell (i.e., 1000 ppm = 0.35 μmol for a cell volume of 8.5 ml and a temperature of 25°C).

The ion currents I_Z/I_{36} were smoothed with the Savitzky-Golay smoothing routine at a window of 120 points (one data point every ≈10 s results in a smoothing range extending over 20 min). In order to describe the change of relevant mass signals in terms of gas evolution/consumption and trans-esterification, three different representations are applied in the following: (i) the original ion currents I_Z/I_{36}; (ii) the ion currents subtracted by the respective background intensity, which was extrapolated from the initial OCV phase; and, (iii) the ion currents normalized to the background intensity. Using the calibration factors (see Table I), the gas concentrations were calculated from the background-corrected signals obtained by procedure (ii). Representation (iii) allows estimating the relative consumption of EMC and thus the extent of trans-esterification.

Table II gives an overview of the OEMS measurements presented within this study, highlighting the different electrolyte compositions.

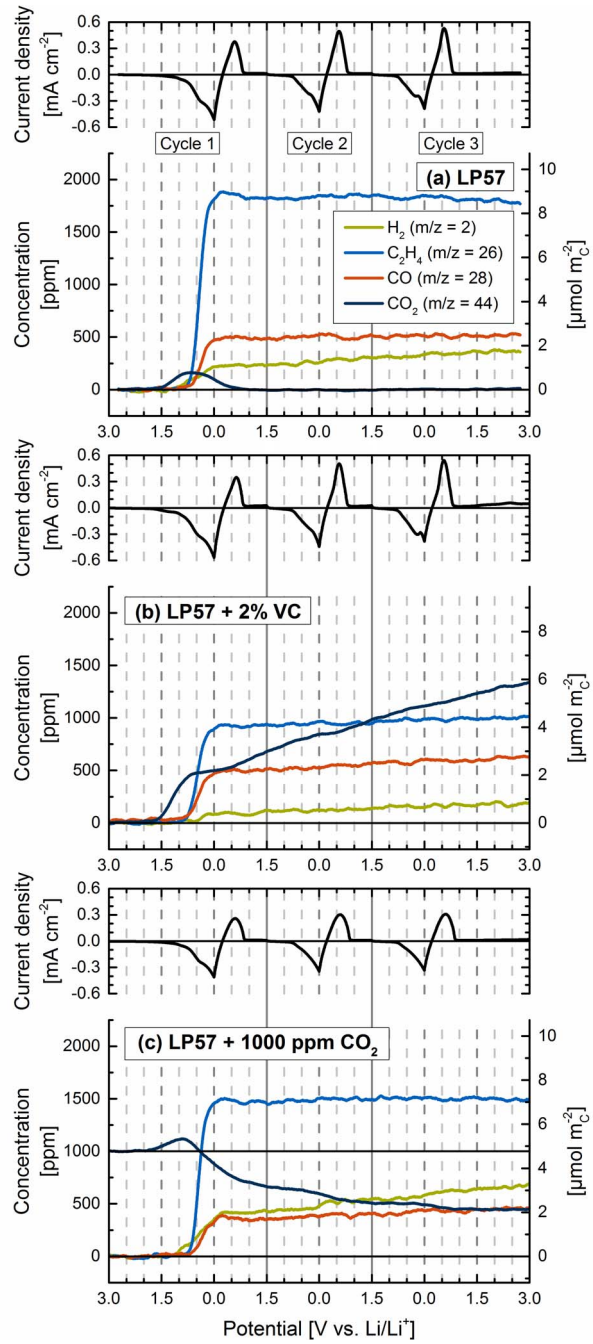

Figure 1. Three CV formation cycles of an SLP30 graphite electrode vs. metallic lithium in a sealed 2-compartment cell (PP/Al/PP edge-sealing) with three different electrolytes: (a) LP57, (b) LP57 + 2% VC, and (c) LP57 + 1000 ppm CO_2. For each electrolyte, the current-potential profile is shown in the upper panel, whereas the evolved concentration of H_2 (m/z = 2), C_2H_4 (m/z = 26), CO (m/z = 28), and CO_2 (m/z = 44) in units of ppm (left axis) and μmol m_C^{-2} (right axis) is depicted in the lower panel. The initial OCV phase prior to formation is omitted. For the last measurement, the baseline of the CO_2 signal is set to 1000 ppm, indicating its initial concentration.

Results and Discussion

Gas evolution in LP57-based electrolytes.—Figure 1 shows three CV formation cycles of an SLP30 graphite electrode vs. a metallic lithium CE for the electrolytes LP57 (a), LP57 + 2% VC (i.e., LP57-2; b), and LP57 + 1000 ppm CO_2 (c). For each electrolyte, the current-potential profiles are shown in the upper panel, while the corresponding gas evolution is shown in the lower panel. Similar

results for LP57 and LP57-2 have already been presented in a previous publication by our group,[27] proving the reproducibility of the OEMS measurements. The gas evolution is given in units of ppm (left axis) and also converted into a surface-normalized concentration in units of μmol m_C^{-2} (right axis). This approach compensates for the small differences in the loading of the graphite electrodes (see Table II).

For the additive-free electrolyte LP57 (see Figure 1a), ethylene is the main gas evolved at the graphite electrode and its concentration amounts to ≈1900 ppm (≈9.0 μmol m_C^{-2}). It is released exclusively in the first cycle at potentials below 0.9 V vs. Li/Li$^+$, accompanied by a reduction peak in the current-potential profile. For graphite electrodes with a comparable loading (in a previous cell design with an unsealed Ohara glass), we reported similar ethylene concentrations after the first cycle of ≈2150 ppm for LP57[27] and ≈2000 ppm for 1 M LiTFSI in EC:EMC (3:7 by weight).[29] Ethylene originates from the reductive decomposition of EC by the following reactions, which were first proposed by Aurbach and co-workers[30] (see also Zhang[7]):

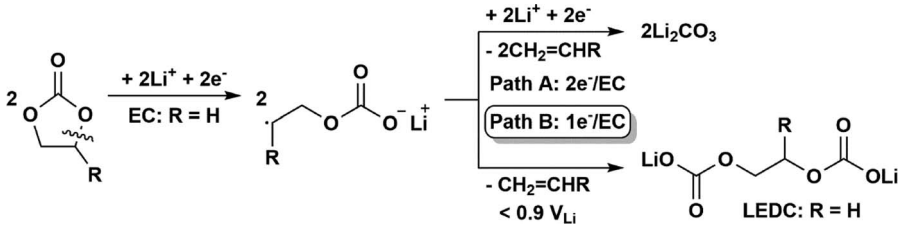

[1]

While lithium ethylene dicarbonate (LEDC) was identified as one of the main components of the SEI on graphite electrodes (Path B),[31] the reductive formation of lithium carbonate is still debated in the literature (Path A).[6] LEDC belongs to the group of semicarbonates ($LiOCO_2R$) and improves the SEI stability due to the formation of a network between organic compounds through the coordination of Li-ions and organic carbonate anions.[7] Regarding Li_2CO_3, Zhao et al. reported that its abundance in the SEI is higher for aged graphite electrodes than for freshly cycled ones,[32] which suggests that Li_2CO_3 might be a degradation product of the initially formed SEI compounds. Other researchers believe that large amounts of Li_2CO_3 can be partially ascribed to poor moisture management and the consequent hydrolysis of semicarbonate species.[30,33] According to this literature, we believe that EC conversion into LEDC is favored over the formation of Li_2CO_3 during the first reductive scan of a graphite electrode.

If one were to assume that Path B (i.e., LEDC formation) is the main pathway for electrolyte reduction, one could estimate the coverage of the graphite surface based on the evolved amount of C_2H_4 for LP57. The hexagonal lattice of a graphene layer with a C-C distance of 0.142 nm corresponds to a surface concentration of ≈65 μmol_C m_C^{-2}, neglecting any edge sites and surface groups. If LEDC were to be bound in a planar configuration with each C and O atom (i.e., 10 atoms) adjacent to one C atom of the graphite surface, the SEI film would correspond to ≈1.4 monolayers of LEDC (based on $(10 \cdot 9.0\ \mu mol_{LEDC}\ m_C^{-2}) / (65\ \mu mol_C\ m_C^{-2})$). This, of course, is only an order of magnitude estimate. Without knowing the exact SEI composition, this calculation provides just a lower limit of the coverage because other frequently reported decomposition products like Li_2CO_3, $LiOCO_2R$, LiF, $Li_xPF_yO_z$ and polymeric species are not taken into account.[6,31,34] Using Faraday's law and $2e^-/C_2H_4$ (correct for both reaction pathways in Equation 1), the associated capacity for C_2H_4 formation alone amounts to ≈3.4 mAh g_C^{-1}, which corresponds to ≈20% of the irreversible capacity loss (ICL) measured during the first CV scan shown in Figure 1a. Consequently, more reduction reactions other than those leading to the evolution of C_2H_4 must be taking place.

Apart from C_2H_4, CO has been observed during the reduction for several electrolyte compositions, e.g., $LiPF_6$/EC/DMC[26] and $LiPF_6$/EC/DEC.[23] As shown in Figure 1a for LP57, its concentration amounts to ≈500 ppm (≈2.4 μmol m_C^{-2}) and is ≈4x smaller than that of C_2H_4, indicating a minor reduction pathway of EC via an intermediate acyl radical:[23]

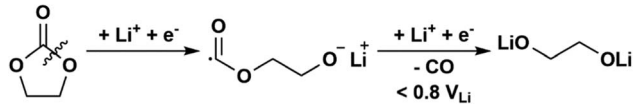

[2]

Using isotopically labeled electrolytes, Onuki et al. have shown that CO originates predominantly from EC and not from the linear carbonates. This was hypothesized by Shin and co-workers to be due to a stronger interaction of EC with the graphite surface due to its cyclic structure and higher polarity.[35] However, since a reductive scan in 1 M $LiPF_6$ in pure EC reveals a higher C_2H_4/CO ratio of ≈9/1,[36] it is likely that CO also derives partially from the reductive decomposition of the co-solvent EMC, as was proposed by Yoshida et al.:[11]

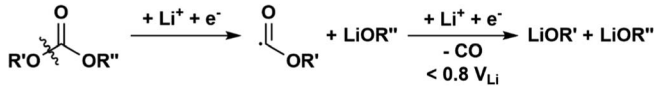

[3]

where R′ represents a methyl group and R″ an ethyl group (or vice versa). The evolution of CO from EC or EMC reduction is accompanied by the release of alkoxide-type species (LiOR).

In our previous publications, the evolution of H_2 was rationalized by the reduction of residual moisture in the electrolyte:[27,29]

$$H_2O \xrightarrow{+e^-} 0.5H_2 + OH^- \quad [4]$$

For this reaction, the released amount of ≈250 ppm H_2 shown in Figure 1a would correspond either to a trace water contamination of ≈30 ppm in the electrolyte or to ≈0.03 wt% in the active material, which seems reasonable. However, Imhof and Novák quote different potential-dependent processes which lead to the evolution of H_2:[37] a first reduction process at approximately 1.3 V vs. Li/Li$^+$, which they assigned to the electrochemical reduction of the H_2O-containing solvation shell of the Li-ions, followed by a second H_2 evolution process starting at ca. 0.8 V vs. Li/Li$^+$, simultaneously with the evolution of C_2H_4, which is thought to have a different origin. Since we detect H_2 only below 1 V vs. Li/Li$^+$, it is rather difficult to determine the underlying mechanism. Except for trace water in the cell, H_2 might also originate from H-containing surface groups of the graphite electrode or the electrolyte solvents and their decomposition products.[38] Furthermore, impurities from the manufacturing process of the solvents could also yield H_2 in a reductive process.

Finally, the CO_2 signal differs from our previous measurements that did not yet employ the PP/Al/PP edge-sealed 2-compartment cell.[27,29] Without the edge-seal, ≈200 ppm CO_2 were consumed in parallel to the evolution of C_2H_4 (see Figure 9 in Ref. 27 or Figure 2 in Ref. 29). Using the PP/Al/PP edge-sealing, we observe in Figure 1a first an increase of the CO_2 signal starting at ≈1.5 V vs. Li/Li$^+$ prior to the evolution of C_2H_4 and reaching a maximum of ≈150 ppm CO_2 at ≈0.9 V vs. Li/Li$^+$. Afterwards, the signal drops back to zero, i.e.,

the evolved amount of CO_2 is completely consumed in the course of the SEI buildup. The difference between the two otherwise identical measurements arises from the improper shielding of the lithium CE in the case of the Ohara glass without an edge-seal. As the reduction of H_2O (Equation 4) is expected to start immediately when the electrolyte comes in contact with metallic lithium, the thus produced OH^- anions would initiate the potential-independent hydrolysis of EC, releasing CO_2 at a reasonably high rate already at room temperature:[39]

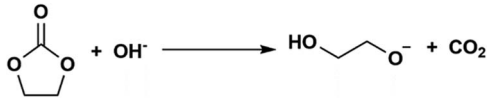

[5]

As the decomposition reaction already takes place during the initial OCV phase and as the unsealed Ohara glass used in References 27 and 29 does not prevent gas diffusion between the CE and WE compartments, CO_2 formed at the lithium CE can react on the surface of the graphite WE when its potential is being decreased during the CV procedure. When applying the PP/Al/PP edge-sealing as in this work, no CO_2 can diffuse into the working-electrode compartment, but we believe that the reduction of a minor fraction of H_2O (or other trace contaminants like HF or alcohols) at the graphite electrode at ≈1.5 V vs. Li/Li^+ initiates the hydrolysis of EC, resulting in the release of CO_2 directly in this compartment. The mechanism of CO_2 consumption below 1.0 V vs. Li/Li^+ will be discussed in detail later.

Upon addition of 2% VC to LP57 electrolyte (see Figure 1b), the evolved amount of C_2H_4 decreases to ≈950 ppm (≈4.2 μmol m_C^{-2}), and thus is reduced by more than 2-fold compared to LP57. An equally striking difference is that the evolution of CO_2 starts at already ≈1.7 V vs. Li/Li^+ and accumulates to ≈700 ppm at the end of the first cycle. CO_2 originates from VC, which is reduced at potentials much higher than EC via the following decomposition pathway, evidenced by OEMS experiments[27] and also supported by ab initio modeling:[40]

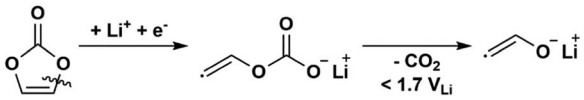

[6]

The intermediate radical anions shown in Equation 6 can react chemically with VC and lead to the potential-independent polymerization of VC, releasing large quantities of CO_2 also in the following cycles.[27] The incorporation of poly(VC) is believed to result in a more stable SEI,[26,41] which in turn lowers the extent of EC reduction, indicated by the ≈2-fold lower amount of C_2H_4 (see Figure 1b). In contrast, the onset potential for CO formation (≈0.8 V vs. Li/Li^+) and the released amount of CO (≈500 ppm) is barely affected by the addition of VC. The CO_2 signal becomes flat concomitant to the evolution of C_2H_4, i.e., CO_2 evolution seems to stop. Even though EC and VC compete in this potential region for being reduced on the graphite surface, it is unlikely that the evolution of CO_2 stops abruptly. Similar to the CO_2 consumption observed for LP57 once C_2H_4 is being evolved (see Figure 1a), this finding rather suggests that CO_2 participates in some way in the processes at the electrode-electrolyte interphase, consistent with past studies on CO_2 as electrolyte additive, where it was suggested to stabilize the SEI.[7,42,43]

In order to further investigate the consumption of CO_2, a cell with LP57 electrolyte was purged with a 1000 ppm CO_2 in Ar mixture (instead of pure Ar) prior to the OEMS measurement (see Figure 1c). This concentration is of the same order of magnitude as the amount released from LP57 + 2% VC shown in Figure 1b (note that the molar ratio of 2% VC added to the electrolyte and 1000 ppm CO_2 introduced in the cell's head space is ca. 65/1). After an initial increase of the CO_2 signal (analogous to that observed for LP57, see Figure 1a), a total of ≈500 ppm CO_2 are consumed within the first cycle once the potential falls below 0.8 V vs. Li/Li^+. The consumption of CO_2 continues to a decreasing extent at the reversing potential at 0 V vs. Li/Li^+ in the following cycles. The released amount of C_2H_4 is slightly reduced to ≈1500 ppm (≈7.0 μmol m_C^{-2}), a clearly smaller effect than that seen for 2% VC. This result indicates that CO_2 has some positive effect on passivating the graphite surface. Consequently, the beneficial impact of VC could also be partially attributed to the release of CO_2 and its subsequent contribution to the SEI buildup.

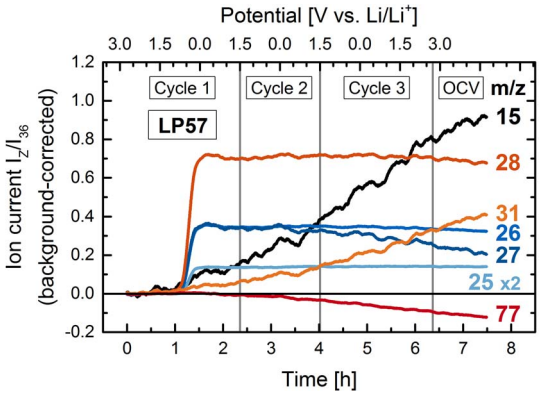

Figure 2. Development of other relevant mass signals in the course of the measurement for the standard electrolyte LP57 shown in Figure 1a. The signals are background-corrected (according to procedure (ii) described in the last paragraph of the Experimental section) and shown for all three CV formation cycles, followed by a final ≈1 h OCV hold. The sharp increase of the signals at m/z = 25–28 at ≈1 h is due to the evolution of C_2H_4, whereas the subsequent changes on all channels are caused by a steady conversion of the co-solvent EMC.

Trans-esterification in LP57-based electrolytes.—So far, we exclusively discussed the mass signals that can be quantified with our calibration gases. In the following, we want to focus on the other mass traces that change during the CV formation procedure. Figure 2 gives an overview of the time- and potential-dependent changes of characteristic mass signals for the LP57 measurement (shown in Figure 1a). It is apparent that the mass signals at m/z = 26, 27, and 28 decrease gradually after their maximum values were reached at ≈1.5 h. Interestingly, the signal m/z = 77 decreases at the same time, indicating the consumption of some species, which must have been in the cell's head space already at the beginning of the experiment. Apart from that, the signal m/z = 25 stays constant, while m/z = 15 and 31 increase strongly. The onset of these changes coincides with the SEI-related gas evolution in the first cycle. In our previous study, the steady decrease of the signal m/z = 26 used for ethylene quantification raised the question whether C_2H_4 might be gradually consumed after its release during the SEI buildup or whether this observation is influenced by the EMC component in the electrolyte.[27] Comparing all relevant mass fragments of ethylene (m/z = 25–28 for C_2H_n, n = 1–4, with m/z = 28 also being a fragment of CO and CO_2, see Table I), the relative intensity ratio of these ion currents would have to remain constant during the entire measurement, if they were to belong to the same species. However, the signal m/z = 25 stays constant, while the signals at m/z = 26–28 decrease at different rates, so that the behavior of these signals cannot be simply explained by a consumption of C_2H_4.

This points toward the possibility that the above discussed changes arise from a notable (bulk) conversion of the co-solvent EMC, which is responsible for most of the background intensity on all channels, owing to its 4 orders of magnitude higher vapor pressure than EC.[28] This assumption is supported by the following facts: (i) the decrease of m/z = 77 can only be attributed to the conversion of EMC, since no gas featuring this fragment was introduced into the cell or evolved earlier during the measurement; (ii) the signals at m/z = 15 and 31 represent the mass fragments CH_3 and OCH_3, which occur in EMC and also in its conversion product(s); and, (iii) the mass traces which show the largest changes have also a significant background intensity during the initial OCV phase (in the sequence m/z = 26 < 77 < 28 < 31 < 27 < 15; later discussed in Figure 3). As the background intensity of m/z = 25 is weak (100 times smaller than m/z = 15), it

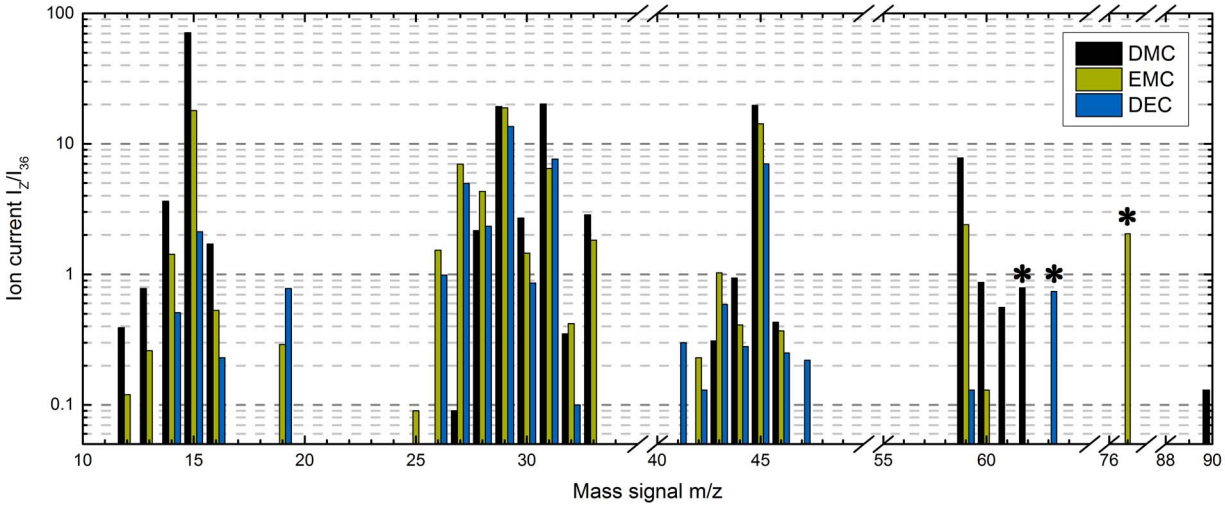

Figure 3. Fragmentation pattern of the pure solvents DMC (black), EMC (green), and DEC (blue). All ion currents between m/z = 1 and 90 with an intensity of $I_z/I_{36} \geq 0.1$ are shown. The signals which also represent mass fragments from H_2 (m/z = 1, 2) and H_2O (m/z = 17, 18) are omitted, because their intensity was already higher than 0.1 in an empty cell. The most intense signals exclusively attributable to one single solvent are indicated by an asterisk: DMC (m/z = 62), EMC (m/z = 77), and DEC (m/z = 63).

reflects only the development of ethylene and stays constant after its release in the first cycle (m/z = 25 corresponds to 13% of the main peak 28, see Table I).

In the literature, it is described that linear carbonates undergo an ester exchange reaction, also called trans-esterification, which in the case of EMC would lead to the formation of DMC and DEC:[11,12]

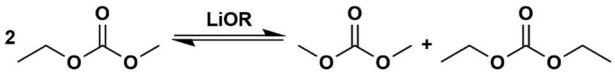

[7]

The conversion of EMC into DMC and DEC is reversible and is initiated during the first formation cycle, i.e., during the lithiation of the anode. Its extent is highly dependent on the reaction conditions (including the electrolyte composition, use of additives, temperature, etc.) and the effectiveness of the anode passivation. Even though the trans-esterification can also be triggered at elevated temperatures by the Lewis acid PF_5, which is in equilibrium with the conducting salt $LiPF_6$,[44] mechanistic studies from Takeuchi et al. found that alkoxide species (LiOR) are responsible for the ester exchange reaction observed at room temperature.[12] LiOR act as a nucleophile and attack the carbonyl atom of EMC to give a tetrahedral intermediate, which either reverts to the starting molecule or proceeds to the trans-esterified product. Its influence on the electrolyte was further confirmed by storage experiments, where the addition of LiOMe to the electrolyte system $LiPF_6$/EC/DMC noticeably alters the gas chromatographic profile, i.e., it yields a larger number and higher concentration of decomposition products.[45] Additionally, the presence of alkoxide species leads to the formation of alkyl dicarbonates through the ester exchange-like dimerization of EC with linear carbonates.[13,15] The alkoxide solubility in alkyl carbonate solvents was determined to be in the range of 10^{-3} to 10^{-2} mol l^{-1}.[46]

LiOR itself are formed by the reductive decomposition of EC and/or EMC (or other alkyl carbonates) on the graphite anode, which is accompanied by the evolution of CO (see Equations 2 and 3). The fact that the mass spectrometric changes in Figure 2 start simultaneously with the evolution of CO (i.e., at ≈0.8 V vs. Li/Li^+ during the first reductive scan) thus supports our above hypothesis that this may be related to the trans-esterification of EMC. Since the trans-esterification is a chemical rather than an electrochemical reaction (see Equation 7), it would thus be expected to be potential-independent (once it has been initiated). This fits well to the observation that the signal changes continue during the final OCV period at ≈3 V vs. Li/Li^+ (see right-hand side of Figure 2). If this explanation were true, i.e., if EMC were to be gradually converted into DMC and DEC, the changes of the OEMS ion currents would have to be related to their differences in vapor pressure and fragmentation pattern.

In order to obtain the fragmentation patterns of the linear carbonates DMC, EMC, and DEC, the cell was assembled with 80 μL of the respective solvent pipetted onto a glass fiber separator. After initial purging with pure Ar, the solvent background signals were recorded for ≈3 h, during which they quickly reached a constant value. Then, the I_Z/I_{36} ion signals were averaged over the last 1.5 h of the measurement. Figure 3 shows all mass signals of DMC, EMC, and DEC, which exceed a relative intensity of $I_z/I_{36} \geq 0.1$. Fortunately, the fragmentation patterns of the linear carbonates allow a clear distinction between them. Regarding the mass signals m/z = 12, 13, 14, and 15, which belong to the fragments CH_n (n = 0–3), DMC has the strongest intensity, followed by EMC and DEC. This difference is probably not only caused by the higher vapor pressure of DMC,[28] but it also reflects the fact that DMC has two methyl groups connected to the carbonate unit.

The mass signals which showed the unexplained changes during the CV procedure with the standard electrolyte LP57, and which were discussed in Figure 2, are indeed the most pronounced traces of EMC (in addition to m/z = 29, 45, and 59). However, it is difficult to evaluate if the overall intensity of the respective channel should increase or decrease due to trans-esterification, because all three carbonates produce notable ion currents on these channels. As EMC is being converted, all of the above mentioned mass signals decrease, but at the same time they increase to different extents due to the formation of DMC and DEC. Based on Equation 7, we can estimate the expected intensity change as follows from Figure 3: $\Delta I = 0.25 \cdot (I_{DMC} + I_{DEC}) - 0.5 \cdot I_{EMC}$. If ΔI is smaller than zero, the ion current decreases in the course of the trans-esterification, whereas it increases when ΔI is greater than zero. Due to this complexity, it is helpful to focus on unique signals for each solvent, such as m/z = 62 for DMC, m/z = 77 for EMC (already considered in Figure 2), and m/z = 63 for DEC. The intensity of the other two solvents is ≈40-fold (DEC), ≈200-fold (DMC), and even ≈800-fold (EMC) smaller on these three selected m/z values.

Figure 4 gives an overview of these three mass traces, namely m/z = 77 (representative of EMC), 62 (representative of DMC), and 63 (representative of DEC), during three CV cycles with LP57, LP57 + 2% VC, and LP57 + 1000 ppm CO_2. This plot enables to evaluate the extent of the trans-esterification for each electrolyte. For LP57 (solid lines in Figure 4), the EMC signal at m/z = 77 falls by ≈10% until the

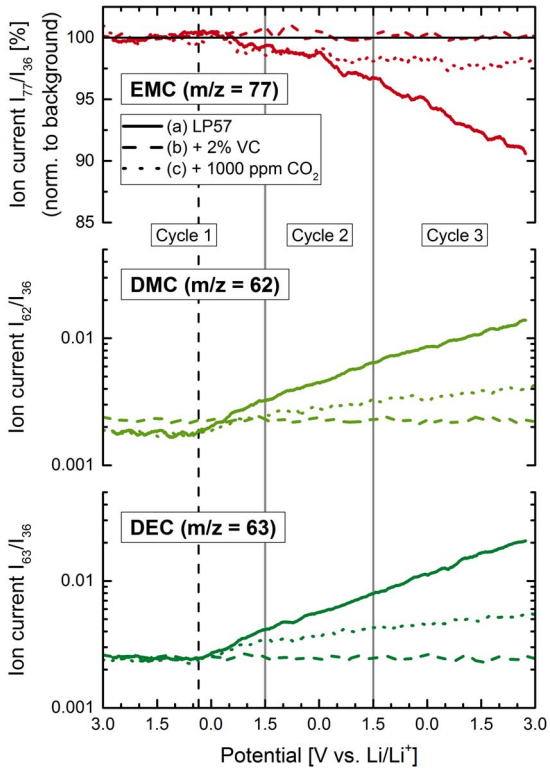

Figure 4. Development of the I_{36}-normalized mass signals at m/z = 77 (top), m/z = 62 (middle), and m/z = 63 (bottom) during the CV formation (experiments shown in Figure 1) in the following electrolytes: (a) LP57 (solid), (b) LP57 + 2% VC (dashed), and (c) LP57 + 1000 ppm CO_2 (dotted). The signal m/z = 77 is normalized to the background intensity during the initial OCV period, whereas the other two are shown as the original signal (according to procedure (iii) and (i) described in the last paragraph of the Experimental section). The dashed vertical black line marks the onset of trans-esterification.

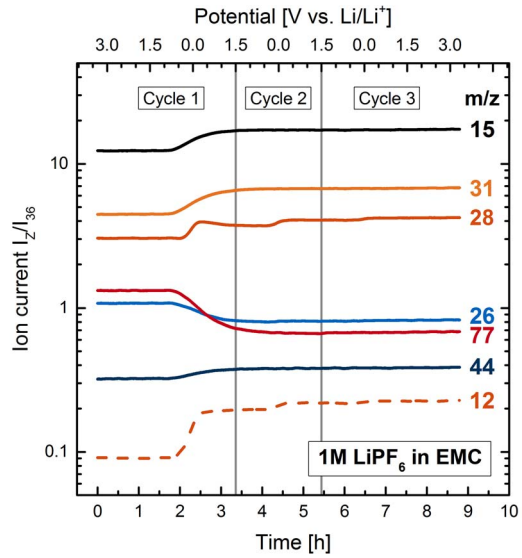

Figure 5. Development of several mass signals in the course of three CV formation cycles for the model electrolyte 1 M $LiPF_6$ in pure EMC on SLP30 graphite (2-compartment cell with metallic lithium CE). The original ion current ratios I_Z/I_{36} (i.e., representation (i) without background correction) are shown to easily identify the variation on each channel due to the fast conversion of EMC into DMC and DEC.

end of the CV procedure. Note that the ion current I_{77}/I_{36} is normalized to its value during the initial OCV period, thus corresponding to 100% EMC. Assuming a complete conversion of EMC to the equilibrium state of the trans-esterification reaction, the electrolyte would ultimately consist of 50% EMC, 25% DMC, and 25% DEC in a dynamic equilibrium (see Equation 7). Here, ≈20% of the conversion seems to be completed by the end of the three CV cycles, i.e., the reaction still has not reached its equilibrium. The formation of DMC and DEC is validated on the channels m/z = 62 and 63, which have an intensity of $I_Z/I_{36} \approx 2 \cdot 10^{-3}$ at the beginning of the measurement, close to their detection limit of $I_Z/I_{36} \approx 0.5 \cdot 10^{-3}$ (note that these ion current ratios are shown in a logarithmic scale, and that the background intensity from EMC is negligible on these channels). However, when the potential falls below ≈0.4 V vs. Li/Li^+ in the first cycle, which corresponds to the maximum of the CO evolution rate during SEI buildup (see Figure 1a), the ion currents start to rise almost linearly by one order of magnitude until the end of the third cycle. Since all three signals change uniformly, one could conclude that the LiOR concentration in the electrolyte is constant once the reaction was initiated in the first cycle. This finding is consistent with the fact that no further CO evolution is observed after the first cycle in LP57 (see Figure 1a). Hence, the concentration of LiOR species should remain constant after the first cycle according to Equations 2 and 3. This would in turn confirm the observed constant and potential-independent trans-esterification rate.

In contrast, all three mass signals stay constant during the whole measurement when VC is added to the electrolyte (dashed lines in Figure 4). This means that the trans-esterification is completely inhibited, in agreement with results from Petibon and co-workers.[19] As the evolution of CO is barely affected by the presence of VC (see Figure 1b), LiOR species are still expected to be formed, so that the released LiOR species have to be trapped before they trigger the conversion of EMC. This type of trapping mechanism is consistent with Sasaki et al., who suggested that VC is vulnerable to the nucleophilic attack by alkoxide anions to form alkoxy ethylene carbonate.[47] Another possibility, however, is the reaction of LiOR with the released CO_2 to form $LiOCO_2R$, thereby preventing the trans-esterification, as will be discussed further below.

As a matter of fact, the addition of 1000 ppm CO_2 to LP57 (dotted lines in Figure 4) significantly reduces the rate of trans-esterification, even though it does not completely suppress it as in the presence of 2% VC. The signal m/z = 77 falls only by ≈2% (vs. ≈10% in pure LP57) and the increase on the other two channels is also lowered by a factor of ca. 6. Even though the trans-esterification is not completely suppressed by 1000 ppm CO_2, its inhibition in the presence of VC might be related, to some extent, to the presence of CO_2 which is produced during VC reduction. The underlying mechanism will be reviewed in detail later. All in all, the time-resolved analysis of the mass signals m/z = 62, 63, and 77 by OEMS is a powerful method to study the conversion of EMC into DMC and DEC in Li-ion batteries.

Reactivity of pure EMC and the impact of CO_2.—The previous part revealed among other things that (i) the co-solvent EMC undergoes a trans-esterification into DMC and DEC in the absence of any electrolyte additive and that (ii) CO_2 is capable of partially suppressing this reaction. Since the reactivity of EMC at the electrode-electrolyte interphase is superimposed by EC in the standard electrolyte LP57, the formation of a graphite electrode was repeated in the model electrolyte 1 M $LiPF_6$ in EMC with and without CO_2 added at two different concentrations. Recently, EC-free electrolytes excited great interest for application in Li-ion batteries.[48,49] Without any influence from the EC component, we sought to gain a better mechanistic insight into the processes at the electrode-electrolyte interphase and elucidate the role of CO_2. Here, it should be noted that previous results suggest that the trans-esterification is accelerated in EMC-only electrolyte and the reaction even happens quantitatively without the use of additives.[11,48,49]

As the gas quantification in EMC-only electrolyte may be more difficult if the extent of trans-esterification is increased compared to that in LP57, we will first present in Figure 5 an overview of the mass signals considered in the previous section for the EMC-only

electrolyte (1 M $LiPF_6$ in EMC). It shows the same set of signals as in the standard electrolyte LP57, namely signals which either increase (m/z = 15, 31) or decrease due to the conversion of EMC (m/z = 26, 28, 77), as shown in Figure 2. In contrast to LP57, these ion currents reach a constant plateau within the second cycle in the EMC-only electrolyte (see Figure 5). This behavior appears on almost all channels and thus suggests that the trans-esterification proceeds to its equilibrium within the second cycle. Apart from H_2, we observe a "real" gas evolution which is not related to trans-esterification only for CO (i.e., C_2H_4 and CO_2 are absent). The stepwise increase of all the mass signals related to CO in every cycle, namely m/z = 28 (main fragment of CO), 16 (not shown), and 12, serves as a characteristic fingerprint for CO. In order to estimate the evolved amount of CO, the gas was not only quantified on the typical channel m/z = 28 but also on m/z = 12 (see Experimental section). Based on the fragmentation patterns of the linear carbonates in Figure 3, however, it is quite likely that both mass signals are superimposed by trans-esterification ($\Delta I > 0$ for m/z = 12 and $\Delta I < 0$ for m/z = 28). Hence, the quantification of CO is not as precise as in the previous experiments and should be considered only semi-quantitative in the following analysis.

Figure 6 shows all three CV formation cycles of an SLP30 graphite electrode vs. metallic lithium in 1 M $LiPF_6$ in EMC without additional CO_2 (a) as well as with 1000 ppm (b) and 10% CO_2 (c) in the cell's head space. In the CO_2-free electrolyte (see Figure 6a), there is a strong evolution of CO that starts at ≈0.7 V vs. Li/Li^+ in the first reduction step (≈100 mV lower than in LP57) and continues until ≈0.5 V vs. Li/Li^+ after scan reversal (the potential values are based on m/z = 12, see dashed red line). Since the passivating properties of the SEI mostly originate from the reductive decomposition products of EC, the graphite surface is less effectively protected against the ongoing reduction of EMC, so that the amount of CO further increases stepwise in the second and third cycle. This result is in contrast to the complete cessation of CO evolution after the first cycle in LP57 (see Figure 1a), but is in accord with the literature where surface analysis techniques have shown that an EMC-derived SEI is non-uniform and thinner compared to an EC-based SEI.[31,50] The decrease of the signal m/z = 28 after the initial release of CO in the first cycle can be ascribed to an enhanced trans-esterification, which is reasonable because the increased evolution of CO implies a higher concentration of LiOR in the electrolyte (see Equation 3). As described above, the CO amount calculated from the signal on m/z = 12 is overestimated due to the conversion of EMC ($\Delta I > 0$), while that calculated from m/z = 28 is underestimated ($\Delta I < 0$). Thus, the concentration in the first cycle extracted from both channels represents limit values. The evolution of ≈4000–5000 ppm CO in the first cycle is followed by an additional amount of ≈1200 ppm and ≈500 ppm CO in the second and the third cycle (independent of the channel used for quantification). As the conversion of EMC into DMC and DEC has already reached equilibrium, it does no longer contribute to the mass signal change ΔI in the second and third cycle. The evolution of CO is restricted to potentials below 0.5 V vs. Li/Li^+ and the rate is maximum at the reversing potential of 0 V vs. Li/Li^+.

When 1000 ppm CO_2 are added to the cell's head space (see Figure 6b), this amount is completely consumed within the first cycle. Note that the plotted "apparent" CO_2 concentration does not fall to zero because the signal m/z = 44 is also superimposed by trans-esterification ($\Delta I > 0$). Since the CO signals are not affected by the addition of 1000 ppm CO_2 (compare Figures 6a and 6b), the conversion of EMC seems to take place in the same way as in the CO_2-free electrolyte. Consequently, the increase of the signal m/z = 44 for 1 M $LiPF_6$ in EMC (without added CO_2) in Figure 5, $\Delta(I_{44}/I_{36}) = 0.055$, matches quite accurately to the apparent 250 ppm CO_2 which are "left" in this experiment ($0.055 \cdot 2000/0.58 \approx 200$ ppm CO_2, using the calibration factor of 0.58 from Table I). Note that the error is transferred to the CO signals, because the intensity from CO_2 is proportionally subtracted from the signals used for CO quantification. In order to keep both measurements comparable, the CO signals in the CO_2-free electrolyte were also corrected by the mass signal m/z = 44.

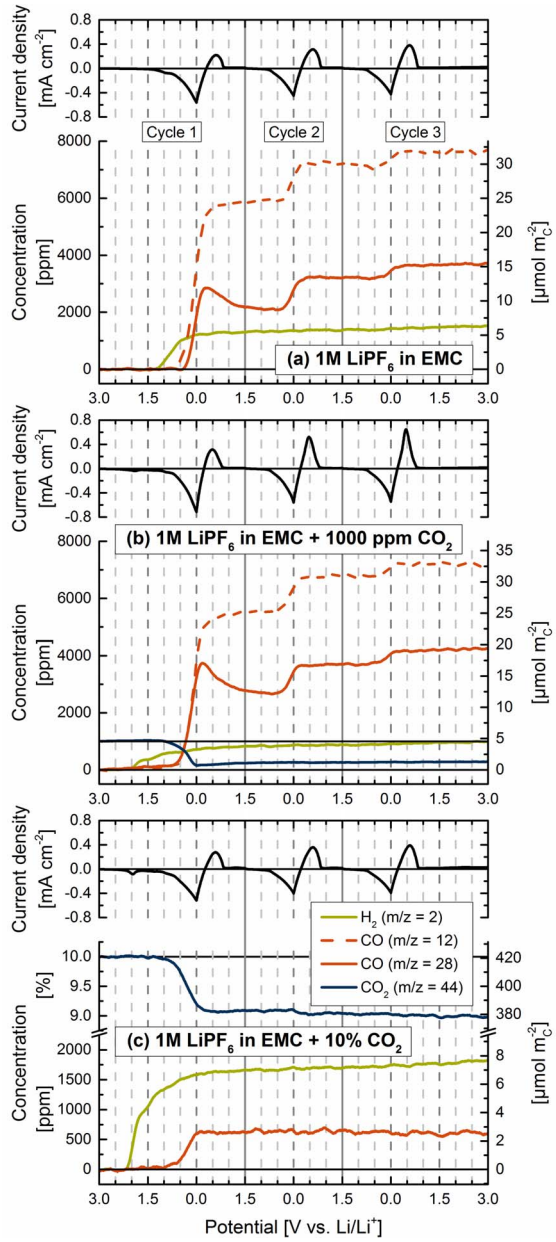

Figure 6. Gas evolution during three CV formation cycles of an SLP30 graphite electrode vs. metallic lithium (2-compartment cell) in the model electrolyte 1 M $LiPF_6$ in (a) EMC (mass signals already shown in Figure 5), (b) EMC + 1000 ppm CO_2, and (c) EMC + 10% CO_2 in the cell's head space. Since C_2H_4 was not detected in the absence of EC, CO is quantified on the channels m/z = 12 and 28 (with CO_2 correction on both channels for all three measurements). Except for the experiment with 10% CO_2 (bottom panel), the mass traces do not only display the evolution of the respective gas, but are superimposed by an additional variation due to trans-esterification, so that the quantification of CO is only semi-quantitative.

The addition of 10% CO_2 changes the situation drastically (see Figure 6c). The consumption of CO_2 starts once the potential falls below ≈1.0 V vs. Li/Li^+ and adds up to a total of ≈9200 ppm (≈40 µmol m_C^{-2}) within the first cycle, followed by a small further decrease of ≈500 ppm at the reversing potential in the second cycle. This means that the gas phase of the cell contains only ≈9% CO_2 at the end of the measurement. The consumption of CO_2 is associated with a substantial decrease of the evolved amount of CO, whose release is restricted to only ≈600 ppm in the first cycle. Here, CO is only quantified on channel m/z = 28, because the high CO_2 content causes

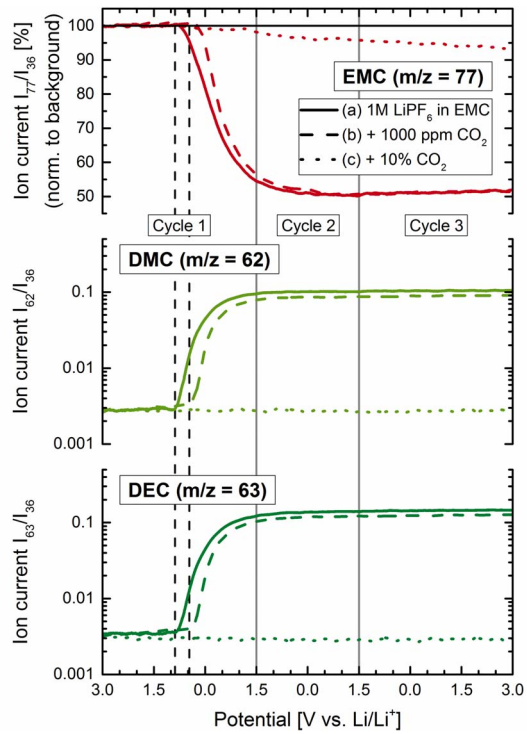

Figure 7. Development of the I_{36}-normalized mass signals for m/z = 77 (top), m/z = 62 (middle), and m/z = 63 (bottom) during the CV formation (shown in Figure 6) in the model electrolyte 1 M $LiPF_6$ in EMC (solid), EMC + 1000 ppm CO_2 (dashed), and EMC + 10% CO_2 (dotted). The dashed vertical black lines mark the onset of the trans-esterification reaction in EMC without CO_2 (left line) and in EMC with 1000 ppm CO_2 (right line).

a noisy background on the fragment m/z = 12. However, the absence of trans-esterification, as will be proven shortly, allows a more precise evaluation of m/z = 28. Additionally, the characteristic increase of the CO signals is missing in the following cycles, i.e., the continuous decomposition of EMC in the presence of large amounts of CO_2 is either suppressed by passivation of the graphite surface (similar to what is found in the presence of EC; see above), or its reduction would have to follow a pathway different from Equation 3.

For all three measurements in Figure 6, there is no clear reduction peak visible in the first-cycle Li-ion intercalation current. This observation is different as in the case LP57, where the reduction peak at ≈0.4 V vs. Li/Li^+ was associated with C_2H_4 formation (see Figure 1a), and which would imply here the reduction of EMC and/or CO_2 in the current-potential profile. Furthermore, the evolution of H_2 is quite high and accounts to more than 1000 ppm in the EMC-based electrolyte (compared to ≈250 ppm in EC-containing electrolyte), and H_2 evolution starts already at potentials greater than 1.0 V vs. Li/Li^+ (as also seen, e.g., in the reduction peak at 2.0 V vs. Li/Li^+ in Figure 6c). As the purity of EMC is only 99%, the H_2 release arises from the reduction of impurities in the solvent. Water, however, can be excluded as a major impurity, since the H_2O content determined by Karl-Fischer titration was <5 ppm for EMC and <10 ppm for EMC with 1 M $LiPF_6$.

Finally, the extent of trans-esterification is evaluated by the help of the characteristic signals from each linear carbonate, as depicted in Figure 7. For the CO_2-free electrolyte (solid lines in Figure 7), all three mass traces change rapidly once the potential is ramped below ≈0.9 V vs. Li/Li^+. Since the EMC signal m/z = 77 falls exactly by 50% and stays almost constant afterwards, we can conclude that the trans-esterification proceeds quantitatively to its dynamic equilibrium with a molar ratio of 50% EMC, 25% DMC, and 25% DEC by the time the first CV cycle is completed. This result is in line with results presented in the literature.[48,49] Interestingly, the conversion of EMC starts ≈200 mV earlier than the evolution of CO (compare Figures 6 and 7). This is consistent with the mechanism for the reductive decomposition of EMC given in Equation 3, which is a two-step process in which CO is only evolved at the end. Thus, the difference in onset potential suggests that 0.9 V vs. Li/Li^+ is the reduction potential for the first step in Equation 3. Note that this reaction involves the release of the first LiOR molecule. EMC seems to split statistically into EtOOC•/LiOMe or MeOOC•/LiOEt because the signals of DMC (m/z = 62) and DEC (m/z = 63) change simultaneously. Furthermore, the potential shift clearly explains why the onset potential for the evolution of CO is different for the signals m/z = 28 and 12 (see Figure 6a): on channel m/z = 28, the increase of the ion current due to the evolution of CO is partially compensated by the simultaneous decrease due to trans-esterification, whereas the ion current on channel m/z = 12 is being increased by both processes.

When 1000 ppm CO_2 are added to the cell's head space, all three mass traces reach the same plateau (dashed lines in Figure 7), i.e., EMC reacts similarly as in the CO_2-free electrolyte. The onset potential of the trans-esterification is down-shifted by ≈400 mV (marked by the vertical dashed lines in Figure 7). Since the trans-esterification now starts after the evolution of CO, there is no shift between the CO signals derived from m/z = 28 and 12 in Figure 6b. The addition of CO_2 in sufficiently high concentrations, here 10% (dotted lines in Figure 7), inhibits the trans-esterification completely, as already indicated by the previous results (see Figure 6c). While the mass signal m/z = 77 falls by ≈5%, we believe this to be due to small errors in background correction and not due to the conversion of EMC into DMC and DEC, because the ion currents on the channels m/z = 62 and 63 remain at their baseline value during the whole measurement. The question how CO_2 may interfere in the decomposition of EMC and even stop the trans-esterification will be discussed in the following section.

How does CO_2 prevent the trans-esterification?—It is well-known in the literature that VC suppresses the trans-esterification, but the underlying process is still debated.[18] In general, there are two explanations how an additive might influence the reaction: (i) the additive may be reduced preferentially over the alkyl carbonate solvents and forms a passivating layer which prevents the release of alkoxide species,[15] or (ii) the alkoxides may be scavenged by the additive and/or its decomposition products.[47]

The reduction of CO_2 in aprotic solvents was extensively studied on a variety of metal electrodes and it was shown that the reaction depends strongly on the electrode material, the type of solvent, the water content, the temperature, and the CO_2 concentration.[51–54] After one-electron reduction, the proposed products are either (i) oxalate from the coupling of two $CO_2^{\bullet-}$ radical anions, (ii) CO and carbonate via an intermediate adduct of CO_2 and $CO_2^{\bullet-}$, or (iii) formate in the presence of H_2O.[51] For a glassy carbon electrode in acetonitrile, Christensen et al. reported the formation of CO and carbonate at potentials below −2.2 V vs. SCE (≡ +1.1 V vs. Li/Li^+).[52] Aurbach and Chusid investigated surface films formed on lithium and noble metal electrodes at 0 V vs. Li/Li^+ in CO_2-saturated salt solutions (including a propylene carbonate-based electrolyte).[55] In this study, lithium carbonate was found to be the major surface species in the presence of CO_2; however, there was no clear evidence for CO.

Even though we observe the reductive consumption of CO_2 at potentials below ≈1.0 V vs. Li/Li^+, the direct reduction to Li_2CO_3 accompanied by CO can be ruled out, because the evolution of CO is strongly decreased in the EMC-only electrolyte with 10% CO_2 (see Figure 6c) and does not correlate with the consumption of CO_2. In principle, the consumed amount of ≈1% CO_2 could be sufficient to build up a passivating film equivalent to ≈1.8 monolayers (from $(3 \cdot 40\ \mu mol_{CO_2}\ m_C^{-2}) / (65\ \mu mol_C\ m_C^{-2})$) and should therefore prevent EMC reduction.

Alternatively, Zhang supposed that CO_2 acts as a reaction-type additive and scavenges LiOR to form $LiOCO_2R$:[7]

$$LiOR + CO_2 \longrightarrow LiOCO_2R \quad [8]$$

In Li-ion battery research, this reaction was specifically applied to synthesize and characterize lithium alkyl carbonates.[30,56–59] The reaction relies on the so-called Dumas-Peligot synthesis, which consists of two stages: HOR → MOR → $MOCO_2R$ (M = Li in our case).[58] Here, the second stage features the nucleophilic attack of an alkoxide on CO_2 and is described to be exothermic. Furthermore, Xu et al. reported that $LiOCO_2R$ species are essentially insoluble in dialkyl carbonates and chemically stable toward common electrolyte solutions such as $LiPF_6$/EC/DMC.[58] Gireaud et al. demonstrated their poor solubility by means of conductivity measurements and also showed the decreased reactivity of lithium alkyl carbonates in comparison to alkoxide species.[59] After storage of $LiPF_6$/EC/DMC at 55°C for 2 days, the prior addition of LiOMe and LiOEt led to the formation of PEG oligomers (analogous to Equation 5); however, identical measurements with several lithium alkyl carbonates did not reveal the presence of any PEG oligomers. This can be rationalized by the finding that $LiOCO_2R$ species are less nucleophilic than LiOR, presumably due to charge delocalization over the oxygen atoms in the carbonate unit.[13] Thus, they probably do not promote the trans-esterification. Note that EC possesses a broader reactivity than the linear carbonates, i.e., OH^- and RO^- could not only attack the carbonyl but also the alkylene carbon atom. The latter represents the preferred reaction pathway in Equation 5. For this reason, the evolution of CO_2 from the nucleophilic attack on EC in LP57 might appear earlier than the trans-esterification from the attack on EMC (compare the onset potential of CO_2 evolution in Figure 1a and the solid line in Figure 4).

Regarding the EMC-only electrolyte, the evolution of CO is substantially decreased in the presence of 10% CO_2 (see Figure 6c). This implies that the second reduction step of EMC in Equation 3 does occur to a much lower extend than without CO_2. Based on our proposed mechanism, CO_2 must also react with R′OOC• to prevent or at least modify the second step of Equation 3, forming, e.g., an oxalate-type species.[7] This hypothesis is supported by the fact that the consumed CO_2 in the EMC-only electrolyte with 10% CO_2 (≈40 μmol m_C^{-2}) is roughly twice as much than the released CO in the EMC-only electrolyte without CO_2 (≈20 μmol m_C^{-2} in the first cycle, see Figure 6a). According to Equation 3, a CO_2:CO ratio of 2:1 would be needed to either scavenge LiOR′/LiOR″ (if EMC reduction undergoes both steps) or R′OOC•/LiOR″ (if EMC reduction stops after the first step). The thus formed products with CO_2 (lithium alkyl carbonates and/or lithium alkyl oxalates) deposit on the graphite surface and inhibit the ongoing reduction of EMC in the following cycles. In the case of 1000 ppm CO_2 (see Figure 6b), the first alkoxide species are trapped; however, their fast release exceeds the available amount of CO_2 and the conversion of EMC is only delayed in time. The presented results from gas phase analysis are currently completed by surface analysis techniques in order to determine the compounds which are deposited on the electrode surface and to answer the question whether CO_2 acts as reduction-type (i.e., forming a passivating SEI) and/or reaction-type additive (i.e., scavenging alkoxides).[36]

Impact of VC and VEC in different concentrations.—The preceding results suggest that CO_2 contributes significantly to prevent the trans-esterification when VC is added to the electrolyte. In a study comparing the effect of VC and VEC (vinyl ethylene carbonate) added to LP57 electrolyte,[19] Petibon and co-workers showed that the conversion of EMC proceeds quantitatively even in the presence of 3% VEC additive (tested in NMC/graphite pouch cells). On the other hand, no trans-esterification was observed with 2% VC as additive (tested in $LiCoO_2$/graphite pouch cells), consistent with our conclusions drawn from Figure 4. Based on their findings, the authors concluded that the passivation of the graphite electrode from VEC reduction is not sufficient. However, the literature seems to be somewhat inconsistent at this point. For the electrolyte system $LiPF_6$/EC/DEC, Kim and co-workers reported that 2% VEC (as well as 2% VC) suppresses almost completely the formation of ethylene glycol bis-(ethyl carbonate), the dimerization product of EC and DEC, which is also induced by alkoxide species.[15]

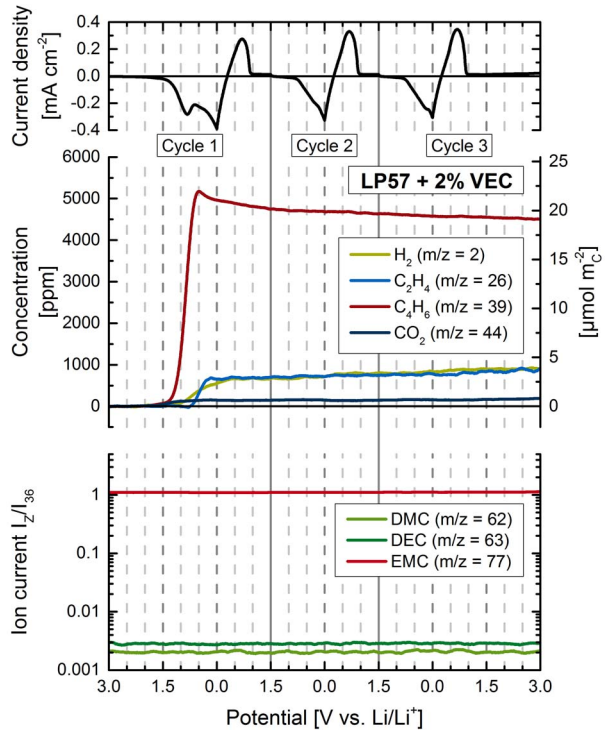

Figure 8. Gas evolution during three CV formation cycles of an SLP30 graphite electrode vs. metallic lithium (2-compartment cell with metallic lithium CE) with LP57 + 2% VEC. C_4H_6 from the reduction of VEC is quantified by the mass signal m/z = 39. As the signal m/z = 28 represents a fragment of four different gases (CO, CO_2, C_2H_4, and C_4H_6; see Table I), the evaluation of CO was omitted here. The lower panel shows the characteristic signals for DMC (m/z = 62), DEC (63), and EMC (77).

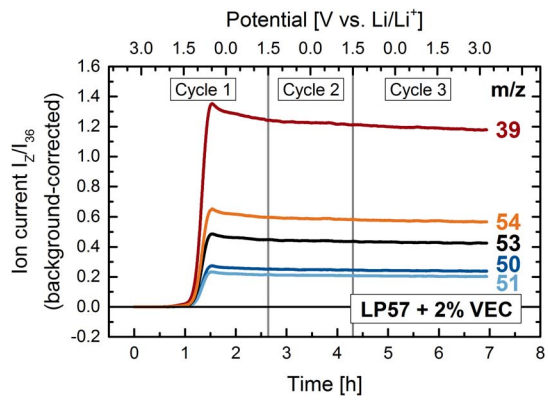

Figure 9. Evolution of C_4H_6 during the formation in the electrolyte LP57 + 2% VEC (from the experiment shown in Figure 8), illustrated by the increase of characteristic mass signals at m/z > 28 (which are not superimposed by C_2H_4).

VEC is a close derivative of EC, so that one might expect a similar reactivity. In contrast to VC, VEC does not produce CO_2 but butadiene upon reduction.[60,61] Consequently, the formation with a VEC-containing electrolyte could help to elucidate if the suppression of the trans-esterification reaction is restricted to CO_2-forming additives. An OEMS measurement with LP57 + 2% VEC is depicted in Figure 8. The addition of VEC leads to a pronounced reduction peak at ≈0.8 V vs. Li/Li^+ in the first cycle (upper panel in Figure 8), which is accompanied by the evolution of C_4H_6 starting at ≈1.5 V vs. Li/Li^+ (middle panel in Figure 8). As illustrated in Figure 9, the mass traces m/z = 39, 50, 51, 53, and 54 serve as a fingerprint for C_4H_6 because they do not overlap with C_2H_4 at m/z ≤ 28.[62] The main peak at m/z = 39 was

used for quantification (see Table I). The evolved amount of C_4H_6 is ≈5200 ppm (≈22 μmol m_C^{-2}) within the first cycle. Interestingly, all C_4H_6 signals fall by ≈10% until the end of CV formation (see Figure 9), i.e., the gas is partially consumed after its initial release. On the other side, the evolved amount of ≈150 ppm CO_2 from the hydrolysis of EC according to Equation 5 (with OH^- produced from trace water reduction) is not consumed in this system.

In the following, we want to compare the evolved amount of C_4H_6 from VEC reduction (see Figure 8) with the amount of C_2H_4 from EC reduction in pure LP57 (see Figure 1a). The alkene evolution from the (initially reduced) cyclic carbonate increases by a factor of ≈2.4 in the VEC-containing electrolyte (i.e., ≈22 $\mu mol_{C_4H_6}$ m_C^{-2} in LP57 with 2% VEC vs. ≈9.0 $\mu mol_{C_2H_4}$ m_C^{-2} in pure LP57). This difference could have the following reasons: (i) VEC reacts in the same way on the graphite surface as EC (Path B in Equation 1), but the analogous decomposition product with one of the H atoms in LEDC replaced with $-CH{=}CH_2$ is less passivating than LEDC, or (ii) VEC undergoes a different reduction mechanism. Since the subsequent evolution of C_2H_4 from EC is only ≈650 ppm (≈3.0 μmol m_C^{-2}), which is even less than in the case of 2% VC (see Figure 1b), the first explanation seems to be implausible. By varying the concentration of VEC, Petibon and co-workers found that VEC is reduced in a two-electron step at a potential window close to ≈1.1 V vs. Li/Li^+ (while an additional one-electron step appears at lower potentials for higher concentrations).[63] In this case, one could conclude that VEC follows predominantly Path A in Equation 1, i.e., a reductive decomposition to lithium carbonate, which would also be consistent with the slightly more than two-fold release of C_4H_6 from VEC vs. that of C_2H_4 from EC (Path A: C_4H_6:VEC ratio of 1:1 vs. Path B: C_2H_4:EC ratio of 1:2). Based on the evolved amount of C_4H_6 shown in Figure 8 (≈22 $\mu mol_{C_4H_6}$ m_C^{-2}), ≈10% of the initially added VEC molecules would have to be converted into Li_2CO_3. In this context, Vollmer et al. hold the opinion that VEC reacts more easily to Li_2CO_3 than EC, because they consider the one-electron disproportionation reaction between neighboring VEC anions to be unlikely at the concentrations typically used for additives.[64] As other researchers reported, however, also alkyl carbonate species and poly(VEC) on the graphite surface,[60,61] the two-electron reduction to Li_2CO_3 might not be the exclusive pathway.

Interestingly, the mass signals m/z = 62, 63, and 77 stay constant at their initial level during the whole measurement (lower panel in Figure 8), proving unambiguously that 2% VEC in our OEMS cell are capable of preventing the trans-esterification reaction. What is not clear, however, is whether the trans-esterification is suppressed due to the fast formation of a protective SEI (i.e., prior to LiOR formation via Equation 3), or due to the effective scavenging of LiOR species. In the former case, no CO should be observed during the first cycle, but unfortunately we are not able to quantify the evolution of CO from VEC-containing electrolytes due to the interference of CO_2, C_4H_6, and C_2H_4 on m/z = 28 and 12. However, in the LP57-based electrolytes, the small fraction of EMC reduction and the accompanied CO evolution were barely affected by the presence of additives (see Figure 1), and it is unlikely that it would be different in the case of VEC. Therefore, we do not believe that a thick passivation layer derived from VEC reduction suppresses the release of LiOR species. We rather favor a scavenging mechanism of VEC and/or C_4H_6. Based on the anion trap function proposed by Sasaki et al. for VC,[47] alkoxides released during EMC reduction (Equation 3) could be removed by their nucleophilic attack on butadiene:

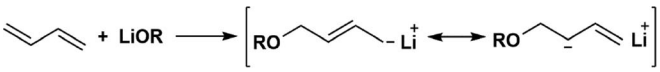

[9]

In contrast to the isolated double bond in VEC (as well as in VC and C_2H_4), the conjugated system of butadiene allows a resonance stabilization of the negative charge in the product formed by C_4H_6 and LiOR in Equation 9. This reaction would not only explain the suppression of the trans-esterification reaction, but also the observed decrease of the C_4H_6 signals which is strongest directly after gas evolution in the first reduction scan (see Figure 9).

The observed suppression of the trans-esterification with 2% VEC in LP57 is consistent with the study by Kim et al. using also 2% VEC in $LiPF_6$/EC/DEC,[15] but contrary to the findings by Petibon and co-workers using 3% VEC in LP57 (both discussed above).[19] This discrepancy at similar VEC concentrations may be caused by differences in the total moles of VEC in the examined cells. This hypothesis is based on the work of Solchenbach et al.,[65] who showed that the impedance buildup by VC on the graphite anode scales with the VC/graphite weight ratio rather than with the VC concentration in the electrolyte. While in the study by Petibon et al. the electrolyte/graphite weight ratio was ≈1.2/1 g_{el}/g_C,[19] much larger electrolyte/graphite weight ratios were used in in our study (≈8.5/1 g_{el}/g_C) and in the work by Kim et al. (≈30/1 g_{el}/g_C).[15] This means that the VEC/graphite weight ratios in the latter two studies are ≈5 (≈0.2 g_{VEC}/g_C) and ≈15 (≈0.6 g_{VEC}/g_C) times higher, respectively, compared to the work by Petibon et al. (≈0.04 g_{VEC}/g_C), which in turn might explain the discussed differences in suppressing the trans-esterification reactions. This hypothesis will now be examined by conducting the CV formation experiments with VC and VEC at 10-fold lower concentrations, so that the resulting additive/graphite weight ratio of ≈0.02 $g_{additive}/g_C$ more closely approaches that used by Petibon and co-workers.

As illustrated in Figure 10a, the accumulated amount of gas with 0.2% VC after the first cycle is ≈1650 ppm C_2H_4 (≈7.0 μmol m_C^{-2}) and ≈350 ppm CO_2 (≈1.5 μmol m_C^{-2}) compared to ≈950 ppm C_2H_4 (≈4.2 μmol m_C^{-2}) and ≈700 ppm CO_2 (≈3.0 μmol m_C^{-2}) with

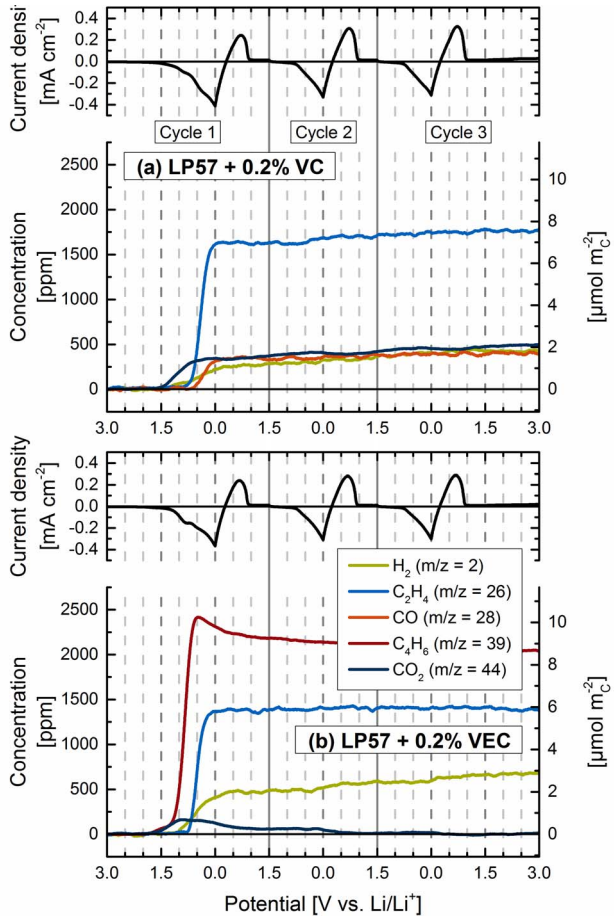

Figure 10. Gas evolution during three CV formation cycles of an SLP30 graphite electrode vs. metallic lithium (2-compartment cell) with LP57 + 0.2% VC (a) and LP57 + 0.2% VEC (b).

2% VC (see Figure 1b). Consequently, the extent of VC reduction (indicated by CO_2 formation) compared to EC reduction (indicated by C_2H_4 formation) decreases significantly when the VC concentration is reduced from 2% to 0.2%. While the CO_2 amount from direct VC reduction within the first cycle is reduced by a factor of roughly 2, the potential-independent CO_2 evolution from poly(VC) formation in the following cycles is 6-fold lower and thus even stronger affected by the initial VC concentration.[27]

For 0.2% VEC (see Figure 10b), the maximum evolved amount of C_4H_6 (≈10 μmol m_C^{-2}) is roughly half of that observed for 2% VEC (≈22 μmol m_C^{-2}, see Figure 8), consistent with also a much smaller reduction feature at ≈0.8 V vs. Li/Li^+. At the same time, the evolved amount of C_2H_4 (≈6.0 μmol m_C^{-2}, from EC reduction) with 0.2% VEC is exactly doubled compared to 2% VEC. After its initial evolution, the C_4H_6 signals again decrease (by ≈15%), similar to what was observed with 2% VEC. In contrast to the measurement with 2% VEC, CO_2 from the hydrolysis of EC is gradually consumed at the lower VEC concentration.

Figure 11 shows the trans-esterification signals from both measurements in comparison to pure LP57 (solid lines). While the signals stay reasonably flat for 0.2% VC (dashed lines), the electrolyte with 0.2% VEC (dotted lines) shows a clear increase on the channels m/z = 62 and 63. Although the signal at m/z = 77 does not change noticeably, the formation of DMC and DEC is undoubtedly verified by the other two mass traces. Thus, while VEC loses its property to suppress the trans-esterification at 0.2%, 0.2% of VC are still able to inhibit the conversion of EMC into DMC and DEC. The trans-esterification with 0.2% VEC starts when the potential falls below ≈0.1 V vs. Li/Li^+ in the first reduction step (see right-hand vertical dashed line in Figure 11), i.e. at a ≈0.3 V lower potential than in pure LP57 (see left-hand vertical dashed line in Figure 11).

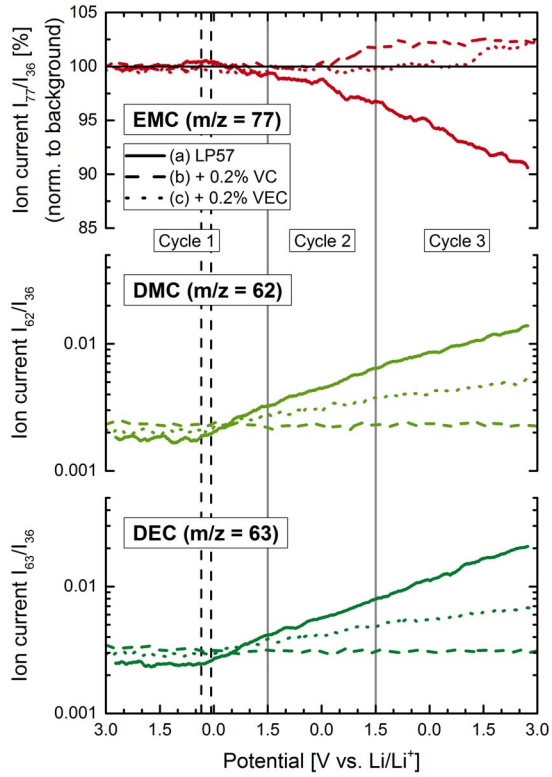

Figure 11. Development of the mass signals m/z = 77 (top), m/z = 62 (middle), and m/z = 63 (bottom) during the CV formation shown in Figure 10 in the electrolyte LP57 (solid), + 0.2% VC (dashed), and + 0.2% VEC (dotted). The dashed vertical black lines mark the onset of the trans-esterification reaction in pure LP57 (left line) and LP57 + 0.2% VEC (right line).

Comparison of lab-scale and commercial-scale cells.—The preceding results emphasize the fundamental importance of the electrolyte/graphite weight ratio and thus the discrepancy which might arise when comparing lab-scale cells with typically high electrolyte/graphite weight ratios to commercial-scale cells with typically low electrolyte/graphite weight ratios. Both the gassing during the SEI buildup on graphite anodes and the subsequent trans-esterification highly depend on the amount of additive rather than simply its concentration in the electrolyte. In the study by Petibon et al. using commercial-scale pouch cells with a low electrolyte/graphite weight ratio,[19] the resulting low additive/graphite weight ratio of ≈0.02–0.04 $g_{additive}/g_C$ is shown to be sufficient to inhibit the trans-esterification in the case of VC, but not in the case of VEC. This is consistent with the OEMS measurements with 0.2% and 2% additive in our lab-scale cells (corresponding to ≈0.02 $g_{additive}/g_C$ and ≈0.2 $g_{additive}/g_C$, respectively). The lower additive/graphite weight ratio with 0.2% additive can suppress the trans-esterification in the case of VC, but not in the case of VEC, while at 2% additive level both additives can inhibit the conversion of EMC into DMC and DEC in our lab-scale cells. The observed differences in terms of gassing and trans-esterification are probably so apparent for VC and VEC, because these two additives are reduced without any competition at potentials where other electrolyte constituents (i.e., EC and EMC) do not yet react. Consequently, the additive conversion rate is only limited by the introduced amount of additive relative to the graphite mass or more precisely, relative to the graphite surface area. Note that the surface area varies among different graphite materials and that the SLP30 graphite powder used in this work has a relatively high BET surface area of 7 $m^2\ g^{-1}$. An important corollary of this analysis is that the additive/graphite weight ratio is a significant parameter to be considered when interpreting additive tests in lab-scale cells, particularly when trying to use lab-scale cell data to predict additive effectiveness in commercial-scale cells.

Role of CO_2 produced during the reduction of VC.—The reduction of EMC was evidenced in every measurement by the evolution of CO, which indicates at the same time the release of LiOR species into the electrolyte (see Equation 3). This means that the trans-esterification is not suppressed by a more passivating SEI layer, but the additives and their decomposition products act as scavengers for alkoxides. As lithium alkyl carbonate, the formed product of LiOR with CO_2 (see Equation 8), is more stable than the product of LiOR with VC,[47] we believe that the scavenging mechanism with CO_2 evolved during VC reduction is favored over the reaction of LiOR with VC itself. The same applies for VEC and C_4H_6 due to the resonance stabilization in the product of LiOR and C_4H_6 (see Equation 9).

In contrast to common additives with negligible vapor pressure (such as VC and VEC), CO_2 and C_4H_6 are in equilibrium between the electrolyte and the gas phase of the cell. The partitioning of the gases into electrolyte and gas phase in turn affects their ability to trap LiOR species, as was shown for CO_2. While 10% CO_2 added to EMC-only electrolyte are able to suppress the trans-esterification (see dotted lines in Figure 7), 1000 ppm CO_2 added to LP57 are not able to do so (see dotted lines in Figure 4), even though ≈2 $\mu mol_{CO_2}\ m_C^{-2}$ are still present in the cell at the end of the measurement (see Figure 1c). This comparison illustrates the rather complex effect of CO_2, which involves the connection of several equilibrium reactions such as the gas-liquid phase transition of CO_2, the LiOR-induced trans-esterification, and their conversion into $LiOCO_2R$. Because only CO_2 dissolved in the electrolyte can scavenge alkoxides, it is important to know the partitioning of CO_2 into electrolyte and gas phase. The CO_2 amount in the electrolyte, $n_{CO_2(el)}$, relative to the CO_2 amount in the gas phase, $n_{CO_2(gas)}$, can be calculated using Henry's law and the ideal gas law as follows:

$$\frac{n_{CO_2(el)}}{n_{CO_2(gas)}} = \frac{V_{el}}{V_{gas}} \cdot \frac{R \cdot T \cdot c_{el}}{K_H} \quad [10]$$

where V_{el} is the electrolyte volume, V_{gas} is the gas phase volume, R is the gas constant, T is the temperature, c_{el} is the molar concentration of the electrolyte, and K_H is the Henry's law constant of CO_2. Equation 10 uses the reasonable assumption that the molar fraction of CO_2 in the electrolyte can be expressed as $x_{CO_2(el)} \approx n_{CO_2(el)}/n_{el}$.

For our lab-scale OEMS cell with $V_{gas} = 8.5$ ml, $V_{el} = 80$ µl (in the WE compartment), $c_{el} = 11.6$ mol l^{-1} (taking the sum of $LiPF_6$, EC, and EMC in LP57), and $K_H \approx 11$–12 MPa for carbonate-based electrolytes at 25°C,[66] the $n_{CO_2(el)}/n_{CO_2(gas)}$ ratio equals ≈2/98. This means that the vast majority of CO_2 accumulates in the head space of our OEMS cell (≈98%) rather than in the electrolyte (≈2%), which is actually an important prerequisite for quantitative mass spectrometry (when sampling the gas phase representative for the entire gas amount evolved in the cell). Since the Henry's law constants of H_2, C_2H_4, CO, and Ar are even higher,[67] this requirement is closely met for all gases in this study. Generally speaking, the accuracy of mass spectrometer experiments for battery applications depends on the V_{el}/V_{gas} ratio and thus on the individual cell design.

The low $n_{CO_2(el)}/n_{CO_2(gas)}$ ratio has severe consequences on the effectiveness of CO_2 as LiOR scavenger. In the case of 10% CO_2 in our OEMS cell (see Figure 6c), which corresponds to ca. 100 mbar (since the cell was purged with 10% CO_2 in Ar at atmospheric pressure), the initially dissolved amount of CO_2 is ≈10 mmol l^{-1} (normalized to the electrolyte volume) or ≈10 µmol m_C^{-2} (normalized to the graphite surface area). For 1000 ppm CO_2, the effective concentration is thus 100-fold lower. This difference probably explains that 10% CO_2 in the OEMS cell are able to suppress the trans-esterification in the EMC-only electrolyte, while 1000 ppm CO_2 added to LP57 are not able to do so due to slower kinetics of the CO_2-dependent scavenging reaction. Note that 1000 ppm CO_2 added to LP57 (≈4 µmol m_C^{-2} in the gas phase, see Figure 1c) do not necessarily correspond to the total amount of CO_2 evolved from VC reduction (≈2 µmol m_C^{-2}, see Figure 1b and Figure 10a), because the apparent CO_2 signal during the first cycle is a superposition of CO_2 evolution (from VC reduction) and CO_2 consumption (from LiOR scavenging). In all LP57-based electrolytes, 2–3 μmol_{CO} m_C^{-2} are released from EMC reduction, which means that according to Equation 3 a minimum of 4–6 μmol_{CO_2} m_C^{-2} are required to scavenge all LiOR molecules. Since the absolute amount of CO_2 evolved from VC reduction is not known, the question if the trans-esterification is solely suppressed by CO_2 when VC is used as additive cannot ultimately answered in our lab-scale OEMS cell.

Finally, we want to evaluate the $n_{CO_2(el)}/n_{CO_2(gas)}$ ratio in a commercial-scale cell, exemplarily estimated for an 18650 Li-ion battery cell with 3 Ah. Based on the kg/kWh_{total} estimate of various cell components from Wagner et al. (estimate and underlying assumptions are given in their Figure 5),[1] a 3 Ah battery is composed of ≈20.4 g cathode active material, ≈8.8 g anode active material, and ≈7.2 g (≈7.6 ml) electrolyte. The electrolyte/graphite weight ratio is ≈0.8 g_{el}/g_c (vs. ≈8.5 g_{el}/g_c in our OEMS cell). If we estimate the gas volume in the head space of an 18650 cell to be on the order of 1 ml (corresponding to ≈6% relative to the total cell volume), the $n_{CO_2(el)}/n_{CO_2(gas)}$ ratio amounts to ≈95/5 and is thus opposite to our OEMS cell (≈2/98). This means that almost the entire CO_2 from VC reduction is directly dissolved in the electrolyte. Even though the released amounts of CO_2 and LiOR relative to the graphite surface area are approximately the same than in our OEMS cell, it is quite plausible that the suppression of the trans-esterification of EMC by VC is solely due to the CO_2 produced by VC reduction in a commercial-scale cell.

Conclusions

In this study, we applied On-line Electrochemical Mass Spectrometry to monitor the processes at the electrode-electrolyte interphase during the formation of graphite anodes and the changes of the bulk electrolyte initiated thereby. By using a 2-compartment cell with an PP/Al/PP edge-sealed Ohara glass, any reaction of the electrolyte (1 M $LiPF_6$ in EC:EMC) or the additives (VC and VEC) with the metallic lithium counter-electrode could be excluded. Our main findings are illustrated and summarized in Figure 12. The numbers in Figure 12 correspond to the reaction equations in this work.

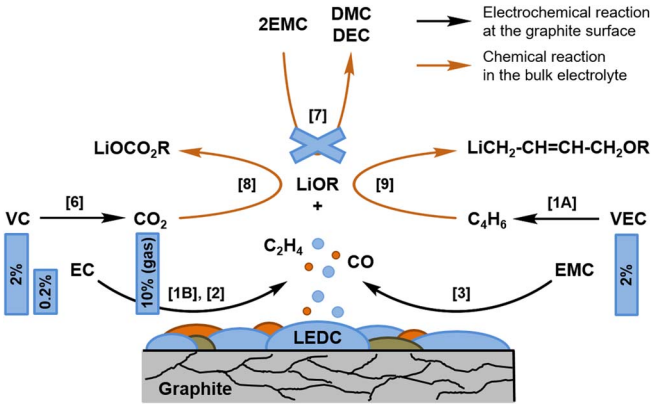

Figure 12. Simplified scheme of the processes at the electrode-electrolyte interphase during formation on a graphite anode. We hypothesize that the evolved gases from the reduction of VC (CO_2) and VEC (C_4H_6) predominantly inhibit the conversion of EMC into its trans-esterification equilibrium (EMC/DMC/DEC ratio of 50/25/25) by scavenging the reactive lithium alkoxide species (LiOR). The numbers in square brackets refer to the corresponding equations in the main text, whereas the blue boxes show the tested concentrations that were sufficient to suppress the trans-esterification.

First, the reduction of EC leads to the formation of lithium ethylene dicarbonate (LEDC), as indicated by the evolved C_2H_4 at potentials below 1 V vs. Li/Li^+. The second-strongest gas CO (in pure LP57) originates from the reduction of both EC and EMC. In contrast to C_2H_4, its amount barely decreases by the use of additives. As CO is accompanied by the formation of lithium alkoxides, which dissolve into the electrolyte, the detection of CO can be used as an indicator for the onset of the trans-esterification reaction. In addition, the progress of trans-esterification can be quantified by monitoring the unique mass signals for EMC, DMC, and DEC.

The investigated additives VC and VEC are capable of suppressing the trans-esterification. We believe that this effect is mainly caused by the evolved gases CO_2 (from VC reduction) and C_4H_6 (from VEC reduction), which scavenge the reactive alkoxides in the form of $LiOCO_2R$ and $LiCH_2$-CH=CH-CH_2OR, respectively. The importance of CO_2 was directly proven during formation in an EMC-only electrolyte. Here, the much stronger evolution of CO and the quantitative establishment of the EMC/DMC/DEC equilibrium (50/25/25) via trans-esterification was completely inhibited in the presence of a sufficiently high concentration of CO_2.

In general, the additive concentrations have a major role on the gassing and the extent of trans-esterification. By lowering the concentration in the electrolyte from 2% to 0.2%, VC still suppresses the trans-esterification, while VEC loses this beneficial property and only slows down the reaction in comparison to pure LP57. In this context, the different electrolyte/graphite weight ratios in lab-scale battery cells (typically 5/1 to 30/1 g_{el}/g_C) compared to commercial-scale cells (typically near 1/1 g_{el}/g_C) were shown to be the most likely cause for discrepancies in literature reports on the effectiveness of additives to suppress the trans-esterification reaction. We want to emphasize that it is important to relate the electrolyte volume and therefore also the concentration of an additive always to the active material mass of the electrodes. As gases such as CO_2 are in equilibrium between the electrolyte and the gas phase, their application as additive also depends on their effective concentration in the electrolyte, which in turn is strongly affected by the cell design.

Acknowledgments

The authors gratefully acknowledge BASF SE for financial support of this research through the framework of its scientific network on electrochemistry and batteries. Furthermore, we want to thank

Stefano Meini and Manuel Mendez for fruitful discussions and great contributions to this work.

References

1. F. T. Wagner, B. Lakshmanan, and M. F. Mathias, *J. Phys. Chem. Lett.*, **1**, 2204 (2010).
2. A. Barré, B. Deguilhem, S. Grolleau, M. Gérard, F. Suard, and D. Riu, *J. Power Sources*, **241**, 680 (2013).
3. O. K. Park, Y. Cho, S. Lee, H.-C. Yoo, H.-K. Song, and J. Cho, *Energy Environ. Sci.*, **4**, 1621 (2011).
4. G. E. Blomgren, *J. Electrochem. Soc.*, **164**, A5019 (2017).
5. K. Xu, *Chem. Rev.*, **104**, 4303 (2004).
6. K. Xu, *Chem. Rev.*, **114**, 11503 (2014).
7. S. S. Zhang, *J. Power Sources*, **162**, 1379 (2006).
8. S. Wilken, M. Treskow, J. Scheers, P. Johansson, and P. Jacobsson, *RSC Adv.*, **3**, 16359 (2013).
9. C. L. Campion, W. Li, and B. L. Lucht, *J. Electrochem. Soc.*, **152**, A2327 (2005).
10. B. Ravdel, K. M. Abraham, R. Gitzendanner, J. DiCarlo, B. Lucht, and C. Campion, *J. Power Sources*, **119–121**, 805 (2003).
11. H. Yoshida, T. Fukunaga, T. Hazama, M. Terasaki, M. Mizutani, and M. Yamachi, *J. Power Sources*, **68**, 311 (1997).
12. E. S. Takeuchi, H. Gan, M. Palazzo, R. A. Leising, and S. M. Davis, *J. Electrochem. Soc.*, **144**, 1944 (1997).
13. T. Sasaki, T. Abe, Y. Iriyama, M. Inaba, and Z. Ogumi, *J. Power Sources*, **150**, 208 (2005).
14. G. Gachot, S. Grugeon, M. Armand, S. Pilard, P. Guenot, J.-M. Tarascon, and S. Laruelle, *J. Power Sources*, **178**, 409 (2008).
15. H. Kim, S. Grugeon, G. Gachot, M. Armand, L. Sannier, and S. Laruelle, *Electrochim. Acta*, **136**, 157 (2014).
16. D. Aurbach, B. Markovsky, A. Schechter, Y. Ein-Eli, and H. Cohen, *J. Electrochem. Soc.*, **143**, 3809 (1996).
17. T. Sasaki, S.-K. Jeong, T. Abe, Y. Iriyama, M. Inaba, and Z. Ogumi, *J. Electrochem. Soc.*, **152**, A1963 (2005).
18. H.-J. Peng, S. Urbonaite, C. Villevieille, H. Wolf, K. Leitner, and P. Novák, *J. Electrochem. Soc.*, **162**, A7072 (2015).
19. R. Petibon, L. Rotermund, K. J. Nelson, A. S. Gozdz, J. Xia, and J. R. Dahn, *J. Electrochem. Soc.*, **161**, A1167 (2014).
20. J.-Y. Eom, I.-H. Jung, and J.-H. Lee, *J. Power Sources*, **196**, 9810 (2011).
21. N. Tsiouvaras, S. Meini, I. Buchberger, and H. A. Gasteiger, *J. Electrochem. Soc.*, **160**, A471 (2013).
22. M. Metzger, B. Strehle, S. Solchenbach, and H. A. Gasteiger, *J. Electrochem. Soc.*, **163**, A798 (2016).
23. M. Onuki, S. Kinoshita, Y. Sakata, M. Yanagidate, Y. Otake, M. Ue, and M. Deguchi, *J. Electrochem. Soc.*, **155**, A794 (2008).
24. K. Leung, *Chem. Phys. Lett.*, **568–569**, 1 (2013).
25. R. Mogi, M. Inaba, Y. Iriyama, T. Abe, and Z. Ogumi, *J. Power Sources*, **119–121**, 597 (2003).
26. H. Ota, Y. Sakata, A. Inoue, and S. Yamaguchi, *J. Electrochem. Soc.*, **151**, A1659 (2004).
27. B. Zhang, M. Metzger, S. Solchenbach, M. Payne, S. Meini, H. A. Gasteiger, A. Garsuch, and B. L. Lucht, *J. Phys. Chem. C*, **119**, 11337 (2015).
28. M. Metzger, C. Marino, J. Sicklinger, D. Haering, and H. A. Gasteiger, *J. Electrochem. Soc.*, **162**, A1123 (2015).
29. R. Bernhard, M. Metzger, and H. A. Gasteiger, *J. Electrochem. Soc.*, **162**, A1984 (2015).
30. D. Aurbach, M. L. Daroux, P. W. Faguy, and E. Yeager, *J. Electrochem. Soc.*, **134**, 1611 (1987).
31. M. Nie, D. Chalasani, D. P. Abraham, Y. Chen, A. Bose, and B. L. Lucht, *J. Phys. Chem. C*, **117**, 1257 (2013).
32. L. Zhao, I. Watanabe, T. Doi, S. Okada, and J. Yamaki, *J. Power Sources*, **161**, 1275 (2006).
33. K. Edström, M. Herstedt, and D. P. Abraham, *J. Power Sources*, **153**, 380 (2006).
34. P. Verma, P. Maire, and P. Novák, *Electrochim. Acta*, **55**, 6332 (2010).
35. J.-S. Shin, C.-H. Han, U.-H. Jung, S.-I. Lee, H.-J. Kim, and K. Kim, *J. Power Sources*, **109**, 47 (2002).
36. K. U. Schwenke, S. Solchenbach, J. Demeaux, B. L. Lucht, and H. A. Gasteiger, Manuscript in preparation.
37. R. Imhof and P. Novák, *J. Electrochem. Soc.*, **145**, 1081 (1998).
38. M. Winter, R. Imhof, F. Joho, and P. Novák, *J. Power Sources*, **81–82**, 818 (1999).
39. M. Metzger, B. Strehle, S. Solchenbach, and H. A. Gasteiger, *J. Electrochem. Soc.*, **163**, A1219 (2016).
40. F. A. Soto, Y. Ma, J. M. Martinez de la Hoz, J. M. Seminario, and P. B. Balbuena, *Chem. Mater.*, **27**, 7990 (2015).
41. L. El Ouatani, R. Dedryvère, C. Siret, P. Biensan, S. Reynaud, P. Iratçabal, and D. Gonbeau, *J. Electrochem. Soc.*, **156**, A103 (2009).
42. J. O. Besenhard, M. W. Wagner, M. Winter, A. D. Jannakoudakis, P. D. Jannakoudakis, and E. Theodoridou, *J. Power Sources*, **44**, 413 (1993).
43. A. Aurbach, Y. Ein-Eli, O. Chusid (Youngman), Y. Carmeli, M. Babai, and H. Yamin, *J. Electrochem. Soc.*, **141**, 603 (1994).
44. S. E. Sloop, J. B. Kerr, and K. Kinoshita, *J. Power Sources*, **119–121**, 330 (2003).
45. G. Gachot, P. Ribière, D. Mathiron, S. Grugeon, M. Armand, J.-B. Leriche, S. Pilard, and S. Laruelle, *Anal. Chem.*, **83**, 478 (2011).
46. J. Jones, M. Anouti, M. Caillon-Caravanier, P. Willmann, P.-Y. Sizaret, and D. Lemordant, *Fluid Phase Equilib.*, **305**, 121 (2011).
47. T. Sasaki, T. Abe, Y. Iriyama, M. Inaba, and Z. Ogumi, *J. Electrochem. Soc.*, **152**, A2046 (2005).
48. R. Petibon, J. Xia, L. Ma, M. K. G. Bauer, K. J. Nelson, and J. R. Dahn, *J. Electrochem. Soc.*, **163**, A2571 (2016).
49. L. Ma, S. L. Glazier, R. Petibon, J. Xia, J. M. Peters, Q. Liu, J. Allen, R. N. C. Doig, and J. R. Dahn, *J. Electrochem. Soc.*, **164**, A5008 (2017).
50. Y. Ein-Eli, S. R. Thomas, V. Koch, D. Aurbach, B. Markovsky, and A. Schechter, *J. Electrochem. Soc.*, **143**, L273 (1996).
51. A. Gennaro, A. A. Isse, M.-G. Severin, E. Vianello, I. Bhugun, and J.-M. Savéant, *J. Chem. Soc. Faraday Trans.*, **92**, 3963 (1996).
52. P. A. Christensen, A. Hamnett, A. V. G. Muir, and N. A. Freeman, *J. Electroanal. Chem. Interfacial Electrochem.*, **288**, 197 (1990).
53. Y. B. Vassiliev, V. S. Bagotzky, O. A. Khazova, and N. A. Mayorova, *J. Electroanal. Chem. Interfacial Electrochem.*, **189**, 295 (1985).
54. B. R. Eggins and J. McNeill, *J. Electroanal. Chem. Interfacial Electrochem.*, **148**, 17 (1983).
55. D. Aurbach and O. Chusid (Youngman), *J. Electrochem. Soc.*, **140**, L155 (1993).
56. R. Dedryvère, L. Gireaud, S. Grugeon, S. Laruelle, J.-M. Tarascon, and D. Gonbeau, *J. Phys. Chem. B*, **109**, 15868 (2005).
57. G. V. Zhuang, H. Yang, P. N. Ross Jr., K. Xu, and T. R. Jow, *Electrochem. Solid-State Lett.*, **9**, A64 (2006).
58. K. Xu, G. V. Zhuang, J. L. Allen, U. Lee, S. S. Zhang, P. R. Ross Jr., and T. R. Jow, *J. Phys. Chem. B*, **110**, 7708 (2006).
59. L. Gireaud, S. Grugeon, S. Laruelle, S. Pilard, and J.-M. Tarascon, *J. Electrochem. Soc.*, **152**, A850 (2005).
60. Y. Hu, W. Kong, H. Li, X. Huang, and L. Chen, *Electrochem. Commun.*, **6**, 126 (2004).
61. S.-C. Kinoshita, M. Kotato, Y. Sakata, M. Ue, Y. Watanabe, H. Morimoto, and S.-I. Tobishima, *J. Power Sources*, **183**, 755 (2008).
62. NIST Mass Spec Data Center, S. E. Stein, director, "Mass Spectra" in NIST Chemistry WebBook, NIST Standard Reference Database Number 69, Eds. P. J. Linstrom and W. G. Mallard, *National Institute of Standards and Technology*, Gaithersburg MD, 20899, http://webbook.nist.gov.
63. R. Petibon, E. C. Henry, J. C. Burns, N. N. Sinha, and J. R. Dahn, *J. Electrochem. Soc.*, **161**, A66 (2013).
64. J. M. Vollmer, L. A. Curtiss, D. R. Vissers, and K. Amine, *J. Electrochem. Soc.*, **151**, A178 (2004).
65. S. Solchenbach, D. Pritzl, E. J. Y. Kong, J. Landesfeind, and H. A. Gasteiger, *J. Electrochem. Soc.*, **163**, A2265 (2016).
66. Y. R. Dougassa, C. Tessier, L. El Ouatani, M. Anouti, and J. Jacquemin, *J. Chem. Thermodyn.*, **61**, 32 (2013).
67. P. Kolář, H. Nakata, J.-W. Shen, A. Tsuboi, H. Suzuki, and M. Ue, *Fluid Phase Equilib.*, **228–229**, 59 (2005).

3.2.3 The impact of CO_2 evolved from VC and FEC during formation of graphite anodes

The manuscript "The impact of CO_2 evolved from VC and FEC during formation of graphite anodes" was submitted to the Journal of the Electrochemical Society in February 2019. Parts of this study were presented by Sophie Solchenbach at the 228th Meeting of the Electrochemical Society in Phoenix, Arizona in October 2015 (Abstract Number 362) and by Uta Schwenke at the 66th Annual Meeting of the International Society of Electrochemistry (ISE) in Taipei, Taiwan in October 2015.

As previously discussed, VC and FEC are both effective SEI-forming additives, and both evolve CO_2 (see chapter 1.3). We found that CO_2 by itself also shows a beneficial effect on the coulombic efficiency (chapter 3.2.1) and the suppression of side reactions (chapter 3.2.2). Therefore, this paper examined the SEI composition on graphite electrodes cycled in VC- or FEC-containing electrolytes or electrolytes dosed with CO_2. By ATR-FTIR and XPS analysis, it was found that higher concentrations of VC led to more polycarbonates in the SEI (in agreement with the impedance results from chapter 3.1.1), whereas increasing the concentration of FEC did not lead to a higher amount of polymeric compounds, thereby confirming a mechanism proposed by Michan et al.[86] For experiments on the reduction reactions of CO_2, we filled cells with isotopically labelled $^{13}CO_2$ in order to distinguish between electrolyte and CO_2 products. Using OEMS, we discovered that while CO_2 suppresses the decomposition of both EC and EMC, the reduction of CO_2 does not yield CO, in contrast to common beliefs in the Li-ion battery literature. A closer look by ATR-FTIR and NMR spectroscopy on graphite electrodes cycled in CO_2-free and $^{12}CO_2$ and/or $^{13}CO_2$-containing cells revealed Li_2CO_3 as the main CO_2 reduction product, along with minor amounts of lithium formate and lithium oxalate. Based on these results, we concluded that the main reduction pathway of CO_2 on graphite leads to Li_2CO_3 and elemental carbon, in agreement with a newly proposed mechanism for the discharge reaction in Li-CO_2 batteries.[179,180] Furthermore, our findings indicated that reduced CO_2 intermediates could act as a scavenger for protons, forming insoluble lithium formate.

Author contributions

K. U. S. performed the electrochemical testing as well as the ATR-FTIR and NMR measurements. J. D. and K. U. S. executed the XPS measurements. S. S. performed and evaluated the OEMS experiments. K. U. S, S. S. and H. A. G. wrote the manuscript. All authors discussed the data and commented the manuscript.

The impact of CO_2 evolved from VC and FEC during formation of graphite anodes in lithium-ion batteries

K. Uta Schwenke[1,=], Sophie Solchenbach[1,=], Julien Demeaux[2], Brett L. Lucht[2] and Hubert A. Gasteiger[1]

[1] Chair of Technical Electrochemistry, Department of Chemistry and Catalysis Research Center, Technical University of Munich, Munich, Germany

[2] Department of Chemistry, University of Rhode Island, Kingston, Rhode Island, USA

[=] equal contribution

Abstract

Additives such as vinylene carbonate (VC) and fluoroethylene carbonate (FEC) are commonly added to lithium-ion battery electrolytes in order to form a solid electrolyte interphase (SEI) on the anode, suppressing continuous solvent reduction. In this work, we directly compare VC and FEC by analyzing the SEI with FTIR and XPS, and the evolved gases with on-line electrochemical mass spectrometry (OEMS) in different model systems. Since both additives evolve mainly CO_2 during formation, the effect of CO_2 as an additive is compared to the addition of VC and FEC. While Li_2CO_3 is as expected the main SEI compound found due to the added CO_2, surprisingly no CO was detected in the gas phase of such cells. Based on FTIR, NMR and OEMS analyses of cells filled with ^{13}C labeled CO_2, we suggest a mechanism explaining the beneficial effects of CO_2 and hence also of CO_2 evolving additives in lithium-ion battery cells.

Introduction

The solid electrolyte interphase (SEI),[1] which is formed on the anode of a lithium-ion battery during the initial cycle(s), provides electrical passivation and lithium ion conduction and thus allows stable lithium ion intercalation without further electrolyte reduction. A typical electrolyte consists of $LiPF_6$ in a mixture of cyclic (e.g., ethylene carbonate (EC)) and linear alkyl carbonates (e.g., ethyl methyl carbonate (EMC)). To tailor the SEI for more efficient protection against continuous solvent reduction, additives such as vinylene carbonate (VC) or fluoroethylene carbonate (FEC) are added to the electrolyte. Both additives are reduced at higher potentials than the standard electrolyte,[2] which prevents the reduction of the main electrolyte components. While VC has been established as a standard additive for graphite-based cell chemistries, FEC is commonly used in combination with silicon anodes[3–8] or high voltage cathodes.[9,10]

In a movement towards a rational design of electrolyte additives, the decomposition mechanisms and products of additives have been studied thoroughly. Regarding VC and FEC, both additives are known to form polymer species during reduction.[4,7,11–13] The decomposition of FEC is often also related to an enhanced formation of LiF.[2,6,8,14] Besides, the use of FEC with silicon anodes in contrast to VC on graphite electrodes makes a direct comparison of these two additives more difficult. Still, it is often overlooked that both additives have been reported to release CO_2 during reduction.[12,15–17] CO_2 has been used as one of the first SEI-forming additives in lithium metal and lithium ion batteries with graphite anodes.[18–27] Recently, Krause et al. demonstrated the beneficial effect of CO_2 as a cycle life extending additive in full pouch cells with silicon alloy anodes.[28] Our group recently showed that CO_2 reduces the FEC consumption in silicon-graphite based full-cells,[29] and can stop the ester exchange reactions caused by lithium alkoxide species,[30] which are a product of the reduction of linear carbonates.[31]

In this work, we investigate the effect of VC and FEC on the SEI composition of graphite electrodes using surface sensitive analytical techniques such as XPS and FTIR spectroscopy. Using different model electrolytes, we take a closer look into the origin of LiF in the SEI. We analyze further the potential-resolved gassing behavior of both VC and FEC. As the gas evolution pattern of both additives shows that CO_2 can also be consumed at low potentials, we investigate the consumption of CO_2 and its effect on the SEI composition. By introducing isotopically labeled $^{13}CO_2$ in the cell's head space, we are able to differentiate between electrolyte decomposition products and products of the CO_2 reduction. Thus, with the combination of FTIR, NMR and OEMS analysis, we elucidate the multi-step CO_2 reduction mechanism occurring on graphite electrodes.

Experimental

Electrode preparation

Graphite electrodes were prepared by mixing SLP30 graphite powder (Timcal, Switzerland, BET surface area 7 m²/g) with polyvinylidene fluoride binder (PVDF, Kynar HSV900, Arkema, France) at a weight ratio of 90/10 in N-methyl-2-pyrrolidone (NMP, anhydrous, 99.5 %, Sigma-Aldrich, Germany). The obtained slurry with a solid content of 33 % was mixed for 15 min at 2000 rpm in a planetary orbital mixer (ARV-310CE, Thinky, USA) and coated with a gap bar onto either a copper foil (thickness 12 µm, MTI Corporation, USA) or a porous separator (H2013, Celgard, USA or FS24316, Freudenberg, Germany) at a wet-film thickness of 250 µm using an automatic coater (RK PrintCoat Instruments, UK). The coating was dried at 50 °C before punching it with a precision punch (Hohsen, Japan) into 15 mm diameter disks and final drying under dynamic vacuum in a glass oven (drying oven 585, Büchi, Switzerland) at 120 °C (for coatings on copper foil or Freudenberg separator) or at 95 °C (for coatings on Celgard separator). The final electrodes had a loading of ≈6 $mg_{graphite}/cm^2$.

LFP electrodes were prepared by mixing lithium iron phosphate powder (LFP with a carbon coating of 1.9 %, Clariant, Germany), PVDF (Solef 5130, Solvay, Germany), Super C65 carbon black (Timcal, Switzerland) and vapor grown carbon fibers (VGCF-H, Showa Denko, USA) at a weight ratio of 80/10/5/5 with NMP (solid content 33 %) in a planetary orbital mixer (15 min at 2000 rpm). The ink was coated with a gap bar onto aluminium foil (thickness 18 µm, MTI corporation, USA) at a wet-film thickness of 500 µm using the automatic coater. The coating was dried at 50 °C before punching it with a precision punch into 14 mm disks and final drying under dynamic vacuum at 120 °C. The final electrodes had a loading of ≈12 mg_{LFP}/cm^2, which results in an anode/cathode capacity ratio of ≈1.1. Based on a theoretical capacity of 170 mAh/g_{LFP}, the areal capacity of the employed LFP electrodes was hence around 2 mAh/cm².

Electrochemical cycling

In order to investigate the influence of CO_2 on the SEI formation, cells must be used which can be filled with gases. Hence, we employed for the study at hand our home-made cell design originally developed for Li-air battery cell studies.[32] Electrolyte solutions of 1 M $LiPF_6$ (BASF) in a mixture of propylene carbonate and ethylene carbonate (PC/EMC, 30/70 by weight, Selectilyte, BASF) were employed to quickly judge whether with the respective additive a stable SEI is formed, which would suppress the otherwise continuous PC intercalation and reduction.

All cells were assembled in an argon filled glovebox (O_2<0.1 ppm, H_2O<0.1 ppm, MBraun, Germany). When building full-cells, LFP electrodes were placed onto the flat bottom part of the cell, followed by 40 µl of electrolyte, 2 Celgard separators H2013, another 40 µl of electrolyte and a graphite electrode coated on a H2013 separator (coated side facing the gas phase), followed by a final 40 µl of electrolyte and a steel mesh (21 mm diameter, 0.22 mm diameter wire, 1.0 mm openings, Spörl KG, Germany) as current collector. In order to study the effect of CO_2, cells were flushed for 35 s at a flow of 15 Nl/h with CO_2 (99.995%, Westfalen, Germany). For comparison, standard 2032 coin cells with graphite electrodes coated on copper and filled with 60 µl of electrolyte were assembled for cells without CO_2 filling.

After 1 h rest at open circuit voltage, the cells were galvanostatically cycled at 25 °C in a climate chamber (Binder, Germany) with a battery cycler (Series 4000, Maccor, USA) between 2.7 and 3.8 V at rates of C/20 (1st cycle) and C/10 (2nd and 3rd cycle), followed by 37 cycles at C/5 without a constant voltage step.

Surface analysis with FTIR, XPS and NMR

Surface characterization of graphite electrodes was conducted after one formation cycle at C/20 at 25 °C between 2.7 and 3.9 V with a potentiostat (VMP3, Biologic, France), using the Li-air cell design for those type of experiments. All cells were either flushed with 1 atm CO_2 or with argon in order to avoid any contamination from remaining CO_2 from the glovebox. Cells with $^{13}CO_2$ were filled via a diffusion procedure. An empty Li-air cell and the assembled, gas-flushed cell to be filled with $^{13}CO_2$ were connected via a Swagelok assembly with a valve between them. The empty cell was evacuated for 1 h and then filled with 1 atm $^{13}CO_2$ (Sigma-Aldrich, 99 % chemical purity, 99 % isotope purity) while the valve between the cells remained closed. Afterwards, the valve to the connected assembled cell was opened to allow intermixing of the gas volumes for 1 h, resulting in approximately 50 % $^{13}CO_2$ in the cell headspace.

Electrodes were harvested from cells with standard electrolyte LP57 (EC:EMC 3:7 (w:w), 1 M $LiPF_6$, Selectilyte, BASF) or for more specific analysis with pure single solvent electrolytes. Cells with LP57 and 1 M $LiPF_6$ in EMC were assembled with graphite electrodes coated on H2013 Celgard separator and the same separator; cells with 1 M $LiPF_6$ in EC, VC or FEC were assembled with electrodes coated on Freudenberg separator FS24316 and the same separator, as those solvents could not wet the H2013 separator.

After the formation cycle, cells were flushed with argon and transferred in an argon-filled glovebox. The graphite electrodes were harvested, rinsed with 3x 0.5 ml dimethyl carbonate (DMC, 99.9 %, anhydrous, Sigma-Aldrich, stored over molecular sieves), subsequently dried

for approximately 5 h under dynamic vacuum in a glass oven at room temperature and brought back to the glovebox without any exposure to air.

Fourier transform infrared spectroscopic (FTIR) analysis was conducted in the glovebox with a MIRacle germanium ATR (Pike Technologies) incorporated in the FTIR spectrometer Spectrum Two (Perkin Elmer) with a resolution of 4 cm^{-1}. The spectra are shown as recorded without normalization.

X-ray photoelectron spectroscopy (XPS) analysis was conducted with a K-alpha spectrometer (Thermo Fisher Scientific) using a pass energy of 50 eV. All electrodes were cut in the glovebox and mounted on an air-tight sample holder with metal clips to avoid any contact with air and glue. The binding energy of the obtained spectra was corrected to the F1s core spectrum of LiF at 685.0 eV. The relative atomic concentration of each element was obtained based on peak areas and sensitivity factors using the Thermo Avantage software.

NMR analysis was conducted of D_2O extracts of the graphite electrodes. The SEI components were dissolved by adding 550 µl of D_2O (99 atom % D in ampoules, Sigma-Aldrich) to the electrode and storing it for 30 min in the glovebox before transferring the solution in an air-tight NMR tube (Screw Cap Tubes, Wilmad). ^{1}H, ^{19}F and ^{31}P NMR spectra were collected on a Bruker Ascend 400 (400 MHz) NMR spectrometer without proton decoupling, accumulating 128, 128 and 256 scans, respectively. ^{13}C NMR spectra were collected with and without proton decoupling on a Bruker Avance-III (500 MHz, equipped with a cryo probe 5 mm CPQNP), accumulating 2500 scans. For quantification, standard solutions of deuterated sodium trimethylsilyl propanoate (TSP) in D_2O (10 µl of 0.05 w.-% TSP in D_2O for ^{1}H NMR, 100 µl of 0.75 w.-% TSP in D_2O for ^{13}C NMR) were added to the samples in the glovebox. ^{13}C NMR spectra for quantification were measured with an increased relaxation time T1 of 100 s and 350 scans to ensure complete relaxation of the spins of Li_2CO_3.

On-Line Electrochemical Mass Spectrometry (OEMS)

For OEMS analysis, high surface area carbon black model electrodes were prepared in order to minimize lithium intercalation and maximize the signals of the evolved gases. Super C65 carbon black (Timcal, Switzerland, BET surface area 68 m^2/g) was mixed with PVDF (Kynar HSV900, Arkema, France) at a 90/10 weight ratio in NMP with a planetary orbital mixer. The obtained slurry was coated on a polyester separator (Freudenberg FS 24316) with a gap bar (500 µm). The coating was dried at 50 °C before punching into 15 mm disks and drying under dynamic vacuum at 120 °C. The final electrodes had a loading of 1.8 mg_{carbon}/cm^2.

To avoid any crosstalk of the evolved gases with the lithium counter electrode, OEMS analysis[33] was conducted in our recently developed 2-compartment cell[34] that employs a lithium ion conducting glass ceramic (LICGC, diameter 1'', thickness 150 µm, 10^{-4} S/cm at 25 °C, Ohara, Japan) with an improved aluminum sealing.[35] In order to assign the evolved gases to the different components of the electrolyte, we employed 1 M $LiPF_6$ in pure VC, FEC, EMC or EC (all Selectilyte, BASF). As a model electrolyte, also 0.5 M LiTFSI (BASF) in diglyme (anhydrous, Sigma-Aldrich, Germany) was used. The counter electrode compartment, which is shielded from the OEMS inlet, contained the Li counter electrode (ø 17 mm, 450 µm thickness, 99.9 %, Rockwood Lithium, USA) and a 22 mm diameter glass fiber separator soaked with 200 µl electrolyte. The working electrode compartment that is connected to the OEMS inlet contained the C65 working electrode (ø 15 mm) and a polyester separator (ø 17 mm) soaked with 100 µl electrolyte. The cells were connected to the OEMS system and purged for 45 s with pure argon to remove any residual trace gases from the glovebox atmosphere. After an OCV period of 4 h, the carbon working electrodes were polarized from OCV (~3 V) to 0.1 V and back to 2 V with a scan rate of 0.1 mV/s. All mass spectrometer currents were normalized to the current at m/z = 36 (Ar isotope) in order to correct for minor pressure and temperature deviations, and afterwards the currents m/z = 2 (H_2), m/z = 26 (C_2H_4), m/z = 28 (CO, corrected for contributions from C_2H_4 and CO_2 as described by Strehle et al.[30]), and m/z = 44 (CO_2) were converted into gas concentrations using a calibration gas containing H_2, O_2, CO_2, and C_2H_4 (each 2000 ppm) or H_2, O_2, CO_2, and CO (each 2000 ppm).

Cells with $^{13}CO_2$ were filled via a diffusion procedure similar to the cells for surface analysis. First, the cell was purged with pure argon for 45 s to remove any residual trace gases from the glovebox atmosphere. A stainless steel tube (~5 ml volume) was connected to the cell, evacuated for 30 min and then filled with $^{13}CO_2$. Then, the valve between the tube and the cell was opened to allow intermixing of the gas volumes for 30 min, resulting in 10 % - 30 % $^{13}CO_2$ in the cell headspace. The exact headspace concentration of $^{13}CO_2$ in each cell was determined by quantification of the m/z = 45 current during the 4 h OCV period prior to the voltage sweep, assuming the same calibration factor as for $^{12}CO_2$ on m/z = 44.

Results

SEI formation in dependence of VC and FEC concentration

Ex situ surface analysis of cycled electrodes is commonly applied to determine the composition of the SEI and draw conclusions about the formation mechanism, whereby FTIR analysis is one of the most convenient and simplest techniques to use. Therefore, we started our comparative study of VC and FEC as SEI additives for graphite anodes using ATR-FTIR

analysis. The corresponding spectra of graphite electrodes after one formation cycle (at C/20 between 2.7 and 3.9 V) in standard LP57 electrolyte with different amounts of VC and FEC additive are displayed in Figure 1. Although the additive content varied from 0 % to 100 %, only very few changes among the electrodes were observed. All electrodes showed bands from stretching vibrations characteristic for Li_2CO_3 (around 1460 cm^{-1}), alkyl carbonates (around 1620 and 1310 cm^{-1}) and carboxylates (around 1580 cm^{-1}). The only major difference occurring due to the additives in comparison to the standard electrolyte consists of a band around 1800 cm^{-1}, which was attributed to the stretching vibration of the carbonyl group of poly(VC).[11] A similar band is observed for the SEI formed with FEC. Interestingly, the intensity of this band is independent of the FEC concentration, whereas the poly(VC) band increases strongly with VC concentration.

The similarities between the observed reduction products of VC and FEC led in the literature to the suggestion that FEC transforms to VC and finally forms also poly(VC).[4,13] Theoretical studies also suggested that FEC and VC reduction may lead to the same reduction products.[36] However, a single IR-band is not sufficient to identify a SEI product, and a carbonyl stretching vibration at such high wavenumbers suggests only that the vibration is quite constrained, as for example would also be the case in non-polymeric cyclic carbonates. As a product remaining in the SEI must be a non-soluble solid, it is commonly assumed that also in the case of FEC a polymer with a constrained carbonyl group is formed, which was named either poly(FEC)[2,8] or was directly assigned to be poly(VC).[4,13] An identical product as in the case of VC is unlikely, as the vibration around 1800 cm^{-1} occurs at a slightly lower wavenumber for FEC than for VC (see Figure 1).

Interestingly, this poly(FEC) is only formed in small quantities, independent of the FEC concentration, in contrast to poly(VC), whose amount increases strongly with VC concentration (see Figure 1). This finding explains why FEC can be added to electrolytes as a co-solvent, whereas the amount of VC has to be well-dosed to avoid the uncontrolled formation of a poorly ion conducting polymer, which leads to high cell impedance.[37–39] As the poly(FEC) concentration is observed to be independent of the initial FEC concentration after the 1st cycle (see Figure 1), the formation of poly(FEC) seems to involve an electron transfer, which is no longer possible after a certain SEI layer thickness has been reached. Nie et al.[5] analyzed the SEI on silicon electrodes after 1, 5 and 20 cycles in a pure single-solvent FEC electrolyte and showed that the amount of poly(FEC) increased for those electrodes with cycle number. This might be one important reason why FEC is the preferred additive for silicon anodes for which the SEI has to be reformed in each cycle, until all FEC is consumed and the cycling performance drops.[16,40]

241 ***The origin of LiF in the SEI***

242 Next to FTIR spectroscopy, XPS is commonly employed to analyze the SEI. Numerous
243 studies exist to identify components formed due to the reductive decomposition of VC[11,12,41,42]
244 or FEC[3–6,43,44], which are the basis of a variety of suggested mechanisms. Since one major
245 difference between VC and FEC is the additional fluorine, it seems obvious that in case of
246 FEC, more LiF should be found on the anode. Indeed, several studies show that more LiF
247 forms on electrodes cycled in FEC containing electrolytes compared to standard electrolytes
248 without FEC.[3,8,43–45] Other articles report, however, no difference in fluorine concentration[2,4]
249 or even a lowered amount when using a FEC containing electrolyte.[46] Whether the effect of
250 LiF in the SEI is positive or negative is under debate: On the one hand, the lithium ion
251 conductivity is relatively low compared to other lithium salts in the SEI;[41,47] on the other hand,
252 it was found that carbon electrodes with fluorinated binders like PTFE or PVDF cycle in a
253 more stable manner than with fluorine-free binders like EPDM, which was attributed to the
254 formation of LiF.[21] Moreover, $LiPF_6$, the most widely-used Li-ion battery electrolyte salt, is
255 known for the formation of LiF,[48,49] which is thus a common and probably also important part
256 of the SEI.

257 In this study, we use XPS to investigate the effect of VC, FEC and also $LiPF_6$ on the
258 formation of LiF. Figure 2a shows the ratios of different elements in the SEI of graphite
259 electrodes after formation in different electrolytes determined by XPS. While the analysis of
260 the core spectra of carbon and oxygen leaves room for interpretation, depending on the
261 number and position of the peaks used for fitting, the F1s peak of LiF at 685 eV can be easily
262 distinguished from other fluorine containing species with C-F or P-F bonds, such as PVDF or
263 $LiPF_6$ with binding energies around 687/688 eV. Therefore, we additionally deconvoluted the
264 ratio of LiF (dark blue) from the other fluorine species (light blue) in Figure 2a.

265 First, we employed model electrolytes containing only 1 M $LiPF_6$ in EMC ((1) in Figure 2a), to
266 which 2 % of VC (2) or FEC (3) were added. As can be seen in Figure 2a, the addition of VC
267 (2) suppressed the decomposition of $LiPF_6$ efficiently and the resulting SEI contained less LiF
268 in comparison to the additive-free electrolyte (1) (6 % vs. 13 %), as already reported in the
269 literature.[2,8,41] In contrast, the amount of LiF was approximately doubled (28 %) when using
270 FEC (3). Interestingly, the elemental composition and also the amount of LiF were
271 surprisingly similar between the standard electrolyte LP57 with EC (5) and the model
272 electrolyte with EMC only (1).

273 In order to understand how much LiF is formed by $LiPF_6$ and PVDF, we analyzed also an
274 electrode cycled in an electrolyte with FEC but with $LiClO_4$ instead of $LiPF_6$ (4) and one
275 electrode with neither FEC nor $LiPF_6$ (6). Please note that we could not use the model
276 electrolyte with only EMC as solvent when $LiPF_6$ was replaced with $LiClO_4$, as LFP/graphite

277 cells with EMC and $LiClO_4$ without additives never reached the upper cut-off potential, but
278 charged without end. This behavior already indicates that LiF formed from $LiPF_6$ is an
279 essential component of the SEI, at least when no other passivating components are
280 available. When the $LiClO_4$-electrolyte was employed with additional EC to form a stable SEI,
281 2 % LiF was still found by XPS, even without FEC and $LiPF_6$ (6). This demonstrates that also
282 PVDF is unstable at the applied potentials and participates in the SEI formation, as
283 demonstrated in the early days of Li-ion battery research.[21] However, as significantly less LiF
284 is found in the SEI of cells with $LiClO_4$ and no additives (6) compared to the same electrolyte
285 with $LiPF_6$ (5) (2 % vs. 15 %), $LiPF_6$ decomposition is indeed the main source of LiF in
286 additive-free cells. In contrast, with $LiClO_4$ and FEC (4) almost the same amount of LiF was
287 found as with $LiPF_6$ and FEC (3) (25 % vs. 28 %). This finding shows that the decomposition
288 of $LiPF_6$ is suppressed by FEC, similar as observed for VC (2). Yet, the additional 3 % of LiF
289 found in EMC+2 % FEC with $LiPF_6$ (3) might stem from the decomposition of $LiPF_6$.

290 To explain the presence of LiF, Markevich et al.[6] suggested a mechanism in which LiF forms
291 exclusively via transformation of Li_2CO_3 with $LiPF_6$. Although it becomes clear from our
292 results that the LiF in FEC-containing electrolytes originates mostly from FEC, we took a
293 closer look at the amounts of Li_2CO_3 and LiF in the SEI of the different electrolytes. Figure 2b
294 displays the core C1s spectra of the same electrodes as in Figure 2a. Interestingly, more
295 carbonate (binding energy 290 eV) was found on the surface after cycling in an electrolyte
296 with $LiClO_4$ in comparison to a $LiPF_6$ containing electrolyte. As the FTIR spectra (not shown)
297 do not present a significant difference in the amount of Li_2CO_3, this difference seems to be
298 highly surface sensitive. Only the top layer of the SEI, which is probed by XPS, may undergo
299 a change from Li_2CO_3 to LiF in a $LiPF_6$ containing electrolyte. When VC is added to the
300 electrolyte the characteristic peaks for poly(VC) at 291 and 187.5 eV were observed as
301 expected.[11,42,50] Furthermore, it is confirmed that the SEI of electrodes after one formation
302 cycle in an electrolyte without EC is quite thin, as the graphite peak at 284.1 eV is clearly
303 visible, whereas the spectra of electrodes after one cycle in EC are showing dominantly
304 peaks characteristic for alkyl carbonates at 284.8 eV, 287.1 eV and 290.7 eV, covering the
305 graphite completely.[11,51]

306 In summary, we can draw the following conclusions from the here conducted XPS study: LiF
307 is an essential part of the SEI which can be found in all electrodes. The lowest amount (2 %)
308 is obtained when neither FEC nor $LiPF_6$ are present in the electrolyte, and hence LiF
309 originates from the decomposition of the binder PVDF. Approximately 15 % of LiF is
310 observed in the SEI of electrodes after a cycle in an electrolyte without additives but with
311 $LiPF_6$. The addition of VC, which gets reduced at high potentials, suppresses the formation of
312 LiF to 6 %, whereas FEC in the electrolyte is the main source of LiF on electrodes as the

amount of LiF is around 25 %, almost independent whether $LiPF_6$ or $LiClO_4$ is used as electrolyte salt.

Gas evolution during the reductive decomposition of VC and FEC

To further investigate the onset and the products of the decomposition of VC and FEC, we performed potential-resolved OEMS measurements in a sealed 2-compartment cell[35] in a pure VC or FEC electrolyte with 1 M $LiPF_6$. Figure 3a and 3b show the current density (upper panel) and the gas evolution (lower panel) during a reductive CV on a carbon black electrode in VC+1 M $LiPF_6$ and FEC+1 M $LiPF_6$ electrolyte, respectively. Both current density and gas evolution are normalized to the BET area of the carbon black working electrode (left y-axis) to be comparable throughout the following datasets. In the VC-only electrolyte, CO_2 starts to evolve around 2.2 V vs. Li^+/Li and rises steeply up to a maximum of 30 µmol/m^2_{BET} around 1.1 V vs. Li^+/Li. Interestingly, no clear current peak can be associated with the strong gas evolution. The CO_2 evolution of the FEC-only electrolyte starts at a lower potential (1.8 V vs. Li^+/Li), but increases even steeper up to 40 µmol/m^2_{BET} at 0.9 V. In contrast to the VC electrolyte, there is a large reduction current with a maximum at 1.1 V vs. Li^+/Li for FEC, coinciding with the maximum rate of CO_2 evolution. The difference in reduction current for VC and FEC is consistent with previous reports suggesting that VC decomposition is catalytic while FEC reduction is stoichiometric.[13] Between 1 and 0.1 V vs. Li^+/Li, the CO_2 concentration decreases slightly in the VC electrolyte, while in the FEC electrolyte CO_2 evolution is slowed down (but not stopped). At the same time, a minor amount of CO is evolved in both experiments. During the positive going scan, the CO_2 evolution increases again linearly for the VC-only electrolyte, whereas it flattens for FEC. Hydrogen and ethylene stay below the detection limit during the entire scan in both VC and FEC.

CO_2 has been previously identified as the major gaseous product of VC reduction,[11,12] and here we confirm that indeed no other species like acetylene, which would be the equivalent to ethylene from EC reduction, are evolved. Also FEC is reported to release CO_2 during reduction on both graphite[17] and silicon,[16] while simultaneously forming LiF.[52] Recently, calculations by Soto et al.[53] have confirmed that the decarboxylated radical anion of a reduced VC molecule could be the starting point for a VC polymerization. The CO_2 evolution observed for VC which continues after the end of the reductive CV scan could belong to a chemical chain reaction which eliminates CO_2.[12,53] In contrast, almost all CO_2 released from FEC is connected to a corresponding current. This observation fits well to the abovementioned differences of VC and FEC at different concentrations (see Figure 1). However, as both poly(VC) and poly(FEC) contain intact carbonate moieties, they therefore must be produced by a decomposition pathway proceeding without any CO_2 evolution.

The change in CO_2 evolution slope between 1 and 0.1 V vs. Li^+/Li in both electrolytes points towards a CO_2-consuming process occurring at low potentials, superimposing the CO_2 evolution. Aurbach et al.[20] suggested that CO_2 can be reduced to CO and Li_2CO_3 in lithium-ion battery electrolytes. In both VC and FEC, the CO evolution starts simultaneously with the consumption of CO_2, although the amount of CO seems too little to quantitatively account for the consumed CO_2. Alternatively, CO could result from the direct 2-electron reduction of VC[54] or FEC.[55]

Since both VC and FEC reduction are characterized by a strong CO_2 evolution, and since in both cases CO_2 is partially consumed or its evolution suppressed at low potentials (< 0.8 V), we further want to investigate how (i) the presence of CO_2 affects the formation of graphite electrodes and (ii) if CO_2 plays a role in the ability of these additives to form a highly effective SEI.

Cycling in PC/EMC based electrolytes with VC, FEC and CO_2

Even though there is a clear difference between the additives VC and FEC in terms of LiF and surface polymer formation, the previous section clearly demonstrated the similar gas evolution pattern during their initial decomposition. In order to investigate whether the evolved and possibly also consumed CO_2 plays a role in the performance and effectiveness of these two SEI forming additives, the cycling performance of cells with VC or FEC were directly compared to cells filled with gaseous CO_2. Since the cycling stability of cells with a standard EC containing electrolyte is rather high even in the absence of SEI forming additives, the effectiveness of SEI forming additives can be determined more easily by cycling cells in EC-free electrolyte. Thus, graphite/LFP cells were built with a 1 M $LiPF_6$ in PC/EMC (30/70 by weight) electrolyte with 2% VC, 2% FEC, 1 atm CO_2 or no additive at all, and cycled with a rate of C/5 after 1 formation cycle at C/20 and 2 formation cycles at C/10. Figure 4a displays the specific charge capacity versus cycle number for different electrolyte formulations. No stable cycling is obtained for a graphite/LFP full-cell with an additive-free PC/EMC electrolyte (orange hexagonals), because PC does not form a stable SEI on graphite[56–60] and is therefore continuously reduced until all extractable Li^+ from LFP is consumed. The solvent co-intercalation in the graphite layers leads to exfoliation exposing fresh, unprotected graphite for further solvent reduction. This results in a first charge at a very low apparent cell voltage (2.6 V), without any discharge capacity after this first charge (see orange curve in Figure 4b). In contrast, all three additives (FEC, VC and CO_2) allow stable cycling in PC/EMC (Figure 4a). While the capacity and the capacity retention of the cells with 2 % VC (red dots) are essentially identical to those of cells with the standard electrolyte EC/EMC (LP57, black squares), cells with 2 % FEC (green diamonds) or CO_2

(blue triangles) have a much larger first cycle irreversible capacity (see Figure 4b) while their capacity fading is similar to that of the cell with VC or LP57. Please note that the irreversible capacity, i.e., the capacity drop between 1st and 2nd cycle, is relatively large for the here presented cells even with LP57 electrolyte. We correlate this behavior to the large specific surface area of the employed SLP30 graphite of 7 m^2/g, which necessitates an increased amount of SEI products for full protection of the active surface area, thereby consuming more Li-cations[58] and leading to a higher irreversible capacity. On the other hand, this higher surface area facilitates better signals for spectroscopic and for gas analysis due to the increased amount of SEI products formed on the surface.

Regarding the voltage profiles in Figure 4b, the similarity between FEC (green curve) and CO_2 (blue curve) is striking. Due to a lower initial voltage plateau at the beginning of charge, during which irreversible processes take place, the first discharge capacity is lowered. Afterwards, stable cycling is possible with coulombic efficiencies almost as high as for LP57 and for PC/EMC+VC. The latter reacts according to the observed gas evolution (cf. Figure 3a) at a potential 500 mV higher than FEC, which might lead to an earlier passivation of the graphite and thus to less irreversible capacity losses in the first cycle. These observations confirm the work of Jeong et al.,[60] who cycled cells with FEC and VC in pure PC and also found higher stabilities for cells with VC.

Overall, it can be concluded that CO_2 is capable of forming a sufficiently protective SEI on graphite to allow stable cycling in a PC/EMC electrolyte, and CO_2 evolution during the initial additive reduction process may thus be an important part of an effective SEI forming additive like VC and FEC. Due to the more complicated handling of CO_2 in comparison to liquid additives, the early successful application of CO_2 in lithium-ion batteries[19–25] may have been forgotten over time.

OEMS analysis of carbon black electrodes with and without $^{13}CO_2$

To better understand the CO_2 consumption process, we investigated the gas concentrations in cells filled with CO_2 during the first CV cycle by OEMS. Both EC and EMC do not form additional CO_2 upon reduction and were therefore chosen for this experiment. However, EMC presumably decomposes to lithium alkoxides,[31] which could chemically react with CO_2.[61] In contrast, lithium ethylene dicarbonate (LEDC), the major product of EC reduction, is not expected to react chemically with CO_2. To distinguish between gases originating from electrolyte reduction and products of CO_2 reduction, the respective cells were filled with isotopically labeled $^{13}CO_2$.

Figure 5a and b show the current profile (upper panels) and the gas evolution (lower panels) during a voltammetric scan at 0.1 mV/s of a C65 electrode from OCV (~3 V) to 0.1 V vs.

421 Li^+/Li and back to 2.0 V vs. Li^+/Li in argon-filled cells with EC + 1 M $LiPF_6$ and EMC + 1 M
422 $LiPF_6$ electrolyte, respectively. For the EC electrolyte (Figure 5a), a characteristic reduction
423 peak can be observed around 0.6 V vs. Li^+/Li. The evolution of ethylene starts just below 1 V
424 vs. Li^+/Li and rises steeply until it reaches a plateau of 17 $\mu mol/m^2_{BET}$ at the vertex potential.
425 Between 0.8 and 0.1 V vs. Li^+/Li, minor amounts of CO and H_2 (~2 $\mu mol/m^2_{BET}$) are observed.
426 Apart from these gases, CO_2 is evolved starting at 2 V vs. Li^+/Li, reaches a maximum of 1
427 $\mu mol/m^2_{BET}$ at 1.5 V vs. Li^+/Li, and drops back to zero below 1 V vs. Li^+/Li. The dominant
428 evolution of ethylene can be attributed to the major reduction pathway of EC to ethylene and
429 lithium ethylene dicarbonate (LEDC).[18,51,62,63] The evolution of CO_2 is presumably initiated by
430 the reaction of OH^-, a product of trace water reduction and EC.[64,65] A reduction of CO_2 to CO
431 seems unlikely here, as CO evolves only below 1 V vs. Li^+/Li, where CO_2 is already
432 completely consumed. However, CO has been suggested as the product of a direct
433 2-electron reduction of EC.[66–68] The simultaneous evolution of H_2 could result from the
434 reduction of residual H_2O,[64] protic impurities such as HF[49] or the direct reduction of EC.[63,69]

435 For an EMC + 1 M $LiPF_6$ electrolyte (Figure 5b), CO is the major evolved gas. Its evolution
436 proceeds in two steps, with a lower rate during the first step between 1.5 and 0.6 V vs. Li^+/Li
437 and a sharp increase between 0.6 and 0.1 V vs. Li^+/Li. Neither CO_2 nor H_2 were observed
438 during the measurement, yet strong signals related to the ester exchange reaction of EMC to
439 DMC and DEC were detected (not shown). Note that for this reason, the m/z = 12 trace was
440 chosen for quantification of the CO signal, as the typically used m/z = 28 is superimposed by
441 trans-esterification signals. A more detailed discussion of the reduction mechanism of EMC
442 and the trans-esterification can be found in Strehle et al.[30]

443 Figure 5c and d show the corresponding EC and EMC model electrolytes in cells filled with a
444 $^{13}CO_2$/Ar mixture. Both current profiles (upper panels) show a peak around 0.6 V vs. Li^+/Li.
445 Between 1.5 V and 0.1 V vs. Li^+/Li, a total of ~70 $\mu mol/m^2_{BET}$ and ~65 $\mu mol/m^2_{BET}$ $^{13}CO_2$ is
446 consumed in EC and EMC, respectively (middle panels). The rate plots (lower panels) show
447 that in both electrolytes, the $^{13}CO_2$ consumption proceeds through 3 steps with their rate
448 maxima at 1.5 V, 0.7 V, and 0.1 V vs. Li^+/Li. Interestingly, no ^{13}CO evolution is observed at
449 any of these steps, clearly disproving the previous assumption that CO_2 could be reduced to
450 CO and Li_2CO_3.[18,20] The additional H_2 evolution in both $^{13}CO_2$ cells is attributed to the
451 different gas filling procedure, which unfortunately seems to introduce some trace moisture
452 into these cells; this should, however, not affect the main finding, namely the consumption of
453 CO_2 without CO evolution. In the cell with EC and $^{13}CO_2$, the ethylene evolution is further
454 roughly halved, amounting to 7 $\mu mol/m^2_{BET}$, compared to the measurement in argon (Figure
455 5c). The CO evolution in the EMC cell with $^{13}CO_2$ (Figure 5d) is even more drastically
456 reduced, yielding only 1/5 of the amount released in the same electrolyte in argon (Figure

5b). Additionally, we could not detect any OEMS signals related to the trans-esterification of EMC[30] in the EMC/$^{13}CO_2$ cell.

The striking similarity of the amount and pattern of the $^{13}CO_2$ consumption in EC and EMC suggests that its pathway is independent of the solvent, and hence proceeds as an electrochemical reduction reaction and not as a chemical reaction with solvent decomposition products. In both cases, the presence of CO_2 can effectively suppress the decomposition of the original solvent. The stronger CO_2 induced suppression of electrolyte decomposition for EMC compared to EC can be explained by their different reduction potentials: While the EC and CO_2 reduction occur in the same potential range (1-0.5 V vs. Li^+/Li), EMC is mainly reduced at lower potentials (< 0.5 V vs. Li^+/Li), where CO_2 has already formed a passivating layer on the electrode. As discussed above, the absence of ^{13}CO further indicates that the commonly assumed reduction of CO_2 to Li_2CO_3 and CO does not take place. Although Li_2CO_3 is commonly observed in the SEI of electrodes cycled in CO_2,[22,24,25,70] a reduction to lithium oxalate[71,72] or lithium formate[73] is also possible in aprotic solvents. Therefore, we take a closer look at the SEI components formed in the presence of CO_2.

FTIR analysis of electrodes after formation in CO_2

In order to get a better understanding of the CO_2 consumption mechanism, FTIR spectra of graphite electrodes after one cycle at C/20 in an EMC or EC based electrolyte with and without CO_2 were analyzed. The cells were filled with both $^{12}CO_2$ and $^{13}CO_2$ to facilitate the assignment of the products formed due to CO_2 by the isotopic shift of the respective IR bands, the magnitude of which was estimated as follows.

The frequency ν of a vibrational band is determined by the coupling constant k and the reduced mass μ.

$$\nu = \frac{1}{2\pi}\sqrt{\frac{k}{\mu}} \qquad \text{with } \mu = \frac{m_1 m_2}{m_1 + m_2} \text{ for a two-atomic molecule} \qquad (1)$$

Assuming that the coupling constant does not change due to an isotopic exchange, the shift of the frequency can be calculated as follows:

$$\nu_{Isotope} = \nu\sqrt{\frac{\mu}{\mu_{Isotope}}} \qquad (2)$$

Even though these equations are only valid for molecules with two atoms, a rough estimation of the expected isotopic shift can be still calculated by considering a C and an O atom for vibrations from carbonates and carboxylates. The replacement of ^{12}C by ^{13}C would result in bands at a value of 97.8 % of that of the original wavenumber.

Figure 6 shows the ATR-FTIR spectra of the graphite electrodes cycled in EMC and EC based electrolytes with and without CO_2. The spectra of the electrodes cycled in argon show mostly alkyl carbonates (vibrations around 1640 cm^{-1}, 1310 cm^{-1}, 1080 cm^{-1} and 820 cm^{-1}) and are similar to the results by Nie et al. who analyzed binder-free electrodes in pure EC and EMC electrolytes.[51] The electrode cycled with $^{12}CO_2$ in EC contains additionally the characteristic asymmetric stretching vibration band of the CO_3^{2-} anion, which is largely increased for the electrodes cycled in $^{12}CO_2$. The asymmetric stretching vibration is split in two due to the degeneration of the symmetry in Li_2CO_3, resulting in a band at 1490 cm^{-1} and at 1420 cm^{-1}. These stretching vibration bands and the bending vibration band at 863 cm^{-1} are marked by the dotted lines in Figure 6 and are clearly shifted for the electrodes cycled in EC+$^{13}CO_2$ within the wave number range expected for a ^{13}C replacement (i.e., for the stretching vibration bands by ca. 30 cm^{-1}). A similar shift is observed for the electrodes after the formation cycle in EMC+$^{13}CO_2$. However, the split stretching vibration band is less pronounced. Therefore, it is likely that it consists of a mixture of $Li_2{}^{12}CO_3$ and $Li_2{}^{13}CO_3$. This finding is surprising, as only very little $^{12}CO_3^{2-}$ (if any) was found on the electrode after formation in EMC and argon (cf. brown line in Figure 6). It suggests that due to the presence of CO_2, Li_2CO_3 is formed both directly from the CO_2 and the EMC molecule.

The dashed lines in Figure 6 mark the strongest vibrations of ^{12}C lithium oxalate. No clear bands are observed at these wavenumbers. However, there is also an isotopic shift of bands observed around 1600 cm^{-1} when changing from $^{12}CO_2$ to $^{13}CO_2$. Unfortunately, these bands may belong to a variety of carbonates or carboxylates. In order to clarify the CO_2 reaction, we further applied NMR spectroscopy of D_2O extracts of cycled graphite electrodes to distinguish carboxylates like lithium formate or acetate from carbonates like lithium methyl or ethyl carbonate, which are unfortunately not clearly distinguishable by FTIR.

NMR analysis of electrodes after formation in CO_2

Figure 7 displays exemplary ^{1}H and proton decoupled ^{13}C NMR spectra of D_2O extracts of graphite electrodes after one formation cycle in a pure EC or EMC based electrolyte. Before analyzing the spectra of the cells with CO_2 added to the gas-phase, the spectra of the argon flushed cells (black and brown line in Figure 7) are compared to a previous study by Nie et al.,[51] who analyzed binder free graphite electrodes in pure EMC and EC based electrolytes. Similar to Nie's study, we obtained for pure EC a strong singlet at 3.67 ppm in the ^{1}H spectrum, which can be related to LEDC formation on the electrode. For EMC the expected singlet of lithium methyl carbonate (LMC) at 3.36 ppm as well as a triplet at 1.19 ppm (J=7.1 Hz) and a quartet at 3.65 ppm (J=7.1 Hz), which can be related to lithium ethyl carbonate (LEC), were found by ^{1}H NMR.[51,74] For both electrolyte systems, a small amount of lithium

acetate (LiAc) and lithium formate (LiForm) was detected and are marked in Figure 7a. Surprisingly, we found also some LEC and LMC in the EC cell, which cannot be explained by the commonly accepted EC decomposition mechanism[69] and which was not observed by Nie et al.[51] As expected, no LEDC was found in the EMC cell.

Regarding the ^{13}C NMR spectra in Figure 7b, only the main signals of LEC (16.7 and 57.3 ppm) and LMC (48.7 ppm) for EMC, as well as of LEDC (62.3 ppm) for EC were detected.[51,61] Furthermore, small signals at 167.8 ppm and 171.0 ppm, which can be related to Li_2CO_3 and lithium formate, were found. As no signal of the carbonate-C of LEDC, LMC or LEC is detectable, it is likely that the alkyl carbonates were quantitatively hydrolyzed by D_2O into alkoxides and Li_2CO_3.[75] This would further explain the detection of Li_2CO_3, which was only observed in traces by FTIR of the same electrodes from Ar-filled cells. The observed ^{13}C NMR signals may hence not directly belong to LEDC, LMC and LEC, but to ethylene glycolate, methoxide and ethoxide. Thus, a distinction between alkoxides and alkyl carbonates is unfortunately not feasible. Since alkoxides are commonly expected to be soluble in the electrolyte[76] and hence are not a major SEI product, we however believe that the NMR signals originate exclusively from the alkyl carbonates. Thus, the NMR signals are labeled as LEDC, LMC and LEC in the following. ^{19}F and ^{31}P NMR did not reveal any more insights, as only remaining trace amounts of $LiPF_6$ and LiF were found, in accordance to Nie et al.[51]

Figure 7a further shows the ^{1}H NMR spectra of cells after formation in a $^{13}CO_2$ enriched atmosphere. Surprisingly, no new products can be detected. However, the decomposition of EC and EMC is substantially reduced by the addition of CO_2, as the signals assigned to LEDC, LMC and LEC are decreased. In order to quantify this effect, TSP was added to the NMR tubes and the molar concentration per electrode surface area is determined and given in Figure 8 and Table S1. It can be clearly seen that the amount of LEDC in the EC cells is approximately halved due to the addition of CO_2. This finding is in line with the results from the above OEMS analysis, where the addition of CO_2 also roughly halved the characteristic decomposition gas ethylene on the Super C65 electrode (cf. Figure 5a and c) as well as on the graphite electrodes (cf. Figure S1 and S2). The decomposition of EMC is even more suppressed, although the decrease of LMC and LEC in the SEI is less than the decrease of the evolved CO (cf. Figure 5b and d). This confirms that the formation mechanism of LMC and LEC is not directly connected to the evolution of CO, which is explained in detail in literature.[74,77] The suppression of solvent decomposition seems not to be related to the partial pressure of CO_2, as the amount of LEDC, LMC and LEC is roughly the same for a cell flushed with 1 atm $^{12}CO_2$ or a cell containing a $^{13}CO_2$/Ar mixture (cf. Table S1). Even though no new water-soluble products are observed due to the addition of CO_2, the incorporation of CO_2 is observed with ^{13}C labeled CO_2 due to ^{1}H-^{13}C coupling. The additional doublet at the

position of lithium formate at 8.4 ppm with a coupling constant $^{1}J_{C\text{-}H}$ of 195 Hz[78] shows that $^{13}CO_2$ forms lithium formate. Furthermore, the lithium acetate signal at 1.9 ppm shows small amounts of a surrounding doublet with a coupling constant $^{2}J_{C\text{-}H}$ of 6 Hz. Even though $^{13}CO_2$ is hence clearly incorporated in the formed lithium acetate and lithium formate, the total amount of these species seems to be independent of whether CO_2 is added or not (cf. Table S1). In contrast, the lithium formate concentration seems to increase with the water concentration, as a larger lithium formate amount is found in cells filled with $^{13}CO_2$/Ar compared to $^{12}CO_2$. Due to the filling procedure and the lower dryness of $^{13}CO_2$ we assume a higher water content in those cells.

Figure 7b displays the ^{13}C NMR spectra of the argon flushed cells and the cells enriched with $^{13}CO_2$. In contrast to the ^{1}H NMR spectra, the signals belonging to products formed with $^{13}CO_2$ are clearly visible due to the signal enhancement by ^{13}C compared to products formed by non ^{13}C enriched species with a ^{13}C content of only 1.1 %. The signals correlated to LEDC, LEC and LMC are diminished in accordance to the ^{1}H NMR spectra, while strong signals arise around 170 ppm which hence must be related to products formed with $^{13}CO_2$. With the help of reference samples, the signals at 167.7 ppm, 171.0 ppm and 173.4 ppm were identified as Li_2CO_3, lithium formate and lithium oxalate ($Li_2C_2O_4$), respectively. The signal of lithium formate was further confirmed by the coupling constant $^{1}J_{C\text{-}H}$ of 195 Hz in the spectrum without proton decoupling, matching the one in the ^{1}H NMR spectrum. A signal belonging to lithium acetate, which should appear around 181 ppm with a coupling constant of 6 Hz, was, however, not found. Several further signals between 174 and 178 ppm must also belong to carboxylates and carbonates, but could not be identified (cf. Figure S4 for magnification). The same is true for a triplet at 75 ppm and a quartet at 85 ppm in the proton decoupled spectrum with coupling constants of 53 and 51 Hz, typical for $^{1}J_{C\text{-}C}$.[78] This implies that the coupling must occur between ^{13}C labeled nuclei, indicating a more complex structure formed by several $^{13}CO_2$ units. The triplet forms an additional doublet ($^{1}J_{C\text{-}H}$=150 Hz) in the spectrum without proton decoupling, indicating a tertiary carbon in the unknown substance.

However, as these signals are rather small, we focus in the following on the three main products observed in the cells filled with $^{13}CO_2$, namely Li_2CO_3, lithium formate and lithium oxalate. In order to quantify the signals, ^{13}C NMR spectra with a 25x prolonged relaxation delay were recorded to allow the full relaxation of the slowly relaxing carbonate nuclei. The surface normalized amounts obtained by referencing to the internal TSP standard are given in Table S2. For comparison with the quantification results from the ^{1}H NMR, the signal of LEDC from the graphite electrode in the $^{13}CO_2$/EC cell was also quantified assuming 1.1 % of ^{13}C, as $^{13}CO_2$ cannot be incorporated in the CH_2-units of LEDC. 10 µmol/m$^2_{BET}$ LEDC were found in ^{13}C NMR of the $^{13}CO_2$/EC graphite electrode compared to 9 µmol/m$^2_{BET}$ by ^{1}H NMR. This difference is probably related to the sample preparation (addition of the standard). A

slightly higher concentration was also determined for lithium formate by ^{13}C NMR in comparison to ^{1}H NMR in both EC-and EMC-based cells filled with $^{13}CO_2$, but the accuracy is reliable enough to quantify the amount of lithium oxalate in comparison to Li_2CO_3. Interestingly, the product distribution for EC and EMC with $^{13}CO_2$ is similar. While lithium oxalate occurs only in small amounts, roughly half of the amount of lithium formate, Li_2CO_3 is clearly the main product, in accordance to the FTIR spectra (cf. Figure 6). It should be, however, mentioned that due to the hydrolysis of alkyl carbonates by D_2O some Li_2CO_3 may arise from alkyl carbonates formed in the reaction of alkoxides and $^{13}CO_2$. This reaction was suggested to be responsible for the alkoxide scavenging effect of CO_2 stopping the trans-esterification of linear alkyl carbonate solvents.[30] The small amount of superposing $Li_2{}^{12}CO_3$ can, however, be neglected.

In order to quantify all the detected NMR products, we finally added C_6F_6 to the D_2O extracts of the electrodes to estimate the amount of LiF in the SEI, which is given in Figure 8 and Table S1. Similar to VC and FEC, the addition of CO_2 suppresses the $LiPF_6$ decomposition, as also less LiF was found in the electrodes of the CO_2 cells.

Discussion

SEI thickness

In order to check whether the thickness of the SEI composed of the products found is reasonable, we estimated the number of monolayers derived from the surface normalized amounts obtained by NMR and summarized the results in Table S3. For this, we assumed that each atom of the found molecules occupies a square with an edge length of a carbon-carbon single bond (0.15 nm[82]). The resulting 2.7 to 5 monolayers seem reasonable. The actual SEI thickness might be higher, as some products may not adsorb flat on the surface, and as products insoluble in D_2O such as polymers are not taken into account. Nevertheless, it appears that the total amount of SEI monolayers is decreased due to the addition of CO_2. This might mean that the main product of CO_2, namely Li_2CO_3, passivates the graphite anode more efficiently than a bulkier alkyl carbonate which may not lie completely flat on the surface. It should, however, also be mentioned that the SEI is thicker in a pure EC cell than in a pure EMC cell. This correlates with the observation from the XPS spectra (cf. Figure 2b), where the graphite peak could be seen in the spectra from electrodes in EMC electrolyte but not for electrodes cycled in EC. As the passivation properties of EC are superior compared to EMC,[83] it is difficult to judge whether a thinner or a thicker SEI is at the end advantageous.

The formation of Li_2CO_3

The FTIR and NMR analyses show clear evidence that Li_2CO_3 is the major product due to intentionally added CO_2 on the graphite electrode in Li-ion battery cells. However, no CO was detected by OEMS upon the consumption of CO_2, which clearly excludes the previously hypothesized mechanism:[20]

$$2\ CO_2 + 2\ e^- + 2\ Li^+ \rightarrow CO + Li_2CO_3 \quad (3)$$

A fraction of the detected Li_2CO_3 can be explained by the reduction of trace water and its subsequent reaction with CO_2:

$$H_2O + e^- \rightarrow 0.5\ H_2 + OH^- \quad (4)$$

$$CO_2 + OH^- + 2\ Li^+ \rightarrow Li_2CO_3 + H^+ \quad (5)$$

Reactions (4) and (5) explain further the effect that more water leads to more Li_2CO_3 and less LEDC in the SEI.[84] Water is expected to be reduced at approximately 1.5 V vs. Li^+/Li.[64,85] As can be seen in Figure 5 a-d, a clear reduction peak can be observed in the voltage profile at this potential. The integration of this peak yields an electric charge which would be required to reduce approximately 40-50 ppm of water. Summing the trace water contained in the electrolyte (a minor amount, as water converts to HF during storage[49]), in the electrodes and introduced by the gas filling procedure, this amount seems reasonable. At this potential, the first (minor) CO_2 consumption process takes place (see Figure 5c and d), in agreement with reaction (5). Surprisingly, no hydrogen is evolved at this potential in argon-filled cells (Figure 5a and b), although hydrogen evolution can be observed in cells filled with $^{13}CO_2$ (Figure 5c and d), which probably contain more moisture due to the $^{13}CO_2$ filling procedure.

The main consumption of CO_2 takes place in a second process around 0.7 V vs. Li^+/Li (see Figure 5c and d), which fits to the suggestion that the reduction of CO_2 to $CO_2^{\bullet-}$ radicals occurs at lower potentials than the water reduction:[86]

$$CO_2 + e^- \rightarrow CO_2^{\bullet-} \quad (6)$$

$CO_2^{\bullet-}$ radicals will recombine forming lithium oxalate:

$$2\ CO_2^{\bullet-} + 2\ Li^+ \rightarrow Li_2C_2O_4 \quad (7)$$

Furthermore, $CO_2^{\bullet-}$ radicals can react in the presence of protons produced by reaction (5) or other protic impurities, e.g. from HF, to lithium formate:

$$CO_2^{\bullet-} + H^+ + Li^+ + e^- \rightarrow HCO_2Li \quad (8)$$

In order to produce the 1.6-3.3 $\mu mol/m^2_{BET}$ of lithium formate detected (cf. Figure 8 as well as Table S1 and S2), about 15-40 ppm of protons in the form of water or HF are needed in the electrolyte. Assuming that water is the only protic impurity and that according to reactions (4) and (5) one proton would be released into the electrolyte per water molecule, the formed

amount of lithium formate is comparable to the amount of water determined by the charge flowing at the water reduction potential of 1.5 V vs. Li^+/Li in the voltage profile. As the amount of water is much smaller than the amount of CO_2 in CO_2-filled cells, it makes sense that the amount of lithium formate scales with the water content (cells filled with $^{13}CO_2$ are suspected to contain more moisture than cells with $^{12}CO_2$ or argon) but not directly with CO_2 as can be seen in Figure 8 and Table S1.

If reactions (4) and (5) were the only occurring processes leading to Li_2CO_3, the ratio of Li_2CO_3:H_2O should be 1:1. However, only around 5 µmol/m²$_{BET}$ Li_2CO_3 of the 14 µmol/m²$_{BET}$ found (cf. Table S2) can be explained by these reactions assuming 40-50 ppm of water. Another possible mechanism for the detection of a substantial amount of Li_2CO_3 by NMR may stem from the Dumas-Peligot reaction,[87] which is utilized to synthesize alkyl carbonates.[61,75,88–90] Alkoxides formed during solvent decomposition[74] react with CO_2 to the corresponding alkyl carbonates, but are hydrolized in D_2O and only the ^{13}C labeled Li_2CO_3 is detected. However, since Li_2CO_3 is also the main product in the FTIR spectra (cf. Figure 6), where any contact of the electrodes with water was carefully avoided, this reaction cannot be responsible for the main share of Li_2CO_3 formed, unless alkyl carbonates can be further reduced to Li_2CO_3. Yet, this seems not very likely, as alkyl carbonates are a major part of the SEI (cf. Figure 8 as well as Table S1 and S3) and only little Li_2CO_3 is found in the absence of CO_2. Furthermore, alkoxides are a major decomposition product of linear, but not of cyclic alkyl carbonates, as can be seen by the significant lower amount of CO evolved from EC reduction compared to EMC reduction (see Figure 5 a and b). Therefore, the similar product distribution for the EMC and the EC cell would be hard to explain with this mechanism. In order to prove that CO is simply just not detected by OEMS due to some consecutive reactions with carbonate electrolyte decomposition products, the gas evolution of a cell with 0.5 M LiTFSI in diglyme as electrolyte and added $^{13}CO_2$ was monitored. Figure 9 indicates a $^{13}CO_2$ consumption in this cell of approximately 110 µmol/m²$_{BET}$, which is higher compared to the cells with carbonate-based electrolytes (65-70 µmol/m²$_{BET}$, see Figure 5c and d). In contrast to the carbonate electrolytes, a small amount of 2 µmol/m²$_{BET}$ ^{13}CO was detected. However, the amount of ^{13}CO detected in the diglyme electrolyte is by far too low to explain the CO_2 consumption via reaction (3).

Zhuang et al.[91] suggested that CO is not evolved due to its further reduction to carbon according to the following mechanism, which would lead to additional Li_2CO_3:

$$2\ CO_2 + 2\ e^- \rightarrow CO_3^{2-} + CO_{ads} \qquad (9)$$

$$CO_{ads} + 2\ e^- \rightarrow C + O^{2-}_{ads}$$

$$CO_2 + O^{2-}_{ads} \rightarrow CO_3^{2-}$$

$$3\ CO_2 + 4\ e^- \rightarrow 2\ CO_3^{2-} + C$$

A similar mechanism is also claimed for the reduction of CO_2 in Li-CO_2 batteries,[92–95] where the formation of amorphous carbon was confirmed by Liu et al.[93] and Qiao et al.[95] Since 5 µmol/m²$_{BET}$ of the Li_2CO_3 detected by NMR (cf. Figure 8 and Table S2) can be explained by reactions (4) and (5), 9 µmol/m²$_{BET}$ (viz., 14 µmol/m²$_{BET}$ - 5 µmol/m²$_{BET}$) must be explained differently. In case that all of the remaining 9 µmol/m²$_{BET}$ Li_2CO_3 is formed according to reactions (9), 4.5 µmol/m²$_{BET}$ of amorphous carbon should be additionally formed from the consumed CO_2.

The consumption of CO_2 is, as can be seen in the gas evolution rate of Figure 5b and d, not continuous, but composed of three different processes. The first one at 1.5 V vs. Li^+/Li is related to the reduction of water and formation of Li_2CO_3 (cf. reactions (4) and (5)). The second one at 0.7 V vs. Li^+/Li belongs to the CO_2 reduction to CO_2^- (cf. reaction (6)) and subsequent formation of lithium oxalate and lithium formate according to reactions (7) and (8). The third CO_2 consumption process around 0.1 V vs. Li^+/Li may hence be explained by further CO_2 reduction according to reactions (9), as (almost) no CO was detected by OEMS.

Reactions (4) to (9) give a plausible explanation for the detected amount of Li_2CO_3, lithium formate and lithium oxalate by ^{13}C NMR (cf. Table S2). However, the total CO_2 consumption observed in the OEMS measurements does not very well match the amount of products found by NMR. The cell with EC and $^{13}CO_2$ consumed ~58 µmol/m²$_{BET}$ CO_2 (Figure 5c), the cell with EMC and $^{13}CO_2$ ~72 µmol/m²$_{BET}$ CO_2 (Figure 5d). The difference between EC and EMC might be related to the above mentioned reaction of alkoxides and CO_2, which should occur in particular for linear carbonates. Still, less than 25 µmol/m²$_{BET}$ of $^{13}CO_2$ was consumed for the products detected in the ^{13}C NMR spectra (cf. Table S2). This mismatch may be related to the two different cell set-ups used: while the OEMS measurements were performed with a 2-compartment half-cell and carbon black electrodes, the NMR analysis was done with LFP-graphite full-cells. To clarify whether this may lead to different SEI compositions, we performed an additional OEMS measurement of a graphite electrode with an EC electrolyte and $^{13}CO_2$ in a 2-compartment cell, and indeed only 36 µmol/m²$_{BET}$ of CO_2 was consumed (see Figure S2). A similar experiment with argon-filled cells revealed that also the ethylene reduction per m²$_{BET}$ is about 1.7 times higher for the C65 carbon black compared to SLP30 graphite (see Figure S1), which is probably related to the different surface structure of edge and basal planes of the graphite. We further hypothesize that the lower consumption of CO_2 with graphite is related to the ≈10x smaller surface area of SLP30 compared to C65, while the amount of trace water in the electrolyte is the same, leading to a more immediate surface passivation by water reduction and Li_2CO_3 formation (see reactions (4) and (5)) and to less CO_2 consumption by subsequent processes on the low-surface area graphite electrodes. An OEMS measurement of a galvanostatically cycled full-cell with an SLP30 graphite anode and LFP as counter electrode instead of lithium, led to a similar CO_2

741 consumption of 32 µmol/m²$_{BET}$ (see Figure S3). Hence, using LFP in a 1-compartment cell
742 instead of the 2-compartment cell with lithium counter electrode does not influence the
743 measurement as much as using C65 carbon instead of graphite. Comparing the products
744 found by NMR (< 25 µmol/m²$_{BET}$) and the CO_2 consumed by OEMS (32 µmol/m²$_{BET}$) in the
745 same cell configuration, leaves a gap of only 7 µmol/m²$_{BET}$. 4.5 µmol/m²$_{BET}$ of the missing
746 7 µmol/m²$_{BET}$ can be explained with the amorphous carbon formed according to reactions (9),
747 which cannot be detected in the D_2O extract by NMR. Furthermore, small amounts of
748 products may not be detected by NMR, because they might be insoluble in D_2O such as
749 polymers. Substantial losses due to the rinsing of the electrodes can, however, be excluded
750 as a non-washed electrode cycled in EMC under a CO_2 atmosphere showed similar results
751 to the rinsed equivalent.

752

753 **Conclusion**

754 In this paper the effect of the two most common SEI forming additives VC and FEC were
755 directly compared on carbonaceous electrodes. The decomposition of both additives leads to
756 a polymeric carbonate. While VC suppresses the formation of LiF, FEC increases the
757 amount of LiF in the electrode. CO_2 is next to trace amounts of CO the only gaseous
758 decomposition product during formation for both additives.

759 Interestingly, the addition of CO_2 to LFP/graphite cells with PC/EMC electrolyte allowed
760 stable cycling, very similar to cells with 2 % FEC in PC/EMC, while cells without additives in a
761 PC/EMC electrolyte could not be discharged even once. Mass spectrometric analysis of the
762 gas evolution during formation of cells filled with gaseous CO_2 revealed that in contrast of
763 common beliefs, no CO is evolved due to the reduction of CO_2, even though Li_2CO_3 was
764 found to be the main additional compound of the SEI in the presence of gaseous CO_2.
765 Furthermore, lithium formate and lithium oxalate were detected for cells with both pure EC
766 and pure EMC electrolyte filled with CO_2. Quantification with NMR demonstrated that the
767 concentration of lithium carbonate, formate and oxalate is comparable for cells with EC and
768 EMC, suggesting a CO_2 reaction mechanism independent of the decomposition pathway of
769 the used solvent. CO_2 led further to a clear suppression of typical solvent decomposition
770 products.

771 Hence, we conclude that the addition of CO_2 or CO_2-evolving additives are clearly beneficial
772 for the formation of the SEI. CO_2 leads in combination with water and HF to a first passivation
773 layer made of lithium formate and carbonate at potentials starting around 1.5 V vs. Li^+/Li,
774 which suppresses the later decomposition of the solvents once potentials are reached. We
775 believe therefore that CO_2 in combination with trace water is advantageous for the initial
776 formation of the SEI. Further tests are necessary to decide to what extent expensive drying

of battery components could be abolished when using additives which evolve CO_2 at high potentials, obtaining similar or even better battery performance.

Acknowledgement

We thank the BASF SE for financial support through the framework of its Scientific Network on Electrochemistry and Batteries. We thank Wolfgang Eisenreich from TUM and his team for their help with the NMR measurements. The authors further acknowledge Stefano Meini and Benjamin Strehle for fruitful discussions.

References

1. E. Peled, *J. Electrochem. Soc.*, **126**, 2047–2051 (1979).
2. M. Nie, J. Demeaux, B. T. Young, D. R. Heskett, Y. Chen, A. Bose, J. C. Woicik, and B. L. Lucht, *J. Electrochem. Soc.*, **162**, A7008–A7014 (2015).
3. H. Nakai, T. Kubota, A. Kita, and A. Kawashima, *J. Electrochem. Soc.*, **158**, A798 (2011).
4. V. Etacheri, O. Haik, Y. Goffer, G. A. Roberts, I. C. Stefan, R. Fasching, and D. Aurbach, *Langmuir*, **28**, 965–76 (2012).
5. M. Nie, D. P. Abraham, Y. Chen, A. Bose, and B. L. Lucht, *J. Phys. Chem. C*, **117**, 13403–13412 (2013).
6. E. Markevich, K. Fridman, R. Sharabi, R. Elazari, G. Salitra, H. E. Gottlieb, G. Gershinsky, A. Garsuch, G. Semrau, M. A. Schmidt, et al., *J. Electrochem. Soc.*, **160**, A1824–A1833 (2013).
7. I. A. Profatilova, C. Stock, A. Schmitz, S. Passerini, and M. Winter, *J. Power Sources*, **222**, 140–149 (2013).
8. C. C. Nguyen and B. L. Lucht, *J. Electrochem. Soc.*, **161**, A1933–A1938 (2014).
9. E. Markevich, G. Salitra, K. Fridman, R. Sharabi, G. Gershinsky, A. Garsuch, G. Semrau, M. A. Schmidt, and D. Aurbach, *Langmuir*, **30**, 7414–7424 (2014).
10. L. Hu, Z. Zhang, and K. Amine, *Electrochem. commun.*, **35**, 76–79 (2013).
11. H. Ota, Y. Sakata, A. Inoue, and S. Yamaguchi, *J. Electrochem. Soc.*, **151**, A1659 (2004).
12. B. Zhang, M. Metzger, S. Solchenbach, M. Payne, S. Meini, H. A. Gasteiger, A. Garsuch, and B. L. Lucht, *J. Phys. Chem. C*, **119**, 11337–11348 (2015).
13. A. L. Michan, B. S. Parimalam, M. Leskes, R. N. Kerber, T. Yoon, C. P. Grey, and B. L. Lucht, *Chem. Mater.*, **28**, 8149–8159 (2016).
14. I. A. Profatilova, S.-S. Kim, and N.-S. Choi, *Electrochim. Acta*, **54**, 4445–4450 (2009).
15. H. Ota, K. Shima, M. Ue, and J. Yamaki, *Electrochim. Acta*, **49**, 565–572 (2004).

16. R. Jung, M. Metzger, D. Haering, S. Solchenbach, C. Marino, N. Tsiouvaras, C. Stinner, and H. A. Gasteiger, *J. Electrochem. Soc.*, **163**, A1705–A1716 (2016).
17. M. E. Spahr, T. Palladino, H. Wilhelm, A. Würsig, D. Goers, H. Buqa, M. Holzapfel, and P. Novák, *J. Electrochem. Soc.*, **151**, A1383–A1395 (2004).
18. D. Aurbach, Y. Gofer, M. Ben-Zion, and P. Aped, *J. Electroanal. Chem.*, **339**, 451–471 (1992).
19. J. O. Besenhard, M. W. Wagner, M. Winter, A. D. Jannakoudakis, P. D. Jannakoudakis, and E. Theodoridou, *J. Power Sources*, **44**, 413–420 (1993).
20. D. Aurbach and O. Chusid, *Electrochem. Soc. Lett.*, **140**, L155-157 (1993).
21. O. Chusid, Y. Ein-Ely, D. Aurbach, M. Babai, and Y. Carmeli, *J. Power Sources*, **43**, 47–64 (1993).
22. D. Aurbach, Y. Ein-Eli, O. Chusid, Y. Carmeli, M. Babai, and H. Yamin, *J. Electrochem. Soc.*, **141**, 603–611 (1994).
23. D. Aurbach, Y. Ein-Ely, and A. Zaban, *J. Electrochem. Soc.*, **141**, L1 (1994).
24. Y. Ein-Eli, B. Markovsky, D. Aurbach, Y. Carmeli, H. Yamin, and S. Luski, *Electrochim. Acta*, **39**, 2559–2569 (1994).
25. D. Aurbach, Y. Ein-Eli, B. Markovsky, A. Zaban, S. Luski, Y. Carmeli, and H. Yamin, *J. Electrochem. Soc.*, **142**, 2882 (1995).
26. T. Osaka, T. Momma, T. Tajima, and Y. Matsumoto, *J. Electrochem. Soc.*, **142**, 1057 (1995).
27. D. Aurbach and Y. S. Cohen, *J. Electrochem. Soc.*, **144**, 3355–3360 (1997).
28. L. J. Krause, V. Chevrier, L. D. Jensen, and T. Brandt, *J. Electrochem. Soc.*, **164**, A2527-2533 (2017).
29. S. Solchenbach, M. Wetjen, D. Pritzl, K. U. Schwenke, and H. A. Gasteiger, *J. Electrochem. Soc.*, **165**, A512–A524 (2018).
30. B. Strehle, S. Solchenbach, M. Metzger, K. U. Schwenke, and H. A. Gasteiger, *J. Electrochem. Soc.*, **164**, A2513-2526 (2017).
31. E. S. Takeuchi, H. Gan, M. Palazzo, R. A. Leising, and S. M. Davis, *J. Electrochem. Soc.*, **144**, 1944–1948 (1997).
32. S. Meini, M. Piana, N. Tsiouvaras, A. Garsuch, and H. A. Gasteiger, *Electrochem. Solid-State Lett.*, **15**, A45 (2012).
33. N. Tsiouvaras, S. Meini, I. Buchberger, and H. A. Gasteiger, *J. Electrochem. Soc.*, **160**, A471–A477 (2013).
34. M. Metzger, C. Marino, J. Sicklinger, D. Haering, and H. A. Gasteiger, *J. Electrochem. Soc.*, **162**, A1123–A1134 (2015).
35. M. Metzger, B. Strehle, S. Solchenbach, and H. A. Gasteiger, *J. Electrochem. Soc.*, **163**, A798–A809 (2016).

36. J. M. Martinez del la Hoz and P. B. Balbuena, *Phys. Chem. Chem. Phys.*, **16**, 17091–8 (2014).
37. D. Wang, N. N. Sinha, J. C. Burns, C. P. Aiken, R. Petibon, and J. R. Dahn, *J. Electrochem. Soc.*, **161**, 467–472 (2014).
38. D. Pritzl, S. Solchenbach, M. Wetjen, and H. A. Gasteiger, *J. Electrochem. Soc.*, **164**, A2625–A2635 (2017).
39. R. Petibon, J. Xia, J. C. Burns, and J. R. Dahn, *J. Electrochem. Soc.*, **161**, A1618–A1624 (2014).
40. R. Petibon, V. Chevrier, C. P. Aiken, D. S. Hall, S. Hyatt, R. Shunmugasundaram, and J. R. Dahn, *J. Electrochem. Soc.*, **163**, 1146–1156 (2016).
41. D. Aurbach, K. Gamolsky, B. Markovsky, Y. Gofer, M. A. Schmidt, and U. Heider, *Electrochim. Acta*, **47**, 1423–1439 (2002).
42. L. El Ouatani, R. Dedryvère, C. Siret, P. Biensan, S. Reynaud, P. Iratçabal, and D. Gonbeau, *J. Electrochem. Soc.*, **156**, A103 (2009).
43. I. A. Profatilova, N.-S. Choi, S. W. Roh, and S.-S. Kim, *J. Power Sources*, **192**, 636–643 (2009).
44. C. Xu, F. Lindgren, B. Philippe, M. Gorgoi, F. Björefors, K. Edström, and T. Gustafsson, *Chem. Mater.*, **27**, 2591–2599 (2015).
45. K. W. Schroder, J. Alvarado, T. A. Yersak, J. Li, N. J. Dudney, L. J. Webb, Y. S. Meng, and K. J. Stevenson, *Chem. Mater.*, **27**, 5531–5542 (2015).
46. S. Dalavi, P. R. Guduru, and B. L. Lucht, *J. Electrochem. Soc.*, **159**, A642 (2012).
47. J. Jones, M. Anouti, M. Caillon-Caravanier, P. Willmann, P. Y. Sizaret, and D. Lemordant, *Fluid Phase Equilib.*, **305**, 121–126 (2011).
48. M. Nie and B. L. Lucht, *J. Electrochem. Soc.*, **161**, A1001–A1006 (2014).
49. D. Strmcnik, I. E. Castelli, J. G. Connell, D. Haering, M. Zorko, P. Martins, P. P. Lopes, B. Genorio, T. Østergaard, H. A. Gasteiger, et al., *Nat. Catal.*, **1**, 255–262 (2018).
50. L. El Ouatani, R. Dedryvère, C. Siret, P. Biensan, and D. Gonbeau, *J. Electrochem. Soc.*, **156**, A468 (2009).
51. M. Nie, D. Chalasani, D. P. Abraham, Y. Chen, A. Bose, and B. L. Lucht, *J. Phys. Chem. C*, **117**, 1257–1267 (2013).
52. I. A. Shkrob, J. F. Wishart, and D. P. Abraham, *J. Phys. Chem. C*, **119**, 14954–14964 (2015).
53. F. A. Soto, Y. Ma, J. M. Martinez del la Hoz, J. M. Seminario, and P. B. Balbuena, *Chem. Mater.*, **27**, 7990–8000 (2015).
54. K. Ushirogata, K. Sodeyama, Y. Okuno, and Y. Tateyama, *J. Am. Chem. Soc.*, **1335**, 11967–11974 (2013).
55. Y. Okuno, K. Ushirogata, K. Sodeyama, and Y. Tateyama, *Phys. Chem. Chem. Phys.*,

18, 8643–8653 (2016).
56. J. O. Besenhard and H. P. Fritz, *Electroanal. Chem. Interfacial Electrochem.*, **53**, 329–333 (1974).
57. A. N. Dey and B. P. Sullivan, *J. Electrochem. Soc.*, **117**, 222 (1970).
58. R. Fong, U. von Sacken, and J. R. Dahn, *J. Electrochem. Soc.*, **137**, 2009 (1990).
59. K. Xu, *J. Electrochem. Soc.*, **156**, A751 (2009).
60. S. Jeong, M. Inaba, R. Mogi, Y. Iriyama, and A. Abouimrane, *Langmuir*, **17**, 8281–8286 (2001).
61. L. Gireaud, S. Grugeon, S. Laruelle, S. Pilard, and J.-M. Tarascon, *J. Electrochem. Soc.*, **152**, A850 (2005).
62. G. V. Zhuang, K. Xu, H. Yang, T. R. Jow, and P. N. Ross, *J. Phys. Chem. B*, **109**, 17567–17573 (2005).
63. R. Imhof and P. Novák, *J. Electrochem. Soc.*, **145**, 1081 (1998).
64. R. Bernhard, M. Metzger, and H. A. Gasteiger, *J. Electrochem. Soc.*, **162**, A1984–A1989 (2015).
65. M. Metzger, B. Strehle, S. Solchenbach, and H. A. Gasteiger, *J. Electrochem. Soc.*, **163**, A1219–A1225 (2016).
66. R. Mogi, M. Inaba, Y. Iriyama, T. Abe, and Z. Ogumi, *J. Power Sources*, **119**–**121**, 597–603 (2003).
67. M. Onuki, S. Kinoshita, Y. Sakata, M. Yanagidate, Y. Otake, M. Ue, and M. Deguchi, *J. Electrochem. Soc.*, **155**, A794 (2008).
68. K. Leung, *Chem. Phys. Lett.*, **568**–**569**, 1–8 (2013).
69. M. Winter, R. Imhof, F. Joho, and P. Novák, *J. Power Sources*, **81**–**82**, 818–823 (1999).
70. D. Aurbach, B. Markovsky, I. Weissman, E. Levi, and Y. Ein-Eli, *Electrochim. Acta*, **45**, 67–86 (1999).
71. C. Amatore and J.-M. Saveant, *J. Am. Chem. Soc.*, **103**, 5021–5023 (1981).
72. U. Kaiser and E. Heitz, *Berichte der Bunsen-Gesellschaft*, **77**, 818–823 (1973).
73. L. V Haynes and D. T. Sawyer, *Anal. Chem.*, **39**, 332 (1958).
74. T. Sasaki, T. Abe, Y. Iriyama, M. Inaba, and Z. Ogumi, *J. Power Sources*, **150**, 208–215 (2005).
75. K. Xu, G. V. Zhuang, J. L. Allen, U. Lee, S. S. Zhang, P. N. Ross, and T. R. Jow, *J. Phys. Chem. B*, **110**, 7708–7719 (2006).
76. G. Gachot, S. Grugeon, M. Armand, S. Pilard, P. Guenot, J.-M. Tarascon, and S. Laruelle, *J. Power Sources*, **178**, 409–421 (2008).
77. H. Yoshida, T. Fukunaga, T. Hazama, M. Terasaki, M. Mizutani, and M. Yamachi, *J. Power Sources*, **68**, 311–315 (1997).
78. J. B. Lambert and E. P. Mazzola, *Nuclear Magnetic Resonance Spectroscopy*, Pearson

Education Inc., (2004).
79. K. Tasaki, K. Kanda, S. Nakamura, and M. Ue, *J. Electrochem. Soc.*, **150**, A1628 (2003).
80. A. V. Plakhotnyk, L. Ernst, and R. Schmutzler, *J. Fluor. Chem.*, **126**, 27–31 (2005).
81. L. Terborg, S. Nowak, S. Passerini, M. Winter, U. Karst, P. R. Haddad, and P. N. Nesterenko, *Anal. Chim. Acta*, **714**, 121–126 (2012).
82. D. R. Lide, *Tetrahedron*, **17**, 125–134 (1962).
83. Y. Ein-Eli, S. R. Thomas, and V. R. Koch, *J. Electrochem. Soc.*, **143**, L273–L277 (1996).
84. K. Edström, M. Herstedt, and D. P. Abraham, *J. Power Sources*, **153**, 380–384 (2006).
85. Y. Ein-Ely and D. Aurbach, *Langmuir*, **8**, 1845–1850 (1992).
86. P. A. Christensen, A. Hamnett, A. V. G. Muir, and N. A. Freeman, *J. Electroanal. Chem.*, **288**, 197–215 (1990).
87. J. Dumas and E. Peligot, *Justus Liebigs Ann. Chem.*, **35**, 281–292 (1840).
88. D. Aurbach, M. L. Daroux, P. W. Faguy, and E. Yeager, *J. Electrochem. Soc.*, **134**, 1611–1620 (1987).
89. R. Dedryvère, L. Gireaud, S. Grugeon, S. Laruelle, J.-M. Tarascon, and D. Gonbeau, *J. Phys. Chem. B*, **109**, 15868–15875 (2005).
90. G. V. Zhuang, H. Yang, P. N. Ross, K. Xu, and T. R. Jow, *Electrochem. Solid-State Lett.*, **9**, A64–A68 (2006).
91. G. V. Zhuang, Y. Chen, and P. N. Ross, *Surf. Sci.*, **418**, 139–149 (1998).
92. S. Xu, S. K. Das, and L. A. Archer, *RSC Adv.*, **3**, 6656–6660 (2013).
93. Y. Liu, R. Wang, Y. Lyu, H. Li, and L. Chen, *Energy Environ. Sci.*, **7**, 677 (2014).
94. X. Li, S. Yang, N. Feng, P. He, and H. Zhou, *Chinese J. Catal.*, **37**, 1016–1024 (2016).
95. Y. Qiao, J. Yi, S. Wu, Y. Liu, S. Yang, P. He, and H. Zhou, *Joule*, **1**, 359–370 (2017).

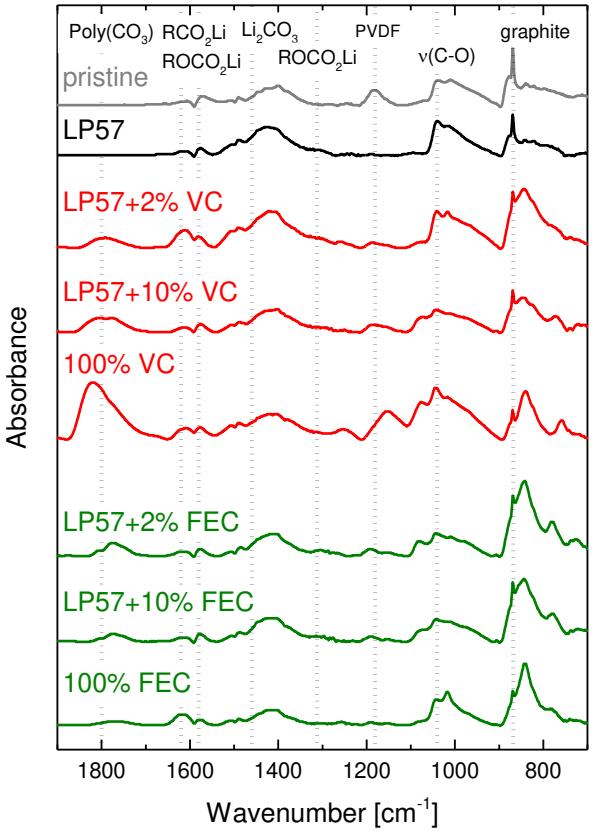

Figure 1: ATR-FTIR spectra of PVDF-bonded graphite electrodes after one formation cycle versus LFP at C/20 between 2.7 and 3.9 V in 1 M $LiPF_6$ in EC/EMC (3:7, LP57) with various amounts of VC (red lines) and FEC (green lines) ranging from 0-100 %. The spectrum nominated “pristine” consists of a pristine graphite electrode.

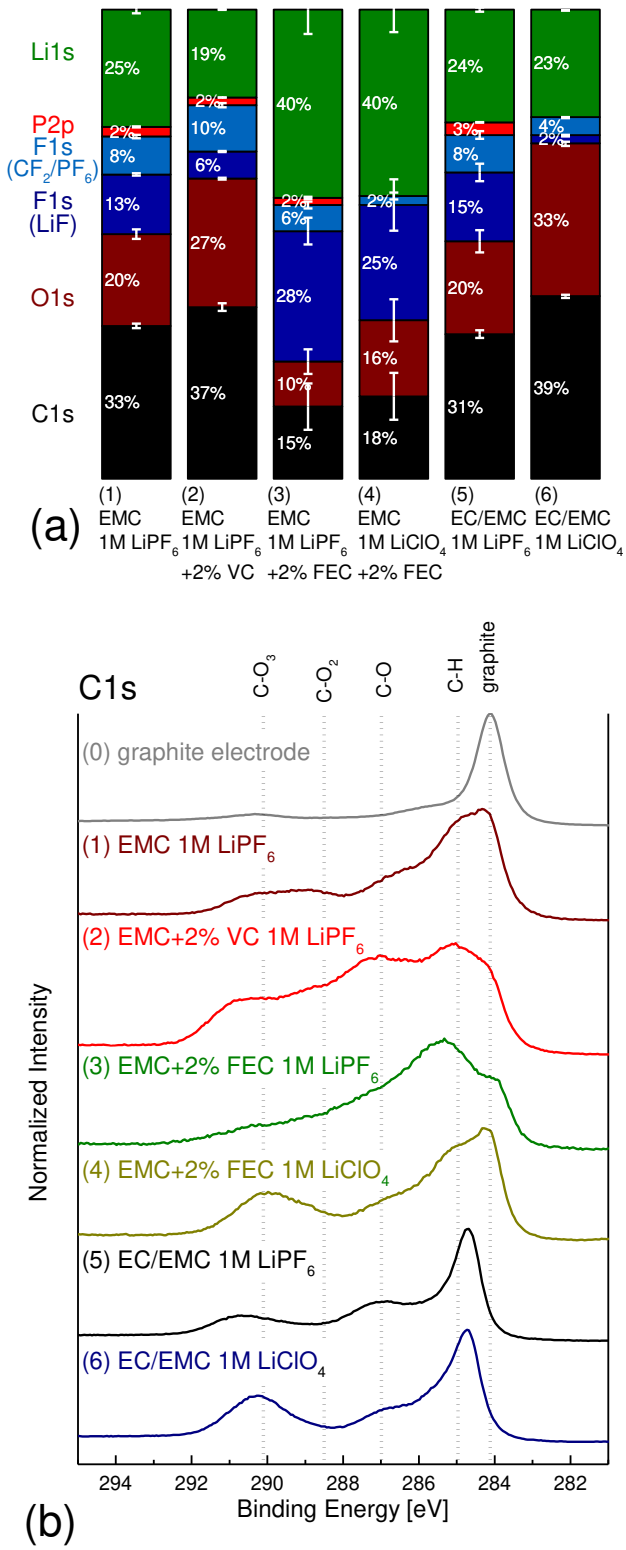

Figure 2: XPS analysis of PVDF-bonded graphite electrodes after one formation cycle at C/20 between 2.7 and 3.9 V versus LFP in various electrolyte solutions with either 1 M $LiPF_6$ or $LiClO_4$ as salt and either EC/EMC or EMC with and without 2% additive as solvent. (a) Molar percentage of the different elements detected by XPS. Molar fractions of F bound in LiF and in C-F/P-F bonds are given separately. The error bars represent the standard deviation of several measurement points on the same electrode. Usually 2 points per electrode were measured. As the deviation for the electrode cycled in EMC+FEC was comparably high, 4 ($LiPF_6$) and 7 ($LiClO_4$) points were analyzed for these electrodes. (b) C1s core spectra normalized between 0 and 1.

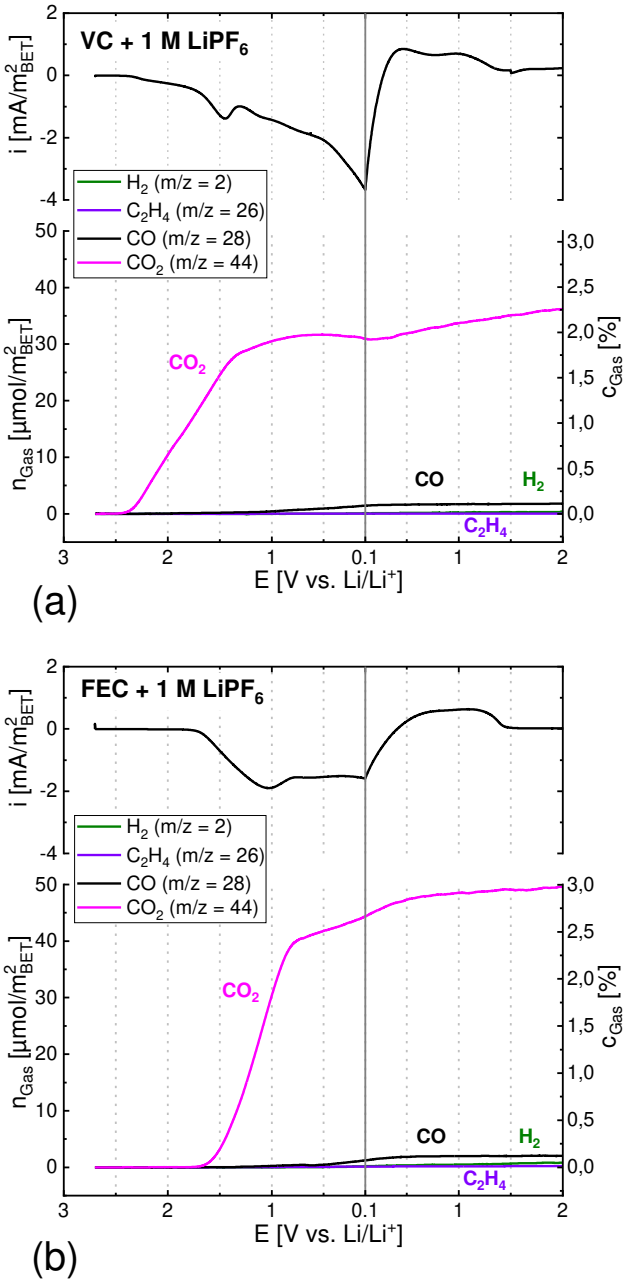

Figure 3: Gas evolution of a Super C65 carbon electrode during one CV cycle at 0.1 mV/s in two model electrolytes with 1 M $LiPF_6$ in (a) VC or in (b) FEC. The carbon working electrode is separated from the metallic lithium counter electrode with an aluminum sealed solid electrolyte diffusion barrier in the here used 2-compartment OEMS cells.

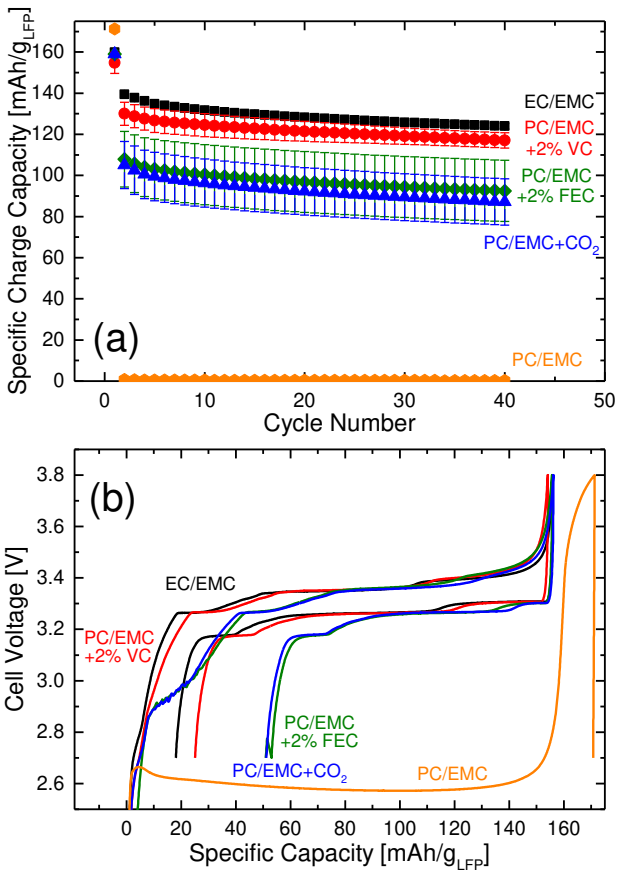

Figure 4: (a) Galvanostatic cycling performance (charge capacity) and (b) exemplary 1st cycle at C/20 of LFP/graphite electrodes in 1 M $LiPF_6$ in EC/EMC (3:7 w:w) or PC/EMC (3:7 w:w) without additives or with 2% of VC, 2% FEC, or under 1 atm CO_2. The cells were cycled between 3.8 V and 2.7 V at rates of C/20 (1st cycle), C/10 (2nd+3rd cycle) and C/5 (4th-40th cycle). The error bars represent the standard deviation of 3 repeat cells. Our in-house developed Li-air 1-compartment cell design was used to cycle the three cells with CO_2; for all other experiments two coin cells each were cycled in comparison to one cell with the Li-air-cell design, whereby no significant differences between the cell types were noted.

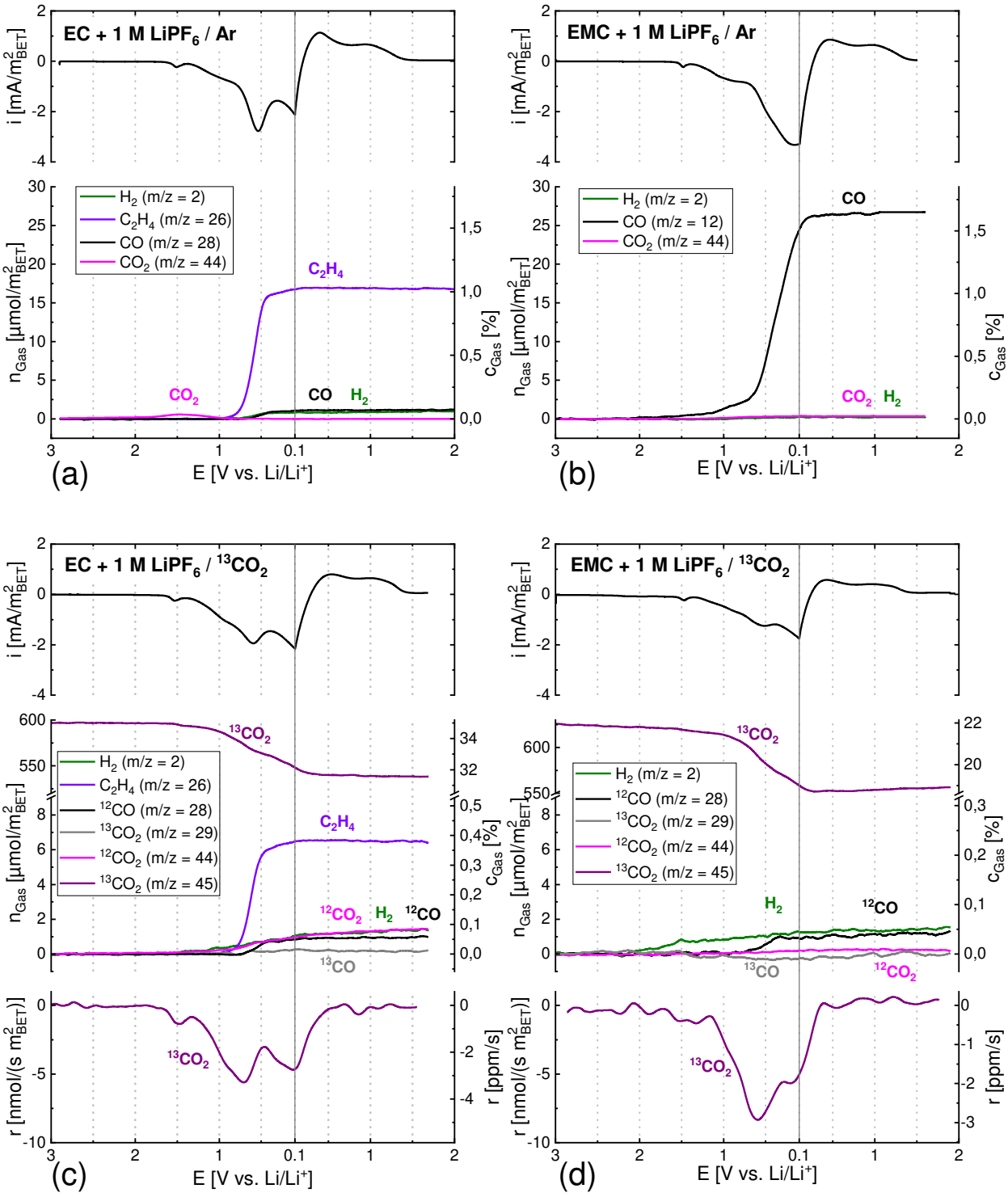

Figure 5: Gas evolution of a Super C65 carbon electrode during the first CV cycle at 0.1 mV/s using various model electrolytes with 1 M $LiPF_6$ in (a) EC, (b) EMC, (c) EC with $^{13}CO_2$ added to the cell head-space, or (d) EMC with added $^{13}CO_2$. The carbon working electrode is separated from the metallic lithium counter electrode with an aluminum sealed solid electrolyte diffusion barrier in the here used 2-compartment OEMS cell.

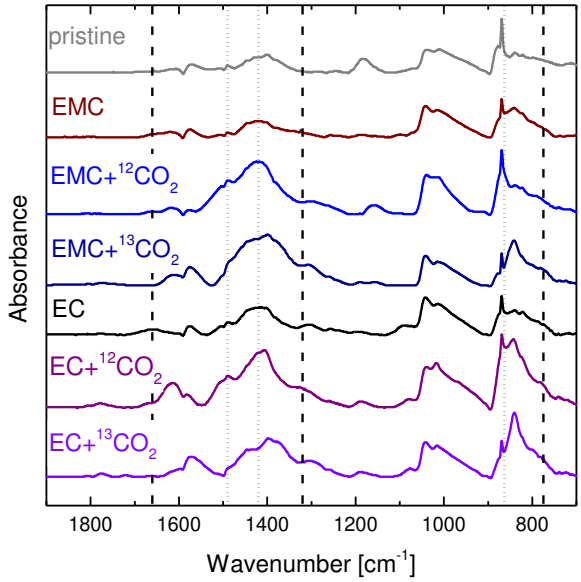

Figure 6: ATR-FTIR spectra of PVDF-bonded graphite electrodes after one formation cycle at C/20 between 2.7 and 3.9 V versus LFP in 1 M $LiPF_6$ in EC or EMC with and without CO_2. Both standard $^{12}CO_2$ and labeled $^{13}CO_2$ were added in order to investigate which SEI components contain the added CO_2. The spectrum nominated "pristine" consists of an unused graphite electrode. The dashed lines mark the band position for lithium oxalate, the dotted lines for lithium carbonate, assuming a standard salt containing ^{12}C.

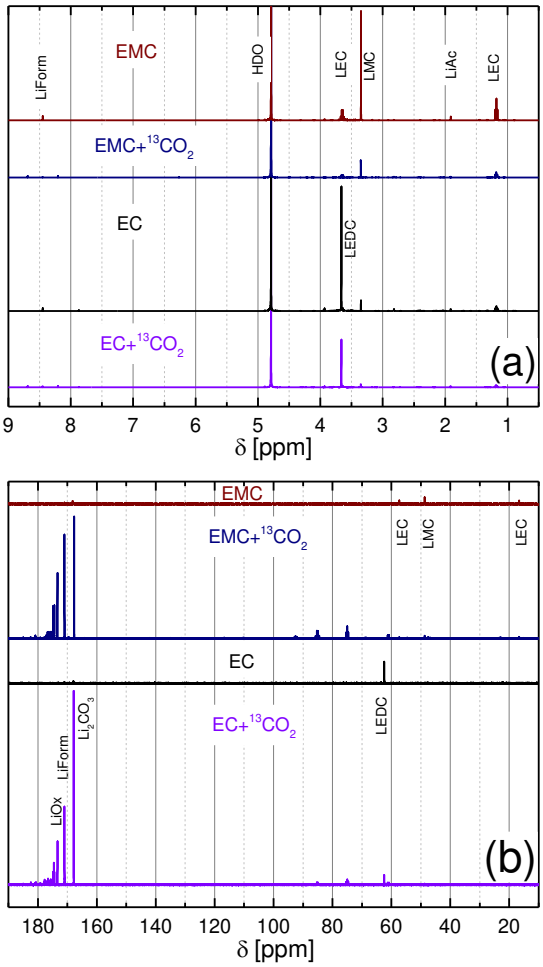

Figure 7: (a) ^{1}H and (b) ^{13}C NMR spectra of the D_2O extract of PVDF-bonded graphite electrodes after one formation cycle versus LFP in 1 M $LiPF_6$ in EC or EMC, with and without added CO_2 to the gas-phase. Both standard $^{12}CO_2$ and labeled $^{13}CO_2$ were added in order to investigate which SEI components contain the gas-phase CO_2. Note that here only the $^{13}CO_2$ labeled NMR data are shown. An enlarged version of the ^{13}C spectra in the 160-190 ppm region can be found in Figure S4.

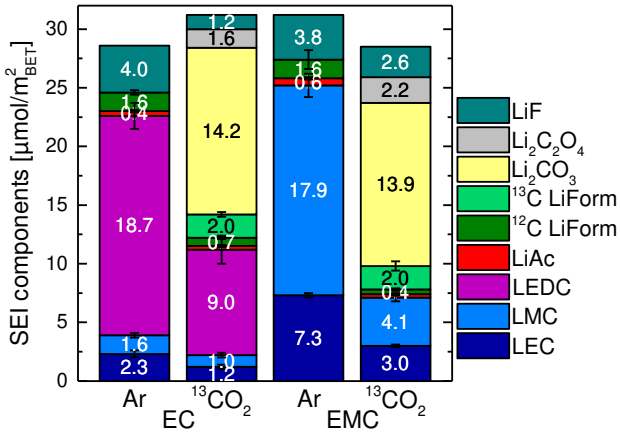

Figure 8: SEI components in µmol/m²$_{BET}$ quantified by ^{1}H NMR (LEC, LMC, LEDC, LiAc = lithium acetate, LiForm = lithium formate), by ^{13}C NMR (Li_2CO_3, $Li_2C_2O_4$) and by ^{19}F NMR (LiF) for graphite electrodes that have undergone formation in EC- or EMC-only electrolytes with or without added $^{13}CO_2$. Please note that Li_2CO_3 was only detected when originating from $^{13}CO_2$. Due to the hydrolysis of alkyl carbonates to alkoxides and Li_2CO_3, the amount of Li_2CO_3 cannot be quantified when no $^{13}CO_2$ for a distinction of the different origins is added. The raw data of this plot can be found in Tables S1 and S2.

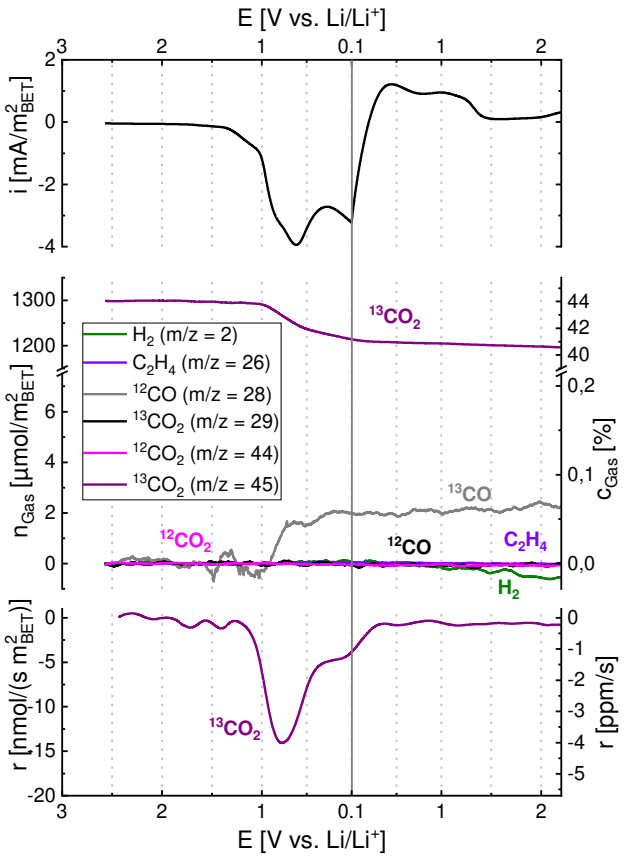

Figure 9: Gas evolution of a Super C65 carbon electrode during one CV cycle at 0.1 mV/s in the model electrolyte 0.5 M LiTFSI in diglyme with $^{13}CO_2$ added to the gas-phase. The carbon working electrode is separated from the metallic lithium counter electrode with an aluminum sealed solid electrolyte diffusion barrier in the here used 2-compartment OEMS cell.

Supporting Information

The impact of CO_2 evolved from VC and FEC during formation of graphite anodes in lithium-ion batteries

K. Uta Schwenke[*,1,=], Sophie Solchenbach[1,=], Julien Demeaux[2], Brett L. Lucht[2] and Hubert A. Gasteiger[1]

[1] Chair of Technical Electrochemistry, Department of Chemistry and Catalysis Research Center, Technical University of Munich, Munich, Germany

[2] Department of Chemistry, University of Rhode Island, Kingston, Rhode Island, USA

[=] equal contribution

E-Mail: uta.schwenke@tum.de

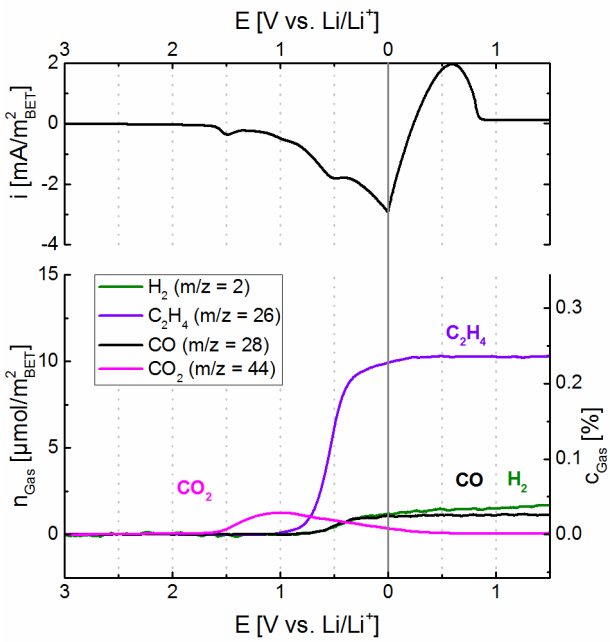

Figure S1: Gas evolution of a graphite electrode during one CV cycle at 0.1 mV/s in the model electrolyte 1 M $LiPF_6$ in EC. The graphite electrode is separated from the metallic lithium counter electrode with an aluminum sealed solid electrolyte diffusion barrier in the here used 2-compartment OEMS cell.

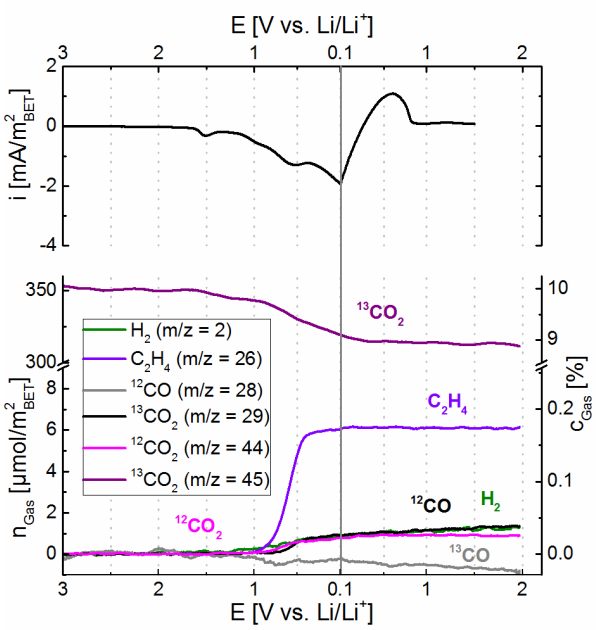

Figure S2: Gas evolution of a graphite electrode during one CV cycle at 0.1 mV/s in the model electrolyte 1 M $LiPF_6$ in EC with $^{13}CO_2$ added to the gas-phase. The graphite electrode is separated from the metallic lithium counter electrode with an aluminum sealed solid electrolyte diffusion barrier in the here used 2-compartment OEMS cell.

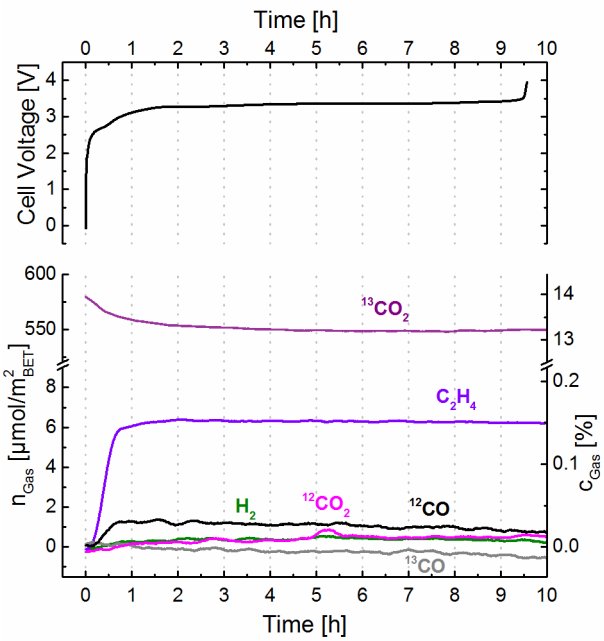

Figure S3: Gas evolution of a 1-compartment LFP-graphite full-cell during the first galvanostatic charge (C/10) in the model electrolyte 1 M $LiPF_6$ in EC with $^{13}CO_2$ added to the gas-phase.

Table S1: Concentration of major SEI products found by ^{1}H and ^{19}F NMR in the D_2O extract of graphite electrodes after one formation cycle at C/20 in 1M $LiPF_6$ in EMC and EC. All cells were flushed with Ar or CO_2 prior to the electrochemical measurements. Some cells were additionally filled with $^{13}CO_2$ after Ar flushing via a diffusion procedure as described in the Experimental part. All concentrations are determined by referencing the integrals to the internal standard TSP or C_6F_6, and are given in µmol/m²$_{BET}$, normalizing them to the BET surface of the respective graphite electrode for better comparison with the OEMS data. The given errors represent the standard deviation of ^{1}H NMR measurements of different electrodes, whereby the superscript behind the sample label stands for the number of repeat experiments. LEC could not be determined at 3.65 ppm for EC cells due to the overlap with the LEDC peak. The LEDC amount was corrected by the integral of LEC determined at 1.19 ppm. It was not possible to identify the substance at 3.94 ppm. In order to estimate its amount, it was assumed that the signal is formed by 2 equivalent protons.

µmol/m²$_{BET}$	LEC	LiAc	LMC	LEDC	LEC	?	LiForm ^{12}C	LiForm ^{13}C	LiF
ppm	1.19	1.92	3.36	3.67	3.65	3.94	8.44	8.44	-123
Signal	t, 3H	s, 3H	s, 3H	s, 4H	q, 2H	s, 2H (?)	s, 1H	d, 1H	s, 1F
EC Ar^4	2.3±0.3	0.4±0.1	1.6±0.2	18.7±1.1	?	0.7±0.1	1.6±0.2	-	4.0
EC CO_2^3	1.0±0.1	0.3±0.0	1.1±0.3	8.2±0.7	?	0.5±0.1	1.6±0.1	-	n.d.
EC $^{13}CO_2^3$	1.2±0.2	0.3±0.1	1.0±0.2	9.0±1.2	?	0.4±0.1	0.7±0.1	2.0±0.2	1.2
EMC Ar^2	7.3±0.0	0.6±0.1	17.9±1.0	-	7.5	0.5±0.1	1.6±0.8	-	3.8
EMC CO_2^2	3.0±0.0	0.8±0.4	4.3±0.0	-	3.2±0.2	0.3±0.0	1.7±0.0	-	n.d.
EMC $^{13}CO_2^3$	3.0±0.1	0.3±0.1	4.1±0.3	-	3.1±0.1	-	0.4±0.1	2.0±0.4	2.6

Table S2: Concentration of major SEI products found by ^{13}C NMR in the D_2O extract of graphite electrodes after one formation cycle at C/20 in 1M $LiPF_6$ in EMC and EC. Quantification was only performed for cells filled with $^{13}CO_2$ via a diffusion procedure after initial argon flushing in order to obtain large enough signals. All concentrations are determined by referencing the integrals to the internal standard TSP and are given in µmol/m², normalizing them to the BET surface of the respective graphite electrode for better comparison with OEMS. It was not possible to identify the substance at 174.6 ppm. In order to estimate its amount, it was assumed that the signal is formed by 1 carbon.

µmol/m²$_{BET}$	LEDC	Li_2CO_3	LiForm	$Li_2C_2O_4$	?
ppm	62.4	167.7	171.0	173.4	174.6
Signal	t, 2C	s, 1C	d, 1C	s, 2C	s/d, 1C (?)
EC $^{13}CO_2$	10.0	14.2	3.3	1.6	1.7
EMC $^{13}CO_2$	-	13.9	3.2	2.2	2.3

Table S3: Estimated number of monolayers formed after one cycle in EC and EMC electrolytes with/without $^{13}CO_2$ added to the gas-phase. The amounts of the respective compounds are derived from the concentrations found by ^{1}H, ^{19}F and ^{13}C NMR given in Table 1 and 2. The estimation is based on the assumption that each atom of the respective species occupies a square with an area of $(0.15\ nm)^2$.

Monolayer	LEC	LiAc	LMC	LEDC	?	LiForm	Li_2CO_3	$Li_2C_2O_4$	LiF	Sum
EC Ar	0.37	0.05	0.20	4.0	0.09	0.16	n.d.	0	0.11	5.0
EC $^{13}CO_2$	0.20	0.03	0.12	2.0	0.04	0.21	1.16	0.18	0.03	4.0
EMC Ar	1.19	0.07	2.2	-	0.06	0.12	n.d.	0	0.10	3.7
EMC $^{13}CO_2$	0.48	0.03	0.51	-	0.07	0.16	1.13	0.21	0.07	2.7

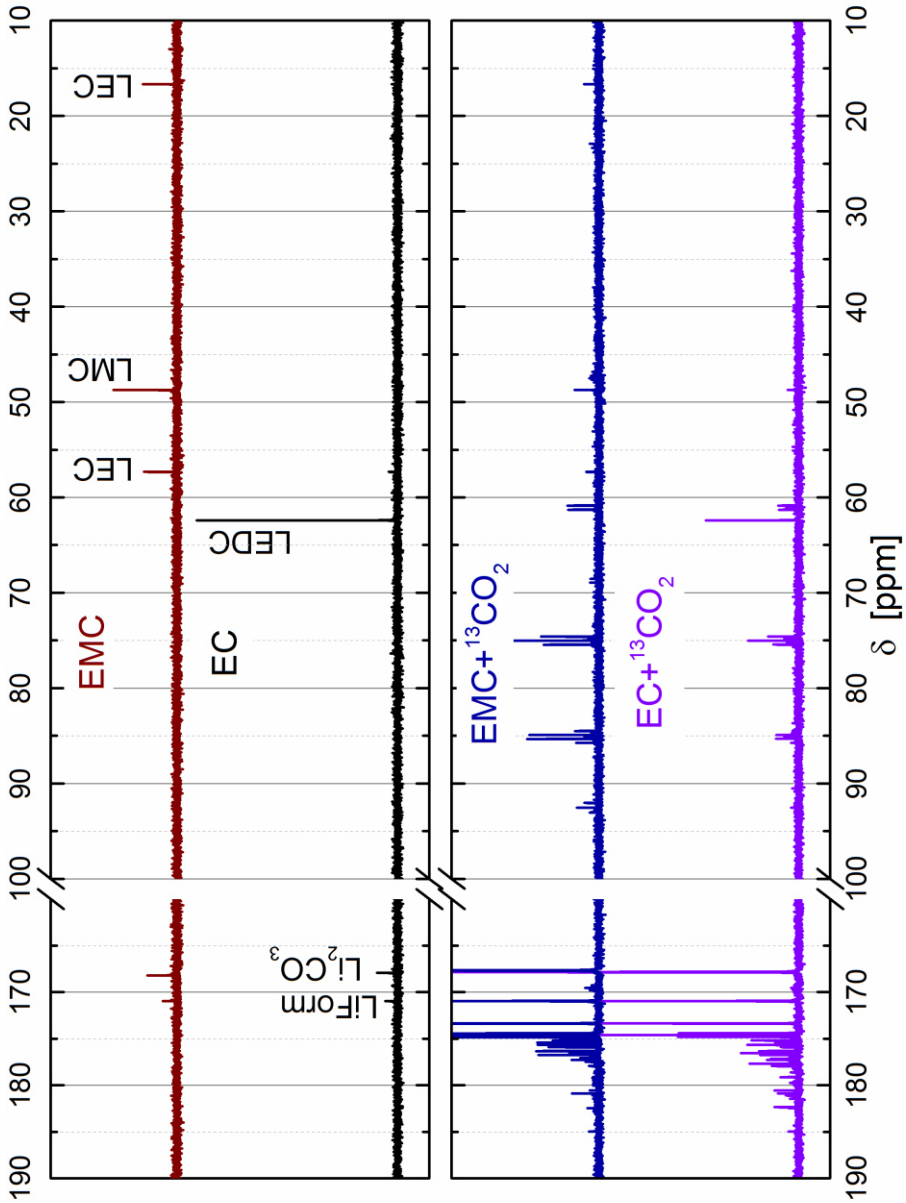

Figure S4: Zoom of ^{13}C-NMR spectra shown in Figure 7b.

3.3 Degradation mechanisms related to the anodic oxidation of electrolyte

In contrast to their reductive counterparts, the electrolyte oxidation mechanisms are far less understood. Borodin and co-workers demonstrated by DFT calculations that oxidized solvent molecules can readily transfer a proton to the PF_6^- anion,[31] which then decomposes to HF and PF_5. Yet, instead of PF_5, POF_3 is commonly observed at high voltages by OEMS.[8,181] Therefore, the study presented in chapter 3.3.1 aims to establish OEMS calibration factors for PF_5 and POF_3. As a result of HF formation, transition metal dissolution from high-voltage cathodes, such as LNMO, is commonly observed (see chapter 1.2). The transition metal ions are known to migrate to the anode, where they impair the SEI properties. The mechanism for this deterioration is currently under debate.[182] In chapter 3.3.2, the effect of transition metal ions on the electrolyte and SEI decomposition reactions on graphite anodes is investigated by OEMS.

3.3.1 Quantification of PF_5 and POF_3 from $LiPF_6$ decomposition in Li-ion batteries

The manuscript entitled "Quantification of PF_5 and POF_3 from $LiPF_6$ decomposition in Li-ion batteries" was submitted to the Journal of the Electrochemical Society in July 2018 and published in September 2018. The main findings of this study were presented by Michael Metzger at the 232nd Meeting of the Electrochemical Society in National Harbor, Maryland in October 2017 (Abstract Number 272). The article was published "open access" under the Creative Commons Attribution 4.0 License (CC BY). A permanent link to this article can be found under: http://jes.ecsdl.org/content/165/13/A3022.full.

Although PF_5 is the predicted product of the reaction of an oxidized solvent molecule with PF_6^-, current gas analysis studies (including our own) only detected POF_3 gas at high voltages from $LiPF_6$-based electrolytes.[8,21,35,183–185] This discrepancy is often explained by the immediate reaction of PF_5 or $LiPF_6$ to POF_3 with water or other R-OH type species. However, creating these species from a purely electrochemical oxidation of organic carbonates, e.g. EC, without the involvement of lattice oxygen or other impurities, could so far not be derived conclusively. In order to better understand the origin of POF_3 at high voltages, the objective of the study presented in this chapter is to determine OEMS calibration factors for PF_5 and POF_3.

After determining the decomposition temperature for dry $LiPF_6$ to LiF and PF_5 by TGA-MS, we developed a modified OEMS cell which was then used to thermally decompose specific amounts of $LiPF_6$. Surprisingly, it was found that these OEMS measurements showed only mass signals belonging to POF_3, but none for PF_5. By examining the experimental setup, we finally concluded that while PF_5 is formed in the OEMS cell, it reacts on its way to the detector with trace water and probably also surface oxides on the stainless steel tubing, so that in the end only POF_3 is detected. Nevertheless, we evaluated these experiments to determine a calibration factor for apparent "POF_3", being the sum of PF_5 and POF_3. Furthermore, we demonstrated that $LiPF_6$ reacts readily with free protons in solution already at room temperature,

whereas the hydrolysis of $LiPF_6$ with water only proceeds in detectable amounts above 60 °C, which indicates that indeed highly acidic species are formed upon electrolyte oxidation, which then react with $LiPF_6$ to PF_5 (detected as POF_3) and HF.

Author contributions

H. B. and M. M. performed the TGA-MS analysis of dry and wet $LiPF_6$. M. E. and S. S. developed the modified OEMS cell setup and conducted and evaluated the $LiPF_6$ decomposition experiments using OEMS. S. S. performed the electrolyte oxidation experiment. M. M. conducted and evaluated the thermal decomposition experiments of EC/$LiPF_6$ with added protic species. S. S. and H. A. G. wrote the manuscript. All authors discussed the data and commented on the manuscript.

Quantification of PF_5 and POF_3 from Side Reactions of $LiPF_6$ in Li-Ion Batteries

Sophie Solchenbach,[=,z] Michael Metzger,[=] Masamitsu Egawa, Hans Beyer,[*] and Hubert A. Gasteiger[**]

Chair of Technical Electrochemistry, Department of Chemistry and Catalysis Research Center, Technical University of Munich, Garching, Germany

The electrochemical oxidation of $LiPF_6$-based electrolytes is reported to generate POF_3 gas. In order to enable a quantitative analysis of the $LiPF_6$ decomposition reactions, we aimed to establish calibration factors for POF_3 and PF_5 in on-line electrochemical mass spectrometry (OEMS). Thermal decomposition of dry $LiPF_6$ is expected to yield PF_5, but instead all PF_5 is detected as POF_3 in our OEMS setup, rendering a differentiation of the two gases impossible and presenting an artefact which likely occurs with most on-line mass spectrometry systems due to the high reactivity of PF_5. However, we can still determine a cumulative calibration factor for $POF_3 + PF_5$ (referred to as "POF_3"), which is then used to investigate the evolution of gases during the oxidation of an EC/$LiPF_6$ electrolyte on a carbon black electrode. Mechanistic experiments with protons or water added to EC/$LiPF_6$ electrolyte show that protons trigger the formation of PF_5, while the kinetics for the hydrolysis of $LiPF_6$ with water at room temperature are too slow to be detectable. These findings let us conclude that the oxidation of EC generates highly acidic species, which cause the decomposition of PF_6^- to PF_5 and HF; the PF_5 is then detected as POF_3 in the OEMS.

 [DOI: 10.1149/2.0481813jes]

Manuscript submitted July 17, 2018; revised manuscript received August 24, 2018. Published September 22, 2018. This was Paper 272 presented at the National Harbor, Maryland Meeting of the Society, October 1–5, 2017.

Lithium hexafluorophosphate ($LiPF_6$) is commonly used as a salt in Li-ion battery electrolyte solutions due to its high ionic conductivity and passivating properties toward the aluminum cathode current collector.[1] However, its thermal instability limits the operating temperature range for Li-ion batteries to $< 60°C$, whereas its reactivity with water calls for dry-room manufacturing of cells. The corresponding primary decomposition pathways are: i) the thermal dissociation of $LiPF_6$, leading to PF_5 and LiF; and, ii) the hydrolysis of $LiPF_6$ or PF_5, resulting in the formation of HF and POF_3.

A quantitative thermal dissociation of dry $LiPF_6$ occurs between 100 and 200°C, depending on the experimental conditions (i.e., sealed or open containers,[2] sample size),[3,4] according to the following equilibrium:[2–5]

$$LiPF_6 \leftrightarrow LiF + PF_5 \quad [1]$$

Common Li-ion battery electrolytes, namely anhydrous solutions of $LiPF_6$ in a mixture of ethylene carbonate (EC) and dialkyl carbonates, show negligible thermal aging up to 60°C.[6,7] If storage temperatures of 80°C are exceeded, the electrolyte solution darkens and forms large amounts of gas within days.[2,8–11] Next to PF_5,[2] also alkyl fluorophosphates,[2,7,9–14] oligomers of the carbonate solvents,[8,10] fluorinated hydrocarbons,[2,10,11] POF_3,[13] and HF[13,14] have been found in thermally aged (80–100°C) electrolyte solutions, indicating that not only $LiPF_6$, but also the organic carbonate solvent itself is decomposed. However, the observed quantities differ significantly across studies. Campion et al.[9,10] and Guillot et al.[11] showed that impurities like alcohols and water increase the amount of side products at high temperatures. Furthermore, electrolytes stored in glass vials between 60–85°C show about 100 times more decomposition products compared to the same electrolytes stored in polymer or aluminum containers,[7,14] as the etching of SiO_2 by HF generates water, leading to a self-accelerating decomposition of the electrolyte solution.[15,16] Hence, it is clear that the purity of the electrolyte and the testing conditions substantially affect the thermal stability of $LiPF_6$-based electrolytes.

The hydrolysis of $LiPF_6$ with trace water in Li-ion battery electrolyte solutions occurs already at room temperature, although a complete conversion needs days to weeks.[17–21] The main product of $LiPF_6$ hydrolysis with H_2O is HF and POF_3 (see Equation 2);[21,22] the latter is further hydrolyzed to HPO_2F_2 according to Equation 3.[18,19,23] The first reactions leads to a 2:1 molar ratio of formed HF to consumed water, as recently found by Strmcnik et al.[21] At temperatures below 60°C, no reactions between the organic electrolyte solvent with $PO_2F_2^-$ or HF generated from $LiPF_6$ hydrolysis have been reported.[19,23]

$$LiPF_6 + H_2O \leftrightarrow POF_3 + 2\,HF + LiF \quad [2]$$

$$POF_3 + H_2O \leftrightarrow HF + HPO_2F_2 \quad [3]$$

Besides these two major decomposition pathways, $LiPF_6$ also affects the stability of the electrolyte solvents at high potentials. Density functional theory (DFT) calculations indicate that the oxidation potential of EC-PF_6^- complexes is lower than for isolated EC, and that HF and PF_5 can be formed from the oxidized complexes at room temperature.[24,25] Tebbe et al.[26] suggested that coordination to PF_5 reduces the activation energy for EC dimer formation or ring opening. In fact, PF_5 has been reported to slowly react with carbonate electrolytes already at room temperature,[8] and alkyl fluorophosphates (the characteristic products of PF_5 with organic carbonates) have been found in cells cycled to potentials above 5.2 V vs. Li/Li^+.[12,27] Still, PF_5 has not been observed directly during electrochemical electrolyte oxidation so far. Instead, POF_3 has been detected at high potentials in $LiPF_6$-based electrolytes,[28–33] where it was ascribed to a reaction of $LiPF_6$ or PF_5 with water or other reactive oxygen-containing species formed during the oxidation of the electrolyte solvent. While this is plausible for experiments where water or reactive oxygen species are likely to be formed, i.e., in the presence of oxygen-releasing cathode materials,[28,29,34] the quantitative formation of POF_3 during electrolyte oxidation on inert materials which do not release oxygen upon charge like high-voltage spinel or carbon black still lacks fundamental understanding.[31–36]

To understand the origin of PF_5 and POF_3 at high potentials in $LiPF_6$-based electrolytes, a quantification of the evolved amounts of these gases is essential. Therefore, this work aims at quantifying PF_5 and POF_3 by on-line electrochemical mass spectrometry (OEMS). As a first step, we investigate the decomposition of dry and wet $LiPF_6$ by thermogravimetric analysis coupled with mass spectrometry (TGA-MS). We then thermally decompose $LiPF_6$ in a modified OEMS cell setup that can be heated up to 250°C. As dry $LiPF_6$ dissociates completely to LiF and PF_5 at temperatures >200°C according to our TGA-MS analysis (consistent with the literature),[2–5] we thus can now

[=]These authors contributed equally to this work.
[*]Electrochemical Society Member.
[**]Electrochemical Society Fellow.
[z]E-mail: sophie.solchenbach@tum.de

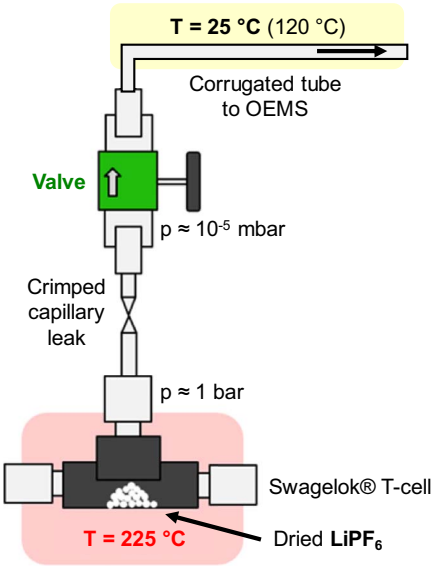

Figure 1. Modified OEMS cell setup used for the thermal decomposition of $LiPF_6$ consisting of a Swagelok T-cell fitted to a crimped capillary tube, which is connected to the mass spectrometer as described in Ref. 37. The T-cell is then heated to 225°C (red shaded area). The corrugated tube connecting the capillary and the OEMS (yellow shaded area) is normally kept at ambient temperature (i.e., 25°C); for the experiment shown in Figure 4c, the corrugated tube was heated to 120°C for 48 h prior to the experiment.

correlate the ion currents at different mass channels to the gas concentration in the cell. The absence of PF_5 signals due to its high reactivity with OEMS system components ultimately provides an explanation why PF_5 so far has never been detected in on-line mass spectrometric measurements on lithium ion battery cells. Lastly, we investigate the oxidative stability of an EC/$LiPF_6$ electrolyte on a carbon black working electrode, thereby focusing on the POF_3 quantification, and resolve the origin of what appears as "POF_3" at high potentials in on-line mass spectrometry measurements on Li-ion batteries.

Experimental

Thermogravimetric analysis coupled with mass spectrometry.—Thermogravimetric analysis of lithium hexafluorophosphate ($LiPF_6$, BASF SE, Germany) was conducted with a Mettler Toledo TGA coupled to a mass spectrometer (Thermostar TGA-MS, Pfeiffer Vacuum, Germany). Prior to the experiments, the $LiPF_6$ was dried at 70°C for 18 h under dynamic vacuum in a glass oven (Buechi, Switzerland) without exposure to air after the drying step. Then, ~150 mg $LiPF_6$ were filled into a sapphire crucible inside an Ar-filled glove box (MBraun, Germany) and transferring the crucible into the TGA chamber. For the "dry" experiment, the sample was heated at 10 K/min to 120°C and then held for 1 h at 120°C in a dry argon flow (5.0 purity, 60 mL/min) to remove any traces of H_2O. The sample was then ramped up to 350°C at 10 K/min, where the temperature was held for another 10 min to ensure a complete decomposition of $LiPF_6$. For the "wet" experiment, the argon gas (60 mL/min) was saturated with water at room temperature and purged over the $LiPF_6$ sample. After resting for 1 hour at room temperature under the wet argon flow, the sample was heated at a rate of 10 K/min to 350°C, where the temperature was again kept constant for 10 min.

Modified on-line electrochemical mass spectrometry setup.—To measure the decomposition of $LiPF_6$ in our on-line electrochemical mass spectrometer (OEMS),[37] we designed a modified cell setup (see Figure 1). As pre-tests showed that typical polymer sealings were either not tight at high temperatures or not stable against the evolving PF_5 gas, we used a Swagelok T-fitting with two metal end caps. The third opening of the T-cell was equipped with the crimped capillary leak that connects the T-fitting to the mass spectrometer (this is also part of our regular OEMS system and has been described previously).[37] All cell parts were dried at 70°C under dynamic vacuum prior to assembly. The modified cell was equipped with a thermocouple to monitor the cell temperature and was wrapped with a heating cord (Horst GmbH, Germany); the entire assembly was thermally insulated by fiber cloth (see red shaded area in Figure 1). Tightness of the modified Ar-filled cell was tested in pre-runs of the actual experiments (i.e., holding the cell at temperatures >200°C during several hours), validating that the mass traces m/z = 28 (N_2) and m/z = 32 (O_2) remained negligible. For the three here shown $LiPF_6$ decomposition runs, 0.26, 0.96, or 1.08 mg $LiPF_6$ (± 0.04 mg) was weighed into a TGA crucible inside an Ar-filled glove box. The crucible was then transferred into the modified OEMS cell. The cell was closed inside the Ar-filled glove box and connected to the OEMS. After a rest period of 40 min at 25°C, the temperature was increased to 225°C and held there for ~4 h. The m/z signals were evaluated by dividing the ion current of the respective channel by the ion current of the ^{36}Ar isotope and subtracting the background during the initial rest period at 25°C.

On-line electrochemical mass spectrometry.—Hydrolysis and electrochemical oxidation of 1.5 M $LiPF_6$ in ethylene carbonate (EC, BASF SE, Germany) was investigated in our regular OEMS cell setup. Note that this system is unfortunately not able to trace HF, as the mass signal for hydrofluoric acid (m/z = 20) superposes with the signal of the ^{20}Ar isotope. For hydrolysis experiments, 5000 ppm H_2O or 5000 ppm methanesufonic acid (99.5%, Sigma-Aldrich, USA) were added to the EC/$LiPF_6$ electrolyte. After stirring for 30 s, 240 µL of the electrolyte were transferred into an empty OEMS cell (without any electrodes or separators present). The cell was then placed into a temperature chamber set to 10°C and connected to the OEMS. In this way, any hydrolysis reactions occurring at room temperature before the start of the experiment were minimized. The temperature chamber was then set to constant temperature hold steps of 10°C, 25°C, 40°C, and 60°C, each for 3 h, as previously described by Metzger et al.[38] Finally, the temperature was set to 80°C for 12 h to follow the long-term reactions of $LiPF_6$ decomposition products.

For electrochemical oxidation measurements, 500 mg carbon black (C65, Timcal, Imerys, Switzerland) was mixed with 500 mg polyvinyl difluoride (PVDF, Kynar HSV 900, Arkema, France) and 10 mL N-methyl-pyrrolidone (NMP, anhydrous, Sigma-Aldrich, United States) in a planetary mixer (Thinky Corp., USA) for 15 min at 2000 rpm and coated onto a PET separator (FS 24316, Freudenberg, Germany). After drying at 50°C, 15 mm electrodes (loading 1.8 mg_C/cm^2) were punched out, dried at 120°C under dynamic vacuum for 12 h, and then transferred to an Ar-filled glove box without exposure to air. The OEMS cell was assembled with a lithium metal counter electrode (450 µm thickness, Rockwood Lithium, USA), the carbon black coating as working electrode, and two 28 mm diameter PET separators (also dried at 120°C) soaked with 150 µL EC + 1.5 M $LiPF_6$. Electrochemical measurements were performed by applying a linear sweep from open circuit voltage (~3 V) to 5.5 V at a rate of 0.1 mV/s using a VMP-300 potentiostat (Biologic, France) after an initial 4 h OCV period.

Results

Thermal decomposition of dry and wet $LiPF_6$.—To understand which conditions are required to produce PF_5 or POF_3 in quantitative amounts, we first investigate the thermal decomposition of $LiPF_6$ under dry and wet conditions by TGA-MS. The possible fragments of PF_5 and POF_3 and their corresponding m/z signals are listed in Table I; to evaluate the experiments, we chose m/z = 107 as a unique signal for PF_5 and m/z = 85 as a unique signal for POF_3.

Figure 2 shows the TGA-MS run of $LiPF_6$ with a dry argon gas flow. As a sample transfer from the glove box to the TGA instrument under inert gas was not possible, we added a 1 hour isothermal period

Table I. Mass signals, corresponding mass fragments, and their relative intensity for PF_5 and POF_3. Data taken from the NIST Mass Spectrometry Data Center Ref. 39. The m/z = 107 and 85 signals (highlighted in bold) are unique for PF_5 and POF_3, respectively, and were chosen for the quantitative analysis of the two gases.

	Relative intensity [%]		
Mass signal [m/z]	PF_5	POF_3	Fragment
47	-	2.2	PO
50	4.9	4.1	PF
66	-	0.7	POF
69	3.8	16.9	PF_2
85	**-**	**85.4**	**POF_2**
88	4.4	2.3	PF_3
104	-	100	POF_3
107	**100**	**-**	**PF_4**
126	0.8	-	PF_5

at 120°C (see 10–70 min in Figure 2) to the ramp of 10 K/min from room temperature to 350°C. Any physisorbed trace water from the sample transfer should be removed during this step. In fact, at the initial ramp from room temperature to 120°C (0–10 min), a small amount of water is released (purple line corresponding to m/z = 18 in Figure 2c) concomitant with a slight endothermic heat flux (orange line in Figure 2b). Both sample mass and heat flow remain constant during the end of the isothermal step at 120°C (10–70 min), meaning that all physisorbed water has been desorbed. Once the temperature in the subsequent ramp from 120 to 350°C (70–93 min) reaches 165°C (see red dotted lines), a significant endothermic mass loss of 83% referenced to the original mass occurs (see Figure 2b). At the same time, a peak in the mass trace m/z = 107 (blue line in Figure 2c) is observed. Both the formation of PF_5 and the mass loss of 83% are consistent with the quantitative thermal decomposition of $LiPF_6$ according to Equation 1. Interestingly, the found decomposition onset is 30–60°C higher compared to previous reports with a comparable setup.[2,4,5] This could be due to the large sample size (150 mg) used in

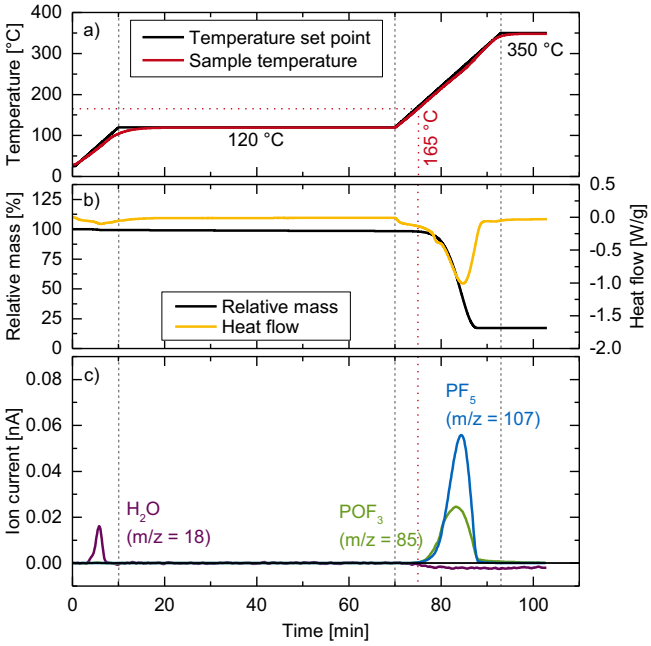

Figure 2. TGA-MS data on the thermal decomposition of dry $LiPF_6$ under dry argon gas flow: a) temperature protocol setpoints (black) and sample temperature (red); b) mass loss (black) and heat flow (orange); c) mass traces of H_2O (purple), PF_5 (blue), and POF_3 (green).

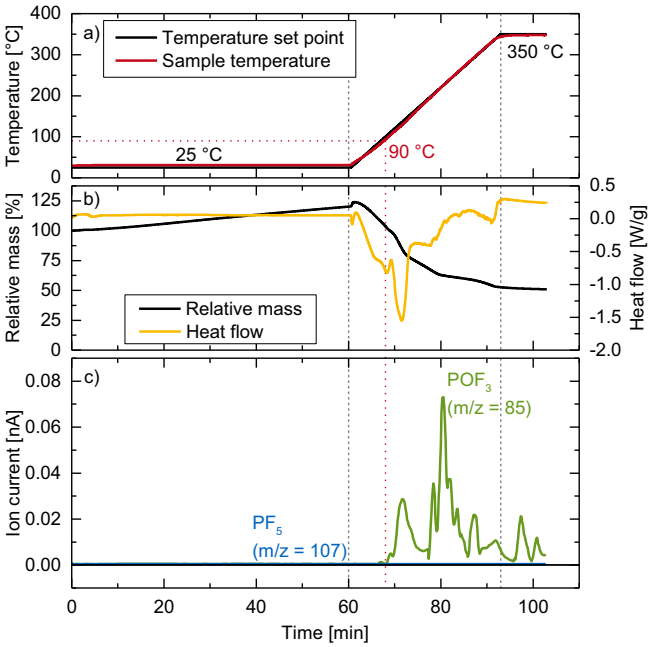

Figure 3. TGA-MS data on the thermal decomposition of dry $LiPF_6$ under wet argon gas flow: a) temperature protocol setpoint (black) and sample temperature (red); b) mass loss (black) and heat flow (orange); c) mass traces of PF_5 (blue) and POF_3 (green).

the present study, as the resulting higher concentration of PF_5 leads to a thermodynamic shift of the equilibrium toward $LiPF_6$.[2,3]

Besides the mass fragments for PF_5, we also observe a signal at m/z = 85 (green line in Figure 2c), which belongs to the POF_2-moiety of POF_3 (see Table I). Furthermore, a slight decrease of the m/z = 18 background can be seen. This suggests that part of the PF_5 reacts with trace water in the instrumentation to form POF_3 (see Equation 4), despite the initial drying step and the use of dry argon (5.0 purity), illustrating the high reactivity of PF_5 with trace water:

$$PF_5 + H_2O \rightarrow POF_3 + 2\,HF \qquad [4]$$

Figure 3 shows the thermal decomposition of $LiPF_6$ in the presence of water. To achieve a significant "wetting" of the $LiPF_6$, water-saturated argon gas (dewpoint of ~20°C) is flown over the sample before the temperature ramp is started (0–60 min in Figure 3). During this time, a mass increase of ~24% is observed (black line in Figure 3b), consistent with the weight gain expected for the formation of an adduct with the nominal stoichiometry of $LiPF_6 \cdot 2\,H_2O$ (note that in this experiment the background of the H_2O signal (m/z = 18) was too high to observe any changes in the water concentration). It is to note that the sample weight still increases after the initial 60 min, which implies that a further uptake of water would have been possible if the wetting time was extended; however to stay in the same time scale as in the "dry" experiment shown in Figure 2, we limited the pre-wetting in Figure 3 to one hour. The subsequent ramp from room temperature to 350°C (10 K/min) correlates with a mass loss of only 49% referenced to the original $LiPF_6$ mass, accompanied by a strong endothermic heat flow. This time, no m/z = 107 signal belonging to PF_5 was observed (see blue line in Figure 3c); instead, only POF_3 (m/z = 85) is detected (green line in Figure 3c). Both the mass loss and the POF_3 evolution start around 90°C (see red dotted lines), i.e., 75°C lower compared to the experiment with dry argon gas flow in Figure 2, which is in good agreement with previous reports on the decomposition of intentionally wetted $LiPF_6$.[4,5] In contrast to these studies, however, the mass loss in our wet experiment (49%) is much lower than the theoretical mass loss based on a complete conversion to LiF according to Equation 2 (83%). This means that another thermally stable species besides LiF must be produced. It is possible that during

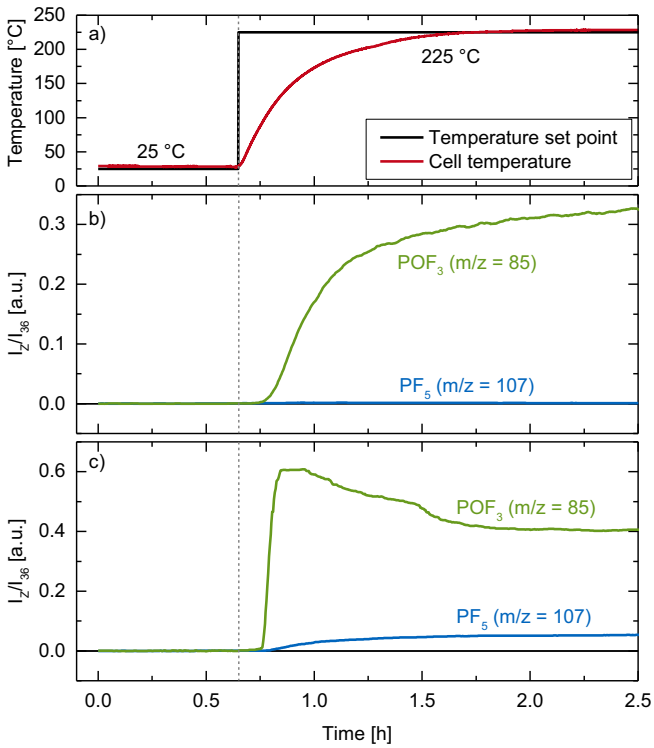

Figure 4. Thermal decomposition experiment with dry $LiPF_6$ in the modified OEMS cell: a) temperature protocol (black) and cell temperature (red); b) mass traces for POF_3 (green) and PF_5 (blue) from 0.26 mg $LiPF_6$ without pre-drying of the OEMS inlet; c) mass traces for POF_3 (green) and PF_5 (blue) from 0.37 mg after heating of the OEMS inlet at 120°C under vacuum for 48 h before the start of the experiment.

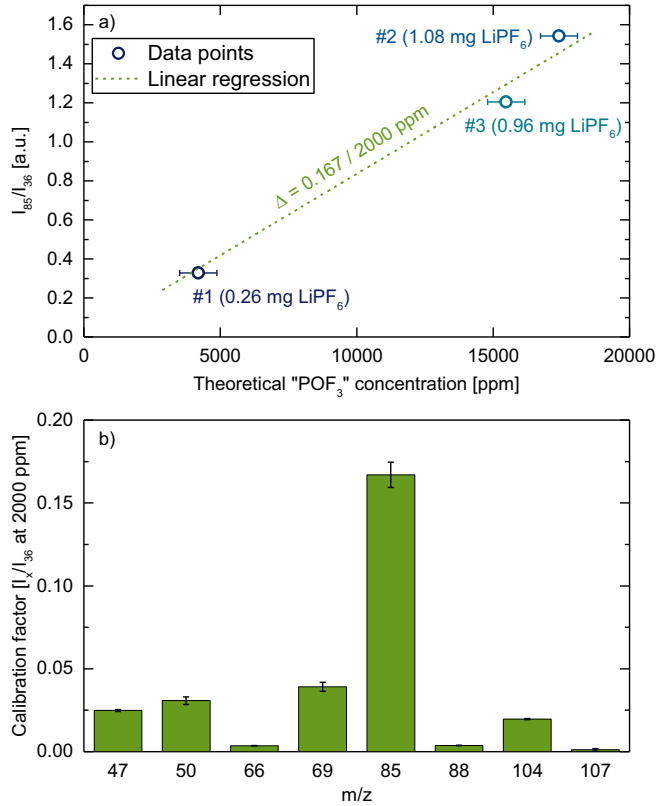

Figure 5. Quantification of the apparent amount of "POF_3" (≡ sum of PF_5 + POF_3) from the thermal decomposition of different amounts of dry $LiPF_6$ at 225°C in the modified OEMS cell. a) Ion current on m/z = 85 normalized to m/z = 36 vs. the theoretical concentration of "POF_3"; error bars reflect the weighing accuracy of ± 0.04 mg. The calibration factor is determined by linear regression between the data points (see green dashed line). b) Calibration factor of "POF_3" normalized to the ^{36}Ar current and to 2000 ppm (≡I_x/I_{36} at 2000 ppm "POF_3") for different m/z channels obtained from linear regression lines, whereby the error bars represent the standard deviation of the determined slopes. Experiments were conducted with 0.26, 0.96, and 1.08 mg dried $LiPF_6$.

the course of the TGA experiment, HPO_2F_2 is formed according to Equation 3, which then reacts with remaining LiF in the following equilibrium:[40]

$$HPO_2F_2 + LiF \leftrightarrow LiPO_2F_2 + HF \quad [5]$$

With a melting point of 360°C,[40] $LiPO_2F_2$ will not decompose but contribute to the remaining mass at the end of the TGA experiment; if the conversion of $LiPF_6$ to $LiPO_2F_2$ were to be quantitative (the sum of Reactions 2, 3, and 5), the overall mass loss referenced to $LiPF_6$ would be 29%. Thus, if we assume that LiF and $LiPO_2F_2$ are the only thermally stable products, the mass loss of 49% would correspond to a composition of 37% LiF and 63% $LiPO_2F_2$, based on the molar masses of M(LiF) = 25.9 g/mol and M($LiPO_2F_2$) = 107.9 g/mol. However, a detailed chemical analysis of the sample residue would be necessary to verify this hypothesis.

Thermal decomposition of $LiPF_6$ by OEMS.—To obtain a quantitative relationship between the ion current measured in our OEMS system and the concentration of PF_5 or POF_3 in the cell headspace, we aimed to thermally decompose $LiPF_6$ inside a cell connected to our OEMS system. Therefore, we assembled a modified OEMS cell which can be heated up to 250°C (see Experimental section and Figure 1 for details). Once the cell would be heated to 225°C, i.e., well above the decomposition temperature of dry $LiPF_6$ at 165°C (see Figure 2), we expected $LiPF_6$ to decompose stoichiometrically to PF_5 according to Equation 1. As the expected partial pressure of PF_5 is less than 20 mbar, a shift of the equilibrium to the left of Equation 1 can also be neglected. Figure 4 shows the cell temperature and the characteristic mass traces for PF_5 (m/z = 107, blue line in Figure 4b) and POF_3 (m/z = 85, green line in Figure 4b) during the decomposition of $LiPF_6$ under regular dry conditions in our modified OEMS cell. Surprisingly, only mass traces belonging to POF_3 were detected, although all cell pieces and the $LiPF_6$ salt had been dried carefully and the cell assembly was done in an Ar-filled glove box. We repeated the experiment twice with different amounts of $LiPF_6$ (see Figure 5), which however still did not lead to detectable amounts of PF_5 on the mass channel m/z = 107. This clearly suggests that the reaction of PF_5 produced in the cell with either trace water in the tubing of the high-vacuum side of the capillary or with the native oxide on stainless steel surfaces leads to a quantitative conversion to POF_3.

In order to remove any trace water within the tubing of the high-vacuum side of the OEMS setup, we conducted another experiment where the corrugated tube which connects the OEMS capillary with the mass spectrometer was heated to 120°C for 48 h under ultra-high vacuum (see yellow shaded area in Figure 1), while the modified OEMS cell was already attached with the capillary leak closed but kept near room temperature. This allowed to subsequently perform the $LiPF_6$ decomposition experiment with the OEMS inlet perfectly dried prior to initiating the thermal decomposition of $LiPF_6$ in the OEMS cell. The results of this experiment are depicted in Figure 4c. While in this experiment POF_3 is still the by far dominant species (green line, m/z = 85), a small amount of PF_5 (blue line, m/z = 107) could now be observed. As the partial pressure of PF_5 in the tubes beyond the capillary is $\sim 10^8$ times lower than in the OEMS cell (10^{-5} vs. 10^3 mbar),[37] very low amounts of adsorbed water or oxides on the stainless steel tubing surface are obviously sufficient to convert most of the thermally formed PF_5 to POF_3 before it reaches the quadrupole. The apparent decrease of POF_3 in the beginning of the experiment (1.0–1.5 h in Figure 4c) is thus most likely because

Table II. Mass signal channels and calibration factors for the quantification of different gases for our OEMS system. The calibration factors are referenced to the ^{36}Ar signal and normalized to 2000 ppm of the respective gas. Data for H_2, C_2H_4, CO, and CO_2 is taken from Ref. 41, whereas the calibration factor for "POF_3" was determined in this work.

Gas	Mass signal m/z	Calibration factor [I_x/I_{36} at 2000 ppm]
H_2	2	0.15
C_2H_4	26	0.38
CO	28	0.64
CO_2	44	0.58
"POF_3"	85	0.17

PF_5 emerging through the capillary reacts with initially present trace amounts of water in the OEMS inlet, leading to a relatively higher POF_3 signal at m/z = 85; after depletion of trace water, increasing amounts of PF_5 at m/z = 107 can be observed, concomitant with a simultaneously lower POF_3 signal.

This experiment shows that even if PF_5 were to form during conventional OEMS experiments in our setup, it will react with trace water (see Equation 4) and/or surface oxides on the stainless steel tubes within the OEMS inlet and thus will predominantly be detected as POF_3. Consequently, at least in our OEMS setup, the above experiment shows that we are not able to differentiate between POF_3 and PF_5 in our measurements. For this reason, it is quite likely that at least part of the m/z = 85 signals which previously had been assigned to POF_3 by our group[31,32] may actually have been due to PF_5. While we do not know whether this artefact might also be occurring with other on-line mass spectrometry systems used for the study of lithium ion batteries, the above experiments certainly suggest that it would be worthwhile to examine the extent of the PF_5 to POF_3 conversion for each system.

Although we cannot distinguish between PF_5 and POF_3 in our OEMS setup, we can still establish an at least semi-quantitative calibration factor for the apparent amount of "POF_3", representing the sum of $PF_5 + POF_3$. This will be done by correlating the amount of thermally decomposed $LiPF_6$ with the measured ion currents, evaluating the ion currents on all significant mass channels once they stayed constant, which was typically 3–4 h after the start of the heating experiment. We only considered the experiments where all PF_5 was converted to POF_3 (i.e., without heated tubing), as this would be the default case for all OEMS measurements conducted in our laboratory. Figure 5a depicts the ion current on m/z = 85 normalized to the ^{36}Ar isotope (I_{85}/I_{36}, y-axis) vs. the theoretical concentration of "POF_3" (referring to apparent POF_3) from the thermal decomposition of $LiPF_6$ (x-axis) for the three measurements with 0.26, 0.96, and 1.08 mg $LiPF_6$ (± 0.04 mg, corresponding to 4200, 15500, and 17400 ppm "POF_3"). Calibration factors were determined by the linear regression slope between the three data points shown in Figure 5a, which was then referenced to 2000 ppm "POF_3". Figure 5b shows the thus determined calibration factors corresponding to 2000 ppm of "POF_3" for the different POF_3 mass channels after normalizing their ion currents to the ion current for ^{36}Ar (I_x/I_{36}) signals. It can be seen that the fragment on m/z = 85 (POF_2) has the highest intensity, corresponding to a calibration factor of 0.167 ($\equiv I_{85}/I_{36}$ at 2000 ppm "POF_3"), while the fragments with m/z = 47 (PO), m/z = 50 (PF), m/z = 69 (PF_2), and m/z = 104 (POF_3) all have much lower relative intensities. Note that this differs significantly from the fragmentation reported by the National Institute of Standards and Technology (NIST) for the same ionization energy of 70 eV (see Table I),[39] which we ascribe to the fact that the ionization chamber in our instrument is heated at 120°C.[37] Table II shows the calibration factors for H_2, C_2H_4, CO, and CO_2 (determined by purging the cell with a test gas containing 2000 ppm of each species), along with the newly determined calibration factor for "POF_3", which lies within the same range (0.1–0.7) as the other calibration factors. Thus, when only POF_3 related signals are observed in our OEMS setup, the sum of $PF_5 + POF_3$ can be quantified, even though their distribution cannot be determined.

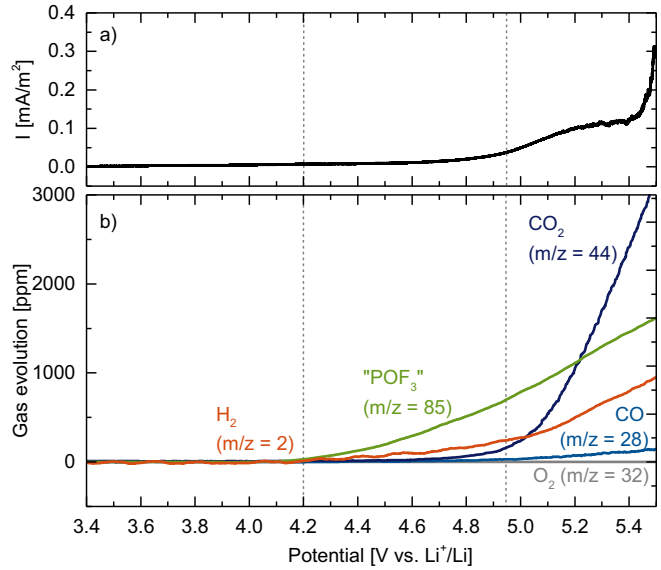

Figure 6. a) Current density and b) gas evolution during a linear oxidative potential scan of a carbon black electrode in EC + 1.5 M $LiPF_6$ electrolyte. The vertical dashed lines at 4.2 V and 4.95 V mark the approximate onset for the oxidation of ethylene glycol and ethylene carbonate, respectively. The mass signals were converted into concentrations using the calibration factors given in Table II.

Electrochemical oxidation of $LiPF_6$ electrolyte.—As already mentioned, POF_3 has been observed at high positive potentials on cathode active materials or on carbon electrodes in $LiPF_6$-containing electrolytes at room temperature, but its amount has never been quantified.[29–32] Therefore, we examined the oxidation reactions of an EC + 1.5 M $LiPF_6$ electrolyte on a carbon black working electrode vs. a lithium counter electrode, focusing on the evolution and quantification of $LiPF_6$ decomposition species. Figure 6 shows the current density (a) and the gas evolution (b) during a linear potential sweep from OCV to 5.5 V vs. Li^+/Li, whereby all signals have been quantified using the calibration factors given in Table II (note that only signals related to POF_3 were observed, so that a quantification of "POF_3" is possible). Around 4.2 V vs. Li^+/Li, the evolution of "POF_3" (i.e., $POF_3 + PF_5$, green line in Figure 6b) sets in, together with the formation of H_2 (orange line in Figure 6b). Starting at 4.95 V vs. Li^+/Li, a significant oxidation current (black line in Figure 6a) and the simultaneous evolution of CO_2 (dark blue line in Figure 6b) are observed, as previously reported from the oxidation of EC-based electrolytes,[35,42,43] along with an enhanced formation of H_2 and "POF_3". Density functional theory calculations by Borodin et al.[24] and Li et al.[25] have pointed out that upon EC oxidation (i.e., after the first electron transfer), the abstraction of a proton by a neighboring PF_6^- anion would occur in $LiPF_6$-based electrolytes, leading to HF and PF_5 formation, and ultimately to the release of CO_2 and a vinyl alcoholate radical (see reaction pathway (1) in Scheme 1). The produced PF_5 would then detected as "POF_3" in our OEMS setup, while the reduction of HF at the Li metal counter electrode[21] would result in the evolution of H_2:

$$2\,HF + 2\,Li \rightarrow LiF + H_2 \qquad [6]$$

However, contrary to this mechanisms, the evolution of H_2 and "POF_3" between 4.2–4.95 V occurs without the simultaneous formation of CO_2, suggesting that a different process is taking place in this potential range. As trace amounts of water gradually react with EC to form ethylene glycol,[22,38] the latter is a likely impurity in EC present at ppm levels (unfortunately below the NMR detection level).

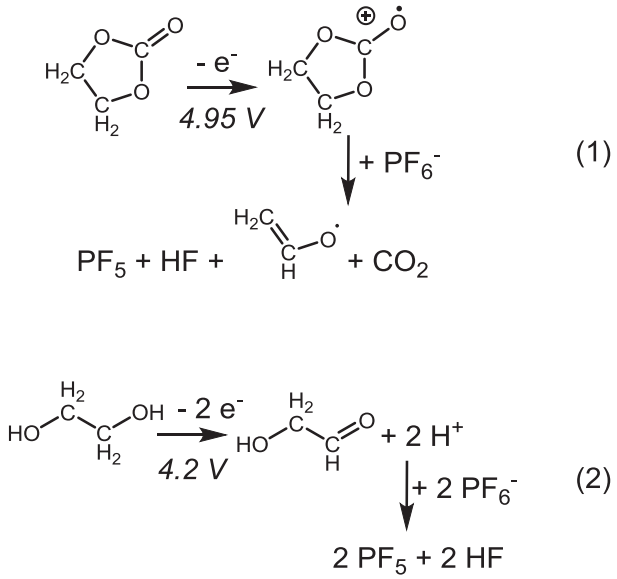

Scheme 1. (1) Oxidation mechanism of EC in the presence of PF_6^-, based on Refs. 25,48. (2) Oxidation of ethylene glycol according to Refs. 44,45.

The oxidation of ethylene glycol in aqueous electrolytes leads to the formation of protons,[44,45] which could also react with PF_6^- to HF and PF_5 (see pathway (2) in Scheme 1). In fact, the amounts of H_2 and "POF_3" evolved up to 4.95 V would correspond to the oxidation of ~20 ppm ethylene glycol, which is a probable concentration for this impurity.

For either mechanism (1) or (2) in Scheme 1, the predicted molar ratio of PF_5/HF would be 1/1, so that the experimental molar ratio of "POF_3" (representing PF_5) and H_2 should be 2/1 (since the reduction of 1 HF produces 0.5 H_2; see reaction 6). This is in good agreement with the data in Figure 6, where the amount of H_2 is indeed about 50% compared to that of "POF_3". In summary, the data shown in Figure 6 lead us to the following hypothesis: a) protons or acidic species from EC or ethylene glycol impurity oxidation lead to a fast dissociation of PF_6^- to HF and PF_5 already at room temperature, and b) POF_3 observed at oxidative potentials in OEMS experiments on a carbon black electrode is in fact mainly PF_5 rather than POF_3 as we had assumed previously.[32]

To verify whether the formation of acidic species (e.g., HF or H^+) can lead to a significant dissociation of $LiPF_6$ at room temperature within the timescale of an OEMS experiment, we investigated the reaction of an EC + 1.5 M $LiPF_6$ electrolyte with 5000 ppm methanesulfonic acid (MSA, $pK_A = 8.3$ in propylene carbonate).[46] With this electrolyte, we performed a similar experiment as described by Metzger et al.,[38] namely monitoring the gas evolution while gradually increasing the temperature of the electrolyte from 10°C to 80°C. Note that for this type of experimental procedure no active electrodes or lithium are present, so that it only probes purely chemical reactions of the electrolyte. The cell temperature and the resulting gas evolution are shown in Figures 7a and 7b. A significant amount of "POF_3" (POF_3 + PF_5, green line in Figure 7b) is already formed at 25°C, leveling off at ~1000 ppm. Going to higher temperatures, the overall "POF_3" concentration increases further (from ~3000 ppm at 40°C to ~11000 ppm at 80°C); however, in contrast to the constant steady-state concentration reached at 25°C, at higher temperatures the "POF_3" evolution reaches a maximum within ~1 hour at the respective temperature step and thereafter decreases gradually (a more detailed discussion follows below). CO_2 (navy line in Figure 7b) is only evolved above 60°C, but remains at a much lower concentration compared to "POF_3"; at 80°C, the amount of CO_2 increases continuously.

Clearly, the detection of "POF_3" at 25°C in the MSA-containing electrolyte demonstrates that protons can rapidly and substantially

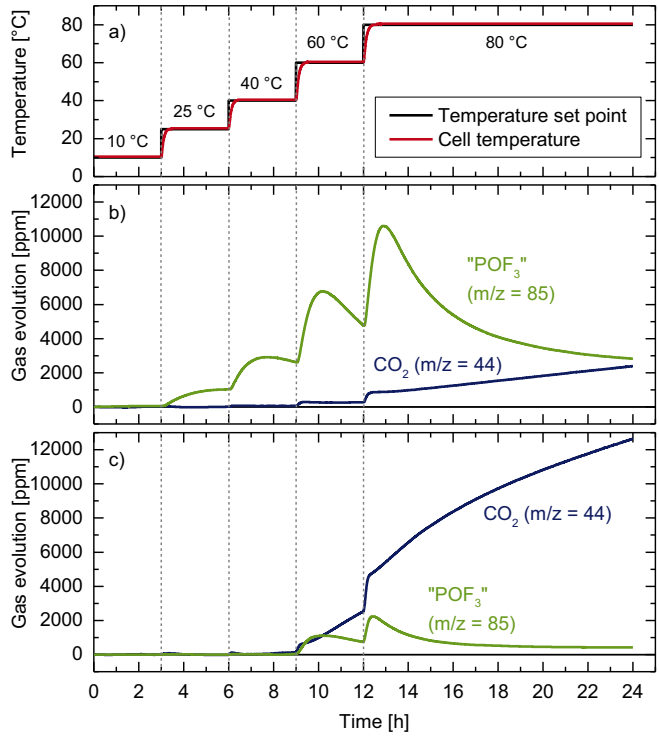

Figure 7. Temperature induced decomposition of EC + 1.5 M $LiPF_6$ electrolyte, measured in an OEMS cell by stepping the temperature from 10 to 80°C: a) temperature protocol (black) and cell temperature (red); b) "POF_3" and CO_2 evolution in the presence of 5000 ppm methanesulfonic acid; c) "POF_3" and CO_2 evolution in the presence of 5000 ppm water. The mass signals were converted into concentrations using the calibration factors given in Table II.

shift the dissociation of PF_6^- toward PF_5 and HF (see Equation 7). This is in good agreement with Freire et al.,[47] who found that PF_6-based ionic liquids hydrolyze in aqueous solutions with pH = 3 at room temperature, but not under neutral conditions.

$$PF_6^- + H^+ \leftrightarrow PF_5 + HF \qquad [7]$$

At 25°C, the establishment of a steady-state "POF_3" concentration and the absence of CO_2 indicate that at this low temperature no PF_5 is consumed in a reaction with the electrolyte or that this reaction is too slow to be detected within the timescale of the OEMS experiment (~3 h). In contrast, the decreasing concentrations of "POF_3" during the second half of the temperature step at >40°C are likely a result of PF_5 reacting with the electrolyte to oligomers[8] or alkyl fluorophosphates.[2,7,9–11] As the rate of chemical PF_5 consumption will depend on both temperature and the concentration of PF_5 dissolved in the electrolyte (which is by Henry's law proportional to the amount of PF_5 in the headspace of the cell), a faster consumption of POF_3 is expected at 60°C and 80°C, where both temperature and overall "POF_3" concentration are higher. Additionally, a stepwise increase of the temperature can cause the desorption of PF_5 or POF_3 from the inner surface of the steel tubing, which leads to a peak in the detected "POF_3" concentration at the initial phase of each temperature step.

Interestingly, the extent of CO_2 formation in Figure 7b is very similar to that observed with an EC/$LiClO_4$ electrolyte with < 20 ppm water reported by Metzger at el.[38] (see Figure 1 in Ref. 36), which means that the direct reaction of PF_5 with EC does not generate additional CO_2. For comparison, Figure 7c shows the same experiment with 5000 ppm of added water instead of MSA. Up to 40°C, neither "POF_3" (green line in Figure 7c) nor CO_2 (navy line in Figure 7c) are observed. Only at temperatures 60°C and above, low amounts (< 2000 ppm) of "POF_3" are detected, in this case likely due to the formation of POF_3 rather than PF_5 (this, however, cannot be discerned

in our OEMS experiments). At the same time, the CO_2 concentration increases linearly at 60°C and 80°C to above 12000 ppm, in agreement with previous experiments on the water-driven hydrolysis of EC in $LiClO_4$-based electrolytes.[38]

Comparing the results of Figures 7b and 7c, it becomes apparent that only highly acidic species can trigger the formation of PF_5 at room temperature. Accordingly, the oxidation of an EC/$LiPF_6$ electrolyte (see Figure 6) must be leading to the formation of species which act as proton donors or Brønsted acids, which is consistent with the mechanism proposed by Borodin et al.[24] and Li et al.[25] (see Scheme 1). Furthermore, the release of PF_5 might explain the strong temperature dependence of the oxidative stability of $LiPF_6$-based electrolytes.[33] In this context, the use of proton-scavenging additives, i.e., bases,[9,18] could be a successful strategy to prevent the dissociation of PF_6^- at high potentials, thereby suppressing HF formation and electrolyte degradation.

Conclusions

In this work, we have investigated the thermal and oxidative decomposition reactions of $LiPF_6$ in Li-ion battery electrolytes. The decomposition onsets of dry and wet $LiPF_6$ were determined by TGA-MS to be 165°C and 90°C, respectively. While dry $LiPF_6$ is known to decompose to PF_5 and HF, some POF_3 was observed by TGA-MS due to trace water impurities in the dry argon carrier gas. On the other hand, the thermal decomposition of wet $LiPF_6$ in water-saturated argon carrier gas resulted in the formation of POF_3, HF, and $LiPO_2F_2$.

Analyzing the thermal decomposition of dry $LiPF_6$ in the on-line electrochemical mass spectrometry (OEMS) system developed by our group, we found that all of the thermally released PF_5 is actually detected as POF_3 (m/z = 85) under standard experimental conditions, so that it is not possible to distinguish between PF_5 and POF_3 in OEMS experiments. As this might also apply to other on-line mass spectrometry systems developed for the study of lithium ion batteries, the calibration of these systems for their ability to distinguish between these two gases is advisable. This information is crucial for mechanistic studies, as otherwise experimental on-line mass spectrometry data may be mis-interpreted. However, by decomposing specific amounts of $LiPF_6$, we could establish a calibration factor for the sum of POF_3 + PF_5 (referred to as "POF_3"), allowing us to quantify the amount of the sum of both gases in our OEMS experiments.

Subsequently, we investigated the oxidation of an EC/$LiPF_6$ electrolyte on a carbon black electrode. Next to CO_2, we observed "POF_3" and H_2 in a ratio of 2:1, suggesting that PF_6^- is decomposed by protic species formed during electrolyte oxidation to PF_5 and HF, whereby the latter is reduced to H_2 on the lithium counter electrode. OEMS studies on the thermal stability of EC/$LiPF_6$ electrolytes with intentionally added protons (in the form of methanesulfonic acid) or water showed that protons can indeed trigger the formation of PF_5 at room temperature, whereas the reaction of $LiPF_6$ with water is too slow at 25°C to be sensed by OEMS. Hence, we confirmed that the oxidation products of battery electrolytes act as Brønsted acids and trigger the decomposition of PF_6^- to PF_5 and HF already at room temperature.

Acknowledgments

The authors gratefully acknowledge the BASF Battery Research Network for financial support. We also thank Anna Freiberg for fruitful discussions and advice.

ORCID

Sophie Solchenbach https://orcid.org/0000-0001-6517-8094
Michael Metzger https://orcid.org/0000-0002-5512-8541

References

1. K. Xu, *Chem. Rev.*, **104**, 4303 (2004).
2. B. Ravdel, D. P. Abraham, R. Gitzendanner, J. F. DiCarlo, B. L. Lucht, and C. L. Campion, *J. Power Sources*, **119–121**, 805 (2003).
3. E. Zinigrad, L. Larush-Asraf, J. S. Gnanaraj, M. Sprecher, and D. Aurbach, *Thermochim. Acta*, **438**, 184 (2005).
4. M. D. S. Lekgoathi, B. M. Vilakazi, J. B. Wagener, J. P. Le Roux, and D. Moolman, *J. Fluor. Chem.*, **149**, 53 (2013).
5. H. Yang, G. V. Zhuang, and P. N. Ross, *J. Power Sources*, **161**, 573 (2006).
6. M. Pyschik, M. Winter, and S. Nowak, *Separations*, 4 (2017).
7. V. Kraft, W. Weber, M. Grützke, M. Winter, and S. Nowak, *RSC Adv.*, **5**, 80150 (2015).
8. S. E. Sloop, J. K. Pugh, J. B. Kerr, K. Kinoshita, S. Wang, J. B. Kerr, and K. Kinoshita, *Electrochem. Solid-State Lett.*, **4**, A42 (2001).
9. C. L. Campion, W. Li, W. B. Euler, B. L. Lucht, B. Ravdel, J. F. DiCarlo, R. Gitzendanner, and D. P. Abraham, *Electrochem. Solid-State Lett.*, **7**, A194 (2004).
10. C. L. Campion, W. Li, and B. L. Lucht, *J. Electrochem. Soc.*, **152**, A2327 (2005).
11. S. L. Guillot, A. Pe, M. L. Usrey, and R. J. Hamers, *J. Electrochem. Soc.*, **164**, 1907 (2017).
12. V. Kraft, W. Weber, B. Streipert, R. Wagner, C. Schultz, M. Winter, and S. Nowak, *RSC Adv.*, **6**, 8 (2015).
13. S. Wilken, M. Treskow, J. Scheers, P. Johansson, and P. Jacobsson, *RSC Adv.*, **3**, 16359 (2013).
14. P. Handel, G. Fauler, K. Kapper, M. Schmuck, C. Stangl, R. Fischer, F. Uhlig, and S. Koller, *J. Power Sources*, **267**, 255 (2014).
15. S. F. Lux, I. T. Lucas, E. Pollak, S. Passerini, M. Winter, and R. Kostecki, *Electrochem. Commun.*, **14**, 47 (2012).
16. S. F. Lux, J. Chevalier, I. T. Lucas, and R. Kostecki, *ECS Electrochem. Lett.*, **2**, A121 (2013).
17. K. Tasaki, K. Kanda, S. Nakamura, and M. Ue, *J. Electrochem. Soc.*, **150**, A1628 (2003).
18. A. V. Plakhotnyk, L. Ernst, and R. Schmutzler, *J. Fluor. Chem.*, **126**, 27 (2005).
19. R. Yazami and A. Martinent, in *Fluorinated Materials for Energy Conversion*, T. Nakajima and H. Groult, Editors, p. 173, Elsevier Ltd (2005).
20. T. Kawamura, S. Okada, and J. Yamaki, *J. Power Sources*, **156**, 547 (2006).
21. D. Strmcnik, I. E. Castelli, J. G. Connell, D. Haering, M. Zorko, P. Martins, P. P. Lopes, B. Genorio, T. Østergaard, H. A. Gasteiger, F. Maglia, B. K. Antonopoulos, V. R. Stamenkovic, J. Rossmeisl, and N. M. Markovic, *Nat. Catal.*, **1**, 255 (2018).
22. U. Heider, R. Oesten, and M. Jungnitz, *J. Power Sources*, 7 (1999).
23. V. Kraft, M. Grützke, W. Weber, M. Winter, and S. Nowak, *J. Chromatogr. A*, **1354**, 92 (2014).
24. O. Borodin, W. Behl, and T. R. Jow, *J. Phys. Chem. C*, **117**, 8661 (2013).
25. T. Li, L. Xing, W. Li, Y. Wang, M. Xu, F. Gu, and S. Hu, *J. Power Sources*, **244**, 668 (2013).
26. J. L. Tebbe, T. F. Fuerst, and C. B. Musgrave, *ACS Appl. Mater. Interfaces*, **8**, 26664 (2016).
27. W. Weber, R. Wagner, B. Streipert, V. Kraft, M. Winter, and S. Nowak, *J. Power Sources*, **306**, 193 (2016).
28. D. Streich, A. Guéguen, M. A. Mendez, F. F. Chesneau, P. Novák, and E. J. Berg, *J. Electrochem. Soc.*, **163**, A964 (2016).
29. A. Guéguen, D. Streich, M. He, M. A. Mendez, F. F. Chesneau, P. Novák, and E. J. Berg, *J. Electrochem. Soc.*, **163**, A1095 (2016).
30. M. He, L. Boulet-Roblin, P. Borel, C. Tessier, P. Novák, C. Villevieille, and E. J. Berg, *J. Electrochem. Soc.*, **163**, A83 (2016).
31. A. Freiberg, M. Metzger, D. Haering, S. Bretzke, S. Puravankara, T. Nilges, C. Stinner, C. Marino, and H. A. Gasteiger, *J. Electrochem. Soc.*, **161**, A2255 (2014).
32. M. Metzger, J. Sicklinger, D. Haering, C. Kavakli, C. Stinner, C. Marino, and H. A. Gasteiger, *J. Electrochem. Soc.*, **162**, A1227 (2015).
33. M. Metzger, P. Walke, S. Solchenbach, G. Salitra, D. Aurbach, and H. A. Gasteiger, *Manuscript in Preparation*.
34. R. Jung, M. Metzger, F. Maglia, C. Stinner, and H. A. Gasteiger, *J. Electrochem. Soc.*, **164**, A1361 (2017).
35. R. Jung, M. Metzger, F. Maglia, C. Stinner, and H. A. Gasteiger, *J. Phys. Chem. Lett.*, **8**, 4820 (2017).
36. J. Wandt, A. Freiberg, A. Ogrodnik, and H. A. Gasteiger, *Mater. Today*, in press (2018).
37. N. Tsiouvaras, S. Meini, I. Buchberger, and H. A. Gasteiger, *J. Electrochem. Soc.*, **160**, A471 (2013).
38. M. Metzger, B. Strehle, S. Solchenbach, and H. A. Gasteiger, *J. Electrochem. Soc.*, **163**, A1219 (2016).
39. http://webbook.nist.gov.
40. T. H. Tan, *Master's Thesis*, The University of British Columbia (1970).
41. B. Strehle, S. Solchenbach, M. Metzger, K. U. Schwenke, and H. A. Gasteiger, *J. Electrochem. Soc.*, **164**, A2513 (2017).
42. D. Pritzl, S. Solchenbach, M. Wetjen, and H. A. Gasteiger, *J. Electrochem. Soc.*, **164**, A2625 (2017).
43. M. Metzger, B. Strehle, S. Solchenbach, and H. A. Gasteiger, *J. Electrochem. Soc.*, **163**, A798 (2016).
44. G. Horanyi, V. E. Kazarinov, Y. B. Vassiliev, and V. N. Andreev, *J. Electroanal. Chem.*, **147**, 263 (1983).
45. B. Wieland, J. P. Lancaster, C. S. Hoaglund, P. Holota, and W. J. Tornquist, *Langmuir*, **12**, 2594 (1996).
46. L. Xing, O. Borodin, G. D. Smith, and W. Li, *J. Phys. Chem. A*, **115**, 13896 (2011).
47. K. Izutsu, M. Kolthoff, T. Fujinaga, M. Hattori, and K. Chantooni, *Anal. Chem.*, **49**, 503 (1977).
48. M. G. Freire, C. M. S. S. Neves, I. M. Marrucho, and A. P. Coutinho, *J. Phys. Chem. A*, **2**, 3744 (2010).

3.3.2 Investigating Electrolyte and SEI Decomposition Reactions by Transition Metal Ions with On-line Electrochemical Mass Spectrometry

The manuscript with the title "Investigating Electrolyte and SEI Decomposition Reactions by Transition Metal Ions with On-line Electrochemical Mass Spectrometry" was submitted to the Journal of the Electrochemical Society in August 2018 and published in October 2018. The main findings of this study were presented by Sophie Solchenbach at the 231st Meeting of the Electrochemical Society in New Orleans, Louisiana in May 2017 (Abstract Number 219). The article was published "open access" under the Creative Commons Attribution 4.0 License (CC BY). A permanent link to this article can be found under: http://jes.ecsdl.org/content/165/14/A3304.full.

The HF-induced transition metal dissolution is a major challenge for high-voltage cathode materials like LNMO (see chapter 1.2). While some researchers believe that transition metal ions such as Mn^{2+} only impair the ionic conductivity of the SEI by an ion-exchange mechanism between lithium and manganese,[186,187] recent studies showed that the manganese deposition on graphite anodes leads to enhanced loss of active lithium and capacity fade.[188–190] An *operando* XAS study by Wandt et al.[191] concluded that manganese ions in the SEI are reduced to Mn^0, but re-oxidize immediately by the reduction of electrolyte, forming a catalytic cycle which leads to continuous electrolyte decomposition and loss of lithium from the graphite anode. In the study presented here, the electrolyte decomposition reactions induced by Mn^{2+} and Ni^{2+} ions were investigated by OEMS. To have defined amounts of transition metal ions in the electrolyte and to reduce the electrolyte background (see chapter 2.2), we chose EC/$LiPF_6$ model electrolytes with concentrations of $Mn(TFSI)_2$ or $Ni(TFSI)_2$ corresponding to the dissolution of 0.3 wt% of a NMC cathode that would match capacitively to the used graphite anodes. Both Ni^{2+} and Mn^{2+} increased the amount of C_2H_4 produced during formation of pristine graphite electrodes; as the additional gas evolution occurred once the graphite potential was decreased below the TM^{2+}/TM^0 redox potential of nickel or of manganese,

respectively, the reduced transition metals are apparently active for the reductive decomposition of the electrolyte. On graphite electrodes which were preformed in a transition metal-free EC/$LiPF_6$ electrolyte, the subsequent addition of Mn^{2+} ions caused a continuous C_2H_4 evolution during all following cycles, whereas the Ni^{2+} addition only initiated a very minor gas evolution after the first cycle. By preformation of a graphite electrode in a VC/DMC/$LiPF_6$ electrolyte, the gas evolution from Mn^{2+} was lowered substantially. Post-mortem ATR-FTIR analysis of graphite electrodes cycled in Ni^{2+}- or Mn^{2+}-containing or in transition metal free electrolyte showed that Mn^{2+} ions led to an accumulation of Li_2CO_3 in the SEI. Hence, we suggest that Mn^{2+} ions catalyze the decomposition of LEDC to Li_2CO_3, which we could further confirm by OEMS measurements of preformed graphite electrodes in DMC/$LiPF_6$ electrolytes. The much higher activity of manganese towards SEI and electrolyte decomposition in comparison to nickel could be an explanation for the better capacity retention of cells with cathode active materials that contain no or only low amounts of manganese.[192,193]

Author contributions

G. H. and S. S. performed and evaluated the OEMS experiments. S. S. performed the post-mortem ATR-FTIR analysis. S. S., A. F. and R. J. discussed and developed the SEI decomposition mechanism. S. S. and H. A. G. wrote the manuscript. All authors discussed the data and commented on the manuscript.

Electrolyte and SEI Decomposition Reactions of Transition Metal Ions Investigated by On-Line Electrochemical Mass Spectrometry

Sophie Solchenbach,*,z Gloria Hong, Anna Teresa Sophie Freiberg, Roland Jung, and Hubert A. Gasteiger**

Chair of Technical Electrochemistry, Department of Chemistry and Catalysis Research Center, Technical University of Munich, Garching, Germany

We use on-line electrochemical mass spectrometry (OEMS) to elucidate and quantify the electrolyte reduction on graphite caused by transition metal ions. To have a controlled system, we use ethylene carbonate (EC) with 1.5 M $LiPF_6$ and representative amounts of $Ni(TFSI)_2$ or $Mn(TFSI)_2$ as model electrolytes, combined with a 2-compartment cell in which anolyte and catholyte are separated by an impermeable solid lithium ion conductor. Focusing on C_2H_4 evolution as a marker for EC reduction, we find that both Ni^{2+} and Mn^{2+} lead to enhanced gas evolution on pristine graphite electrodes once the potential is decreased to below the TM^{2+}/TM^0 redox potential, demonstrating that the reduced transition metals are active toward electrolyte reduction. If the electrodes are preformed in a TM-free electrolyte and subsequently cycled in an electrolyte containing either Mn^{2+} or Ni^{2+}, the activity of nickel toward electrolyte decomposition is greatly reduced, whereas the electrolyte with manganese still shows a strong ongoing C_2H_4 generation. The use of vinylene carbonate during formation partially suppresses the gas evolution from manganese. Using OEMS and post-mortem ATR-FTIR, we finally show that reduced manganese can decompose organic SEI components into Li_2CO_3, thereby compromising the integrity of the SEI and enabling the additional reduction of electrolyte.

 [DOI: 10.1149/2.0511814jes]

Manuscript submitted August 30, 2018; revised manuscript received October 11, 2018. Published October 23, 2018.

Transition metal (TM) dissolution is a long-known degradation phenomenon of lithium manganese spinel-type cathode active materials for Li-ion batteries. It is amplified by temperature,[1,2] high cathode potentials,[3] and large BET surface area of the particles.[3] As layered lithium nickel cobalt manganese oxide (NCM) cathode materials are cycled to higher cutoff potentials to maximize the energy density of Li-ion cells, transition metal dissolution also becomes significant for NCMs.[4–11] Experimental and ab initio modeling studies suggest that the electrochemical oxidation of $LiPF_6$-based electrolytes at high voltages[8,12–17] and/or follow-up reactions of the electrolyte with oxygen released from the NCM host lattice[18–22] can generate HF, which then corrodes the layered transition metal oxide cathode materials. Upon lattice oxygen release (occurring upon delithiation to ∼80% in NCMs),[18,19] not only manganese, but also nickel and cobalt are dissolved as TM^{2+} ions into the electrolyte[4] at concentration ratios that reflect the stoichiometry of the bulk material.[5,7,23]

The most apparent consequences of transition metal dissolution are capacity and power fade.[3,6–9,24–28] However, the amount of dissolved cathode active material is typically less than 1%,[7,9,26,28–30] which is too low to explain the observed capacity losses. Instead, the transition metal ions deposit on the graphite anode, where they lead to a significant decrease of the coulombic efficiency and to a large increase in anode impedance.[5–7,9,24,25,31–34] It is not fully understood how transition metal ions can cause these detrimental effects, yet the negative impact of manganese on graphite anode capacity retention is considerably worse compared to nickel and cobalt.[5,7,31]

Recent studies have shown that Mn^{2+} ions exchange rapidly with Li^+ ions contained in the solid electrolyte interphase (SEI), as evidenced by soaking either preformed graphite electrodes[24,35,36] or single SEI compounds such as LiF or Li_2CO_3[25,37] in Mn^{2+}-containing electrolytes. Furthermore, Mn^{2+} ions were found to accumulate at the interface between organic (outer) and inorganic (inner) SEI in EC-based electrolytes without additives.[25,32,37,38] While some groups identified exclusively Mn(+II) species like $MnCO_3$ and MnF_2,[24,35,39–41] others found also reduced manganese in its 0 or +1 oxidation state on lithiated graphite.[33,38,42,43] Considering that nano-sized transition metal carbonates and -fluorides have been tested as conversion-type anode materials,[44–48] a reduction of these species in the SEI to metallic manganese seems likely. However, since the irreversible capacity on graphite anodes is typically 30–50 times higher than the capacity required for a 2-electron reduction of the accumulated manganese,[2,7,28] additional side reactions must be taking place, consuming active lithium. One proposed hypothesis is that reduced manganese in contact with electrolyte re-oxidizes to Mn^{2+} by simultaneously reducing solvent molecules,[4,33,39] as supported by DFT calculations from Han et al.[49] If then the Mn^{2+} ions can be reduced again, a catalytic cycle would be established by which active lithium would be lost continuously into the SEI. While this appears plausible, the question remains why manganese would not eventually be covered by SEI species that would prevent new solvent molecules from reaching the active TM center, and thus would stop the electrolyte reaction with the TM center. To resolve this question, Leung[50] and Joshi et al.[32] suggested that transition metals also decompose organic SEI species, thus compromising the passivating properties of the SEI.

Despite the many mechanistic insights gained by the above described studies, the nature of the electrolyte or SEI decomposition reactions associated with manganese deposited on graphite anodes remains unclear. Moreover, the number of analogous studies on the effect of nickel ions is limited,[31] although nickel is the most commonly dissolved transition metal from Ni-rich NCMs and NCA.[5,7] The scientific debate is further complicated, as the typical sample washing and/or drying steps required for conducting detailed ex-situ diagnostics like X-ray photoelectron spectroscopy (XPS), X-ray absorption spectroscopy (XAS) or scanning electron microscopy (SEM) can easily affect the transition metal oxidation state.[4,43] Therefore, the use of operando techniques for investigating the transition metal redox mechanism in the SEI has become imperative.

In this work, we use on-line electrochemical mass spectrometry (OEMS) to investigate the fundamental reactions of carbonate based electrolytes with nickel and manganese ions on a graphite anode. In order to mimic the effect of a typical dissolution of ∼0.3 wt% of the cathode active material observed in the above discussed studies, we use an ethylene carbonate (EC)/$LiPF_6$ model electrolyte containing Mn^{2+} or Ni^{2+} ions at the corresponding amounts. To avoid deposition of the transition metal ions on the lithium counter electrode, we use a sealed 2-compartment cell setup, separating the working and counter electrode compartments by a lithium ion conducting solid electrolyte.[12] As ethylene is the major gaseous product of the reductive decomposition of EC,[51,52] we will especially focus on its evolution during formation and cycling of graphite electrodes in Mn- or Ni-containing electrolytes. Considering that in real lithium-ion cells, transition metal dissolution occurs predominantly after the battery formation process

*Electrochemical Society Student Member.
**Electrochemical Society Fellow.
zE-mail: sophie.solchenbach@tum.de

is completed, we also investigate the effect of manganese and nickel ions on graphite electrodes that were preformed in a TM-free electrolyte. Finally, we use attenuated total reflection Fourier-transformed infrared (ATR-FTIR) spectroscopy and OEMS to elucidate the reactions of transition metal ions with SEI species.

Experimental

Preparation of electrodes and electrolytes.—Graphite electrodes were prepared by mixing graphite (SLP30, 7 m^2_{BET}/g, Timcal, Switzerland) and polyvinyl difluoride (PVDF, Kynar HSV 900, Arkema, France) in a ratio of 95:5 with N-methyl-pyrrolidone (NMP, anhydrous, Sigma-Aldrich, Germany; ink solid content 40%) in a planetary mixer (Thinky Corp., USA) at 2000 rpm for 15 min. The ink was then coated onto a polyester separator (FS 24316, Freudenberg, Germany) and dried at 50°C for 10 h. Electrodes with 15 mm diameter were punched out, dried in a glass oven (Büchi, Switzerland) under dynamic vacuum at 120°C for 12 h and transferred into the glove box without exposure to air. The final electrodes had a loading of 6.1 ± 0.2 mg_{SLP30}/cm^2 (≡ 2.3 mAh/cm^2). Glassfiber and polyester separators were also dried at 120°C under dynamic vacuum prior to use.

Electrolytes were prepared by mixing $LiPF_6$ (BASF SE, Germany) with ethylene carbonate (EC, BASF SE, Germany) or dimethyl carbonate (DMC, BASF SE, Germany) to yield a 1.5 M $LiPF_6$ concentration. For preformation of graphite anodes with an SEI-forming additive, vinylene carbonate (VC, BASF SE, Germany) was added at a concentration of 2 wt% to the as-prepared DMC/$LiPF_6$ electrolyte. Manganese bis-(trifluorosulfonyl)imide ($Mn(TFSI)_2$, 99.5%, Solvionic, France) and nickel bis-(trifluorosulfonyl)imide ($Ni(TFSI)_2$, 97%, Alfa Aesar, United States) were dried under dynamic vacuum at 120°C for 3 days and added to the electrolytes to yield a metal concentration of 10 mM, corresponding to a total amount of 1.5 μmol in the cell or 0.85 μmol/cm^2 per geometric graphite electrode area (based on 150 μL electrolyte and ø15 mm electrodes). For a full-cell with our graphite anodes and a balanced cathode with a loading of 13.5 mg_{CAM}/cm^2 (≡2.2 mAh/g for a specific capacity of 165 mAh/g), the total amount of dissolved transition metal would translate to ∼3.4 mg_{TM}/g_{CAM} or ∼0.3 wt%.

On-line electrochemical mass spectrometry.—The online electrochemical mass spectrometry (OEMS) system and a standard one-compartment electrochemical cell have been described in our previous publication.[53] To avoid the deposition of TM ions on the Li metal counter electrode, a sealed 2-compartment cell was used, where working and counter electrode compartments are separated by an impermeable lithium-ion conductive glass ceramic (LICGC, Ohara Corp., Japan) with an aluminum foil edge-seal.[12,54] The counter electrode compartment, which is shielded from the OEMS inlet, contained the Li counter electrode (ø 17 mm, 450 μm thickness, Rockwood Lithium, United States) and a 22 mm diameter glass fiber separator soaked with 250 μL EC + 1.5 M $LiPF_6$ or DMC + 1.5 M $LiPF_6$ without any transition metal ions added. The working electrode compartment that is connected to the OEMS inlet contained the graphite working electrode (ø 15 mm) and a polyester separator (ø 17 mm), both soaked with 150 μL of the test electrolyte, i.e., with or without TM salts added. After connection to the OEMS inlet and a rest period at open circuit voltage (OCV) for 4 h, we performed cyclic voltammetry at a rate of 0.2 mV/s, starting from OCV (∼3 V vs. Li^+/Li) and then scanning between 0.1 V and 2 V or 3 V vs. Li^+/Li. For quantification of the mass spectrometer currents, a calibration gas containing H_2, O_2, CO_2, and C_2H_4 (each 2000 ppm) or H_2, O_2, CO_2, and CO (each 2000 ppm) in Argon (Linde AG, Germany) was used. All currents were normalized to the current at m/z = 36 (Ar isotope) in order to correct for effects of minor pressure and temperature deviations, and afterwards the currents m/z = 2 (H_2), m/z = 26 (C_2H_4), m/z = 28 (CO, corrected for contributions from C_2H_4 and CO_2 as described by Strehle et al.),[55] and m/z = 44 (CO_2) were converted into gas concentrations.

For experiments with preformed electrodes, graphite electrodes coated on polyester separator were cycled 2 times with a rate of C/8 (based on graphite capacity) vs. a LFP electrode (3.5 mAh/cm^2, Custom Cells, Germany) in EC/1.5 M $LiPF_6$ electrolyte between 3.45 and 2 V cell voltage. The preformed cells were then discharged to 0.3 V cell voltage (corresponding to a graphite potential ∼2.9 V vs. Li^+/Li) and held at this potential for 10 h. Subsequently, the cells were disassembled inside a glove box, and the graphite electrodes were transferred without further washing into another OEMS cell with freshly prepared electrolyte and separators. For the experiments with graphite electrodes stored/preformed in EC and cycled in DMC as well as for graphite electrodes preformed in DMC/1.5 M $LiPF_6$ + 2 wt% VC, the graphite electrodes were washed with 5 mL DMC prior to the assembly of the OEMS cell in order to remove any remaining electrolyte contained in the pores of the harvested graphite electrodes.

Attenuated total reflection fourier-transform infrared spectroscopy (ATR-FTIR).—For ATR-FTIR analysis, both LFP cathode and graphite anode from the preformed cells (cycled at C/8 in EC + 1.5 M $LiPF_6$ between 2.0–3.45 V_{cell}) were transferred into a new cell with fresh separators and electrolyte with/without transition metals, and cycled again for 2 cycles at C/8 between the same cell voltages. The cells were then disassembled inside an Ar-filled glove box. The graphite electrodes were washed with 1.5 mL DMC and dried for 20 min under dynamic vacuum in the glove box antechamber at room temperature. ATR-FTIR spectra of the electrodes were then measured inside the glove box using a Spectrum Two spectrometer (Perkin Elmer) with a resolution of 4 cm^{-1} with 128 scans on a MIRacle germanium ATR (Pike Technologies). The spectra were normalized to the intensity of the PVDF peak at 1190 cm^{-1} (-CF_2- stretching vibrations).[56]

Results

Pristine graphite electrodes.—As a first step, we investigate the effect of transition metal ions on the electrolyte decomposition reactions of pristine graphite electrodes, i.e., when no SEI is present. This represents the situation in commercial Li-ion cells prior to battery formation, where dissolved transition metals are observed upon electrolyte storage of the pristine materials,[26] likely formed by the reaction of cathode active materials with HF, which is present in commercial $LiPF_6$ based electrolytes at the level of several tens of ppm, or at even higher concentration if cell components are dried improperly.[57,58] As ethylene carbonate (EC) is reduced to mostly lithium ethylene dicarbonate (LEDC) and C_2H_4,[51,59–62] so that the latter is the main gaseous product during graphite SEI formation in EC-based electrolytes,[52,55,63] we first focus on C_2H_4 as a marker of the reductive decomposition of EC. Figure 1 shows the current density (a) and the integral C_2H_4 evolution (b), both normalized to the active material mass of the graphite electrode, during 4 CV cycles of pristine graphite electrodes in EC/$LiPF_6$ without added transition metal salts, or with either 1.5 μmol Mn^{2+} or 1.5 μmol Ni^{2+} added as TFSI salts (equating to ∼140 $\mu mol_{TM}/g_{Graphite}$, which would correspond to ∼0.3 wt% dissolution of a NCM cathode active material in a balanced full-cell; for details see Experimental section).

The blue lines in Figure 1 show the baseline for the transition metal-free electrolyte. During the first cycle, a reduction peak current around 0.5 V vs. Li^+/Li appears (Figure 1a), alongside with the evolution of ∼80 μmol/g C_2H_4 (Figure 1b), in good quantitative agreement with the ∼10 μmol/m^2_{BET} C_2H_4 found in earlier studies on the same graphite (BET: 7 m^2/g).[12,55] In the following cycles, the C_2H_4 evolution stops (as indicated by the constant concentration), also consistent with our previous reports.[12,52,55,64] When 1.5 μmol $Ni(TFSI)_2$ are added to the electrolyte, an additional reduction feature in the first cycle, starting at ∼2.5 V vs. Li^+/Li, can be seen in the current response (see green line in Figure 1a). For the Ni-containing electrolyte, C_2H_4 is evolved at much less negative potentials in the first reduction cycle (at ∼1.6 V vs. Li^+/Li) and at higher amounts (112 μmol/g, see green lines in Figure 1b; for details please also refer

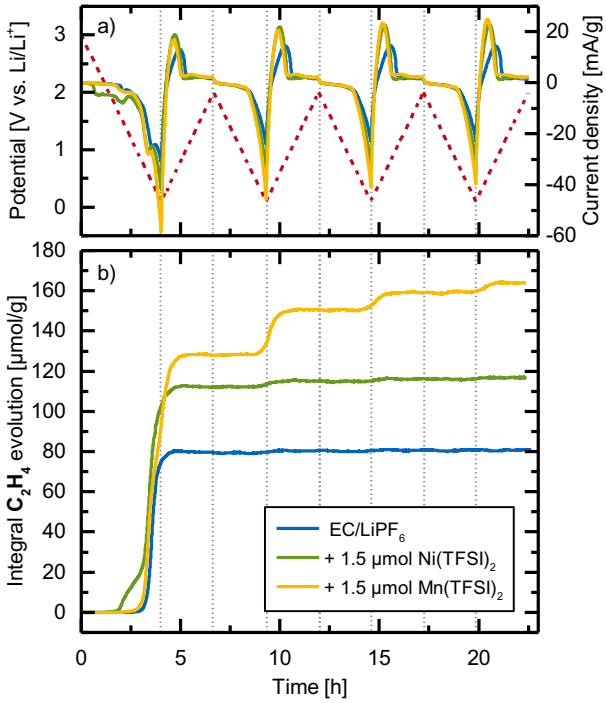

Figure 1. Currents and ethylene evolution during the first 4 voltammetric cycles of pristine graphite electrodes in EC/1.5 M $LiPF_6$ electrolyte without added metal salts (blue lines), with 1.5 µmol $Ni(TFSI)_2$ (green lines), or with 1.5 µmol $Mn(TFSI)_2$ (yellow lines). a) Currents normalized to graphite mass (solid lines) and potential (red dashed line); b) integral ethylene evolution normalized to graphite mass. The voltammetric cycles were conducted at 0.2 mV/s between 0.1–2.0 V vs. Li^+/Li, starting the first reductive scan from OCV (~3 V vs. Li^+/Li).

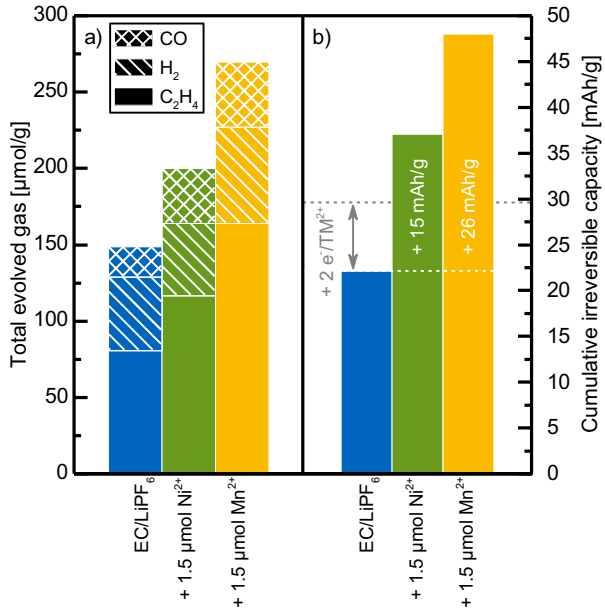

Figure 2. Total evolved gas and cumulative irreversible capacity (both normalized to graphite mass) over the first 4 cycles of the pristine graphite electrodes shown in Figure 1, i.e., in EC/1.5 M $LiPF_6$ electrolyte without added metal salts (blue bars), with 1.5 µmol $Ni(TFSI)_2$ (green bars), or with 1.5 µmol $Mn(TFSI)_2$ (yellow bars). a) Total evolved C_2H_4 (solid bars), H_2 (dashed bars), and CO (squared bars). b) Cumulative irreversible capacity, with the gray arrow indicating the theoretical charge for 2-electron reduction of the added Ni^{2+} or Mn^{2+} ions.

to Figure 5), which increases slightly up to 117 µmol/g by the end of 4 charge/discharge cycles. As previous studies showed an identical gassing behavior of graphite electrodes cycled in either transition metal-free LiTFSI[64] or $LiPF_6$[52,55] based electrolytes, the effect of the $TFSI^-$ anions on gassing should be negligible, so that the changes upon the addition of $Ni(TFSI)_2$ must be due to the presence of Ni^{2+}. The addition of 1.5 µmol $Mn(TFSI)_2$ (see yellow lines in Figure 1) leads to the highest C_2H_4 evolution in the 1st cycle, namely 128 µmol/g. Quite strikingly, with Mn^{2+}, a distinct C_2H_4 evolution is seen in each cycle, accumulating to 164 µmol/g C_2H_4 after 4 charge/discharge cycles. A more detailed discussion on the potentials at which the 1st cycle reduction current peaks and the onset of C_2H_4 evolution occur can be found in the Discussion section (see Figure 5).

While C_2H_4 is the main gaseous product from EC reduction, H_2,[12,51] CO,[55,62,65,66] and CO_2[63,65] are also commonly observed during the formation of graphite in carbonate-based electrolytes. The total quantities of C_2H_4, H_2, and CO after 4 cycles are shown in Figure 2a. After 4 cycles in the TM-free electrolyte (blue bars in Figure 2a), 48 µmol/g H_2 and 20 µmol/g CO have been evolved in addition to the 81 µmol/g of C_2H_4. For Ni^{2+}- and Mn^{2+}-containing electrolytes (green and yellow bars in Figure 2a), the concentration of CO is almost twice as high as in the TM-free electrolyte (36 and 43 µmol/g, respectively). In contrast, the amount of H_2 is similar in the absence and presence of dissolved transition metals (TM-free: 48 µmol/g; with Ni^{2+}: 47 µmol/g; Mn^{2+}: 63 µmol/g). While H_2 is the reduction product of trace water and/or HF in the electrolyte,[57,64] CO evolution has been ascribed to a direct 2-electron reduction of EC,[65–68] a minor pathway for EC reduction. Note that we also see small quantities of CO_2 (<20 µmol/g) during the first cycle of all experiments, which is however consumed during the subsequent cycles and thus does not appear in Figure 2.

Figure 2b shows the cumulative irreversible capacities (i.e., the summed-up differences between lithiation and delithiation capacity) after the 4 CV cycles depicted in Figure 1a. For the TM-free electrolyte (blue bars), the cumulative irreversible capacity is 22 mAh/g, which fits well to the expected formation losses of 7–10% of the initial capacity for graphite electrodes.[9] The cumulative irreversible capacity over 4 cycles in an electrolyte with Ni^{2+} ions (green bars) is significantly higher (37 mAh/g), but still smaller than that of the Mn^{2+}-containing electrolyte (48 mAh/g), which fits to the observation that the latter also exhibits the highest amount of evolved gas (Figure 2a). Note that the additional cumulative irreversible capacity losses in the Ni-containing and the Mn-containing electrolytes (+15 mAh/g and +26 mAh/g, respectively) substantially exceed the capacity of ~7.5 mAh/g required for a simple 2-electron reduction of the TM^{2+} ions (see horizontal gray dashed line in Figure 2b; based on the added salt concentration of 0.85 µmol/cm² and the graphite loding of 6.1 mg/cm²), namely by a factor of ~2 for Ni^{2+} and of ~3.5 for Mn^{2+}. This clearly indicates that at least the difference between the measured cumulative irreversible capacity and the theoretical charge for the TM ion reduction to the metal (i.e., the ~7.5 mAh/g) must have gone into the irreversible reduction of the electrolyte.

The results from Figure 1 and Figure 2 show that in the presence of TM ions, especially Mn^{2+}, strong additional electrolyte reduction takes place, consuming lithium and generating gas. As the composition of the evolved gas is comparable for all electrolytes, the fundamental reactions during SEI formation in TM-free and TM-containing electrolytes are apparently very similar. Moreover, the results demonstrate that manganese species continuously decompose electrolyte, whereas the activity of nickel species toward electrolyte reduction subsides much quicker.

Preformed graphite electrodes.—In commercial cells, the majority of transition metal dissolution occurs typically during cycling at high temperatures or voltages over extended periods of time. In this case, the SEI is already formed when the transition metal ions reach the anode. Therefore, we also investigate the effect of Ni^{2+} and

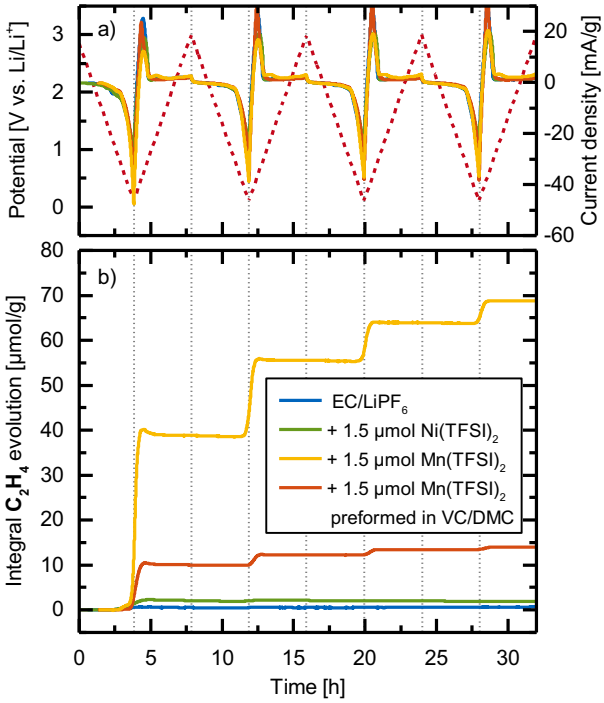

Figure 3. a) Currents and b) ethylene evolution, normalized to graphite mass, during the first 4 voltammetric cycles of preformed graphite electrodes in EC/1.5 M $LiPF_6$ electrolyte with/without added metal salts. Preformation was done with TM-free electrolyte in a separate cell vs. an LFP cathode (2 cycles at C/8), using two different preformation electrolytes: i) EC/1.5 M $LiPF_6$ for the OEMS experiments in TM-free electrolyte (blue) or electrolyte with either 1.5 µmol $Ni(TFSI)_2$ (green lines) or 1.5 µmol $Mn(TFSI)_2$ (yellow); ii) DMC/1.5 M $LiPF_6$ + 2% VC for the OEMS experiment in electrolyte with 1.5 µmol $Mn(TFSI)_2$ (orange). The voltammetric cycles at 0.2 mV/s were done between 0.1–3.0 V vs. Li^+/Li, starting from OCV (~2.9 V vs. Li^+/Li).

Mn^{2+} ions on preformed graphite electrodes. The SEI formation was achieved by pre-cycling (2 cycles at C/8) the graphite electrodes in a 1-compartment OEMS cell with capacitively oversized LFP counter electrodes in a TM-free EC + 1.5 M $LiPF_6$ electrolyte; the resulting SEI is known to consist mostly of LEDC and LiF, with only traces of Li_2CO_3 present.[60] Afterwards, the cells were deep-discharged to a cell voltage of 0.3 V_{cell} (corresponding to a graphite electrode potential of ~2.9 V vs. Li^+/Li), and the graphite electrodes were then transferred without further washing into the 2-compartment OEMS cell in an Ar-filled glove box. The discharge capacity over these first two formation cycles was 350–355 mAh/g, while the irreversible capacity accumulated to 25–27 mAh/g.

Figure 3 shows the current density (a) and the integral C_2H_4 evolution (b) during 4 CV cycles of the thus preformed graphite electrodes in electrolytes containing 1.5 µmol Mn^{2+} (yellow lines), 1.5 µmol Ni^{2+} (green lines) or no transition metal ions (blue lines). As one would expect, the TM-free electrolyte baseline for the preformed graphite electrode does no longer show the EC reduction current peak at ~0.5 V vs. Li^+/Li, consistent with the observation that only traces of C_2H_4 (~0.5 µmol/g) are evolved compared to the ~80 µmol/g C_2H_4 evolved on a pristine graphite electrode (blue line in Figure 1b). Hence, the passivating properties of the SEI preformed in EC/$LiPF_6$ remained largely intact after transferring the preformed graphite electrode into the 2-compartment OEMS cell. On the other hand, with 1.5 µmol Ni^{2+} in the electrolyte, ~2 µmol/g C_2H_4 are evolved during the first cycle (see green lines in Figure 3b), without any further C_2H_4 evolution in the subsequent cycles. If we compare the additional C_2H_4 evolution over 4 charge/discharge cycles induced by the presence of Ni^{2+} in the electrolyte on pristine graphite electrodes (~36 µmol/g; green line in Figure 1b) vs. on preformed graphite electrodes (~2 µmol/g; green line in Figure 3b), it becomes apparent that the effect of Ni^{2+} in the electrolyte is greatly suppressed by the presence of an SEI. Besides, also the additional reduction peaks between 2.5–1.5 V vs Li^+/Li seen in Figure 1a (green line) are no longer observed on the preformed graphite electrode (green line in Figure 3a). This suggests that nickel ions released into the electrolyte from cathode active materials over the course of extended charge/discharge cycling should hardly compromise the stability of the SEI, and thus should only have a very minor negative impact on the active lithium inventory of the cell.

On the contrary, the addition of 1.5 µmol Mn^{2+} to a graphite electrode preformed in EC/$LiPF_6$ (yellow lines in Figure 3) leads to a ~20-fold higher C_2H_4 evolution in the first cycle (39 µmol/g) compared to Ni^{2+}, which continues in subsequent cycles, accumulating to a total amount of evolved C_2H_4 of ~69 µmol/g after 4 cycles. This amounts to ~80% of the additional C_2H_4 evolved on a pristine graphite electrode upon the addition of Mn^{2+} ions to the electrolyte (see difference between blue and yellow lines in Figure 1), which therefore implies that even if the SEI is formed in an Mn^{2+}-free electrolyte, it is not able to suppress the detrimental electrolyte reduction reactions triggered by Mn^{2+} ions. In summary, while an SEI preformed in EC/$LiPF_6$ almost completely suppresses the negative effect of Ni^{2+} ions on electrolyte decomposition, it is not very effective in the presence of Mn^{2+} ions.

To better understand the effect of the SEI on the reactions caused by Mn^{2+} ions, we used the same graphite preformation procedure, but replaced the electrolyte for formation with DMC/$LiPF_6$ + 2 wt% vinylene carbonate (VC). In this case, the SEI formed with VC consists mainly of poly(VC) and Li_2CO_3,[69] and has been reported to partially mitigate the poor coulombic efficiency[70] and impedance growth[35] caused by transition metal ions; furthermore, due to the absence of EC, no LEDC is being formed.[62] After formation (2 cycles at C/8, yielding a cumulative irreversible capacity of ~31 mAh/g), the electrode was rinsed with pure DMC to remove any remaining VC, and was transferred into the 2-compartment OEMS cell. The orange lines in Figure 3 show the current profile and the C_2H_4 evolution of the VC-preformed graphite electrode cycled in EC/$LiPF_6$ + 1.5 µmol Mn^{2+} electrolyte. Although C_2H_4 is still evolved throughout all 4 cycles, its overall amount after 4 cycles is only ~20% of that obtained with the graphite electrode preformed in EC/$LiPF_6$ electrolyte (viz., 14 µmol/g vs. 69 µmol/g, comparing the orange vs. the yellow lines in Figure 3).

Figure 4a shows the evolution of C_2H_4, H_2, and CO after 4 cycles from all the experiments shown in Figure 3. The gas evolution in the TM-free electrolyte (blue bar) is limited to low amounts of H_2 (~7 µmol/g), probably from the reduction of newly introduced HF or trace water of the fresh electrolyte, its reduction largely perhibited by the preformed SEI. All of the TM-containing electrolytes evolve more H_2 (~23 µmol/g (Ni^{2+}) and ~32 µmol/g (Mn^{2+}) for electrodes preformed in EC/$LiPF_6$; ~28 µmol/g (Mn^{2+}) for electrodes preformed in DMC/2%VC/$LiPF_6$), suggesting that TM ions can catalyze the reduction of protic species, which is normally hindered by the SEI.[64] While for the electrode cycled in Ni^{2+}-containing electrolyte (green bars), only traces of CO (~1 µmol/g) are observed, the Mn^{2+}-containing electrolyte evolves ~32 µmol/g CO after 4 cycles if preformed in EC/$LiPF_6$ (yellow bars), lowered to ~12 µmol/g CO if preformed in DMC/2%VC/$LiPF_6$ (orange bars).

The corresponding cumulative irreversible capacity for the preformed electrodes after 4 cycles is displayed in Figure 4b. As expected from the gas evolution, the electrode cycled in the TM-free electrolyte (blue bars) shows the lowest irreversible capacity (~6 mAh/g). For the Ni^{2+}-containing electrolyte (green bars), the cumulative irreversible capacity is ~13 mAh/g, so that the excess irreversible loss (~7 mAh/g) is rather close to the theoretical capacity required for the 2-electron reduction of all Ni^{2+} ions (~7.5 mAh/g, see above). The highest irreversible capacity (~29 mAh/g) comes from the electrode preformed in EC and cycled in Mn^{2+}-containing electrolyte (yellow bars). The excess irreversible capacity measured for the EC/$LiPF_6$ preformed electrode caused by Mn^{2+} (~23 mAh/g more than in the TM-free electrolyte) is comparable to the additional irreversible capacity in

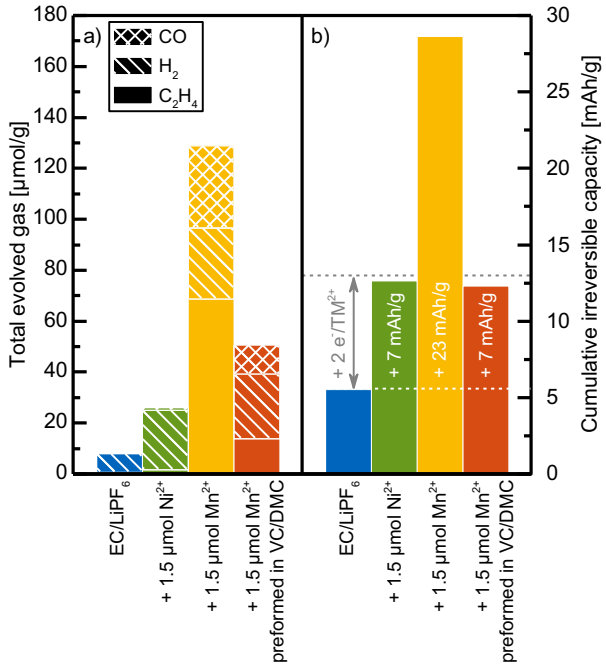

Figure 4. Total evolved gas and cumulative irreversible capacity (both normalized to graphite mass) over the first 4 cycles of the preformed graphite electrodes in EC/+1.5 M $LiPF_6$ with/without added metal salts, as shown in Figure 3. a) Total evolved C_2H_4 (solid bars), H_2 (dashed bars), and CO (squared bars). b) Cumulative irreversible capacity, with the gray arrow indicating the theoretical charge for 2-electron reduction of the added Ni^{2+} or Mn^{2+} ions. Preformation was done in two different electrolytes: i) EC/1.5 M $LiPF_6$ for the OEMS experiments in TM-free electrolyte (blue) or electrolyte with either 1.5 µmol $Ni(TFSI)_2$ (green lines) or 1.5 µmol $Mn(TFSI)_2$ (yellow); ii) DMC/1.5 M $LiPF_6$ + 2% VC for the OEMS experiment in electrolyte with 1.5 µmol $Mn(TFSI)_2$ (orange).

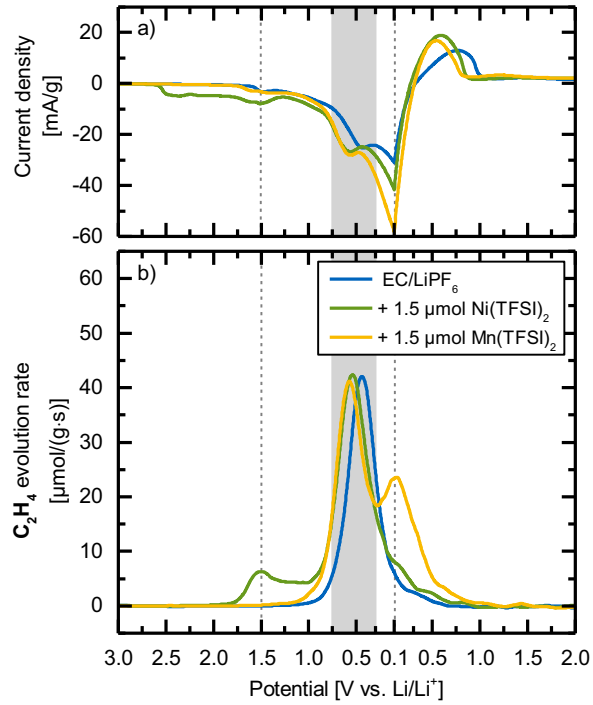

Figure 5. Currents and ethylene evolution rate during the first voltammetric cycle of pristine graphite electrodes in EC/1.5 M $LiPF_6$ electrolyte without added metal salts (blue lines), with 1.5 µmol $Ni(TFSI)_2$ (green lines), or with 1.5 µmol $Mn(TFSI)_2$ (yellow lines). a) Currents normalized to graphite mass (solid lines) and potential (red dashed line); b) integral ethylene evolution normalized to graphite mass. The data are extracted from Figure 1.

the experiment with pristine electrodes (~26 mAh/g, see yellow bars in Figure 2b), in agreement with the similar additional total gas evolution (C_2H_4 + H_2 + CO with respect to the TM-free electrolyte) of ~120 µmol/g on preformed electrodes (see yellow bars in Figure 4a) and ~121 µmol/g on pristine electrodes (see yellow bars in Figure 2a). On the contrary, the electrode preformed in DMC/$LiPF_6$ + 2%VC and cycled in an electrolyte with Mn^{2+} ions (orange bars in Figure 4b) shows a largely reduced irreversible capacity that is only ~7 mAh/g higher compared to the ~6 mAh/g obtained in the TM-free electrolyte, and thus this difference is very close again to the theoretical capacity required for the 2-electron reduction of all Mn^{2+} ions (~7.5 mAh/g, see above). While this additional capacity found for DMC/$LiPF_6$ + 2%VC preformed graphite in Mn^{2+}-containing electrolyte is identical to that for Ni^{2+}-containing electrolyte for EC/$LiPF_6$ preformed graphite (compare orange vs. green bars in Figure 4b), the additional amount of gas produced in the presence of Mn^{2+} ions is substantially larger (~44 µmol/g vs. ~16 µmol/g; compare orange vs. green bars in Figure 4a) compared to Ni^{2+}, suggesting that Mn^{2+} ions more effectively catalyze SEI and/or solvent reduction.

The results of Figure 3 and Figure 4 show that the activity of Ni^{2+} ions toward electrolyte reduction is suppressed by an EC-derived SEI, but that this SEI does not lead to significantly less side reactions for a Mn^{2+}-containing electrolyte. Hence, the dissolution of manganese will be far more detrimental toward long-term cell performance compared to that of nickel, which has previously been observed by Gilbert et al.[7] and Jung et al.[5] However, additives like VC can help to mitigate the detrimental effect of manganese, as apparently the SEI composition plays a crucial role on the reactivity of manganese toward electrolyte reduction.

Discussion

In order to obtain further insights into the effect of dissolved transition metals on the formation, the passivating properties, and the stability of the SEI on graphite electrodes, we will initially examine the very first voltammetric reduction and oxidation cycle on a pristine graphite electrode. Figure 5 magnifies the current density and plots the C_2H_4 evolution rate (obtained by taking the derivative of the integral OEMS signals) vs. the graphite potential for the first voltammetric cycle shown in Figure 1b. For the TM-free electrolyte (see blue lines in Figures 5a and 5b), the first main reduction peak is observed at ~0.5 V vs. Li^+/Li, which coincides with a maximum in ethylene evolution rate (see gray-shaded area in Figure 5). This peak appears for all three electrolytes and is ascribed to the reduction of EC to lithium ethylene dicarbonate (LEDC) and C_2H_4 on graphite.[51,52,55,59–63]

The electrolyte containing 1.5 µmol Ni^{2+} ions (green lines in Figure 5) shows an additional reduction current already at ~2.5 V vs. Li^+/Li, merging into a second small reduction current peak at ~1.5 V vs. Li^+/Li that is accompanied by a first peak in the C_2H_4 evolution rate. Jung et al.[5] observed the reduction of Ni^{2+} in a carbonate-based electrolyte at ~2.22 V vs. Li^+/Li, so that we ascribe the first reduction peak in the Ni-containing electrolyte at ~2.5 V vs. Li^+/Li (green line in Figure 5a) to the onset of Ni^{2+} reduction. By up-integrating the current density difference between the Ni-containing and the TM-free electrolyte during this initial part of the first reduction scan, it becomes apparent that the ~7.5 mAh/g needed for the reduction of Ni^{2+} to Ni^0 are only reached at ~1.4 V vs. Li^+/Li, which suggests that also the second peak around 1.5 V vs. Li^+/Li belongs to the reduction of Ni^{2+}. The concurrent C_2H_4 evolution initiating at below ~1.8 V vs. Li^+/Li is likely related to a reduction of EC on the nascent Ni^0 surface, which occurs apparently at higher potentials than the EC reduction on the graphite surface in TM-free EC/$LiPF_6$ electrolyte (blue line in Figure 5b), initiating at ~0.9 V vs. Li^+/Li (the same onset potential for C_2H_4 formation was observed for EC/EMC (3/7) with 1 M $LiPF_6$[52] or 1 M LiTFSI).[64] Interestingly, after the first two

reduction peaks (i.e., at 1.25 V vs. Li^+/Li), the integrated current accounts to ~7.9 mAh/g, whereas the charge required for the two-electron reduction of the formed C_2H_4 (11.8 μmol/g ≡ 0.63 mAh/g) and CO (9.3 μmol/g ≡ 0.50 mAh/g) together with the reduction of Ni^{2+} to Ni^0 (7.5 mAh/g) would require a total charge of ~8.6 mAh/g. This suggests that some of the electrolyte must have been reduced chemically rather than electrochemically, possibly via the re-oxidation of Ni^0 back to Ni^{2+} in a similar mechanism as suggested for manganese.[33,39]

When Mn^{2+} ions are added (see yellow lines in Figure 5), no additional current peak can be seen, even though the onset for C_2H_4 evolution (~1.1 V) is shifted ~0.2 V more positively compared the TM-free electrolyte. Since the onset for Mn^{2+} reduction was reported to occur at ~1.29 V vs. Li+/Li,[5] the more positive onset for C_2H_4 evolution in Mn^{2+}-containing electrolyte compared to TM-free electrolyte suggests that EC reduction is catalyzed by Mn° formed at the graphite electrode. Overall, these results with Ni^{2+}- and Mn^{2+}-containing electrolyte indicate that the earlier onset of C_2H_4 evolution occurs only below the respective reduction potential of the transition metal ions, suggesting that only the reduced transition metals are active toward electrolyte reduction. Rather noteworthy in the case of Mn^{2+}-containing electrolyte is that the C_2H_4 evolution rate increases again during the first positive-going potential scan, with a maximum at ~0.1 V vs. Li^+/Li (see gray dashed line at 0.1 V vs. Li^+/Li in Figure 5), in stark contrast to the vanishing C_2H_4 evolution rate in TM-free or Ni_{2+}-containing electrolyte. This is a clear evidence for the SEI decomposing properties of Mn^{2+} in contrast to Ni^{2+}.

That transition metals can affect the composition and stability of the SEI on graphite was proposed, e.g., by Joshi et al.,[32] who added 10 mM concentrations of each Ni^{+2}, Mn^{2+}, and Co^{2+} to a EC/DEC/$LiPF_6$ electrolyte and found evidence that transition metal ions catalyze the decomposition of LEDC in the SEI to Li_2CO_3, presumably by the release of C_2H_4, CO_2, and O_2. Later on, Leung[50] proposed that Mn^{2+} trapped in the SEI could decompose LEDC to alkoxides by releasing CO_2^-, which could convert to CO_2 by transferring the excess electron to a solvent molecule. This is consistent with the catalytic effect of Mn^{2+} on SEI decomposition deduced from Figure 3 and Figure 4, where continuous electrolyte decomposition even on a preformed graphite electrode is observed in the presence of Mn^{2+} ions. To better understand how transition metal ions in the electrolyte affect the SEI composition on a preformed electrode (in a TM-free EC/$LiPF_6$ electrolyte according to the above described procedure), they were transferred without washing into a new cell which we assembled with a fresh separators, a capacitively oversized LFP counter electrode, and an EC/$LiPF_6$ electrolyte with 1.5 μmol Mn^{2+} ions, 1.5 μmol Ni^{2+} ions, or without any transition metals. Subsequently, the cells were cycled between 2.0–3.45 V_{cell} at C/8 for two cycles, after which the harvested graphite electrodes were washed with DMC and then investigated by attenuated total reflection Fourier-transform infrared (ATR-FTIR) spectroscopy.

Figure 6 shows the ATR-FTIR spectra of the pristine (i.e., unused) graphite electrodes (gray spectra) as well as preformed electrodes cycled in the TM-free (blue spectra), Ni^{2+}-containing (green spectra), or Mn^{2+}-containing (yellow spectra) electrolyte. All spectra were normalized to have the same intensity for the PVDF peak at 1190 cm^{-1}, marked by the gray dashed line. For the cycled electrodes, the new peaks arising at ~1630 cm^{-1} and 1300 cm^{-1} can be assigned to LEDC,[71,72] whereas the peak at ~1750 cm^{-1} belongs to organic carbonate oligomers.[52] While no major differences could be found between the electrodes cycled in a TM-free and in an electrolyte with Ni^{2+} ions, the electrode cycled in the Mn^{2+}-containing electrolyte shows strongly pronounced peaks around 1420-1480 cm^{-1} (marked by the navy colored dashed lines), which is characteristic for inorganic carbonates like Li_2CO_3; for comparison, the spectra of pure Li_2CO_3 is also given in Figure 6 (navy line). Unfortunately, the Li_2CO_3 peak at ~850 cm^{-1} coincides with a PVDF peak (see gray line in Figure 6). Nevertheless, these results indicate that a Mn^{2+}-contaminated SEI contains more inorganic carbonates, in agreement with Joshi et al.[32] It is to note that this observation also fits to the mechanism proposed

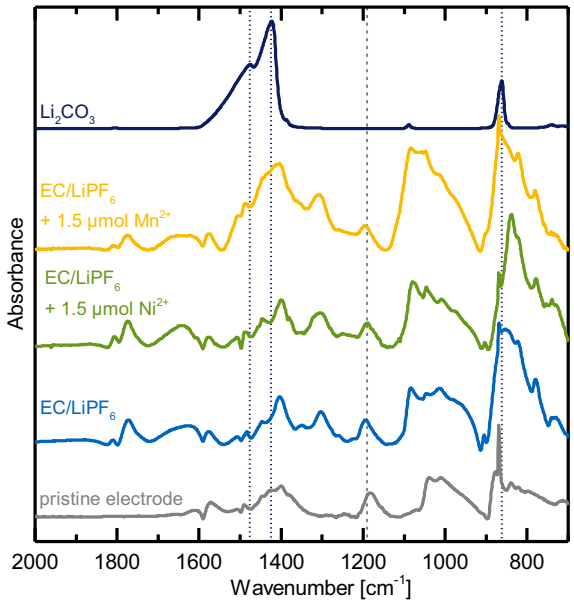

Figure 6. ATR-FTIR-spectra of a pristine graphite electrode (gray line) and of preformed graphite electrodes after two cycles at C/8 between 2.0–3.45 V_{cell} (in a cell with an LFP cathode) in different EC/1.5 M $LiPF_6$ electrolytes: i) without transition metal (blue line); ii) with 1.5 μmol $Ni(TFSI)_2$ (green line); or, iii) with 1.5 μmol $Mn(TFSI)_2$ (yellow line). Preformation was done in TM-free EC/1.5 M $LiPF_6$ for two cycles at C/8; prior to ATR-FTIR analysis, the cycled electrodes were washed with DMC. The spectra were normalized to the PVDF peak at 1190 cm^{-1} (see gray dashed line). The reference spectrum of Li_2CO_3 is also given, with characteristic peaks marked by the navy colored dotted lines.

by Leung,[50] as CO_2 (or CO_2^-) is readily reduced on graphite to form Li_2CO_3,[73] but due to the simultaneous consumption and evolution of CO_2 in our closed-cell system, this process would not be traceable by OEMS.

As both the reduction of EC and the decomposition of LEDC to Li_2CO_3 as proposed by Joshi et al.[32] would lead to the evolution of C_2H_4, we designed an experiment where these two processes could be separated. For this, we carefully washed graphite electrodes preformed in TM-free EC/$LiPF_6$ with 5 mL DMC, and then cycled them in the 2-compartment OEMS cell with DMC/$LiPF_6$ electrolyte containing either 1.5 μmol Mn^{2+} ions or no TM ions. As the reduction of DMC generates CO, but no C_2H_4,[66] we should now be able to differentiate between electrolyte reduction and SEI decomposition. To first test if any EC remains in the pores of the electrode after washing, we additionally soaked a graphite electrode with the EC/$LiPF_6$ electrolyte, rinsed it, and then cycled it in the TM-free DMC/$LiPF_6$ electrolyte. Figure 7 shows the current density (a) and the C_2H_4 evolution (b) over the course of 4 voltammetric cycles. The electrode that was stored in EC/$LiPF_6$ and cycled in DMC/$LiPF_6$ shows a strong CO evolution (dashed navy colored line), amounting to ~148 μmol/g CO over 4 cycles, as no passivating SEI layer is present; these results are similar to a previous gas evolution study on EMC/$LiPF_6$ electrolytes by our group, where CO is the only gas evolved upon the reduction of EMC.[55] However, for the EC/$LiPF_6$ soaked graphite electrode, ~11 μmol/g C_2H_4 (solid navy colored line) are evolved over the 4 cycles, which originate from the remaining EC that could not be removed by the washing step (however, still a minor amount compared to the evolved CO). In contrast, the preformed electrode that was cycled in the TM-free DMC/$LiPF_6$ electrolyte (superimposing blue solid and dashed lines in Figure 7) shows neither CO nor C_2H_4 (<0.1 μmol/g), meaning that the SEI has not been damaged due to the washing process.

Lastly, the yellow lines in Figure 7 show the behavior of the preformed graphite electrode cycled in the Mn^{2+}-containing DMC/$LiPF_6$ electrolyte. In this case, both CO and C_2H_4 are evolved throughout

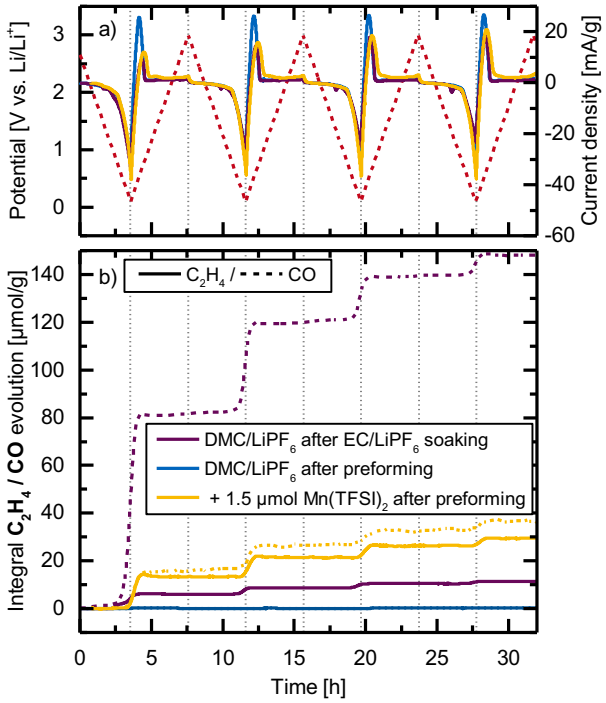

Figure 7. a) Currents normalized to graphite mass and b) evolution of ethylene (solid lines) and CO (dashed lines) during the first 4 voltammetric cycles of preformed graphite electrodes in DMC/1.5 M $LiPF_6$ electrolyte without (blue lines) and with 1.5 µmol Mn^{2+} ions (yellow lines). Preformation was done with TM-free EC/1.5 M $LiPF_6$ electrolyte in a separate cell vs. an LFP cathode (2 cycles at C/8); harvested electrodes were washed with DMC prior to building the 2-compartment OEMS cells. To determine the efficacy of the washing procedure, a pristine graphite electrode soaked in EC/1.5 M $LiPF_6$ electrolyte and then washed was also examined (dark purple lines). The voltammetric cycles at 0.2 mV/s were done between 0.1–3.0 V vs. Li^+/Li, starting from OCV (~2.9 V vs. Li^+/Li).

all 4 cycles. As the C_2H_4 evolution from the Mn^{2+}-containing electrolyte is ~30 µmol/g after 4 cycles (see solid yellow line in Figure 7b) while the EC residuals from the EC-soaked electrode account to only ~11 µmol/g C_2H_4 (see solid navy line in Figure 7b), we hypothesize that this additional ~19 µmol/g C_2H_4 originate from the decomposition of LEDC. This LEDC-derived amount of C_2H_4 may be compared to the higher amount of ~69 µmol/g C_2H_4 evolved for an identically preformed graphite electrode but cycled in EC/$LiPF_6$ + Mn^{2+} (Figure 3b, yellow lines). From this it becomes clear that the Mn catalyzed LEDC decomposition must compromise the integrity of the SEI, so that further electrolyte reduction can occur, namely of EC to C_2H_4 in the EC/$LiPF_6$ electrolyte. This hypothesis is confirmed by the strong CO evolution upon cycling of preformed graphite electrodes in the Mn^{2+}-containing DMC/$LiPF_6$ electrolyte (dashed yellow line in Figure 7b), where a major fraction of the evolved gas is produced by the direct reduction of DMC to CO. In summary, the comparison of the gas evolution of graphite electrodes preformed in EC/$LiPF_6$ and then cycled in Mn^{2+}-containing EC/$LiPF_6$ (Figure 3b) vs. Mn^{2+}-containing DMC/$LiPF_6$ (Figure 7b) reveals that the Mn catalyzed LEDC decomposition of LEDC must be leading to morphological changes in the SEI which leads to further electrolyte decomposition.

Based on our here presented results and numerous previous studies, we suggest the following mechanism for the catalytic decomposition of electrolyte by manganese ions, which is sketched in Scheme 1: After the Mn^{2+} ions are absorbed into the SEI by ion exchange (process (1) in Scheme 1), they diffuse through the SEI until they are close enough for an electron transfer from the lithiated graphite via tunneling, which leads to the deintercalation of lithium from graphite (2). If the reduced manganese is surrounded by LEDC, the latter is reduced to Li_2CO_3 and C_2H_4, while the manganese is simultaneously oxidized back to

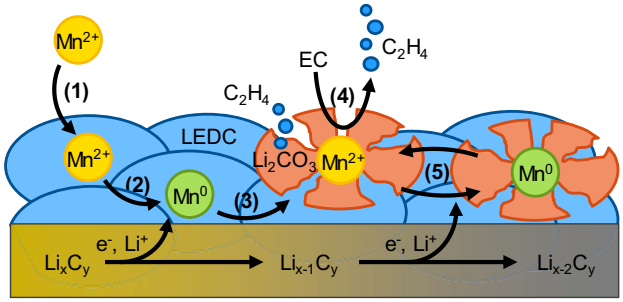

Scheme 1. Proposed mechanism for the continuous decomposition of SEI and electrolyte as monitored by C_2H_4 evolution for a preformed electrode with a Mn^{2+}-containing electrolyte (see text for details): (1) Absorption of Mn^{2+} ions into the SEI; (2) reduction of Mn^{2+} ions in the SEI and deintercalation of Li^+ from graphite; (3) re-oxidation of Mn^0 to Mn^{2+}; (4) recurrent electrolyte reduction; (5) catalytic cycle of electrolyte decomposition.

Mn^{2+} (3). Alternatively, LEDC could be reduced to lithium alkoxides and CO_2^- as suggested by Leung,[50] eventually also forming Li_2CO_3. The reduction contracts the SEI in the vicinity, leading to cracks which are filled with fresh electrolyte. This electrolyte will be reduced (4), and, if EC-based, produce additional C_2H_4. Consequently, Mn^{2+} would be located at the border between organic and inorganic SEI, in agreement with previous observations.[25,32,37,38] The Mn^{2+} ion can now accept further electrons and pass them on to surrounding LEDC or EC molecules (5), thereby leading to a catalytic cycle of electrolyte decomposition and active lithium loss from the lithiated graphite. This cycle can continue until the Mn^{2+} ion is eventually fully encapsulated by non-reducible decomposition products, so that an electron transfer from the lithiated graphite is no longer feasible. As Wandt et al.[4] found manganese almost exclusively in its 2+ oxidation state by operando XAS, the re-oxidation of Mn^0 to Mn^{2+} must be faster than the reduction of Mn^{2+}, i.e., the diffusion within the SEI and the electron transfer (steps 2 and 5 in Scheme 1) are the rate-limiting steps.

While both nickel and manganese have shown activity toward electrolyte decomposition in their reduced state (i.e., on pristine electrodes, see Figure 1), the presence of a preformed SEI greatly suppressed the effect of Ni^{2+}containing electrolyte on both gas evolution (see Figure 3b, green line) and the enrichment of Li_2CO_3 in the SEI (see Figure 6, green line). Hence, we can assume that the diffusion and/or the electron transfer of Ni^{2+} within the SEI is slowed down compared to Mn^{2+}. As suggested by Shkrob et al.,[38] it is possible that nickel and manganese are not fully reduced, but only one electron is transferred through the SEI to the transition metal ion. DFT-calculations by Leung[50] indicate that a Ni(I) species is far less likely to transfer an electron to neighboring SEI molecules compared to its Mn(I) counterpart. In this case, the catalytic cycle for Ni would be effectively interrupted. Additionally, Wandt at al.[4] found that Mn^{2+} in the SEI is reduced within minutes once the electrolyte is completely removed, whereas nickel stays in its 2+ state. As the reduction potential of Ni^{2+}/Ni is ~1 V higher than the reduction potential of Mn^{2+}/Mn,[5,74] the electron transfer from lithiated graphite to Ni^{2+} should have a higher thermodynamic driving force. Hence, another possible reason for the apparent difference between Ni and Mn is that the Li^+/Ni^{2+} exchange and the diffusion of Ni^{2+} within the SEI is much slower compared to Mn^{2+}.

For Li-ion batteries, this has two implications: i) The same amount of TM dissolution leads to less severe capacity fading if the cathode active material is Ni-rich and Mn-poor, which is advantageous for Ni-rich NMCs and especially Mn-free NCA (as seen by Gilbert et al.[7]); ii) future additive design should focus on the formation of an SEI which enables Li^+ ion transport while slowing down the diffusion of all transition metal ions, or which form SEI products which consist of chemically stable species that cannot be further reduced. In this context, a thermally aged SEI that contains more LiF and other

stable inorganic species[75] might be more robust toward the detrimental side reactions induced by manganese ions. However, as Mn^{2+} rapidly exchanges with Li^+ from LiF in the SEI,[25,37] a high LiF content will likely not act as a barrier for Mn^{2+} diffusion.

Conclusions

In this work, we applied on-line electrochemical mass spectrometry (OEMS) to follow the reactions triggered by manganese and nickel that ultimately lead to the loss of active lithium and poor capacity retention in full-cells. For the first time, we have investigated the effect of Mn^{2+} and Ni^{2+} on the gassing behavior of graphite, using EC/$LiPF_6$ model electrolytes with $Mn(TFSI)_2$ or $Ni(TFSI)_2$ in a 2-compartment cell. Both manganese and nickel significantly increase the C_2H_4 evolution and thus ethylene carbonate (EC) reduction on pristine graphite electrodes. Furthermore, the Mn^{2+}-containing electrolyte showed an ongoing EC reduction and C_2H_4 evolution throughout several cycles after formation.

As a second step, we investigated the effect of Mn^{2+} and Ni^{2+} on graphite electrodes which already featured an SEI by preforming them in a TM-free electrolyte. We found that the effect of nickel is greatly suppressed by the SEI, whereas manganese showed almost the same activity toward electrolyte reduction as on pristine electrodes. However, a preformation in a VC-containing electrolyte could significantly lower the side reactions caused by Mn^{2+} ions. As this showed that the SEI chemistry plays a crucial role, we found by post-mortem ATR-FTIR spectroscopy that the graphite electrodes cycled in an Mn^{2+}-containing electrolyte consisted of more Li_2CO_3 compared to electrodes cycled in an electrolyte with Ni^{2+} ions or no transition metals. Further OEMS experiments with preformed graphite electrodes and a DMC electrolyte (which allowed us to distinguish between electrolyte reduction and SEI decomposition) indicated that Mn^{2+} leads to the decomposition of LEDC to C_2H_4 and Li_2CO_3; however, the major part of the gas evolution still originated directly from the electrolyte reduction. Our results suggest that cathode active materials with low or zero manganese contents should be advantageous with respect to the detrimental effects of transition metal dissolution, and that SEI-stabilizing additives can be an efficient way to decrease the side reactions caused by transition metal ions in Li-ion batteries.

Acknowledgments

Sophie Solchenbach gratefully acknowledges the BASF Battery Research Network for financial support. Funding for Roland Jung was provided by BMW AG. The authors thank Prof. Brett Lucht for fruitful discussions.

ORCID

Sophie Solchenbach https://orcid.org/0000-0001-6517-8094
Roland Jung https://orcid.org/0000-0003-1135-7438

References

1. Y. Terada, Y. Nishiwaki, I. Nakai, and F. Nishikawa, *J. Power Sources*, **97–98**, 420 (2001).
2. H. Tsunekawa, S. Tanimoto, R. Marubayashi, M. Fujita, K. Kifune, and M. Sano, *J. Electrochem. Soc.*, **149**, A1326 (2002).
3. D. H. Jang, Y. J. Shin, and S. M. Oh, *J. Electrochem. Soc.*, **143**, 2204 (1996).
4. J. Wandt, A. Freiberg, R. Thomas, Y. Gorlin, A. Siebel, R. Jung, H. A. Gasteiger, and M. Tromp, *J. Mater. Chem. A*, **4**, 18300 (2016).
5. R. Jung, F. Linsenmann, R. Thomas, J. Wandt, S. Solchenbach, F. Maglia, C. Stinner, M. Tromp, and H. A. Gasteiger, *manuscript in preparation* (2018).
6. H. Zheng, Q. Sun, G. Liu, X. Song, and V. S. Battaglia, *J. Power Sources*, **207**, 134 (2012).
7. J. A. Gilbert, I. A. Shkrob, and D. P. Abraham, *J. Electrochem. Soc.*, **164**, 389 (2017).
8. D. R. Gallus, R. Schmitz, R. Wagner, B. Hoffmann, S. Nowak, I. Cekic-Laskovic, R. W. Schmitz, and M. Winter, *Electrochim. Acta*, **134**, 393 (2014).
9. I. Buchberger, S. Seidlmayer, A. Pokharel, M. Piana, J. Hattendorff, P. Kudejova, R. Gilles, and H. A. Gasteiger, *J. Electrochem. Soc.*, **162**, A2737 (2015).
10. D. P. Abraham, T. Spila, M. M. Furczon, and E. Sammann, *Electrochem. Solid-State Lett.*, **11**, A226 (2008).
11. X. Liao, Q. Huang, S. Mai, X. Wang, M. Xu, L. Xing, Y. Liao, and W. Li, *J. Power Sources*, **286**, 551 (2015).
12. M. Metzger, B. Strehle, S. Solchenbach, and H. A. Gasteiger, *J. Electrochem. Soc.*, **163**, A798 (2016).
13. S. Solchenbach, M. Metzger, M. Egawa, H. Beyer, and H. A. Gasteiger, *J. Electrochem. Soc.*, **165**, A3022 (2018).
14. T. Li, L. Xing, W. Li, Y. Wang, M. Xu, F. Gu, and S. Hu, *J. Power Sources*, **244**, 668 (2013).
15. O. Borodin, W. Behl, and T. R. Jow, *J. Phys. Chem. C*, **117**, 8661 (2013).
16. D. H. Jang and S. M. Oh, *J. Electrochem. Soc.*, **144**, 3342 (1997).
17. K. Amine, J. Liu, S. Kang, I. Belharouak, Y. Hyung, D. R. Vissers, and G. L. Henriksen, *J. Power Sources*, **129**, 14 (2004).
18. R. Jung, M. Metzger, F. Maglia, C. Stinner, and H. A. Gasteiger, *J. Electrochem. Soc.*, **164**, A1361 (2017).
19. R. Jung, M. Metzger, F. Maglia, C. Stinner, and H. A. Gasteiger, *J. Phys. Chem. Lett.*, **8**, 4820 (2017).
20. J. Wandt, A. Freiberg, A. Ogrodnik, and H. A. Gasteiger, *Mater. Today*, in press (2018).
21. D. Streich, C. Erk, A. Gue, P. Mu, F.-F. Chesneau, and E. J. Berg, *J. Phys. Chem. C*, **121**, 13481 (2017).
22. D. Streich, A. Guéguen, M. A. Mendez, F. F. Chesneau, P. Novák, and E. J. Berg, *J. Electrochem. Soc.*, **163**, A964 (2016).
23. A. Freiberg, S. Solchenbach, B. Strehle, A. Siebel, M. Tromp, and H. A. Gasteiger, *ECS Meet. Abstr.*, **2**, 179 (2018).
24. C. Zhan, J. Lu, A. J. Kropf, T. Wu, A. N. Jansen, Y. K. Sun, X. Qiu, and K. Amine, *Nat. Commun.*, **4**, 2437 (2013).
25. D. R. Vissers, Z. Chen, Y. Shao, M. H. Engelhard, U. Das, P. C. Redfern, L. A. Curtiss, B. Pan, J. Liu, and K. Amine, *ACS Appl. Mater. Interfaces*, **8**, 14244 (2016).
26. W. Choi and A. Manthiram, *J. Electrochem. Soc.*, **153**, A1760 (2006).
27. C. Zhan, T. Wu, J. Lu, and K. Amine, *Energy Environ. Sci.*, **11**, 243 (2018).
28. T. Tsujikawa, K. Yabuta, and T. Matsushita, *J. Electrochem. Soc.*, **158**, 322 (2011).
29. N. P. W. Pieczonka, Z. Liu, P. Lu, K. L. Olson, J. Moote, B. R. Powell, and J. Kim, *J. Phys. Chem. C*, **117**, 15947 (2013).
30. L. M. Thompson, W. Stone, A. Eldesoky, N. K. Smith, C. R. M. Mcfarlane, J. S. Kim, M. B. Johnson, R. Petibon, and J. R. Dahn, **165**, 2732 (2018).
31. S. Komaba, N. Kumagai, and Y. Kataoka, *Electrochim. Acta*, **47**, 1229 (2002).
32. T. Joshi, K. Eom, G. Yushin, and T. F. Fuller, *J. Electrochem. Soc.*, **161**, A1915 (2014).
33. M. Ochida, Y. Domi, T. Doi, S. Tsubouchi, H. Nakagawa, T. Yamanaka, A. Abouimrane, and Z. Ogumi, *J. Electrochem. Soc.*, **159**, A961 (2012).
34. D. Pritzl, J. Landesfeind, S. Solchenbach, and H. A. Gasteiger, *J. Electrochem. Soc.*, **165**, A2145 (2018).
35. C. Zhan, X. Qiu, J. Lu, and K. Amine, *Adv. Mater. Interfaces*, **3**, 1500856 (2016).
36. Y. K. Lee, J. Park, and W. Lu, *J. Electrochem. Soc.*, **164**, 2812 (2017).
37. H. Shin, J. Park, A. M. Sastry, and W. Lu, *J. Power Sources*, **284**, 416 (2015).
38. I. A. Shkrob, A. J. Kropf, T. W. Marin, Y. Li, O. G. Poluektov, J. Niklas, and D. P. Abraham, *J. Phys. Chem. C*, **118**, 24335 (2014).
39. C. Delacourt, A. Kwong, X. Liu, R. Qiao, W. L. Yang, P. Lu, S. J. Harris, and V. Srinivasan, *J. Electrochem. Soc.*, **160**, A1099 (2013).
40. T. Nordh, S. R. Younesi, M. Hahlin, R. F. Duarte, C. Tengstedt, D. Brandell, and K. Edström, *J. Phys. Chem. C*, **120**, 3206 (2016).
41. S. Komaba, T. Itabashi, T. Ohtsuka, H. Groult, N. Kumagai, B. Kaplan, and H. Yashiro, *J. Electrochem. Soc.*, **152**, A937 (2005).
42. X. Xiao, Z. Liu, L. Baggetto, G. M. Veith, K. L. More, and R. R. Unocic, *Phys. Chem. Chem. Phys.*, **16**, 10398 (2014).
43. S. R. Gowda, K. G. Gallagher, J. R. Croy, M. Bettge, M. M. Thackeray, and M. Balasubramanian, *Phys. Chem. Chem. Phys.*, **16**, 6898 (2014).
44. M. J. Aragon, C. Pérez-Vicente, and J. L. Tirado, *Electrochem. commun.*, **9**, 1744 (2007).
45. S. Mirhashemihaghighi, B. Leo, C. Pe, J. L. Tirado, and E. M. Arroyo, *Inorg. Chem.*, **51**, 5554 (2012).
46. Y. T. Teng, S. S. Pramana, J. Ding, T. Wu, and R. Yazami, *Electrochim. Acta*, **107**, 301 (2013).
47. D. H. Lee, K. J. Carroll, K. W. Chapman, O. J. Borkiewicz, S. Calvin, E. E. Fullerton, and Y. S. Meng, *Phys. Chem. Chem. Phys.*, **16**, 3095 (2014).
48. K. Rui, Z. Wen, Y. Lu, J. Jin, and C. Shen, *Adv. Energy Mater.*, **5**, 1401716 (2015).
49. Y.-K. Han, K. Lee, S. Kang, Y. Suk, and H. Lee, *Comput. Mater. Sci.*, **81**, 548 (2014).
50. K. Leung, *Chem. Mater.*, **29**, 2550 (2016).
51. R. Imhof and P. Novák, *J. Electrochem. Soc.*, **145**, 1081 (1998).
52. B. Zhang, M. Metzger, S. Solchenbach, M. Payne, S. Meini, H. A. Gasteiger, A. Garsuch, and B. L. Lucht, *J. Phys. Chem. C*, **119**, 11337 (2015).
53. N. Tsiouvaras, S. Meini, I. Buchberger, and H. A. Gasteiger, *J. Electrochem. Soc.*, **160**, A471 (2013).
54. M. Metzger, C. Marino, J. Sicklinger, D. Haering, and H. A. Gasteiger, *J. Electrochem. Soc.*, **162**, A1123 (2015).
55. B. Strehle, S. Solchenbach, M. Metzger, K. U. Schwenke, and H. A. Gasteiger, *J. Electrochem. Soc.*, **164**, A2513 (2017).
56. Y. Peng and P. Wu, *Polymer (Guildf).*, **45**, 5295 (2004).
57. D. Strmcnik, I. E. Castelli, J. G. Connell, D. Haering, M. Zorko, P. Martins, P. P. Lopes, B. Genorio, T. Østergaard, H. A. Gasteiger et al., *Nat. Catal.*, **1**, 255 (2018).
58. U. Heider, R. Oesten, and M. Jungnitz, *J. Power Sources*, 7 (1999).
59. D. Aurbach, Y. Gofer, M. Ben-Zion, and P. Aped, *J. Electroanal. Chem.*, **339**, 451 (1992).
60. M. Nie, D. Chalasani, D. P. Abraham, Y. Chen, A. Bose, and B. L. Lucht, *J. Phys. Chem. C*, **117**, 1257 (2013).

61. D. Aurbach, Y. Ein-Ely, and A. Zaban, *J. Electrochem. Soc.*, **141**, L1 (1994).
62. H. Ota, Y. Sakata, A. Inoue, and S. Yamaguchi, *J. Electrochem. Soc.*, **151**, A1659 (2004).
63. R. Bernhard, S. Meini, and H. A. Gasteiger, *J. Electrochem. Soc.*, **161**, A497 (2014).
64. R. Bernhard, M. Metzger, and H. A. Gasteiger, *J. Electrochem. Soc.*, **162**, A1984 (2015).
65. M. Onuki, S. Kinoshita, Y. Sakata, M. Yanagidate, Y. Otake, M. Ue, and M. Deguchi, *J. Electrochem. Soc.*, **155**, A794 (2008).
66. H. Yoshida, T. Fukunaga, T. Hazama, M. Terasaki, M. Mizutani, and M. Yamachi, *J. Power Sources*, **68**, 311 (1997).
67. K. Leung, *Chem. Phys. Lett.*, **568–569**, 1 (2013).
68. R. Mogi, M. Inaba, Y. Iriyama, T. Abe, and Z. Ogumi, *J. Power Sources*, **119–121**, 597 (2003).
69. A. L. Michan, B. S. Parimalam, M. Leskes, R. N. Kerber, T. Yoon, C. P. Grey, and B. L. Lucht, *Chem. Mater.*, **28**, 8149 (2016).
70. D. Pritzl, S. Solchenbach, M. Wetjen, and H. A. Gasteiger, *J. Electrochem. Soc.*, **164**, A2625 (2017).
71. L. Gireaud, S. Grugeon, S. Laruelle, S. Pilard, and J.-M. Tarascon, *J. Electrochem. Soc.*, **152**, A850 (2005).
72. D. M. Seo, D. Chalasani, B. S. Parimalam, R. Kadam, M. Nie, and B. L. Lucht, *ECS Electrochem. Lett.*, **3**, A91 (2014).
73. Y. Ein-Eli, B. Markovsky, D. Aurbach, Y. Carmeli, H. Yamin, and S. Luski, *Electrochim. Acta*, **39**, 2559 (1994).
74. P. Vanýsek, in *CRC Handbook of Chemistry and Physics*, W. Haynes, Editor, CRC Press LLC (2000).
75. B. S. Parimalam, A. D. Macintosh, R. Kadam, and B. L. Lucht, *J. Phys. Chem. C*, **121**, 22733 (2017).

4 Conclusions

The aim of this thesis was the investigation of electrolyte decomposition reactions in high-voltage Li-ion batteries, and the development of suitable experimental methods for this purpose. As the decomposition reactions of electrolyte components and their products are interrelated (see Figure 4.1), a separate examination of individual reactions can be challenging. Accordingly, this thesis used single-solvent model electrolytes in a 2-compartment cell setup to study reactions under well-defined conditions, but also employed Li-ion full cells with commercial electrolyte mixtures to evaluate the effect of additives on the full cell system. The use of different analytical techniques to examine the formation of solid electrolyte films (ATR-FTIR, NMR, impedance spectroscopy), to follow changes in the liquid electrolyte composition (NMR, OEMS in case of transesterification reactions), and to quantify the evolution of gas (OEMS), resulted in a comprehensive picture of the occurring reactions. In this context, a main point of this thesis was the development of a gold wire micro-reference electrode (GWRE) for impedance measurements of individual electrodes in full cells, which proved as a valuable tool to *in-situ* study film-formation processes on Li-ion battery electrodes.

To summarize the findings of this thesis, the reduction of ethylene carbonate (EC) to lithium ethylene dicarbonate (LEDC) and C_2H_4 on the anode side (see **(1)** in Figure 4.1) served as a starting point to evaluate the extent of electrolyte decomposition and the effectivity of SEI additives. We found that the use of vinylene carbonate (VC) lowered the decomposition of EC, while forming CO_2 and poly(VC)-type polycarbonate species **(2)** which accumulated and increased the anode resistance when VC was used in high concentrations. In this context, we demonstrated that electrolyte additives in lab-scale test cells are often "overdosed", as the higher relative amount of electrolyte compared to commercial-scale cells

results in a larger additive to active material ratio at the same nominal concentration.

Moreover, VC proved efficient in suppressing the transesterification of ethylmethyl carbonate (EMC) to dimethyl carbonate (DMC) and diethyl carbonate (DEC) caused by alkoxide (RO^-) species formed during EMC reduction **(3)**. A possible explanation for this effect is the trapping of alkoxides to lithium methylcarbonate (LMC) and lithium ethylcarbonate (LEC) with CO_2 from the VC reduction, as high concentrations of CO_2 by itself also stopped the EMC transesterification. We further found that CO_2 is electrochemically reduced to Li_2CO_3 **(4)**, although without the often-claimed release of CO, which points towards a different reduction mechanism than commonly assumed. Besides, the formation of small amounts of lithium formate from CO_2 indicated that CO_2 or its reduction intermediates can be effective in scavenging protons from the electrolyte.

The reduction of fluoroethylene carbonate (FEC) yielded similar product as the closely related molecule VC, namely CO_2 and poly(FEC) species, along with additional lithium fluoride **(5)**. Yet opposite to VC, high FEC concentrations did not lead to increased amounts of polycarbonates, and an SEI formed with FEC showed a significantly lower resistance compared to a VC-derived SEI. Apparently, the reduction of FEC on graphite is self-limiting, which allows its use as a co-solvent in high concentrations (> 10 wt%). For silicon-graphite anodes, the combination of FEC and CO_2 as additives proved to be particularly effective, as lithium oxalate, a cathode sacrificial salt which releases CO_2 during the initial charge, significantly lowered the FEC consumption and improved the capacity retention in LNMO/SiG full cells.

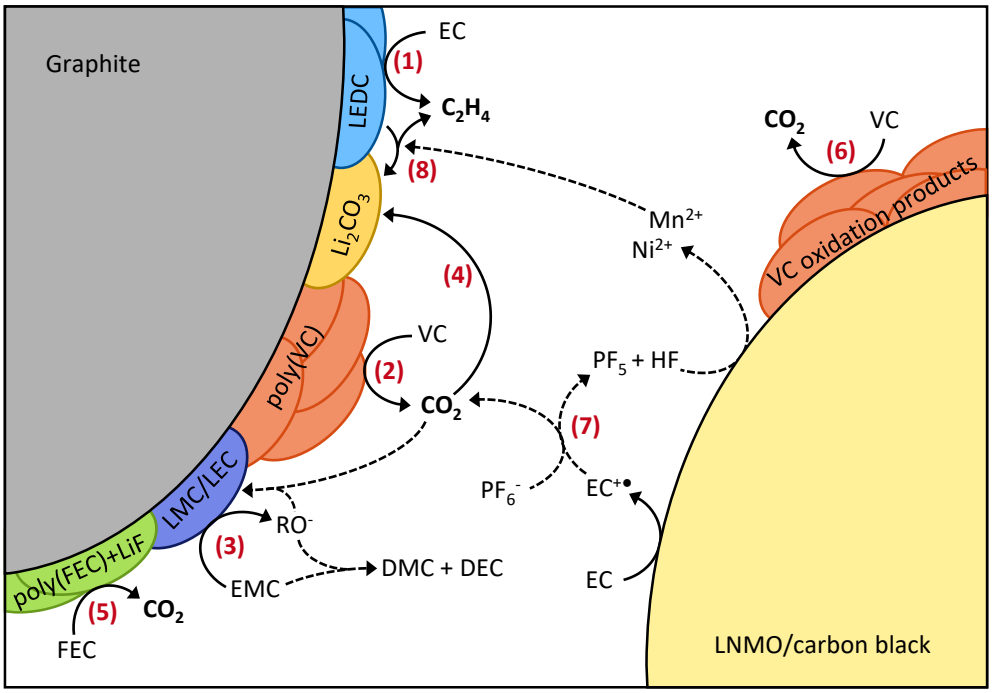

Figure 4.1: Graphical summary of selected investigated reaction mechanisms and their products; bold labels mark gaseous species as detected by OEMS. Solid arrows represent electrochemical reduction or oxidation reactions, whereas dashed arrows indicate chemical follow-up reaction of the created species.

As LNMO cathodes operate on the verge of the anodic stability limit of Li-ion battery electrolytes, we also took a closer look at electrolyte oxidation and related follow-up reactions. Besides CO_2, we found that the oxidation of VC creates highly resistive species **(6)**, which increase the LNMO cathode impedance and deteriorate cell performance, thereby consuming VC that would otherwise be incorporated into the SEI. Accordingly, only the lowest VC concentration tested showed an improved cycling performance, as here all VC was consumed at the anode **(2)** before the cathode potential exceeded the VC oxidation onset.

A proposed follow-up reaction of the oxidation of EC is the formation of PF_5 and HF by proton transfer between an oxidized EC radical cation and the PF_6^- anion **(7)**.[31] However, in previous experimental studies, POF_3 and CO_2 were the main gaseous oxidation products of EC/$LiPF_6$ electrolytes. Thus, we investigated the thermal, chemical and electrochemical decomposition reactions of $LiPF_6$ in more detail. Here, we found that PF_5 is detected as POF_3 by OEMS, thereby confirming the original hypothesis of HF formation. By model experiments with methanesulfonic

acid and water as proton sources, we further demonstrated that the radical cation species formed upon EC oxidation are highly acidic and readily release protons.

As a result of HF attack on the cathode active material, transition metal ions are dissolved into the electrolyte, where they accumulate at the anode and impair the SEI. To simulate this phenomenon, we investigated the effect of deliberately added Mn^{2+} and Ni^{2+} ions on the electrolyte and SEI decomposition reactions. While both transition metals amplified the amount of electrolyte decomposition during initial SEI formation, the detrimental effect of Mn^{2+} ions was significantly worse and persisted also during the cycles after formation. We found that Mn^{2+} ions trigger the decomposition of LEDC to Li_2CO_3 and C_2H_4 **(8)**, which leads to in additional electrolyte reduction and increased irreversible capacities. These results offer not only an explanation for the large discrepancy in capacity retention between LNMO/graphite full cells (where the amount of active lithium is limited) and LNMO/Li half cells (which contain a large lithium reservoir),[12] but could also be a reason for the better full cell performance of layered oxides with lower manganese contents.[192,193]

References

1. U. Eberle, B. Müller, and R. von Helmolt, *Energy Environ. Sci.*, **5**, 8780–8798 (2012).

2. D. Andre, S. J. Kim, P. Lamp, S. F. Lux, F. Maglia, O. Paschos, and B. Stiaszny, *J. Mater. Chem. A*, **3**, 6709–6732 (2015).

3. O. Gröger, H. A. Gasteiger, and J.-P. Suchsland, *J. Electrochem. Soc.*, **162**, A2605–A2622 (2015).

4. G. E. Blomgren, *J. Electrochem. Soc.*, **164**, A5019–A5025 (2017).

5. A. Manthiram, *ACS Cent. Sci.*, **3**, 1063–1069 (2017).

6. E. J. Berg, C. Villevieille, D. Streich, S. Trabesinger, and P. Novák, *J. Electrochem. Soc.*, **162**, A2468–A2475 (2015).

7. T. Yim, S.-G. Woo, S. H. Lim, W. Cho, J. H. Song, Y.-K. Han, and Y.-J. Kim, *J. Mater. Chem. A*, **3**, 6157–6167 (2015).

8. A. Freiberg, M. Metzger, D. Haering, S. Bretzke, S. Puravankara, T. Nilges, C. Stinner, C. Marino, and H. A. Gasteiger, *J. Electrochem. Soc.*, **161**, A2255–A2261 (2014).

9. R. Petibon, J. Xia, L. Ma, M. K. G. Bauer, K. J. Nelson, and J. R. Dahn, *J. Electrochem. Soc.*, **163**, A2571–A2578 (2016).

10. J. Xia, R. Petibon, D. Xiong, L. Ma, and J. R. Dahn, *J. Power Sources*, **328**, 124–135 (2016).

11. D. R. Gallus, R. Schmitz, R. Wagner, B. Hoffmann, S. Nowak, I. Cekic-Laskovic, R. W. Schmitz, and M. Winter, *Electrochim. Acta*, **134**, 393–398 (2014).

12. J.-H. Kim, N. P. W. Pieczonka, and L. Yang, *ChemPhysChem*, **15**, 1940–54 (2014).

13. D. J. Xiong, L. D. Ellis, R. Petibon, T. Hynes, Q. Q. Liu, and J. R. Dahn, *J. Electrochem. Soc.*, **164**, A340–A347 (2017).

14. R. Hausbrand, G. Cherkashinin, H. Ehrenberg, M. Gröting, K. Albe, C. Hess, and W. Jaegermann, *Mater. Sci. Eng. B Solid-State Mater. Adv. Technol.*, **192**, 3–25 (2015).

15. L. A.-W. Ellingsen, C. R. Hung, G. Majeau-Bettez, B. Singh, Z. Chen, M. S. Whittingham, and A. H. Strømman, *Nat. Nanotechnol.*, **11**, 1039–1051 (2016).

16. K. Amine, H. Tukamoto, H. Yasuda, and Y. Fujita, *J. Electrochem. Soc.*, **143**, 1607–1613 (1996).

17. J. R. Dahn and E. W. Fuller, *J. Power Sources*, **69**, 265–270 (1994).

18. J. Reed, G. Ceder, and A. Van Der Ven, *Electrochem. Solid-State Lett.*, **4**, A78 (2001).

19. A. Rougier, P. Gravereau, and C. Delmas, *J. Electrochem. Soc.*, **143**, 1168–1175 (1996).

20. Y. Wang, J. Jiang, and J. R. Dahn, *Electrochem. commun.*, **9**, 2534–2540 (2007).

21. R. Jung, M. Metzger, F. Maglia, C. Stinner, and H. A. Gasteiger, *J. Electrochem. Soc.*, **164**, A1361–A1377 (2017).

22. E. M. Erickson, F. Schipper, T. R. Penki, J. Shin, C. Erk, F. F. Chesneau, B. Markovsky, and D. Aurbach, *J. Electrochem. Soc.*, **164**, A6341–A6348 (2017).

23. H. J. Noh, S. Youn, C. S. Yoon, and Y. K. Sun, *J. Power Sources*, **233**, 121–130 (2013).

24. R. Jung, R. Morasch, P. Karayaylali, K. Phillips, F. Maglia, C. Stinner, Y. Shao-Horn, and H. A. Gasteiger, *J. Electrochem. Soc.*, **165**, A132–A141 (2018).

25. J. R. Dahn, *Phys. Rev. B*, **44**, 9170–9177 (1991).

26. O. Yariv, D. Hirshberg, E. Zinigrad, A. Meitav, D. Aurbach, M. Jiang, and B. R. Powell, *J. Electrochem. Soc.*, **161**, A1422–A1431 (2014).

27. M. Nie, D. Chalasani, D. P. Abraham, Y. Chen, A. Bose, and B. L. Lucht, *J. Phys. Chem. C*, **117**, 1257–1267 (2013).

28. K. Xu, *Chem. Rev.*, **104**, 4303–4418 (2004).

29. E. M. Erickson, F. Schipper, T. R. Penki, J. Shin, C. Erk, F. F. Chesneau, B. Markovsky, and D. Aurbach, *J. Electrochem. Soc.*, **164**, A6341–A6348 (2017).

30. H. Yang, G. V. Zhuang, and P. N. Ross, *J. Power Sources*, **161**, 573–579 (2006).

31. O. Borodin, W. Behl, and T. R. Jow, *J. Phys. Chem. C*, **117**, 8661–8682 (2013).

32. D. Strmcnik, I. E. Castelli, J. G. Connell, D. Haering, M. Zorko, P. Martins, P. P. Lopes, B. Genorio, T. Østergaard, H. A. Gasteiger, et al., *Nat. Catal.*, **1**, 255–262 (2018).

33. U. Heider, R. Oesten, and M. Jungnitz, *J. Power Sources*, **81–82**, 119–122 (1999).

34. M. Metzger, B. Strehle, S. Solchenbach, and H. A. Gasteiger, *J. Electrochem. Soc.*, **163**, A1219–A1225 (2016).

35. J. Wandt, A. Freiberg, A. Ogrodnik, and H. A. Gasteiger, *Mater. Today*, **21**, 825–833 (2018).

36. T. Ohzuku, S. Takeda, and M. Iwanaga, *J. Power Sources*, **81–82**, 90–94 (1999).

37. Q. Zhong, A. Bonakdarpour, M. Zhang, Y. Gao, and J. R. Dahn, *J. Electrochem. Soc.*, **144**, 205–213 (1997).

38. W. Choi and A. Manthiram, *J. Electrochem. Soc.*, **153**, A1760 (2006).

39. A. Manthiram, K. Chemelewski, and E.-S. Lee, *Energy Environ. Sci.*, **7**, 1339–1350 (2014).

40. Y. Dong, J. Demeaux, and B. L. Lucht, *J. Electrochem. Soc.*, **163**, 2413–2417 (2016).

41. H. Lee, S. Choi, S. Choi, H. Kim, Y. Choi, S. Yoon, and J.-J. Cho, *Electrochem. commun.*, **9**, 801–806 (2007).

42. M. N. Obrovac and L. Christensen, *Electrochem. Solid-State Lett.*, **7**, A93 (2004).

43. M. N. Obrovac, L. Christensen, D. B. Le, and J. R. Dahn, *J. Electrochem. Soc.*, **154**, A849 (2007).

44. N.-S. Choi, K. H. Yew, K. Y. Lee, M. Sung, H. Kim, and S.-S. Kim, *J. Power Sources*, **161**, 1254–1259 (2006).

45. E. Markevich, K. Fridman, R. Sharabi, R. Elazari, G. Salitra, H. E. Gottlieb, G. Gershinsky, A. Garsuch, G. Semrau, M. A. Schmidt, et al., *J. Electrochem. Soc.*, **160**, A1824–A1833 (2013).

46. H. Nakai, T. Kubota, A. Kita, and A. Kawashima, *J. Electrochem. Soc.*, **158**, A798 (2011).

47. M. Nie, D. P. Abraham, Y. Chen, A. Bose, and B. L. Lucht, *J. Phys. Chem. C*, **117**, 13403–13412 (2013).

48. R. Petibon, V. L. Chevrier, C. P. Aiken, D. S. Hall, S. R. Hyatt, R. Shunmugasundaram, and J. R. Dahn, *J. Electrochem. Soc.*, **163**, A1146–A1156 (2016).

49. R. Jung, M. Metzger, D. Haering, S. Solchenbach, C. Marino, N. Tsiouvaras, C. Stinner, and H. A. Gasteiger, *J. Electrochem. Soc.*, **163**, A1705–A1716 (2016).

50. M. Wetjen, D. Pritzl, R. Jung, S. Solchenbach, R. Ghadimi, and H. A. Gasteiger, *J. Electrochem. Soc.*, **164**, A2840–A2852 (2017).

51. M. Klett, J. A. Gilbert, K. Z. Pupek, S. E. Trask, and D. P. Abraham, *J. Electrochem. Soc.*, **164**, A6095–A6102 (2017).

52. K. Kimura, T. Matsumoto, H. Nishihara, T. Kasukabe, T. Kyotani, and H. Kobayashi, *J. Electrochem. Soc.*, **164**, A995–A1001 (2017).

53. T. Yoon, C. C. Nguyen, D. M. Seo, and B. L. Lucht, *J. Electrochem. Soc.*, **162**, A2325–A2330 (2015).

54. M. N. Obrovac and V. L. Chevrier, *Chem. Rev.*, **114**, 11444–11502 (2014).

55. A. N. Dey, *Thin Solid Films*, **43**, 131–171 (1977).

56. E. Peled, *J. Electrochem. Soc.*, **126**, 2047 (1979).

57. N. Paul, J. Wandt, S. Seidlmayer, S. Schebesta, M. J. Mühlbauer, O. Dolotko, H. A. Gasteiger, and R. Gilles, *J. Power Sources*, **345**, 85–96 (2017).

58. I. Buchberger, S. Seidlmayer, A. Pokharel, M. Piana, J. Hattendorff, P. Kudejova, R. Gilles, and H. A. Gasteiger, *J. Electrochem. Soc.*, **162**, A2737–A2746 (2015).

59. Y. Abu-Lebdeh and I. J. Davidson, *J. Electrochem. Soc.*, **156**, A60 (2009).

60. J. Heine, P. Hilbig, X. Qi, P. Niehoff, M. Winter, and P. Bieker, *J. Electrochem. Soc.*, **162**, A1094–A1101 (2015).

61. K. Xu, *J. Electrochem. Soc.*, **156**, A751 (2009).

62. R. Fong, U. von Sacken, and J. R. Dahn, *J. Electrochem. Soc.*, **137**, 2009 (1990).

63. M. Nie and B. L. Lucht, *J. Electrochem. Soc.*, **161**, A1001–A1006 (2014).

64. J. C. Burns, A. Kassam, N. N. Sinha, L. E. Downie, L. Solnickova, B. M. Way, and J. R. Dahn, *J. Electrochem. Soc.*, **160**, A1451–A1456 (2013).

65. D. Aurbach, K. Gamolsky, B. Markovsky, Y. Gofer, M. A. Schmidt, and U. Heider, *Electrochim. Acta*, **47**, 1423–1439 (2002).

66. S. S. Zhang, *J. Power Sources*, **162**, 1379–1394 (2006).

67. D. Y. Wang and J. R. Dahn, *J. Electrochem. Soc.*, **161**, A1890–A1897 (2014).

68. H. H. Lee, Y. Y. Wang, C. C. Wan, M. H. Yang, H.-C. Wu, and D.-T. Shieh, *J. Appl. Electrochem.*, **35**, 615–623 (2005).

69. M. Herstedt, H. Rensmo, H. Siegbahn, and K. Edström, *Electrochim. Acta*, **49**, 2351–2359 (2004).

70. J. C. Burns, R. Petibon, K. J. Nelson, N. N. Sinha, A. Kassam, B. M. Way, and J. R. Dahn, *J. Electrochem. Soc.*, **160**, A1668–A1674 (2013).

71. W. Lu, Z. Chen, H. Joachin, J. Prakash, J. Liu, and K. Amine, *J. Power Sources*, **163**, 1074–1079 (2007).

72. L. J. Krause, V. L. Chevrier, L. D. Jensen, and T. Brandt, *J. Electrochem. Soc.*, **164**, A2527–A2533 (2017).

73. J. Wandt, C. Marino, H. A. Gasteiger, P. Jakes, R.-A. Eichel, and J. Granwehr, *Energy Environ. Sci.*, **8**, 1358–1367 (2015).

74. D. Aurbach, Y. Gofer, M. Ben-Zion, and P. Aped, *J. Electroanal. Chem.*, **339**, 451–471 (1992).

75. T. Osaka, T. Momma, T. Tajima, and Y. Matsumoto, *J. Electrochem. Soc.*, **142**, 1057 (1995).

76. R. Mogi, M. Inaba, S.-K. Jeong, Y. Iriyama, A. Abouimrane, and Z. Ogumi, *J. Electrochem. Soc.*, **149**, A1578 (2002).

77. A. J. Loebl, C. J. Oldham, C. K. Devine, B. Gong, S. E. Atanasov, G. N. Parsons, and P. S. Fedkiw, *J. Electrochem. Soc.*, **160**, A1971–A1978 (2013).

78. A. M. Andersson, K. Edström, N. Rao, and Å. Wendsjö, *J. Power Sources*, **81–82**, 286–290 (1999).

79. H. Bryngelsson, M. Stjerndahl, T. Gustafsson, and K. Edström, *J. Power Sources*, **174**, 970–975 (2007).

80. L. El Ouatani, R. Dedryvère, C. Siret, P. Biensan, and D. Gonbeau, *J. Electrochem. Soc.*, **156**, A468 (2009).

81. L. El Ouatani, R. Dedryvère, C. Siret, P. Biensan, S. Reynaud, P. Iratçabal, and D. Gonbeau, *J. Electrochem. Soc.*, **156**, A103 (2009).

82. L. Gireaud, S. Grugeon, S. Laruelle, S. Pilard, and J.-M. Tarascon, *J. Electrochem. Soc.*, **152**, A850 (2005).

83. D. M. Seo, D. Chalasani, B. S. Parimalam, R. Kadam, M. Nie, and B. L. Lucht, *ECS Electrochem. Lett.*, **3**, A91–A93 (2014).

84. B. S. Parimalam and B. L. Lucht, *J. Electrochem. Soc.*, **165**, 251–255 (2018).

85. M. Nie, J. Demeaux, B. T. Young, D. R. Heskett, Y. Chen, A. Bose, J. C. Woicik, and B. L. Lucht, *J. Electrochem. Soc.*, **162**, A7008–A7014 (2015).

86. A. L. Michan, B. S. Parimalam, M. Leskes, R. N. Kerber, T. Yoon, C. P. Grey, and B. L. Lucht, *Chem. Mater.*, **28**, 8149–8159 (2016).

87. D. Aurbach, M. L. Daroux, P. W. Faguy, and E. Yeager, *J. Electrochem. Soc.*, **134**, 1611–1620 (1987).

88. D. Aurbach, *J. Electrochem. Soc.*, **136**, 3198 (1989).

89. D. Aurbach, Y. Ein-Eli, O. Chusid, Y. Carmeli, M. Babai, and H. Yamin, *J. Electrochem. Soc.*, **141**, 603–611 (1994).

90. D. Aurbach, A. Zaban, Y. Gofer, Y. E. Ely, I. Weissman, O. Chusid, and O. Abramson, *J. Power Sources*, **54**, 76–84 (1995).

91. D. Aurbach, Y. Ein-Ely, and A. Zaban, *J. Electrochem. Soc.*, **141**, L1 (1994).

92. A. N. Dey and B. P. Sullivan, *J. Electrochem. Soc.*, **117**, 222 (1970).

93. R. Imhof and P. Novák, *J. Electrochem. Soc.*, **145**, 3313–3319 (1998).

94. M. Winter, R. Imhof, F. Joho, and P. Novák, *J. Power Sources*, **81–82**, 818–823 (1999).

95. H. Ota, Y. Sakata, A. Inoue, and S. Yamaguchi, *J. Electrochem. Soc.*, **151**, A1659 (2004).

96. F. La Mantia and P. Novák, *Electrochem. Solid-State Lett.*, **11**, A84 (2008).

97. M. Onuki, S. Kinoshita, Y. Sakata, M. Yanagidate, Y. Otake, M. Ue, and M. Deguchi, *J. Electrochem. Soc.*, **155**, A794 (2008).

98. H. Yoshida, T. Fukunaga, T. Hazama, M. Terasaki, M. Mizutani, and M. Yamachi, *J. Power Sources*, **68**, 311–315 (1997).

99. E. Endo, M. Ata, K. Tanaka, and K. Sekai, *J. Electrochem. Soc.*, **145**, 3757–3764 (1998).

100. T. Li and P. B. Balbuena, *Chem. Phys. Lett.*, **317**, 421–429 (2000).

101. Y. Wang, S. Nakamura, M. Ue, and P. B. Balbuena, *J. Am. Chem. Soc.*, **123**, 11708–11718 (2001).

102. K. Leung, *Chem. Phys. Lett.*, **568–569**, 1–8 (2013).

103. Y. Wang, S. Nakamura, K. Tasaki, and P. B. Balbuena, *J. Am. Chem. Soc.*, **124**, 4408–4421 (2002).

104. K. Leung, S. B. Rempe, M. E. Foster, Y. Ma, J. M. Martinez del la Hoz, N. Sai, and P. B. Balbuena, *J. Electrochem. Soc.*, **161**, A213–A221 (2014).

105. J. M. Martinez del la Hoz and P. B. Balbuena, *Phys. Chem. Chem. Phys.*, **16**, 17091–8 (2014).

106. F. A. Soto, Y. Ma, J. M. Martinez del la Hoz, J. M. Seminario, and P. B. Balbuena, *Chem. Mater.*, acs.chemmater.5b03358 (2015).

107. E. S. Takeuchi, H. Gan, M. Palazzo, R. A. Leising, and S. M. Davis, *J. Electrochem. Soc.*, **144**, 1944–1948 (1997).

108. B. Zhang, M. Metzger, S. Solchenbach, M. Payne, S. Meini, H. A. Gasteiger, A. Garsuch, and B. L. Lucht, *J. Phys. Chem. C*, 150512180451000 (2015).

109. R. Petibon, E. C. Henry, J. C. Burns, N. N. Sinha, and J. R. Dahn, *J. Electrochem. Soc.*, **161**, A66–A74 (2013).

110. V. Etacheri, O. Haik, Y. Goffer, G. A. Roberts, I. C. Stefan, R. Fasching, and D. Aurbach, *Langmuir*, **28**, 965–76 (2012).

111. M. E. Spahr, T. Palladino, H. Wilhelm, A. Würsig, D. Goers, H. Buqa, M. Holzapfel, and P. Novák, *J. Electrochem. Soc.*, **151**, A1383–A1395 (2004).

112. I. A. Profatilova, S.-S. Kim, and N.-S. Choi, *Electrochim. Acta*, **54**, 4445–4450 (2009).

113. D. Y. Wang, N. N. Sinha, J. C. Burns, C. P. Aiken, R. Petibon, and J. R. Dahn, *J. Electrochem. Soc.*, **161**, 467–472 (2014).

114. Y. Ein-Eli, B. Markovsky, D. Aurbach, Y. Carmeli, H. Yamin, and S. Luski, *Electrochim. Acta*, **39**, 2559–2569 (1994).

115. L. D. Ellis, J. P. Allen, L. M. Thompson, J. E. Harlow, W. J. Stone, I. G. Hill, and J. R. Dahn, *J. Electrochem. Soc.*, **164**, A3518–A3528 (2017).

116. V. F. Lvovich, in *Impedance Spectroscopy*,, p. 1–21 (2012).

117. J. Y. Song, H. H. Lee, Y. Y. Wang, and C. C. Wan, *J. Power Sources*, **111**, 255–267 (2002).

118. C. H. Chen, J. Liu, and K. Amine, *J. Power Sources*, **96**, 321–328 (2001).

119. R. Petibon, C. P. Aiken, N. N. Sinha, J. C. Burns, H. Ye, C. M. VanElzen, G. Jain, S. Trussler, and J. R. Dahn, *J. Electrochem. Soc.*, **160**, A117–A124 (2013).

120. S. N. Victoria and S. Ramanathan, *Electrochim. Acta*, **56**, 2606–2615 (2011).

121. D. W. Dees, A. N. Jansen, and D. P. Abraham, *J. Power Sources*, **174**, 1001–1006 (2007).

122. M. Ender, A. Weber, and E. Ivers-Tiffée, *J. Electrochem. Soc.*, **159**, A128 (2012).

123. S. Klink, E. Madej, E. Ventosa, A. Lindner, W. Schuhmann, and F. La Mantia, *Electrochem. commun.*, **22**, 120–123 (2012).

124. S. Klink, D. Höche, F. La Mantia, and W. Schuhmann, *J. Power Sources*, **240**, 273–280 (2013).

125. C. Delacourt, P. Ridgway, V. Srinivasan, and V. S. Battaglia, *J. Electrochem. Soc.*, **161**, A1253–A1260 (2014).

126. C. Bünzli, H. Kaiser, and P. Novák, *J. Electrochem. Soc.*, **162**, A218–A222 (2015).

127. M. D. Levi, V. Dargel, Y. Shilina, D. Aurbach, and I. C. Halalay, *Electrochim. Acta*, **149**, 126–135 (2014).

128. L. H. J. Raijmakers, M. J. G. Lammers, and P. H. L. Notten, *Electrochim. Acta*, **259**, 517–533 (2018).

129. J. Costard, M. Ender, M. Weiss, and E. Ivers-Tiffée, *J. Electrochem. Soc.*, **164**, 80–87 (2017).

130. F. La Mantia, C. D. D. Wessells, H. D. D. Deshazer, and Y. Cui, *Electrochem. commun.*, **31**, 141–144 (2013).

131. M. W. Verbrugge, D. R. Baker, and B. J. Koch, *J. Power Sources*, **110**, 295–309 (2002).

132. J. L. Gómez-Cámer and P. Novák, *Electrochem. commun.*, **34**, 208–210 (2013).

133. D. P. Abraham, S. D. Poppen, A. N. Jansen, J. Liu, and D. W. Dees, *Electrochim. Acta*, **49**, 4763–4775 (2004).

134. F. J. Simon, L. Blume, M. Hanauer, U. Sauter, and J. Janek, *J. Electrochem. Soc.*, **165**, A1363–A1371 (2018).

135. V. R. Koch, C. Nanjundiah, G. B. Appetecchi, and B. Scrosati, *J. Electrochem. Soc.*, **142**, L116 (1995).

136. M. Ender, J. Illig, and E. Ivers-Tiffée, *J. Electrochem. Soc.*, **164**, 71–79 (2017).

137. D. R. Baker, M. W. Verbrugge, and X. X. Hou, *J. Electrochem. Soc.*, **164**, A407–A417 (2017).

138. J. Zhou and P. H. L. Notten, *J. Electrochem. Soc.*, **151**, A2173 (2004).

139. P. Bach, M. Stratmann, I. Valencia-Jaime, A. H. Romero, and F. U. Renner, *Electrochim. Acta*, **164**, 81–89 (2015).

140. K. Nishio, K. Yuda, and H. Masuda, *ECS Electrochem. Lett.*, **2**, C1–C3 (2012).

141. G. Taillades, N. Benjelloun, J. Sarradin, and M. Ribes, *Solid State Ionics*, **152–153**, 119–124 (2002).

142. J. Landesfeind, D. Pritzl, and H. A. Gasteiger, *J. Electrochem. Soc.*, **164**, A1773–A1783 (2017).

143. D. Pritzl, J. Landesfeind, S. Solchenbach, and H. A. Gasteiger, *J. Electrochem. Soc.*, **165**, A2145-2153 (2018).

144. J. Landesfeind, J. Hattendorff, A. Ehrl, W. A. Wall, and H. A. Gasteiger, *J. Electrochem. Soc.*, **163**, A1373–A1387 (2016).

145. J. Illig, M. Ender, A. Weber, and E. Ivers-Tiffée, *J. Power Sources*, **282**, 335–347 (2015).

146. N. Ogihara, S. Kawauchi, C. Okuda, Y. Itou, Y. Takeuchi, and Y. Ukyo, *J. Electrochem. Soc.*, **159**, A1034–A1039 (2012).

147. N. Ogihara, Y. Itou, T. Sasaki, and Y. Takeuchi, *J. Phys. Chem. C*, **119**, 4612–4619 (2015).

148. J. Landesfeind, M. Ebner, A. Eldiven, V. Wood, and H. A. Gasteiger, **165**, 469–476 (2018).

149. M. D. Levi and D. Aurbach, *J. Phys. Chem. B*, **5647**, 4630–4640 (1997).

150. H. Schranzhofer, J. Bugajski, H. J. Santner, C. Korepp, J. O. Besenhard, M. Winter, and W. Sitte, **153**, 391–395 (2006).

151. M. Gaberscek, J. Moskon, B. Erjavec, R. Dominko, and J. Jamnik, *Electrochem. Solid-State Lett.*, **11**, A170 (2008).

152. M. Steinhauer, S. Risse, N. Wagner, and K. A. Friedrich, *Electrochim. Acta*, **228**, 652–658 (2017).

153. M. Arakawa and J. Yamaki, *J. Power Sources*, **54**, 250–254 (1995).

154. R. Imhof and P. Novák, *J. Electrochem. Soc.*, **146**, 1702–1706 (1998).

155. M. Metzger, B. Strehle, S. Solchenbach, and H. A. Gasteiger, *J. Electrochem. Soc.*, **163**, A798–A809 (2016).

156. H. Ota, K. Shima, M. Ue, and J. Yamaki, *Electrochim. Acta*, **49**, 565–572 (2004).

157. R. Bernhard, S. Meini, and H. A. Gasteiger, *J. Electrochem. Soc.*, **161**, A497–A505 (2014).

158. N. Tsiouvaras, S. Meini, I. Buchberger, and H. A. Gasteiger, *J. Electrochem. Soc.*, **160**, A471–A477 (2013).

159. S. Meini, M. Piana, H. Beyer, J. Schwammlein, and H. A. Gasteiger, *J. Electrochem. Soc.*, **159**, A2135–A2142 (2012).

160. M. Metzger, C. Marino, J. Sicklinger, D. Haering, and H. A. Gasteiger, *J. Electrochem. Soc.*, **162**, A1123–A1134 (2015).

161. M. Metzger, *PhD thesis* (2017).

162. M. R. Busche, T. Drossel, T. Leichtweiss, D. A. Weber, M. Falk, M. Schneider, M.-L. Reich, H. Sommer, P. Adelhelm, and J. Janek, *Nat. Chem.*, 1–9 (2016).

163. M. Egawa, (2017).

164. H.-G. Schweiger, M. Multerer, U. Wietelmann, J.-C. Panitz, T. Burgemeister, and H. J. Gores, *J. Electrochem. Soc.*, **152**, A622 (2005).

165. C. L. Campion, W. Li, W. B. Euler, B. L. Lucht, B. Ravdel, J. F. DiCarlo, R. Gitzendanner, and D. P. Abraham, *Electrochem. Solid-State Lett.*, **7**, A194 (2004).

166. C. L. Campion, W. Li, and B. L. Lucht, *J. Electrochem. Soc.*, **152**, A2327 (2005).

167. S. Wilken, M. Treskow, J. Scheers, P. Johansson, and P. Jacobsson, *RSC Adv.*, **3**, 16359–16364 (2013).

168. P. Handel, G. Fauler, K. Kapper, M. Schmuck, C. Stangl, R. Fischer, F. Uhlig, and S. Koller, *J. Power Sources*, **267**, 255–259 (2014).

169. S. L. Guillot, A. Peña-Hueso, M. L. Usrey, and R. J. Hamers, *J. Electrochem. Soc.*, **164**, A1907–A1917 (2017).

170. A. V. Plakhotnyk, L. Ernst, and R. Schmutzler, *J. Fluor. Chem.*, **126**, 27–31 (2005).

171. R. Yazami and A. Martinent, in *Fluorinated Materials for Energy Conversion*, T. Nakajima and H. Groult, Editors, p. 173, Elsevier Ltd (2005).

172. L. Ma, L. D. Ellis, S. L. Glazier, X. Ma, Q. Liu, J. Li, and J. R. Dahn, **165**, 891–899 (2018).

173. M. Wetjen, G. Hong, S. Solchenbach, D. Pritzl, and H. A. Gasteiger, *Manuscr. Prep.*

174. I. A. Profatilova, T. Langer, J. P. Badillo, A. Schmitz, H. Orthner, H. Wiggers, S. Passerini, and M. Winter, *J. Electrochem. Soc.*, **159**, A657 (2012).

175. Y.-M. Song, J.-G. Han, S. Park, K. T. Lee, and N.-S. Choi, *J. Mater. Chem. A*, **2**, 9506–9513 (2014).

176. D. Shanmukaraj, S. Grugeon, S. Laruelle, G. Douglade, J.-M. Tarascon, and M. Armand, *Electrochem. commun.*, **12**, 1344–1347 (2010).

177. Y. Hu, W. Kong, H. Li, X. Huang, and L. Chen, *Electrochem. commun.*, **6**, 126–131 (2004).

178. J. Dumas and E. Peligot, *Justus Liebigs Ann. Chem.*, **35**, 281–292 (1840).

179. Y. Qiao, J. Yi, S. Wu, Y. Liu, S. Yang, P. He, and H. Zhou, *Joule*, **1**, 359–370 (2017).

180. Y. Liu, R. Wang, Y. Lyu, H. Li, and L. Chen, *Energy Environ. Sci.*, **7**, 677 (2014).

181. A. Guéguen, D. Streich, M. He, M. A. Mendez, F. F. Chesneau, P. Novák, and E. J. Berg, *J. Electrochem. Soc.*, **163**, A1095–A1100 (2016).

182. C. Zhan, T. Wu, J. Lu, and K. Amine, *Energy Environ. Sci.*, **11**, 243–257 (2018).

183. M. Metzger, J. Sicklinger, D. Haering, C. Kavakli, C. Stinner, C. Marino, and H. A. Gasteiger, *J. Electrochem. Soc.*, **162**, A1227–A1235 (2015).

184. M. Metzger, P. Walke, S. Solchenbach, G. Salitra, D. Aurbach, and H. A. Gasteiger, *Manuscr. Prep.* (2018).

185. R. Jung, M. Metzger, F. Maglia, C. Stinner, and H. A. Gasteiger, *J. Phys. Chem. Lett.*, **8**, 4820–4825 (2017).

186. C. Zhan, J. Lu, A. J. Kropf, T. Wu, A. N. Jansen, Y.-K. Sun, X. Qiu, and K. Amine, *Nat. Commun.*, **4**, 2437 (2013).

187. C. Zhan, X. Qiu, J. Lu, and K. Amine, *Adv. Mater. Interfaces*, **3**, 1500856–1500862 (2016).

188. C. Delacourt, A. Kwong, X. Liu, R. Qiao, W. L. Yang, P. Lu, S. J. Harris, and V. Srinivasan, *J. Electrochem. Soc.*, **160**, A1099–A1107 (2013).

189. D. R. Vissers, Z. Chen, Y. Shao, M. H. Engelhard, U. Das, P. C. Redfern, L. A. Curtiss, B. Pan, J. Liu, and K. Amine, *ACS Appl. Mater. Interfaces*, **8**, 14244–14251 (2016).

190. R. Jung, F. Linsenmann, R. Thomas, J. Wandt, S. Solchenbach, F. Maglia, C. Stinner, M. Tromp, and H. A. Gasteiger, *J. Electrochem. Soc.*, **166**, A378–A389 (2019).

191. J. Wandt, A. Freiberg, R. Thomas, Y. Gorlin, A. Siebel, R. Jung, H. A. Gasteiger, and M. Tromp, *J. Mater. Chem. A*, **4**, 18300–18305 (2016).

192. J. A. Gilbert, I. A. Shkrob, and D. P. Abraham, *J. Electrochem. Soc.*, **164**, A389–A399 (2017).

193. L. De Biasi, A. O. Kondrakov, H. Geßwein, T. Brezesinski, P. Hartmann, and J. Janek, *J. Phys. Chem. C*, **121**, 26163–26171 (2017).

Acknowledgements

First of all, I would like to thank Prof. Hubert A. Gasteiger for giving me the wonderful opportunity to work and to learn in his group. Thank you for your inspirational guidance and encouraging support. Your commitment to science and the knowledge and energy you share with us are the roots of the work in this thesis. Many thanks go to Veronika Pichler for her dedication to keep the chair running. Thank you for your tremendous help and patience.

I also thank all current and former members of the Chair of Technical Electrochemistry who keep this great place of curiosity and collaboration alive. I'm proud and happy to have been sharing this with you. Special thanks go to Anna Freiberg, Benjamin Strehle, Michael Metzger, Morten Wetjen, Daniel Pritzl and Johannes Landesfeind for their hands-on support and our helpful discussions. Furthermore, I would like to thank Gülen Ceren Tok for the great office atmosphere (yes you are the funniest person) and Armin Siebel for his technical and moral backing since day 1. A big "thank you" goes to my former students Benjamin Strehle, Daniel Pritzl, Edmund Kong, Michael Szostak, Gloria Hong, Masamitsu Egawa, Jianing Hu, Xinyi Huang, and Susanne Pieper, for their enthusiasm, time, and very good questions.

I especially thank Prof. Michele Pavone, Prof. Ana Muñoz-García and the FPM3 group at the University of Naples Federico II, who allowed me a wonderful stay in Naples and an extremely insightful crash course on computational chemistry. Thank you for giving me such a good time.

I also acknowledge the financial support and scientific exchange provided by BASF SE through its network on electrochemistry. I want to thank Prof. Brett L. Lucht and his group at the University of Rhode Island, USA, for the great collaborations that have emerged during this time. Also, I thank the German Academic Exchange Service (DAAD), the ECS Battery Division and the Gesellschaft Deutscher Chemiker (GDCh) for travel scholarships to the 2016 ECS PRiME in Honolulu (USA), the 231st ECS meeting in New Orleans (USA) and the 2018 AiMES in Cancun (Mexico).

Lastly, I would like to thank my family and Klemens Niehues for their unconditional support and invaluable input throughout my PhD time.

Scientific Contributions

Articles

K. U. Schwenke,[=] **S. Solchenbach**,[=] J. Demeaux, B. L. Lucht, and H. A. Gasteiger, "The Impact of CO_2 Evolved from VC and FEC during Formation of Graphite Anodes in Lithium-Ion Batteries", *submitted*.

T. Teufl, D. Pritzl, **S. Solchenbach**, H. A. Gasteiger, and M. Mendez, "State of Charge Dependent Resistance Build-Up in Li- and Mn-Rich Layered Oxides During Lithium Extraction and Insertion", *submitted.*

D. Pritzl, A. Bumberger, M. Wetjen, J. Landesfeind, **S. Solchenbach**, and H. A. Gasteiger, "Identifying Contact Resistances in High-Voltage Cathodes by Impedance Spectroscopy", *Journal of the Electrochemical Society*, **166** (4), A582-A590 (2019).

R. Jung, F. Linsenmann, R. Thomas, J. Wandt, **S. Solchenbach**, F. Maglia, C. Stinner, M. Tromp, and H. A. Gasteiger, "Nickel, Manganese, and Cobalt Dissolution from Ni-rich NMC and Their Effects on NMC622-graphite cells", *Journal of the Electrochemical Society*, **166** (2), A378-A389 (2019).

S. Solchenbach, G. Hong, A. T. S. Freiberg, R. Jung, and H. A. Gasteiger, "Investigating Electrolyte and SEI Decomposition Reactions by Transition Metal Ions with On-line Electrochemical Mass Spectrometry", *Journal of the Electrochemical Society*, **165** (14), A3304-A3312 (2018)

S. Solchenbach,[=] M. Metzger,[=] M. Egawa, H. Beyer, and H. A. Gasteiger, "Quantification of PF_5 and POF_3 from side reactions of $LiPF_6$ in Li-ion batteries", *Journal of the Electrochemical Society*, **165** (13), A3022-A3028 (2018)

D. Pritzl,[=] J. Landesfeind,[=] **S. Solchenbach**, and H. A. Gasteiger, "An Analysis Protocol for Three-Electrode Li-Ion Battery Impedance Spectra: Part II. Analysis of a Graphite Anode Cycled vs. LNMO", *Journal of the Electrochemical Society*, **165** (10), A2145-A2153 (2018).

[=] equal contribution

M. Wetjen, **S. Solchenbach**, D. Pritzl, J. Hou, V. Tileli, and H. A. Gasteiger, "Morphological Changes of Silicon Nanoparticles and the Influence of Cutoff Potentials in Silicon-Graphite Electrodes", *Journal of the Electrochemical Society*, **165** (7), A1503-A1514 (2018).

S. Solchenbach, M. Wetjen, D. Pritzl, K. U. Schwenke, and H. A. Gasteiger, "Lithium Oxalate as Capacity and Cycle-Life Enhancer in LNMO/Graphite and LNMO/SiG Full Cells" *Journal of the Electrochemical Society*, **165** (3), A512-A524 (2018).

M. Wetjen, D. Pritzl, R. Jung, **S. Solchenbach**, R. Ghadimi, and H. A. Gasteiger, "Differentiating the Degradation Phenomena in Silicon-Graphite Electrodes for Lithium-Ion Batteries" *Journal of the Electrochemical Society*, **164** (12), A2840-A2852 (2017).

D. Pritzl, **S. Solchenbach**, M. Wetjen, and H. A. Gasteiger, "Analysis of Vinylene Carbonate (VC) as Additive in Graphite/$LiNi_{0.5}Mn_{1.5}O_4$ Cells", *Journal of the Electrochemical Society*, **164** (12), A2625-A2635 (2017).

B. Strehle, **S. Solchenbach**, M. Metzger, K. U. Schwenke, and H. A. Gasteiger, "The Effect of CO_2 on Alkyl Carbonate Trans-Esterification during Formation of Graphite Electrodes in Li-Ion Batteries", *Journal of the Electrochemical Society*, **164** (12), A2513-A2526 (2017).

S. Solchenbach, D. Pritzl, E. Kong, J. Landesfeind, and H. A. Gasteiger, "A Gold Micro-Reference Electrode for Potential and Impedance Measurements in Lithium Ion Batteries" *Journal of the Electrochemical Society*, **163** (10), A2265-A2272 (2016).

R. Jung, M. Metzger, D. Haering, **S. Solchenbach**, C. Marino, N. Tsiouvaras, C. Stinner, and H. A. Gasteiger, "Consumption of Fluoroethylene Carbonate (FEC) on Si-C Composite Electrodes for Li-Ion Batteries", *Journal of the Electrochemical Society*, **163** (8), A1705-A1716 (2016).

M. Metzger, B. Strehle, **S. Solchenbach**, and H. A. Gasteiger, "Hydrolysis of Ethylene Carbonate with Water and Hydroxide under Battery Operating Conditions" *Journal of the Electrochemical Society*, **163** (7), A1219-A1225 (2016).

M. Metzger, B. Strehle, **S. Solchenbach**, H. A, Gasteiger, "Origin of H_2 Evolution in LIBs: H_2O Reduction vs. Electrolyte Oxidation", *Journal of the Electrochemical Society*, 163 (5), A798-A809 (2016).

B. Zhang, M. Metzger, **S. Solchenbach**, M. Payne, S. Meini, H. A. Gasteiger, A. Garsuch, and B. L. Lucht, "Role of 1,3-Propane Sultone and Vinylene Carbonate in Solid Electrolyte Interface Formation and Gas Generation" *Journal of Physical Chemistry C*, **119** (21), 11337-11348 (2015).

S. Meini, **S. Solchenbach**, M. Piana, and H. A. Gasteiger, "The Role of Electrolyte Solvent Stability and Electrolyte Impurities in the Electrooxidation of Li_2O_2 in Li-O_2 Batteries" *Journal of the Electrochemical Society*, **161** (9), A1306-A1314 (2014).

Articles in preparation

S. Solchenbach, J. Landesfeind, X. Huang, D. Pritzl, and H. A. Gasteiger, "Monitoring SEI Formation on Graphite Anodes by Impedance Spectroscopy", *manuscript in preparation*.

M. Wetjen, G. Hong, **S. Solchenbach**, D. Pritzl, and H.A. Gasteiger, "Evaluating EC, FEC, and DiFEC as Electrolyte Constituents for Silicon-Graphite Electrodes: Reduction Mechanism and Consumption," *manuscript in preparation*.

N. Laszczynski, **S. Solchenbach**, H. A. Gasteiger, B. L. Lucht, "Understanding Electrolyte Decomposition of Graphite/NCM811 Cells at Elevated Operating Voltage", *manuscript in preparation*.

Oral presentations

"Monitoring SEI Resistance during Formation of Li-ion Batteries by Impedance Spectroscopy", Americas International Meeting in Electrochemistry and Solid State Science (AiMES), Cancun, Mexico, Abstract #442 (October 2018).

"Electrolyte Decomposition on Graphite Anodes in the Presence of Transition Metal Ions", 231st Meeting of the Electrochemical Society, New Orleans, Louisiana, USA, Abstract #219 (May 2017).

"A Micro-Reference Electrode for Potential and Impedance Measurements in Li-Ion Batteries" Pacific Rim Meeting on Electrochemical and Solid-State Science (PRiME), Honolulu, Hawaii, USA, Abstract #211 (October 2016).

"A Comparative Study of the Anodic and Cathodic Decomposition of EC, VC and FEC", 228th Meeting of the Electrochemical Society, Phoenix, Arizona, USA, Abstract #362 (October 2015).

Poster presentations

"Monitoring SEI Resistance during Formation by Impedance Spectroscopy", Gordon Research Conference & Seminar on Batteries, Ventura, California, USA (February 2018).

"Lithium Oxalate As Capacity Enhancer in $LiMn_{1.5}Ni_{0.5}O_4$/Graphite and $LiMn_{1.5}Ni_{0.5}O_4$/Si:G Full Cells", 232nd Meeting of the Electrochemical Society, National Harbor, Maryland, USA, Abstract #393 (October 2017).